学 位 論 文

Development of a Time-Resolved Method and Electric Quadrupolar Theory for Heterodyne-Detected Vibrational Sum Frequency Generation at Air/Liquid Interfaces

（気液界面におけるヘテロダイン検出振動和周波発生のための時間分解測定法と電気四極子理論の開発）

平成 25 年 12 月 博士（理学）申請

東京大学大学院理学系研究科
化学専攻

松 﨑　維 信

Abstract

Interfaces play a crucial role in various chemical, physical, and biological processes. Air/liquid interfaces are often utilized as the model of those interfaces, and heterodyne-detected vibrational sum frequency generation (HD-VSFG) spectroscopy is now regarded as one of the most powerful techniques for studying those interfaces. However, there are two cases in which HD-VSFG spectroscopy has never been utilized: It has never been used to study the short-lived transient species in chemical reactions, and it has never been applied to the interfaces where the ordinary dipolar mechanism of VSFG fails. This thesis reports experimental and theoretical developments to realize the application of HD-VSFG to these two cases.

First, from the experimental perspective, UV-excited time-resolved HD-VSFG spectroscopy is developed to enable the observation of short-lived intermediate species in chemical reactions in the interface-selective manner. In this method, chemical reactions are initiated by the electronic excitation of molecules by the UV pump light, and after a certain delay, the transient species are probed by HD-VSFG with the irradiation of visible and IR light. Owing to the femtosecond pulse duration of UV pump light and IR probe light, the instrumental response as short as 130 fs is achieved. Using this novel technique, the structural properties and temporal behavior of hydrated electrons at the air/water interfaces are investigated. The air/neat water and air/indole aqueous solution interfaces are chosen as the sample, where the electrons are prepared by the two-photon ionization of water and by the one-photon ionization of indole, respectively. In the transient spectra, one transient component is observed in common at both interfaces and it is assigned to water molecules interacting with an electron. The result indicates that the electrons are partially hydrated at the air/water interfaces, and they escape into bulk water phase within 100 ps.

Second, from the theoretical perspective, the extended theory of VSFG which takes account of the electric quadrupole contribution is developed to account for VSFG at interfaces that are made up of centrosymmetric molecules or where molecules are randomly oriented. Previously, it was impossible to interpret VSFG observed at those interfaces, because the ordinary theory within the electric dipole approximation predicts the absence of VSFG at those interfaces. The mechanism of VSFG at the air/benzene, air/cyclohexane, and air/decane interfaces is examined using the developed theory. It is shown that VSFG at the air/benzene and air/cyclohexane interfaces is due to the electric quadrupole contribution. These results demonstrate for the first time that VSFG can actually take place through the quadrupole contribution. Meanwhile, VSFG at the air/decane interface is due to the ordinary dipolar mechanism, indicating that decane molecules have a polar alignment at the air/decane interface in spite of the low polarity of decane.

These two developments make HD-VSFG spectroscopy available for wider application. Hence, the present study contributes to bringing the HD-VSFG spectroscopy up to its higher maturity.

Contents

Part I Introduction

Part II UV-excited time-resolved HD-VSFG spectroscopy

Part III Electric quadrupolar theory for VSFG

Part IV Conclusion

Part I

Introduction

Chapter 1

Purpose of the present study

1.1 Importance of studying interfaces

An interface is defined as the boundary between two media, and it exhibits various unique and important properties distinct from the bulk [1]. For instance, at the catalytic surface, molecules undergo a characteristic reaction through the interaction with the surface of catalyst, and such catalytic reactions play important roles in many industrial processes [2]. Understanding the specific interaction between the catalyst surface and the reactant molecules is crucial to design an efficient catalyst. In biological systems, membranes can be regarded as the interface separating the interior and exterior of organelles or cells, and they are responsible for the transportation of various chemical species and ions from one side to the other, which is essential to our life and to all living things [3]. The detailed molecular-level understanding of these processes is highly desirable because it will contribute, for instance, to the development of a new medicine for curing diseases. Aerosols are increasingly important in atmospheric chemistry these days in relation to the air pollution, because the chemical reactions at the aerosol surface are considered to have negative impacts on the environment such as the destruction of the ozone layer [4]. Clarifying the reaction scheme at the surface of aerosols and taking a countermeasure for these environmental disasters are an urgent issue. Hence, it is critically important to study interfaces and improve our understanding about them. In this study, I focus on air/liquid interfaces as the simplest model of these interfaces.

For the bulk phenomena, many simple and useful spectroscopic techniques are at our hands to study the molecular properties in detail, such as IR absorption spectroscopy, Raman spectroscopy, and UV-vis absorption spectroscopy to name only a few. However, all of these ordinary spectroscopic techniques are not applicable to the investigation of the interfacial properties. This is because the number of molecules within the interfacial region is many orders smaller than that in the bulk, and the faint signal from those interfacial molecules is easily concealed in the intense background signal arising from the bulk molecules. Hence, interface-selective spectroscopic techniques are essentially important for studying the interfaces, and it is crucial to develop novel methods or theories for that purpose. Such a development is the main theme of the present study.

1.2 Methods for studying interfaces

For solid surfaces in vacuum, the most common methods for studying those surfaces are X-ray photoelectron spectroscopy (XPS), low energy electron diffraction (LEED), and electron energy-loss spectroscopy (EELS) [5]. While these techniques provide useful information for the surface characterization, their application is limited to the surfaces in ultrahigh vacuum (UHV). This is because the electrons used in these experiments are easily scattered by the molecules in the air at the ambient pressure, which makes it impossible to utilize these methods for studying other interfaces.

In contrast to electrons, photons are less affected by the gas-phase molecules. Photons can freely propagate inside gas, liquid, and even inside some solids. Hence, for the wider applicability, the methods that use only photons are advantageous and preferable. Surface enhanced infrared absorption spectroscopy (SEIRAS) [6] and surface enhanced Raman spectroscopy (SERS) [7, 8] belong to this class of techniques for the interface characterization. The interface selectivity of SEIRAS and SERS originates from the fact that the enhancement of IR absorption or Raman scattering occurs only for the molecules in the vicinity of the metal surface. The disadvantage of these techniques is the limitation as to the applicable samples. Since the signal enhancement is observed only for certain metal surfaces such as silver and gold, the surface of these metals are the only samples that can be studied by these techniques. Recently, surface sensitive detection of molecules by resonance hyper-Raman scattering combined with Fano resonance has been suggested, but it also has a strict limitation about the applicable sample [9]. None of these techniques allow us to study soft interfaces such as air/liquid or liquid/liquid interfaces.

The most general technique for studying interfaces is probably the even-order nonlinear spectroscopy. Within the dipole approximation, even-order nonlinear optical processes occur only in the region where the inversion symmetry is broken. In the bulk liquid and gas, the inversion symmetry is macroscopically preserved due to the random orientation of molecules. Many solids also preserve the inversion symmetry in the bulk due to the centrosymmetric lattice structure. Meanwhile, at the interface, the inversion symmetry is broken because the molecules tend to be oriented in one particular direction due to the anisotropic environment. Hence, these nonlinear processes occur only at the interface, and the properties of interfacial molecules can be selectively studied. In this principle of interface selectivity, no specific molecular properties are involved, and these even-order nonlinear spectroscopic techniques can be applied to various kinds of interfaces. Examples of even-order nonlinear spectroscopy are vibrational sum frequency generation (VSFG) spectroscopy (second order) [10] and $\chi^{(4)}$ Raman spectroscopy (fourth order) [11,12]. Because the signal from the $\chi^{(4)}$ Raman process is extremely weak, VSFG is practically the most useful method of these kinds at the moment. The interface selectivity of VSFG spectroscopy was first demonstrated by Zhu *et al.* [10], and since then it has evolved into an extremely powerful technique for studying interfaces.

The property probed by VSFG is a complex quantity called the second-order nonlinear susceptibility,

$\chi^{(2)}$. The sign of $\chi^{(2)}$ reflects the orientation of interfacial molecules, and the complex phase of $\chi^{(2)}$ shows vibrational resonances of those molecules. In fact, the imaginary part of $\chi^{(2)}$ (Im $\chi^{(2)}$) can be interpreted as the vibrational spectra of interfaces that can be directly compared, for instance, with IR spectra or Raman spectra in the bulk. In the actual experiments, the sign and phase information of $\chi^{(2)}$ is carried in the phase of the oscillating electric field generated by the VSFG process at the sample surface. Unfortunately, this valuable information is lost in the conventional detection method, in which only the intensity of the sum frequency electric field is detected ("homodyne detection"). In terms of the nonlinear susceptibility, $|\chi^{(2)}|^2$ is obtained in these measurements, and the information about the sign and complex phase of $\chi^{(2)}$ is lost.

1.3 Heterodyne-detected vibrational sum frequency generation spectroscopy

As discussed in the previous paragraph, in order to fully extract the information contained in the sum frequency electric field, it is necessary to determine the phase of this electric field. This can be realized by introducing another electric field at the same wavelength, which is called the local oscillator, and causing the interference between these two electric fields. The phase information of the sum frequency electric field can be recovered by detecting and analyzing this interference pattern. This is called the "heterodyne detection". (Some people prefer to use the phrase "phase-sensitive detection", but it essentially refers to the same detection scheme [13].)

Heterodyne detection of the sum frequency electric field was independently reported by three groups. The Shen group was the first to successfully determine the complex phase of $\chi^{(2)}$ [14–16]. However, in their method, it was necessary to scan the wavelength of the narrowband IR light to cover the entire spectral region, and it required a long measurement time. In 2008, the Benderskii group demonstrated a multiplex scheme for the heterodyne detection using the broadband IR light [17]. With this method, they were able to obtain a spectrum in the entire CH stretch region with only one measurement, significantly shortening the acquisition time of the spectra. However, in spite of the use of the heterodyne detection, they reported only the $|\chi^{(2)}|^2$ spectra, probably because it was difficult to measure the interference between the sum frequency electric field and the local oscillator with a fixed phase difference. Actually, since the wavelength of the sum frequency light in their experiment is about 650 nm, the optical path length for these two electric fields must be kept constant with the accuracy of $\sim$ 10 nm, which is difficult to be achieved due to the fluctuation of the room temperature and many other factors. On the same year in 2008, a different multiplex scheme for the heterodyne detection of electronic SFG was reported by the Tahara group [18]. Due to its unique optical configuration, the interference between the two electric fields can occur stably with a fixed phase difference for a sufficiently long time. The following year, in 2009, the same group reported a heterodyne-detected VSFG apparatus using the same optical scheme [19], and this optical configuration is now adopted by several other groups [20–22].

Heterodyne-detected VSFG (HD-VSFG) spectroscopy has greatly contributed to deepening our understanding about the air/water interfaces. For example, before the development of HD-VSFG spectroscopy, it had been believed based on the conventional homodyne-detected VSFG spectroscopy that an ice-like structure exists at the air/water interface even at room temperature and it contributes to the $|\chi^{(2)}|^2$ spectra at $\sim$ 3200 cm^{-1} [23]. However, HD-VSFG spectroscopy revealed that the vibrational band is due to a pair of strongly hydrogen bonded water molecules, and it has nothing to do with the ice-like structure [24]. Recently, this technique has been extended to IR-excited time-resolved HD-VSFG spectroscopy [25] and 2D HD-VSFG spectroscopy [26,27] to probe the interfacial dynamics after vibrational excitation. These techniques are now actively developed and utilized as the interface counterpart of the IR pump-probe spectroscopy [28] and 2D IR spectroscopy [29].

1.4 Present study

As described in the previous section, HD-VSFG spectroscopy is a powerful and promising spectroscopic technique for studying interfaces. However, its possibility is not fully exploited yet in both experimental and theoretical sense.

First, HD-VSFG spectroscopy has never been applied to the observation of chemical reactions involving electronic excitation at the interface. Interfaces provide a unique reaction site for various chemical and biological processes as discussed earlier in this chapter, and it is highly desirable to understand the molecular-level mechanism of those interfacial reactions. In the bulk, such reaction dynamics are studied using the pump-probe method with UV or visible pump light. For instance, time-resolved IR absorption spectroscopy [30] and time-resolved Raman spectroscopy [31] have been used for such a purpose. These methods have made significant contributions to gaining our knowledge about the mechanism of photo-initiated chemical reactions in the bulk solution. Thus, it is desirable to develop an interface-selective counterpart to these bulk time-resolved spectroscopic techniques. For this purpose, UV-excited time-resolved HD-VSFG spectroscopy is developed in the present study. The developed apparatus and its application will be discussed in the second part of this thesis.

Second, HD-VSFG spectroscopy has never been used to study the interfaces comprised of centrosymmetric molecules due to the lack of theory for interpreting the spectra obtained at those interfaces. For instance, homodyne-detected VSFG spectrum of the air/benzene interface is reported in the literature [32], but it was not clear how the observed spectrum could be understood. This is because VSFG is forbidden at such interfaces according to the ordinary theory of VSFG within the electric dipole approximation. Since the electric dipole approximation is not sufficient to account for the experimental result, it is natural to consider the contribution beyond this approximation. In fact, although the electric dipole approximation is very precise in the bulk media and the higher order contribution such as the electric quadrupole contribution can be safely neglected, its validity is questionable at the interface. This

is because a large electric field gradient exists within the interface layer of ~ 1 nm thickness due to the refractive index mismatch of the two media, which may give rise to a large quadrupole contribution. Although the quadrupole contribution was widely recognized in the early days of the even-order nonlinear spectroscopy [33], the possibility of a higher order contribution to VSFG has become mostly forgotten as VSFG spectroscopy grew into a well-established interface-selective technique [34]. What is worse, the theoretical framework to describe and understand the higher order contribution in $\chi^{(2)}$ spectra, e.g. what kind of vibrational modes will appear in the spectra, has never been developed. In order to remedy the situation and to make HD-VSFG a truly versatile technique for probing various interfaces, the theory for describing the quadrupole contribution in VSFG is developed and discussed in the third part of this thesis.

With these developments, HD-VSFG spectroscopy becomes available for wider application. I believe that the present study brings the interfacial properties more accessible for us and helps us have a better insight into the interfaces.

Chapter 2

Theory of VSFG within the dipole approximation

2.1 Introduction

This chapter reviews the theory of vibrational sum frequency generation (VSFG) within the dipole approximation. VSFG is now widely accepted as an interface-selective vibrational probe, but it is important to understand why and under what condition the interfacial properties can be selectively probed. In particular, it is my aim to show that VSFG is forbidden within this theoretical framework based on the dipole approximation when molecules at the interface have the inversion symmetry or are randomly oriented.

In the optical process of VSFG, the second order nonlinear polarization, $\mathbf{P}^{(2)}$, is first induced by the interaction among the molecular system and two electric fields, one in the visible wavelength (ω_1) and another in the mid-infrared wavelength (ω_2). Because of the IR light, ω_2, the vibrational resonances of the molecules can be probed. When the bulk part of the molecular system has the inversion symmetry, only the molecules at the interface contribute to the induced polarization under the dipole approximation. This is true for liquids and gases, and it is the origin of the interface selectivity in VSFG. Meanwhile, when the bulk part lacks the inversion symmetry, polarization is mostly induced in the bulk. This is true for many solids such as quartz. The sum frequency light resulting from this nonlinear polarization in each case can then be evaluated based on the Maxwell equations. Each of these steps is theoretically shown in the following part.

2.2 Induced nonlinear polarization

The second-order nonlinear polarization $\mathbf{P}^{(2)}$ is induced in the molecular system by two incident laser beams at the angular frequencies ω_1 (visible light) and ω_2 (IR light). Under the dipole approximation, this quantity can be understood as the sum of induced molecular dipoles over all the molecules.

$$\mathbf{P}^{(2)} = \langle \boldsymbol{\mu} \rangle. \tag{2.1}$$

Here, $\boldsymbol{\mu}$ is the induced molecular dipole and $\langle\cdot\rangle$ gives the summation over all the molecules. In the following part, $\boldsymbol{\mu}$ is first evaluated quantum mechanically, and then the expression for the induced nonlinear polarization is derived by taking the summation of the induced molecular dipoles.

2.2.1 General expression for the second-order nonlinear optical processes

The molecular dipole moment, $\boldsymbol{\mu}$, is expressed using a density matrix as

$$\boldsymbol{\mu} = \mathrm{Tr}[\hat{\boldsymbol{\mu}}\rho]. \tag{2.2}$$

Here, $\hat{\boldsymbol{\mu}}$ is the dipole moment operator and ρ is the density matrix. The time evolution of the density matrix is given by the Liouville equation.

$$i\hbar\frac{d\rho}{dt} = [\mathcal{H}, \rho]. \tag{2.3}$$

Using these two equations, the induced molecular dipole can be evaluated.

In the Liouville equation, the Hamiltonian, $\mathcal{H}$, can be separated into the Hamiltonian of the isolated molecular system, $\mathcal{H}_0$, and the interaction Hamiltonian, $\mathcal{H}_{\mathrm{int}}$, representing the interaction between the molecular system and the light.

$$\mathcal{H} = \mathcal{H}_0 + \mathcal{H}_{\mathrm{int}}. \tag{2.4}$$

The density matrix, ρ, is expressed using the eigenvectors of $\mathcal{H}_0$ as

$$\rho = \sum_m p_m |m\rangle\langle m|, \tag{2.5}$$

$$\mathcal{H}_0|m\rangle = \varepsilon_m|m\rangle, \tag{2.6}$$

where p_m gives the probability that the system is in the state $|m\rangle$ $\left(\sum_m p_m = 1\right)$. Then, the Liouville equation becomes

$$i\hbar\frac{d\rho}{dt} = \sum_m p_m \{(\mathcal{H}_0 + \mathcal{H}_{\mathrm{int}})|m\rangle\langle m| - |m\rangle\langle m|(\mathcal{H}_0 + \mathcal{H}_{\mathrm{int}})\} \tag{2.7}$$

$$= \sum_m p_m \{(\varepsilon_m + \mathcal{H}_{\mathrm{int}})|m\rangle\langle m| - |m\rangle\langle m|(\varepsilon_m + \mathcal{H}_{\mathrm{int}})\} \tag{2.8}$$

$$= [\mathcal{H}_{\mathrm{int}}, \rho]. \tag{2.9}$$

This equation can be formally solved as

$$\rho = \frac{1}{i\hbar}\int dt[\mathcal{H}_{\mathrm{int}}, \rho]. \tag{2.10}$$

Assuming that the molecular system is initially in the ground state, the initial density matrix is given by

$$\rho_0 = |g\rangle\langle g|. \tag{2.11}$$

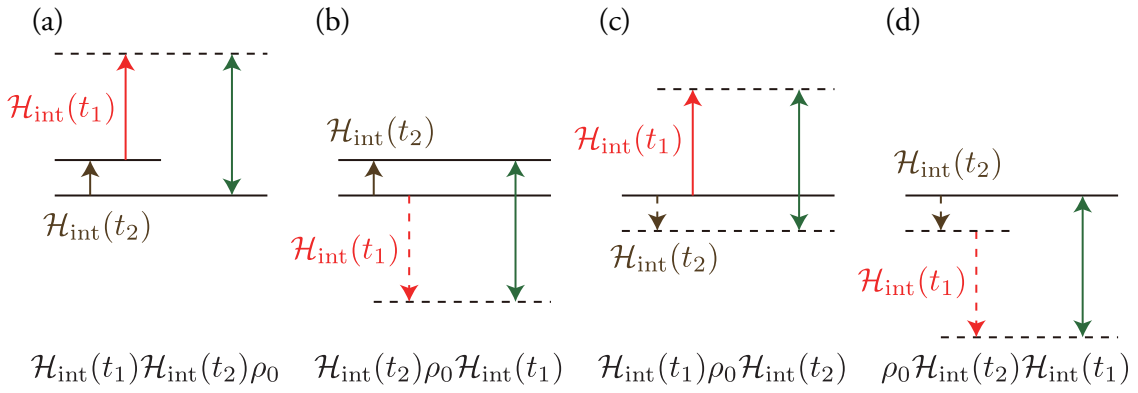

Figure 2.1: Energy diagrams that potentially contribute to VSFG. Solid and dashed arrows represent the time evolution of the ket and bra vectors, respectively ($t_1 > t_2$).

Inserting this initial density matrix into the right hand side of Eq. (2.10), a new density matrix, $\rho^{(1)}$, can be obtained.

$$\rho^{(1)} = \frac{1}{i\hbar}\int_{-\infty}^{t} dt_1[\mathcal{H}_{\rm int}(t_1), \rho_0]. \tag{2.12}$$

This can be understood as the density matrix for the molecular system after one interaction with light at $t = t_1$.

In the optical process of VSFG, the molecular system interacts twice with light. The density matrix after two interactions at $t = t_1$ and $t = t_2$ ($t_1 > t_2$) is given as

$$\rho^{(2)} = \frac{1}{i\hbar}\int_{-\infty}^{t} dt_1[\mathcal{H}_{\rm int}(t_1), \rho^{(1)}] \tag{2.13}$$

$$= \left(\frac{1}{i\hbar}\right)^2 \int_{-\infty}^{t} dt_1 \int_{-\infty}^{t_1} dt_2[\mathcal{H}_{\rm int}(t_1), [\mathcal{H}_{\rm int}(t_2), \rho_0]] \tag{2.14}$$

$$= \left(\frac{1}{i\hbar}\right)^2 \int_{-\infty}^{t} dt_1 \int_{-\infty}^{t_1} dt_2 \left(\mathcal{H}_{\rm int}(t_1)\mathcal{H}_{\rm int}(t_2)\rho_0 - \mathcal{H}_{\rm int}(t_2)\rho_0\mathcal{H}_{\rm int}(t_1)\right.$$
$$\left. -\mathcal{H}_{\rm int}(t_1)\rho_0\mathcal{H}_{\rm int}(t_2) + \rho_0\mathcal{H}_{\rm int}(t_2)\mathcal{H}_{\rm int}(t_1)\right). \tag{2.15}$$

The energy diagrams corresponding to each of these terms are shown in Fig. 2.1. Among these four terms, only the first two terms give rise to vibrationally resonant signal, with the IR light (ω_2) interacting at $t = t_2$ (Fig. 2.1(a) and (b)). Furthermore, the contribution from the first term is expected to be larger than that from the second term, because no energy levels exist below the ground state energy. Hence, for simplicity, the contribution from the second term (Fig. 2.1(b)) is neglected, and only the first term (Fig. 2.1(a)) will be considered here. In this case, the induced dipole can be more explicitly evaluated as

$$\boldsymbol{\mu} = \left(\frac{1}{i\hbar}\right)^2 \int_{-\infty}^{t} dt_1 \int_{-\infty}^{t_1} dt_2 \mathrm{Tr}\left[\hat{\boldsymbol{\mu}}\mathcal{H}_{\rm int}(t_1)\mathcal{H}_{\rm int}(t_2)\rho_0\right] \tag{2.16}$$

$$= \left(\frac{1}{i\hbar}\right)^2 \int_{-\infty}^{t} dt_1 \int_{-\infty}^{t_1} dt_2 \sum_m \langle m|\hat{\boldsymbol{\mu}}\mathcal{H}_{\rm int}(t_1)\mathcal{H}_{\rm int}(t_2)|g\rangle\langle g|m\rangle \tag{2.17}$$

$$= \left(\frac{1}{i\hbar}\right)^2 \int_{-\infty}^{t} dt_1 \int_{-\infty}^{t_1} dt_2 \langle g|\hat{\boldsymbol{\mu}}\mathcal{H}_{\rm int}(t_1)\mathcal{H}_{\rm int}(t_2)|g\rangle \tag{2.18}$$

$$= \left(\frac{1}{i\hbar}\right)^2 \int_{-\infty}^{t} dt_1 \int_{-\infty}^{t_1} dt_2 \sum_{s,v} \langle g|\hat{\boldsymbol{\mu}}|s\rangle\langle s|\mathcal{H}_{\rm int}(t_1)|v\rangle\langle v|\mathcal{H}_{\rm int}(t_2)|g\rangle. \tag{2.19}$$

More detailed examination of this expressions requires an explicit expression of the interaction Hamiltonian, $\mathcal{H}_{\rm int}$.

2.2.2 Light-matter interaction within the electric dipole approximation

The interaction between the molecular system and light can be taken into account by using the minimal coupling Hamiltonian given as [35]

$$\mathcal{H} = \sum_l \frac{\left(\hat{\mathbf{p}}_l - z_l \mathbf{A}(\hat{\mathbf{r}}_l, t)\right)^2}{2m_l} + \hat{V} \tag{2.20}$$

$$= \left[\sum_l \frac{\hat{\mathbf{p}}_l^2}{2m_l} + \hat{V}\right] + \sum_l \left[-\frac{z_l}{2m_l}\left(\hat{\mathbf{p}}_l \cdot \mathbf{A} + \mathbf{A} \cdot \hat{\mathbf{p}}_l\right) + \frac{z_l^2}{2m_l}\mathbf{A}^2\right]. \tag{2.21}$$

Here, l represents the particles in the system (nuclei and electrons), and $\hat{\mathbf{r}}_l$, $\hat{\mathbf{p}}_l$, m_l, and z_l give the coordinate operator, momentum operator, mass, and charge of the lth particle, respectively. $\hat{V}$ is the potential energy and $\mathbf{A}$ is the vector potential. Under the semiclassical treatment adopted here, $\mathbf{A}$ is treated as a classical quantity. The first term is the Hamiltonian of the isolated molecular system, $\mathcal{H}_0$, without any perturbation from the light.

$$\mathcal{H}_0 = \sum_l \frac{\hat{\mathbf{p}}_l^2}{2m_l} + \hat{V}. \tag{2.22}$$

The second term is the interaction Hamiltonian, $\mathcal{H}_{\rm int}$.

$$\mathcal{H}_{\rm int} = \sum_l \left[-\frac{z_l}{2m_l}\left(\hat{\mathbf{p}}_l \cdot \mathbf{A} + \mathbf{A} \cdot \hat{\mathbf{p}}_l\right) + \frac{z_l^2}{2m_l}\mathbf{A}^2\right]. \tag{2.23}$$

This can be simplified using the property of the Coulomb gauge.

$$\hat{\mathbf{p}}_l \cdot \mathbf{A} = \left(\frac{\hbar}{i}\boldsymbol{\nabla}_l\right) \cdot \mathbf{A} \tag{2.24}$$

$$= \frac{\hbar}{i}(\boldsymbol{\nabla}_l \cdot \mathbf{A}) + \frac{\hbar}{i}\mathbf{A} \cdot \boldsymbol{\nabla}_l \tag{2.25}$$

$$= 0 + \mathbf{A} \cdot \hat{\mathbf{p}}_l \tag{2.26}$$

Furthermore, the term $(z_l^2/2m_l)\mathbf{A}^2$ can be neglected because it has no interaction with the molecular system and its contribution is known to be small [35]. Then,

$$\mathcal{H}_{\rm int} = \sum_l \left[-\frac{z_l}{m_l}\mathbf{A}(\hat{\mathbf{r}}_l, t) \cdot \hat{\mathbf{p}}_l\right]. \tag{2.27}$$

It is convenient to expand the vector potential as

$$\mathbf{A}(\hat{\mathbf{r}}, t) = \int d\mathbf{k} \int d\omega \mathbf{A}(\mathbf{k}, \omega) e^{i\mathbf{k}\cdot\hat{\mathbf{r}} - i\omega t}. \tag{2.28}$$

Here, one important approximation is made, i.e. the electric dipole approximation. In this approximation, the electromagnetic field is regarded to be constant within one molecule. In other words, the electromagnetic field gradient is neglected at the molecular scale of $\sim$ 1 nm. For this purpose, the coordinate operator is separated into two parts.

$$\hat{\mathbf{r}} = \mathbf{R} + \Delta\hat{\mathbf{r}}. \tag{2.29}$$

Here, $\mathbf{R}$ is the center of mass of a molecule, and $\Delta\hat{\mathbf{r}}$ corresponds to the intramolecular coordinate. $\hat{\mathbf{r}}$ and $\Delta\hat{\mathbf{r}}$ need to be treated quantum mechanically as operators, but $\mathbf{R}$ can be treated classically simply as a parameter. Using this definition and the electric dipole approximation, the coordinate dependence of the vector potential is simplified to

$$e^{i\mathbf{k}\cdot\hat{\mathbf{r}}} \equiv e^{i\mathbf{k}\cdot(\mathbf{R}+\Delta\hat{\mathbf{r}})} = e^{i\mathbf{k}\cdot\mathbf{R}}\left(1 + i\mathbf{k}\cdot\Delta\hat{\mathbf{r}} + \cdots\right) \simeq e^{i\mathbf{k}\cdot\mathbf{R}}, \tag{2.30}$$

and the interaction Hamiltonian becomes

$$\mathcal{H}_{\mathrm{int}} = \sum_l \left[-\frac{z_l}{m_l}\mathbf{A}(\hat{\mathbf{r}}_l, t)\cdot\hat{\mathbf{p}}_l\right] \tag{2.31}$$

$$\simeq \sum_l \int d\mathbf{k}\int d\omega \left[-\frac{z_l}{m_l}\mathbf{A}(\mathbf{k},\omega)\cdot\hat{\mathbf{p}}_l e^{i\mathbf{k}\cdot\mathbf{R}-i\omega t}\right] \tag{2.32}$$

$$\equiv \mathcal{H}_{\mathrm{int}}^{\mathrm{dipole}}. \tag{2.33}$$

This is the interaction Hamiltonian within the electric dipole approximation. In the electric dipole approximation, the coordinate dependence of the electromagnetic field inside one molecule ($\Delta\hat{\mathbf{r}}$) is neglected. For VSFG at the interface, this approximation is not always valid, and the contribution from a higher order term will be discussed later in this thesis.

Before discussing the transition probability due to this interaction Hamiltonian, it is necessary to rewrite the momentum operator, $\hat{\mathbf{p}}_l$, in terms of the molecular Hamiltonian, $\mathcal{H}_0$, and the coordinate operator, $\hat{\mathbf{r}}_l$. The commutation relation of $\mathcal{H}_0$ and $\hat{\mathbf{r}}_l$ is given as

$$[\mathcal{H}_0, \hat{\mathbf{r}}_l] = \left[\frac{\hat{\mathbf{p}}_l^2}{2m_l}, \hat{\mathbf{r}}_l\right] = -\frac{i\hbar}{m_l}\hat{\mathbf{p}}_l. \tag{2.34}$$

Using this equation, the momenum operator can be rewritten as

$$\hat{\mathbf{p}}_l = \frac{im_l}{\hbar}[\mathcal{H}_0, \hat{\mathbf{r}}_l] = \frac{im_l}{\hbar}[\mathcal{H}_0, \Delta\hat{\mathbf{r}}_l]. \tag{2.35}$$

Then, the interaction Hamiltonian within the dipole approximation, $\mathcal{H}_{\mathrm{int}}^{\mathrm{dipole}}$, can be expressed as

$$\mathcal{H}_{\mathrm{int}}^{\mathrm{dipole}} = \sum_l \int d\mathbf{k}\int d\omega \left[-\frac{iz_l}{\hbar}\mathbf{A}(\mathbf{k},\omega)\cdot[\mathcal{H}_0, \Delta\hat{\mathbf{r}}_l]e^{i\mathbf{k}\cdot\mathbf{R}-i\omega t}\right] \tag{2.36}$$

$$= \int d\mathbf{k}\int d\omega \left[-\frac{i}{\hbar}\mathbf{A}(\mathbf{k},\omega)\cdot\left[\mathcal{H}_0, \sum_l z_l\Delta\hat{\mathbf{r}}_l\right]e^{i\mathbf{k}\cdot\mathbf{R}-i\omega t}\right] \tag{2.37}$$

$$\equiv \int d\mathbf{k} \int d\omega \left[-\frac{i}{\hbar} \mathbf{A}(\mathbf{k}, \omega) \cdot [\mathcal{H}_0, \hat{\boldsymbol{\mu}}] e^{i\mathbf{k}\cdot\mathbf{R} - i\omega t} \right]. \tag{2.38}$$

Here, the definition of the dipole moment operator was used.

$$\hat{\boldsymbol{\mu}} \equiv \sum_l z_l \Delta \hat{\mathbf{r}}_l. \tag{2.39}$$

Using these expressions, it is now possible to discuss the transition probability from $|i\rangle$ to $|f\rangle$ due to $\mathcal{H}_{\text{int}}^{\text{dipole}}$.

$$\langle f|\mathcal{H}_{\text{int}}^{\text{dipole}}|i\rangle = \int d\mathbf{k} \int d\omega \left[-\frac{i}{\hbar} \mathbf{A}(\mathbf{k}, \omega) \cdot \langle f|[\mathcal{H}_0, \hat{\boldsymbol{\mu}}(t)]|i\rangle e^{i\mathbf{k}\cdot\mathbf{R} - i\omega t} \right] \tag{2.40}$$

$$= \int d\mathbf{k} \int d\omega \left[-\frac{i}{\hbar} \mathbf{A}(\mathbf{k}, \omega) \cdot \langle f|\hat{\boldsymbol{\mu}}(t)|i\rangle (\varepsilon_f - \varepsilon_i) e^{i\mathbf{k}\cdot\mathbf{R} - i\omega t} \right]. \tag{2.41}$$

The time dependence of this transition probability amplitude is given as

$$\langle f|\hat{\boldsymbol{\mu}}(t)|i\rangle e^{-i\omega t} = \langle f|\hat{\boldsymbol{\mu}}|i\rangle \exp\left[i \frac{\varepsilon_f - \varepsilon_i - \hbar\omega}{\hbar} t \right]. \tag{2.42}$$

Here, the time dependence was taken into account using the Heisenberg picture.

$$\hat{\boldsymbol{\mu}}(t) = e^{\frac{i\mathcal{H}t}{\hbar}} \hat{\boldsymbol{\mu}} e^{-\frac{i\mathcal{H}t}{\hbar}}. \tag{2.43}$$

In this equation, the exponential factor averages to zero within a short period of time due to the rapid phase change unless $|\varepsilon_f - \varepsilon_i - \hbar\omega| \simeq 0$. Hence, the transition occurs only when $\varepsilon_f - \varepsilon_i \simeq \hbar\omega$. Then, this transition amplitude is finally given as

$$\langle f|\mathcal{H}_{\text{int}}^{\text{dipole}}|i\rangle \simeq \int d\mathbf{k} \int d\omega \left[-i\omega \mathbf{A}(\omega) e^{i\mathbf{k}\cdot\mathbf{R} - i\omega t} \cdot \langle f|\hat{\boldsymbol{\mu}}(t)|i\rangle \right] \tag{2.44}$$

$$= -\mathbf{E}(\mathbf{R}, t) \cdot \langle f|\hat{\boldsymbol{\mu}}(t)|i\rangle. \tag{2.45}$$

Here, the relation between the electric field and the vector potential,

$$\mathbf{E}(\mathbf{R}, t) = -\frac{\partial \mathbf{A}(\mathbf{R}, t)}{\partial t} = -\frac{\partial}{\partial t} \int d\mathbf{k} \int d\omega \mathbf{A}(\mathbf{k}, \omega) e^{i\mathbf{k}\cdot\mathbf{R} - i\omega t} \tag{2.46}$$

$$= \int d\mathbf{k} \int d\omega \, i\omega \mathbf{A}(\mathbf{k}, \omega) e^{i\mathbf{k}\cdot\mathbf{R} - i\omega t}, \tag{2.47}$$

was used. The final result shows that the dipole transition probability amplitude is given by the product of $\langle f|\hat{\boldsymbol{\mu}}(t)|i\rangle$ and the electric field, $\mathbf{E}(\mathbf{R}, t)$, of the light.

2.2.3 Quantum mechanical evaluation of the induced molecular dipole

As shown in Eq. (2.19), the induced dipole can be evaluated using the equation shown below.

$$\boldsymbol{\mu}(\mathbf{R}, t) = \left(\frac{1}{i\hbar} \right)^2 \int_{-\infty}^{t} dt_1 \int_{-\infty}^{t_1} dt_2 \sum_{s,v} \langle g|\hat{\boldsymbol{\mu}}(t)|s\rangle \langle s|\mathcal{H}_{\text{int}}(t_1)|v\rangle \langle v|\mathcal{H}_{\text{int}}(t_2)|g\rangle. \tag{2.48}$$

Within the dipole approximation, this is reduced to

$$\boldsymbol{\mu}(\mathbf{R},t) = \left(\frac{1}{i\hbar}\right)^2 \int_{-\infty}^{t} dt_1 \int_{-\infty}^{t_1} dt_2 \sum_{J,K} \sum_{s,v} E_{1J}(\mathbf{R},t_1) E_{2K}(\mathbf{R},t_2) \times \langle g|\hat{\boldsymbol{\mu}}(t)|s\rangle\langle s|\hat{\mu}_J(t_1)|v\rangle\langle v|\hat{\mu}_K(t_2)|g\rangle. \tag{2.49}$$

Here, J and K are the laboratory-fixed coordinates ($J, K = X, Y, Z$), and E_{1J} and E_{2K} are the electric field for the ω_1 and ω_2 beams, respectively. These integrations in time can be executed by using the time dependence of the electric fields

$$E_{1J}(\mathbf{R},t) = \int d\omega_1 E_{1J}(\mathbf{R},\omega_1) e^{-i\omega_1 t}, \tag{2.50}$$

$$E_{2K}(\mathbf{R},t) = \int d\omega_2 E_{2K}(\mathbf{R},\omega_2) e^{-i\omega_2 t}, \tag{2.51}$$

and the dipole moment operator shown in Eq. (2.43). First, the integration with respect to t_2 can be evaluated as follows.

$$\begin{aligned}
&\int_{-\infty}^{t_1} dt_2 E_{2K}(\mathbf{R},t_2)\langle v|\hat{\mu}_K(t_2)|g\rangle \\
&\quad = \int_{-\infty}^{t_1} dt_2 \int d\omega_2 E_{2K}(\mathbf{R},\omega_2) e^{-i\omega_2 t_2} \langle v| e^{\frac{i\varepsilon_v t_2}{\hbar}} \hat{\mu}_K e^{-\frac{i\varepsilon_g t_2}{\hbar}} |g\rangle && (2.52)\\
&\quad = \int d\omega_2 E_{2K}(\mathbf{R},\omega_2)\langle v|\hat{\mu}_K|g\rangle \int_{-\infty}^{t_1} dt_2 e^{\frac{i}{\hbar}(\varepsilon_v - \varepsilon_g - \hbar\omega_2)t_2} && (2.53)\\
&\quad = \frac{\hbar}{i} \int d\omega_2 E_{2K}(\mathbf{R},\omega_2)\langle v|\hat{\mu}_K|g\rangle \frac{e^{\frac{i}{\hbar}(\varepsilon_v - \varepsilon_g - \hbar\omega_2)t_1}}{\varepsilon_v - \varepsilon_g - \hbar\omega_2}. && (2.54)
\end{aligned}$$

Using this result, the integration with respect to t_1 can also be performed.

$$\begin{aligned}
&\int_{-\infty}^{t} dt_1 \int_{-\infty}^{t_1} dt_2 E_{1J}(\mathbf{R},t_1) E_{2K}(\mathbf{R},t_2)\langle s|\hat{\mu}_J(t_1)|v\rangle\langle v|\hat{\mu}_K(t_2)|g\rangle \\
&\quad = \frac{\hbar}{i} \int d\omega_1 \int d\omega_2 \frac{\langle s|\hat{\mu}_J|v\rangle\langle v|\hat{\mu}_K|g\rangle}{\varepsilon_v - \varepsilon_g - \hbar\omega_2} E_{1J}(\mathbf{R},\omega_1) E_{2K}(\mathbf{R},\omega_2) \int_{-\infty}^{t} dt_1 e^{\frac{i}{\hbar}\{\varepsilon_s - \varepsilon_g - \hbar(\omega_1+\omega_2)\}t_1} && (2.55)\\
&\quad = \left(\frac{\hbar}{i}\right)^2 \int d\omega_1 \int d\omega_2 \frac{\langle s|\hat{\mu}_J|v\rangle\langle v|\hat{\mu}_K|g\rangle}{(\varepsilon_v - \varepsilon_g - \hbar\omega_2)\{\varepsilon_s - \varepsilon_g - \hbar(\omega_1+\omega_2)\}} \\
&\qquad \times E_{1J}(\mathbf{R},\omega_1) E_{2K}(\mathbf{R},\omega_2) e^{\frac{i}{\hbar}\{\varepsilon_s - \varepsilon_g - \hbar(\omega_1+\omega_2)\}t}. && (2.56)
\end{aligned}$$

Finally, the expectation value for $\boldsymbol{\mu}^{\mathrm{dipole}}(\mathbf{R},t)$ can be evaluated.

$$\begin{aligned}
&\boldsymbol{\mu}^{\mathrm{dipole}}(\mathbf{R},t) \\
&\quad = \left(\frac{1}{i\hbar}\right)^2 \sum_{J,K} \sum_{s,v} \langle g| e^{\frac{i}{\hbar}\varepsilon_g t} \hat{\boldsymbol{\mu}} e^{-\frac{i}{\hbar}\varepsilon_s t} |s\rangle \\
&\qquad \times \left(\frac{\hbar}{i}\right)^2 \int d\omega_1 \int d\omega_2 \frac{\langle s|\hat{\mu}_J|v\rangle\langle v|\hat{\mu}_K|g\rangle}{(\varepsilon_v - \varepsilon_g - \hbar\omega_2)\{\varepsilon_s - \varepsilon_g - \hbar(\omega_1+\omega_2)\}} \\
&\qquad \times E_{1J}(\mathbf{R},\omega_1) E_{2K}(\mathbf{R},\omega_2) e^{\frac{i}{\hbar}\{\varepsilon_s - \varepsilon_g - \hbar(\omega_1+\omega_2)\}t} && (2.57)
\end{aligned}$$

$$= \sum_{J,K} \sum_{s,v} \int d\omega_1 \int d\omega_2 \frac{\langle g|\hat{\boldsymbol{\mu}}|s\rangle\langle s|\hat{\mu}_J|v\rangle\langle v|\hat{\mu}_K|g\rangle}{(\varepsilon_v - \varepsilon_g - \hbar\omega_2)\{\varepsilon_s - \varepsilon_g - \hbar(\omega_1+\omega_2)\}} \times E_{1J}(\mathbf{R},\omega_1)E_{2K}(\mathbf{R},\omega_2)e^{-i(\omega_1+\omega_2)t}. \tag{2.58}$$

The I component of $\boldsymbol{\mu}^{\mathrm{dipole}}$ can be expressed as

$$\mu_I^{\mathrm{dipole}}(\mathbf{R},t) = \sum_{J,K} \int d\omega_1 \int d\omega_2 \beta_{IJK}^{\mathrm{dipole}}(\omega_1,\omega_2)E_{1J}(\mathbf{R},\omega_1)E_{2K}(\mathbf{R},\omega_2)e^{-i(\omega_1+\omega_2)t}, \tag{2.59}$$

with the molecular hyperpolarizability tensor, $\beta_{IJK}^{\mathrm{dipole}}(\omega_1,\omega_2)$, defined using the laboratory-fixed coordinates as

$$\beta_{IJK}^{\mathrm{dipole}}(\omega_1,\omega_2) \equiv \sum_{s,v} \frac{\langle g|\hat{\mu}_I|s\rangle\langle s|\hat{\mu}_J|v\rangle\langle v|\hat{\mu}_K|g\rangle}{(\varepsilon_v - \varepsilon_g - \hbar\omega_2)\{\varepsilon_s - \varepsilon_g - \hbar(\omega_1+\omega_2)\}}. \tag{2.60}$$

This hyperpolarizability tensor diverges when $\omega_2 = (\varepsilon_v - \varepsilon_g)/\hbar$ or $\omega_1 + \omega_2 = (\varepsilon_s - \varepsilon_g)/\hbar$. To avoid the divergence, damping constants, γ_{vg} and γ_{sg}, are phenomenologically added to this hyperpolarizability tensor. (It is also possible to avoid this divergence by adding a relaxation term to the original Liouville equation [36].)

$$\beta_{IJK}^{\mathrm{dipole}}(\omega_1,\omega_2) \equiv \sum_{s,v} \frac{\langle g|\hat{\mu}_I|s\rangle\langle s|\hat{\mu}_J|v\rangle\langle v|\hat{\mu}_K|g\rangle}{(\varepsilon_v - \varepsilon_g - \hbar\omega_2 - i\gamma_{vg})\{\varepsilon_s - \varepsilon_g - \hbar(\omega_1+\omega_2) - i\gamma_{sg}\}}. \tag{2.61}$$

In this expression,

$$\frac{\langle g|\hat{\mu}_I|s\rangle\langle s|\hat{\mu}_J|v\rangle}{\varepsilon_s - \varepsilon_g - \hbar(\omega_1+\omega_2) - i\gamma_{sg}} \tag{2.62}$$

corresponds to anti-Stokes Raman scattering, and

$$\langle v|\hat{\mu}_K|g\rangle \tag{2.63}$$

corresponds to IR absorption. Hence, this hyperpolarizability is nonzero only for the vibrational modes that are IR active and Raman active at the same time. For centrosymmetric molecules, such vibrational modes never exist due to the rule of mutual exclusion, and the hyperpolarizability tensor is always zero.

2.2.4 Induced nonlinear polarization

As shown in Eq. (2.1), the nonlinear polarization can be evaluated by summing up the molecular dipole moment, μ_I^{dipole}, over all the molecules.

$$\mathbf{P}^{(2)}(\mathbf{R},t) = \langle \mu_I^{\mathrm{dipole}} \rangle = \sum_{n=1}^{N} \mu_I^{\mathrm{dipole}}(n) \tag{2.64}$$

$$= \sum_{J,K} \int d\omega_1 \int d\omega_2 \left(\sum_{n=1}^{N} \beta_{IJK}^{\mathrm{dipole}}(n) \right) E_{1J}(\mathbf{R},\omega_1)E_{2K}(\mathbf{R},\omega_2)e^{-i(\omega_1+\omega_2)t}, \tag{2.65}$$

where $n = 1, 2, \cdots, N$ accounts for the individual molecules in the system. However, the summation of the molecular hyperpolarizability, $\beta^{\mathrm{dipole}}_{IJK}$, is not straightforward, because $\beta^{\mathrm{dipole}}_{IJK}$ is described using the laboratory-fixed coordinates, and its value varies depending on the molecular orientation. The summation is facilitated by introducing the molecular hyperpolarizability tensor, $\beta^{\mathrm{dipole}}_{ijk}$, defined using the molecular-fixed coordinates, $i, j, k = x, y, z$. This can be related to $\beta^{\mathrm{dipole}}_{IJK}$ using the rotation matrix, R, as [37]

$$\beta^{\mathrm{dipole}}_{IJK} = \sum_{i,j,k} R_{Ii} R_{Jj} R_{Kk} \beta^{\mathrm{dipole}}_{ijk}. \tag{2.66}$$

By definition, $\beta^{\mathrm{dipole}}_{ijk}$ is the intrinsic property of a molecule, and it is independent of the molecular orientation. Then, the summation of the hyperpolarizability can be given as

$$\sum_{n=1}^{N} \beta^{\mathrm{dipole}}_{IJK}(n) = \sum_{n=1}^{N} \sum_{i,j,k} R_{Ii}(n) R_{Jj}(n) R_{Kk}(n) \beta^{\mathrm{dipole}}_{ijk} \tag{2.67}$$

$$\equiv N \sum_{i,j,k} \langle R_{Ii} R_{Jj} R_{Kk} \rangle_{\mathrm{av}} \beta^{\mathrm{dipole}}_{ijk} \tag{2.68}$$

$$\equiv \varepsilon_0 \chi^{(2),\mathrm{dipole}}_{IJK}. \tag{2.69}$$

Here, $\langle R_{Ii} R_{Jj} R_{Kk} \rangle_{\mathrm{av}}$ is the product of three rotation matrices averaged over N molecules, and $\chi^{(2),\mathrm{dipole}}_{IJK}$ is the second-order nonlinear susceptibility. Using the nonlinear susceptibility, the induced nonlinear polarization can be expressed in a simple form.

$$\mathbf{P}^{(2)}(\mathbf{R}, t) = \varepsilon_0 \sum_{J,K} \int d\omega_1 \int d\omega_2 \chi^{(2),\mathrm{dipole}}_{IJK}(\omega_1, \omega_2) E_{1J}(\mathbf{R}, \omega_1) E_{2K}(\mathbf{R}, \omega_2) e^{-i(\omega_1+\omega_2)t}. \tag{2.70}$$

It is obvious from the derivation shown here that VSFG is forbidden within the dipole approximation when molecules are randomly oriented ($\langle R_{Ii} R_{Jj} R_{Kk} \rangle_{\mathrm{av}} = 0$) or are centrosymmetric $\left(\beta^{\mathrm{dipole}}_{ijk} = 0\right)$, because the nonlinear susceptibility, $\chi^{(2),\mathrm{dipole}}$, and the induced nonlinear polarization, $\mathbf{P}^{(2)}$, will vanish in those cases.

In the actual VSFG experiments, the bandwidth of the visible ω_1 light is narrow [19, 38], and it can be regarded as a monochromatic wave. In such a case, the expression for the nonlinear polarization becomes very simple in the frequency domain.

$$P^{(2)}_I(\mathbf{R}, \omega_3) = \frac{1}{2\pi} \int dt\, P^{(2)}_I(\mathbf{R}, t) e^{i\omega_3 t} \tag{2.71}$$

$$= \frac{\varepsilon_0}{2\pi} \sum_{J,K} \int d\omega_2\, \chi^{(2),\mathrm{dipole}}_{IJK}(\omega_1, \omega_2) E_{1J}(\mathbf{R}, \omega_1) E_{2K}(\mathbf{R}, \omega_2) \int dt\, e^{i(\omega_3-\omega_1-\omega_2)t} \tag{2.72}$$

$$= \frac{\varepsilon_0}{2\pi} \sum_{J,K} \int d\omega_2\, \chi^{(2),\mathrm{dipole}}_{IJK}(\omega_1, \omega_2) E_{1J}(\mathbf{R}, \omega_1) E_{2K}(\mathbf{R}, \omega_2) \cdot 2\pi\delta(\omega_3 - \omega_1 - \omega_2) \tag{2.73}$$

$$= \varepsilon_0 \sum_{J,K} \chi^{(2)}_{IJK}(\omega_1, \omega_2) E_{1J}(\omega_1) E_{2K}(\omega_2). \tag{2.74}$$

Here, $\omega_3 = \omega_1 + \omega_2$. This simple expression in the frequency domain is conveniently used in some cases.

2.3 Interface selectivity of VSFG within the dipole approximation

The most important property of VSFG is its interface selectivity. The origin of the interface selectivity is discussed in this section. As will be seen, this proof is valid only when both of the two bulk media separated by the interface have the inversion center. This is true for gas/liquid and liquid/liquid interfaces due to the random orientation of molecules in gas and liquid. For the interfaces involving a solid, this proof may not be valid any more, because the crystal lattice does not necessarily have the inversion symmetry.

The induced polarization due to the IJK component of the nonlinear susceptibility, $\chi^{(2),\mathrm{dipole}}_{IJK}$, is given in the frequency domain as

$$P^{(2)}_I(\omega_3) = \varepsilon_0 \chi^{(2),\mathrm{dipole}}_{IJK}(\omega_1,\omega_2) E_{1J}(\omega_1) E_{2K}(\omega_2). \tag{2.75}$$

Since $\mathbf{P}^{(2)}$, $\mathbf{E}_1$, and $\mathbf{E}_2$ are polar vector quantities, their elements change the sign by the inversion of the coordinates. On the other hand, the effect of the coordinate inversion on $\chi^{(2),\mathrm{dipole}}_{IJK}$ is different for the bulk and for the interface.

In the bulk with the inversion symmetry (such as gases, liquids, and some solids), the sign of $\chi^{(2),\mathrm{dipole}}_{IJK}$ does not change by the coordinate inversion. In this case, the following expression can be obtained by the parity inversion operation ($I \longrightarrow -I$, $J \longrightarrow -J$, and $K \longrightarrow -K$).

$$-P^{(2)}_I(\omega_3) = \varepsilon_0 \chi^{(2),\mathrm{dipole}}_{IJK} \{-E_{1J}(\omega_1)\} \{-E_{2K}(\omega_2)\} \tag{2.76}$$

$$= \varepsilon_0 \chi^{(2),\mathrm{dipole}}_{IJK} E_{1J}(\omega_1) E_{2K}(\omega_2). \tag{2.77}$$

Comparing with Eq. (2.75), it follows that

$$\chi^{(2),\mathrm{dipole}}_{IJK} = -\chi^{(2),\mathrm{dipole}}_{IJK} = 0. \tag{2.78}$$

This result shows that VSFG does not occur in the bulk within the dipole approximation.

At the interface, there is an anisotropy in the surface normal direction (Z), and the sign of $\chi^{(2),\mathrm{dipole}}_{IJK}$ may change by the inversion of the Z coordinate. For example, when $I, J \neq Z$ and $K = Z$, $\chi^{(2),\mathrm{dipole}}_{IJZ}$ can be expressed using the rotation matrix as

$$\chi^{(2),\mathrm{dipole}}_{IJZ} = \frac{N}{\varepsilon_0} \sum_{i,j,k} \langle R_{Ii} R_{Jj} R_{Zk} \rangle_{\mathrm{av}} \beta^{\mathrm{dipole}}_{ijk}. \tag{2.79}$$

The parity inversion with respect to Z yields

$$\chi^{(2),\mathrm{dipole}}_{IJ(-Z)} = \frac{N}{\varepsilon_0} \sum_{i,j,k} \langle R_{Ii} R_{Jj} (-R_{Zk}) \rangle_{\mathrm{av}} \beta^{\mathrm{dipole}}_{ijk} \tag{2.80}$$

$$= -\frac{N}{\varepsilon_0} \sum_{i,j,k} \langle R_{Ii} R_{Jj} R_{Zk} \rangle_{\mathrm{av}} \beta^{\mathrm{dipole}}_{ijk} \tag{2.81}$$

$$= -\chi^{(2),\mathrm{dipole}}_{IJZ}. \tag{2.82}$$

Under this condition, the equation for the induced polarization changes with the inversion of the Z coordinate as

$$P_I^{(2)}(\omega_3) = \varepsilon_0 \left\{-\chi_{IJZ}^{(2),\mathrm{dipole}}\right\} E_{1J}(\omega_1) \left\{-E_{2Z}(\omega_2)\right\} \tag{2.83}$$

$$= \varepsilon_0 \chi_{IJZ}^{(2),\mathrm{dipole}} E_{1J}(\omega_1) E_{2Z}(\omega_2). \tag{2.84}$$

This is identical to Eq. (2.75) with $K = Z$, and $\chi_{IJZ}^{(2),\mathrm{dipole}}$ does not need to be zero. To have nonzero $\chi_{IJZ}^{(2),\mathrm{dipole}}$, similar relations need to be obtained also for the parity inversion with respect to I and J. Because $I, J \neq Z$, the sign of $\chi_{IJZ}^{(2),\mathrm{dipole}}$ is not changed by the parity inversion assuming the in-plane isotropy of the interface. If $I \neq J$, the parity inversion of I and J respectively gives

$$-P_I^{(2)}(\omega_3) = \varepsilon_0 \chi_{IJZ}^{(2),\mathrm{dipole}} E_{1J}(\omega_1) E_{2Z}(\omega_2), \tag{2.85}$$

$$P_I^{(2)}(\omega_3) = \varepsilon_0 \chi_{IJZ}^{(2),\mathrm{dipole}} \left\{-E_{1J}(\omega_1)\right\} E_{2Z}(\omega_2). \tag{2.86}$$

These two equations require $\chi_{IJZ}^{(2),\mathrm{dipole}} = 0$, and VSFG due to this tensor element is forbidden. When $I = J$, the inversion of the $I = J$ coordinate gives

$$-P_I^{(2)}(\omega_3) = \varepsilon_0 \chi_{IIZ}^{(2),\mathrm{dipole}} \left\{-E_{1I}(\omega_1)\right\} E_{2Z}(\omega_2). \tag{2.87}$$

This is identical to Eq. (2.75). Hence, $\chi_{IIZ}^{(2),\mathrm{dipole}} \neq 0$ and VSFG can arise from this tensor element. (To be more precise, $\chi_{IIZ}^{(2),\mathrm{dipole}} \neq 0$ if the molecules are not centrosymmetric $\left(\beta_{ijk}^{\mathrm{dipole}} \neq 0\right)$ and if they have the orientational alignment ($\langle R_{Ii} R_{Jj} R_{Zk} \rangle_{\mathrm{av}} \neq 0$), as I have already mentioned.) This is the origin of the interface-selectivity of VSFG within the electric dipole approximation.

By considering a more general case, it can be shown that $\chi_{IJK}^{(2),\mathrm{dipole}}$ at the interface is nonzero only when the suffix contains an odd number (1 or 3) of Z and an even number (0 or 2) of X or Y. Thus, the nonzero tensor elements of $\chi_{IJK}^{(2),\mathrm{dipole}}$ are

$$\chi_{IIZ}^{(2),\mathrm{dipole}}, \chi_{IZI}^{(2),\mathrm{dipole}}, \chi_{ZII}^{(2),\mathrm{dipole}}, \chi_{ZZZ}^{(2),\mathrm{dipole}}. \tag{2.88}$$

All the seven nonzero tensor elements can be explicitly listed up as

$$\chi_{XXZ}^{(2),\mathrm{dipole}} = \chi_{YYZ}^{(2),\mathrm{dipole}}, \tag{2.89}$$

$$\chi_{XZX}^{(2),\mathrm{dipole}} = \chi_{YZY}^{(2),\mathrm{dipole}}, \tag{2.90}$$

$$\chi_{ZXX}^{(2),\mathrm{dipole}} = \chi_{ZYY}^{(2),\mathrm{dipole}}, \tag{2.91}$$

$$\chi_{ZZZ}^{(2),\mathrm{dipole}}. \tag{2.92}$$

Hence, the interfacial properties can be elucidated by measuring these four independent tensor elements by VSFG spectroscopy.

It is important to remember that this interface selectivity is valid only when the bulk media have the inversion symmetry. For many of the air/solid interfaces, for instance, this condition is not satisfied, and $\chi_{IJK}^{(2),\mathrm{dipole}} \neq 0$ even in the bulk.

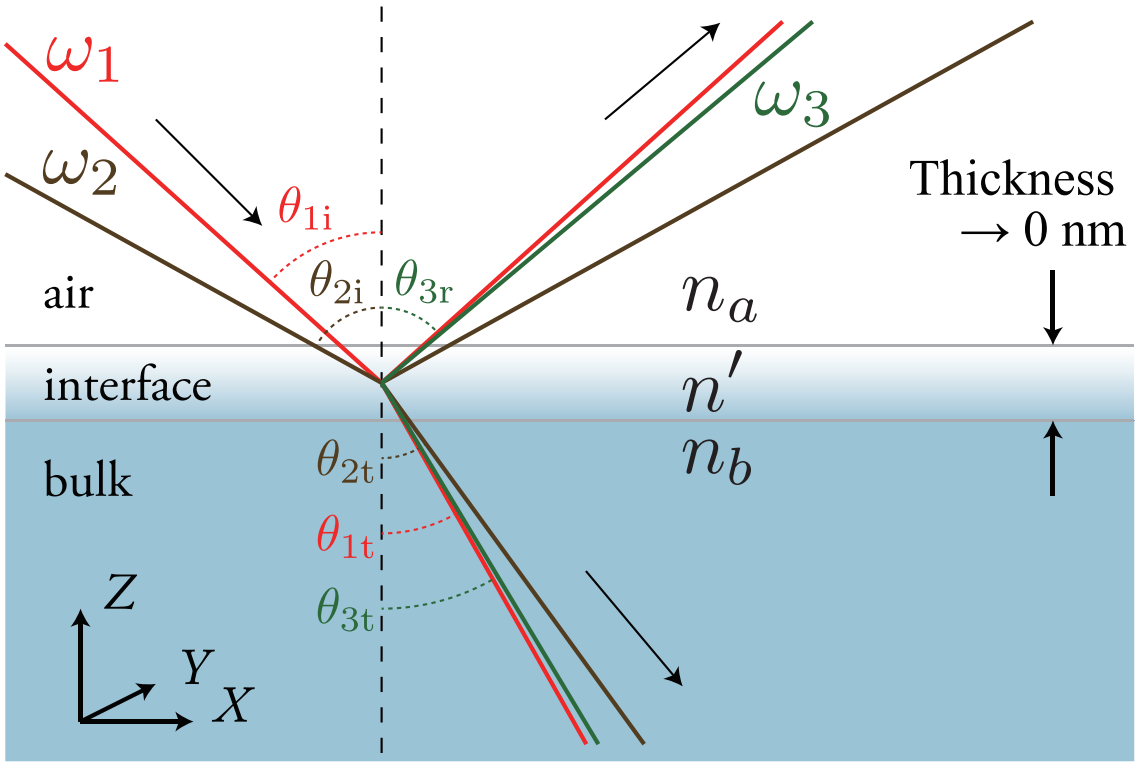

Figure 2.2: Optical configuration of VSFG. The nonlinear polarization is localized at the interface.

2.4 VSFG due to the polarization localized at the interface

For air/liquid interfaces discussed in this thesis, the bulk media have the inversion symmetry, and the induced nonlinear polarization, $\mathbf{P}^{(2)}$, is nonzero only at the interface. It is shown in this section how the sum frequency light is generated from the nonlinear polarization, and what kind of physical quantity is observed in the actual experiments [39].

2.4.1 Wave propagation in the bulk media

For the sake of simplicity, all the beams are treated as monochromatic plane waves in this section.

$$\mathbf{E}(\mathbf{R},t) = \mathbf{E}(\mathbf{k},\omega)e^{i\mathbf{k}\cdot\mathbf{R}-i\omega t}. \tag{2.93}$$

To further simplify the situation, it is helpful to parametrize the light using a limited number of parameters, which can be done by considering the properties of the electromagnetic fields based on the Maxwell equations.

In the isotropic bulk, the electric field, $\mathbf{E}$, and the electric displacement, $\mathbf{D}$, are related by a scalar dielectric constant, ε, as

$$\mathbf{D}(\mathbf{R},t) = \varepsilon\mathbf{E}(\mathbf{R},t). \tag{2.94}$$

Substituting this relation into the Maxwell equation, $\boldsymbol{\nabla}\cdot\mathbf{D}(\mathbf{R},t) = 0$,

$$-i\varepsilon\mathbf{k}\cdot\mathbf{E}(\mathbf{R},t) = 0 \tag{2.95}$$

is obtained. This result requires that the electric field, $\mathbf{E}$, be perpendicular to the wave vector, $\mathbf{k}$, meaning that the electric field is a transverse wave and can be expressed in terms of only two components, i.e. S-polarized component and P-polarized component. The S-polarization is parallel to the Y-axis in Fig. 2.2, and the P-polarization exists in the XZ-plane.

Next, the magnetic induction is expressed in terms of the electric field again using the Maxwell equation.

$$\boldsymbol{\nabla} \times \mathbf{E}(\mathbf{R}, t) + \frac{\partial \mathbf{B}(\mathbf{R}, t)}{\partial t} = 0. \tag{2.96}$$

Using the coordinate and time dependence of the fields ($e^{i\mathbf{k}\cdot\mathbf{R}-i\omega t}$), this can be transformed into

$$i\mathbf{k} \times \mathbf{E}(\mathbf{R}, t) - i\omega \mathbf{B}(\mathbf{R}, t) = 0. \tag{2.97}$$

Then, the magnetic induction can be given as

$$\mathbf{B}(\mathbf{R}, t) = \frac{1}{\omega}\mathbf{k} \times \mathbf{E}(\mathbf{R}, t). \tag{2.98}$$

Using these relations, $\mathbf{k}$, $\mathbf{E}$, $\mathbf{D}$, $\mathbf{B}$, and $\mathbf{H}$ of each light can be expressed using a limited number of parameters.

- Incident ω_1

$$\mathbf{k}_{1\mathrm{i}} = \frac{n_a(\omega_1)\omega_1}{c} \begin{pmatrix} \sin\theta_{1\mathrm{i}} \\ 0 \\ -\cos\theta_{1\mathrm{i}} \end{pmatrix} \tag{2.99}$$

$$\mathbf{E}_{1\mathrm{i}} = \begin{pmatrix} E_{1\mathrm{iP}}\cos\theta_{1\mathrm{i}} \\ E_{1\mathrm{iS}} \\ E_{1\mathrm{iP}}\sin\theta_{1\mathrm{i}} \end{pmatrix} = \frac{\mathbf{D}_{1\mathrm{i}}}{\varepsilon_0 n_a(\omega_1)^2} \tag{2.100}$$

$$\mathbf{B}_{1\mathrm{i}} = \frac{n_a(\omega_1)}{c} \begin{pmatrix} E_{1\mathrm{iS}}\cos\theta_{1\mathrm{i}} \\ -E_{1\mathrm{iP}} \\ E_{1\mathrm{iS}}\sin\theta_{1\mathrm{i}} \end{pmatrix} = \frac{\mathbf{H}_{1\mathrm{i}}}{c^2\varepsilon_0} \tag{2.101}$$

- Transmitted ω_1

$$\mathbf{k}_{1\mathrm{t}} = \frac{n_b(\omega_1)\omega_1}{c} \begin{pmatrix} \sin\theta_{1\mathrm{t}} \\ 0 \\ -\cos\theta_{1\mathrm{t}} \end{pmatrix} \tag{2.102}$$

$$\mathbf{E}_{1\mathrm{t}} = \begin{pmatrix} E_{1\mathrm{tP}}\cos\theta_{1\mathrm{t}} \\ E_{1\mathrm{tS}} \\ E_{1\mathrm{tP}}\sin\theta_{1\mathrm{t}} \end{pmatrix} = \frac{\mathbf{D}_{1\mathrm{t}}}{\varepsilon_0 n_b(\omega_1)^2} \tag{2.103}$$

$$\mathbf{B}_{1\mathrm{t}} = \frac{n_b(\omega_1)}{c} \begin{pmatrix} E_{1\mathrm{tS}}\cos\theta_{1\mathrm{t}} \\ -E_{1\mathrm{tP}} \\ E_{1\mathrm{tS}}\sin\theta_{1\mathrm{t}} \end{pmatrix} = \frac{\mathbf{H}_{1\mathrm{t}}}{c^2\varepsilon_0} \tag{2.104}$$

- Incident ω_2

$$\mathbf{k}_{2\mathrm{i}} = \frac{n_a(\omega_2)\omega_2}{c} \begin{pmatrix} \sin\theta_{2\mathrm{i}} \\ 0 \\ -\cos\theta_{2\mathrm{i}} \end{pmatrix} \tag{2.105}$$

$$\mathbf{E}_{2\mathrm{i}} = \begin{pmatrix} E_{2\mathrm{iP}} \cos\theta_{2\mathrm{i}} \\ E_{2\mathrm{iS}} \\ E_{2\mathrm{iP}} \sin\theta_{2\mathrm{i}} \end{pmatrix} = \frac{\mathbf{D}_{2\mathrm{i}}}{\varepsilon_0 n_a(\omega_2)^2} \tag{2.106}$$

$$\mathbf{B}_{2\mathrm{i}} = \frac{n_a(\omega_2)}{c} \begin{pmatrix} E_{2\mathrm{iS}} \cos\theta_{2\mathrm{i}} \\ -E_{2\mathrm{iP}} \\ E_{2\mathrm{iS}} \sin\theta_{2\mathrm{i}} \end{pmatrix} = \frac{\mathbf{H}_{2\mathrm{i}}}{c^2 \varepsilon_0} \tag{2.107}$$

- Transmitted ω_2

$$\mathbf{k}_{2\mathrm{t}} = \frac{n_b(\omega_2)\omega_2}{c} \begin{pmatrix} \sin\theta_{2\mathrm{t}} \\ 0 \\ -\cos\theta_{2\mathrm{t}} \end{pmatrix} \tag{2.108}$$

$$\mathbf{E}_{2\mathrm{t}} = \begin{pmatrix} E_{2\mathrm{tP}} \cos\theta_{2\mathrm{t}} \\ E_{2\mathrm{tS}} \\ E_{2\mathrm{tP}} \sin\theta_{2\mathrm{t}} \end{pmatrix} = \frac{\mathbf{D}_{2\mathrm{t}}}{\varepsilon_0 n_b(\omega_2)^2} \tag{2.109}$$

$$\mathbf{B}_{2\mathrm{t}} = \frac{n_b(\omega_2)}{c} \begin{pmatrix} E_{2\mathrm{tS}} \cos\theta_{2\mathrm{t}} \\ -E_{2\mathrm{tP}} \\ E_{2\mathrm{tS}} \sin\theta_{2\mathrm{t}} \end{pmatrix} = \frac{\mathbf{H}_{2\mathrm{t}}}{c^2 \varepsilon_0} \tag{2.110}$$

- ω_3 in the reflection direction

$$\mathbf{k}_{3\mathrm{r}} = \frac{n_a(\omega_3)\omega_3}{c} \begin{pmatrix} \sin\theta_{3\mathrm{r}} \\ 0 \\ \cos\theta_{3\mathrm{r}} \end{pmatrix} \tag{2.111}$$

$$\mathbf{E}_{3\mathrm{r}} = \begin{pmatrix} -E_{3\mathrm{rP}} \cos\theta_{3\mathrm{r}} \\ E_{3\mathrm{rS}} \\ E_{3\mathrm{rP}} \sin\theta_{3\mathrm{r}} \end{pmatrix} = \frac{\mathbf{D}_{3\mathrm{r}}}{\varepsilon_0 n_a(\omega_3)^2} \tag{2.112}$$

$$\mathbf{B}_{3\mathrm{r}} = \frac{n_a(\omega_3)}{c} \begin{pmatrix} -E_{3\mathrm{rS}} \cos\theta_{3\mathrm{r}} \\ -E_{3\mathrm{rP}} \\ E_{3\mathrm{rS}} \sin\theta_{3\mathrm{r}} \end{pmatrix} = \frac{\mathbf{H}_{3\mathrm{r}}}{c^2 \varepsilon_0} \tag{2.113}$$

- ω_3 in the transmission direction

$$\mathbf{k}_{3\mathrm{t}} = \frac{n_b(\omega_3)\omega_3}{c} \begin{pmatrix} \sin\theta_{3\mathrm{t}} \\ 0 \\ -\cos\theta_{3\mathrm{t}} \end{pmatrix} \tag{2.114}$$

$$\mathbf{E}_{3\mathrm{t}} = \begin{pmatrix} E_{3\mathrm{tP}} \cos\theta_{3\mathrm{t}} \\ E_{3\mathrm{tS}} \\ E_{3\mathrm{tP}} \sin\theta_{3\mathrm{t}} \end{pmatrix} = \frac{\mathbf{D}_{3\mathrm{t}}}{\varepsilon_0 n_b(\omega_3)^2} \tag{2.115}$$

$$\mathbf{B}_{3\mathrm{t}} = \frac{n_b(\omega_3)}{c} \begin{pmatrix} E_{3\mathrm{tS}} \cos\theta_{3\mathrm{t}} \\ -E_{3\mathrm{tP}} \\ E_{3\mathrm{tS}} \sin\theta_{3\mathrm{t}} \end{pmatrix} = \frac{\mathbf{H}_{3\mathrm{t}}}{c^2 \varepsilon_0} \tag{2.116}$$

2.4.2 Nonlinear polarization

In this section, it is assumed that the nonlinear polarization is localized within an infinitesimally thin interface layer. This can be theoretically expressed using Dirac's delta function in the surface-normal Z direction.

$$\mathbf{P}^{(2)}(\mathbf{R}, t) \equiv \mathbf{P}_S^{(2)}(X, Y, t)\delta(Z). \tag{2.117}$$

Here, $\mathbf{P}_S^{(2)}$ is called the surface nonlinear polarization. Because the polarization is induced at the interface, it should be expressed in terms of the electric fields at the interface, E'.

$$P_I^{(2)}(\mathbf{R},t) = \varepsilon_0 \sum_{J,K} \chi_{IJK}^{(2),\mathrm{dipole}} E'_{1J}(\mathbf{R},t) E'_{2K}(\mathbf{R},t) \tag{2.118}$$

These interfacial electric fields, E', can be conveniently given in terms of the incident electric field, E_i, using the interfacial Fresnel factors [39].

$$E'_{1J} = L_J^{\omega_1} E_{1\mathrm{i}J}, \tag{2.119}$$

$$E'_{2K} = L_K^{\omega_2} E_{2\mathrm{i}K}, \tag{2.120}$$

where

$$L_X^\omega = \frac{2n_a(\omega)\cos\theta_\mathrm{t}}{n_a(\omega)\cos\theta_\mathrm{t} + n_b(\omega)\cos\theta_\mathrm{i}}, \tag{2.121}$$

$$L_Y^\omega = \frac{2n_a(\omega)\cos\theta_\mathrm{i}}{n_a(\omega)\cos\theta_\mathrm{i} + n_b(\omega)\cos\theta_\mathrm{t}}, \tag{2.122}$$

$$L_Z^\omega = \frac{2n_b(\omega)\cos\theta_\mathrm{i}}{n_a(\omega)\cos\theta_\mathrm{t} + n_b(\omega)\cos\theta_\mathrm{i}} \left(\frac{n_a(\omega)}{n'(\omega)}\right)^2. \tag{2.123}$$

Here, n_a, n_b, and n' are the refractive indices of the upper bulk medium (air), the lower bulk medium (liquid), and the interface, respectively, and θ_i and θ_t are the incident and transmission angle, respectively, as shown in Fig. 2.2. Using the seven nonzero tensor elements,

$$\chi_{XXZ}^{(2),\mathrm{dipole}} = \chi_{YYZ}^{(2),\mathrm{dipole}}, \quad \chi_{XZX}^{(2),\mathrm{dipole}} = \chi_{YZY}^{(2),\mathrm{dipole}}, \quad \chi_{ZXX}^{(2),\mathrm{dipole}} = \chi_{ZYY}^{(2),\mathrm{dipole}}, \quad \chi_{ZZZ}^{(2),\mathrm{dipole}}, \tag{2.124}$$

and the formulae for the incident electric fields shown above, the induced polarization in each direction can be expressed as

$$P_X^{(2)} = \varepsilon_0 \left(\chi_{XXZ}^{(2),\mathrm{dipole}} E'_{1X} E'_{2Z} + \chi_{XZX}^{(2),\mathrm{dipole}} E'_{1Z} E'_{2X}\right) \tag{2.125}$$

$$= \varepsilon_0 \left(L_X^{\omega_1} L_Z^{\omega_2} \cos\theta_{1\mathrm{i}} \sin\theta_{2\mathrm{i}} \chi_{XXZ}^{(2),\mathrm{dipole}} + L_Z^{\omega_1} L_X^{\omega_2} \sin\theta_{1\mathrm{i}} \cos\theta_{2\mathrm{i}} \chi_{XZX}^{(2),\mathrm{dipole}}\right) E_{1\mathrm{iP}} E_{2\mathrm{iP}}, \tag{2.126}$$

$$P_Y^{(2)} = \varepsilon_0 \left(\chi_{YYZ}^{(2),\mathrm{dipole}} E'_{1Y} E'_{2Z} + \chi_{YZY}^{(2),\mathrm{dipole}} E'_{1Z} E'_{2Y}\right) \tag{2.127}$$

$$= \varepsilon_0 L_Y^{\omega_1} L_Z^{\omega_2} \sin\theta_{2\mathrm{i}} \chi_{YYZ}^{(2),\mathrm{dipole}} E_{1\mathrm{iS}} E_{2\mathrm{iP}} + \varepsilon_0 L_Z^{\omega_1} L_Y^{\omega_2} \sin\theta_{1\mathrm{i}} \chi_{YZY}^{(2),\mathrm{dipole}} E_{1\mathrm{iP}} E_{2\mathrm{iS}}, \tag{2.128}$$

$$P_Z^{(2)} = \varepsilon_0 \left(\chi_{ZXX}^{(2),\mathrm{dipole}} E'_{1X} E'_{2X} + \chi_{ZYY}^{(2),\mathrm{dipole}} E'_{1Y} E'_{2Y} + \chi_{ZZZ}^{(2),\mathrm{dipole}} E'_{1Z} E'_{2Z}\right) \tag{2.129}$$

$$= \varepsilon_0 \left(L_X^{\omega_1} L_X^{\omega_2} \cos\theta_{1\mathrm{i}} \cos\theta_{2\mathrm{i}} \chi_{ZXX}^{(2),\mathrm{dipole}} + L_Z^{\omega_1} L_Z^{\omega_2} \sin\theta_{1\mathrm{i}} \sin\theta_{2\mathrm{i}} \chi_{ZZZ}^{(2),\mathrm{dipole}}\right) E_{1\mathrm{iP}} E_{2\mathrm{iP}}$$
$$+ \varepsilon_0 L_Y^{\omega_1} L_Y^{\omega_2} \chi_{ZYY}^{(2),\mathrm{dipole}} E_{1\mathrm{iS}} E_{2\mathrm{iS}}. \tag{2.130}$$

Because $\mathbf{P}^{(2)}$ is localized at the interface ($Z = 0$), its coordinate and time dependence can be expressed as

$$\mathbf{P}^{(2)}(\mathbf{R},t) = \mathbf{P}^{(2)}(\mathbf{k}_\mathrm{p},\omega_3) e^{i\mathbf{k}_\mathrm{p}\cdot\mathbf{R} - i\omega_3 t} \delta(Z), \tag{2.131}$$

with

$$\mathbf{k}_{\mathrm{p}} = \begin{pmatrix} k_{\mathrm{p}X} \\ 0 \\ k_{\mathrm{p}Z} \end{pmatrix}. \tag{2.132}$$

The surface nonlinear polarization, $\mathbf{P}_S^{(2)}$, can be obtained from these formulae as

$$P_{S,I}^{(2)}(\mathbf{R},t) = \int dZ P_I^{(2)}(\mathbf{R},t) = P_I^{(2)}(\mathbf{k}_{\mathrm{p}},\omega_3) e^{ik_{\mathrm{p}X}X - i\omega_3 t}. \tag{2.133}$$

2.4.3 Boundary conditions

The boundary conditions at the interface can be derived from each of the four Maxwell equations, and using these boundary conditions, the generated sum frequency electric field can be expressed in terms of the induced nonlinear polarization. Before going into the details, one obvious but important property of the boundary conditions is discussed. Namely, the boundary conditions must be satisfied everywhere at the interface simultaneously. Since the interface exists on the XY-plane as shown in Fig. 2.2, the X- and Y-components of the wave vectors (k_X and k_Y) must be the same for all the light and polarization with the same frequency at ω_3 (the sum frequency light in the reflection and transmission directions, and the induced nonlinear polarization). Because $k_Y = 0$ for all the beams and the polarization, only the matching of the X-components need to be considered.

$$\frac{n_a(\omega_3)\omega_3}{c}\sin\theta_{3\mathrm{r}} = \frac{n_b(\omega_3)\omega_3}{c}\sin\theta_{3\mathrm{t}} = k_{\mathrm{p}X} = \frac{n_a(\omega_1)\omega_1}{c}\sin\theta_{1\mathrm{i}} + \frac{n_a(\omega_2)\omega_2}{c}\sin\theta_{2\mathrm{i}}. \tag{2.134}$$

This relation specifies the emission angle of the sum frequency radiation in the reflection and transmission directions.

In the following part, the boundary conditions are derived from each of the four Maxwell equations by considering the nonlinear polarization and the sum frequency light in reflection and transmission directions.

- $\nabla \cdot \left(\mathbf{D} + \mathbf{P}^{(2)}\right) = 0$

  The volume integral inside the cuboid shown in Fig. 2.3(a) is considered.

  $$\int \boldsymbol{\nabla} \cdot \left(\mathbf{D} + \mathbf{P}^{(2)}\right) dV = 0. \tag{2.135}$$

  Using Gauss' theorem, the volume integral of $\boldsymbol{\nabla} \cdot \mathbf{D}$ can be converted to the surface integral of $\mathbf{D}$, in which only the integration at the top and bottom surfaces need to be considered due to the symmetry reason.

  $$\int \boldsymbol{\nabla} \cdot \mathbf{D} dV = \int \mathbf{D} \cdot d\mathbf{S} \tag{2.136}$$

  $$= \iint dX dY (D_{3\mathrm{r}Z} - D_{3\mathrm{t}Z}) \tag{2.137}$$

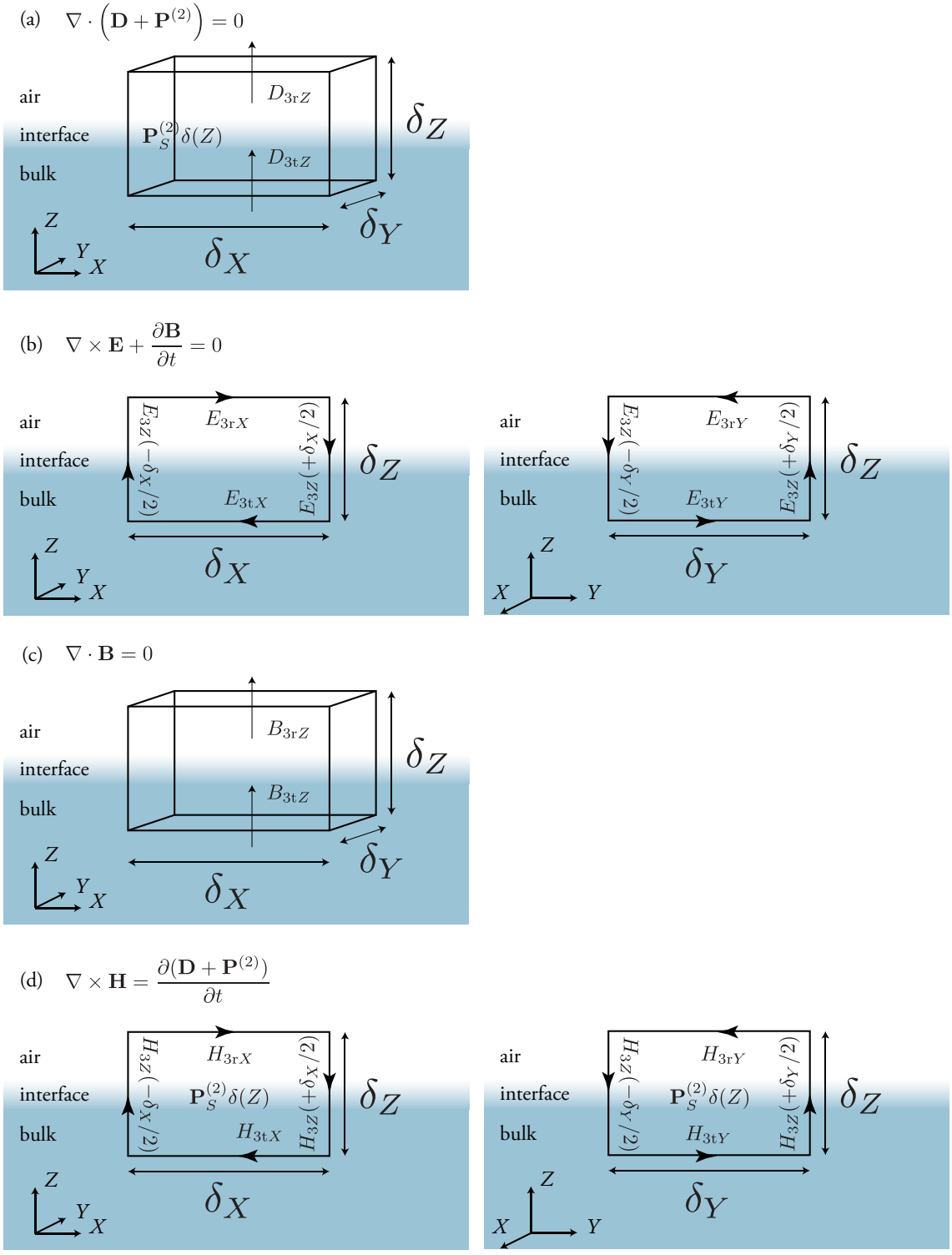

Figure 2.3: Figures showing the surface integration (a, c) and the contour integration (b, d) used for evaluating the integrated form of the Maxwell equations. Nonlinear polarization, $\mathbf{P}^{(2)} = \mathbf{P}_S^{(2)}\delta(Z)$, is localized at the interface. δ_X, δ_Y, and δ_Z are all sufficiently smaller than the wavelength of the light.

$$= (D_{3\mathrm{r}Z} - D_{3\mathrm{t}Z})\delta_X\delta_Y. \tag{2.138}$$

As for the volume integral of $\boldsymbol{\nabla}\cdot\mathbf{P}^{(2)}$, this can be directly evaluated by remembering that it can be rewritten using the surface polarization as $\mathbf{P}^{(2)}(X,Y,Z) = \mathbf{P}_S^{(2)}(X,Y)\delta(Z)$.

$$\int \boldsymbol{\nabla}\cdot\mathbf{P}^{(2)}dV = \int \boldsymbol{\nabla}\cdot\mathbf{P}_S^{(2)}\delta(Z)dV \tag{2.139}$$

$$= \iiint dXdYdZ \left(\frac{\partial P_{S,X}^{(2)}(X,Y)}{\partial X} + \frac{\partial P_{S,Y}^{(2)}(X,Y)}{\partial Y} + \frac{\partial P_{S,Z}^{(2)}(X,Y)}{\partial Z}\right)\delta(Z) \tag{2.140}$$

$$= \iint dXdY \left(\frac{\partial P_{S,X}^{(2)}}{\partial X} + \frac{\partial P_{S,Y}^{(2)}}{\partial Y}\right) \tag{2.141}$$

$$= \left(\frac{\partial P_{S,X}^{(2)}}{\partial X} + \frac{\partial P_{S,Y}^{(2)}}{\partial Y}\right)\delta_X\delta_Y. \tag{2.142}$$

Hence,

$$0 = \int \boldsymbol{\nabla}\cdot\left(\mathbf{D} + \mathbf{P}^{(2)}\right)dV \tag{2.143}$$

$$= (D_{3\mathrm{r}Z} - D_{3\mathrm{t}Z})\delta_X\delta_Y + \left(\frac{\partial P_{S,X}^{(2)}}{\partial X} + \frac{\partial P_{S,Y}^{(2)}}{\partial Y}\right)\delta_X\delta_Y. \tag{2.144}$$

This boundary condition can be expressed in terms of the electric field as

$$\varepsilon_0 n_a(\omega_3)^2 E_{3\mathrm{r}\mathrm{P}}\sin\theta_{3\mathrm{r}} - \varepsilon_0 n_b(\omega_3)^2 E_{3\mathrm{t}\mathrm{P}}\sin\theta_{3\mathrm{t}} = -ik_{\mathrm{p}X}P_{S,X}^{(2)}. \tag{2.145}$$

Using Eq. (2.134), following equation is finally obtained.

$$n_a(\omega_3)E_{3\mathrm{r}\mathrm{P}} - n_b(\omega_3)E_{3\mathrm{t}\mathrm{P}} = -\frac{i\omega_3}{c\varepsilon_0}P_{S,X}^{(2)}. \tag{2.146}$$

- $\nabla\times\mathbf{E} + \frac{\partial\mathbf{B}}{\partial t} = 0$

  Surface integrals within the rectangles shown in Fig. 2.3(b) are considered.

$$\int (\nabla\times\mathbf{E})\cdot d\mathbf{S} + \int \frac{\partial\mathbf{B}}{\partial t}\cdot d\mathbf{S} = 0. \tag{2.147}$$

First, the integration within the rectangle in the XZ-plane is evaluated. Using the Stokes' theorem, the surface integral of $\boldsymbol{\nabla}\times\mathbf{E}$ can be converted to the contour integral of $\mathbf{E}$.

$$\int (\nabla\times\mathbf{E})\cdot d\mathbf{S} = \oint \mathbf{E}\cdot d\mathbf{r} \tag{2.148}$$

$$= \int dX(E_{3\mathrm{r}X} - E_{3\mathrm{t}X}) - \int dZ\left\{E_{3Z}(+\delta_X/2) - E_{3Z}(-\delta_X/2)\right\} \tag{2.149}$$

$$= (E_{3\mathrm{r}X} - E_{3\mathrm{t}X})\delta_X - \int dZ\frac{\partial E_{3Z}}{\partial X}\delta_X. \tag{2.150}$$

Care must be taken for the integration of E_{3Z} in the Z-direction, because E_{3Z} has a singularity at the interface due to the localized nonlinear polarization at the interface.

$$E_{3Z} = \frac{\left(D_{3Z} + P_Z^{(2)}\right) - P_Z^{(2)}}{\varepsilon_0 n(\omega_3)^2}. \tag{2.151}$$

In this formula, E_{3Z} and $P_Z^{(2)}$ are singular at the interface ($Z = 0$), while $D_{3Z} + P_Z^{(2)}$ is smoothly continuous across the interface. Then, in the limit of $\delta_Z \to 0$,

$$\int dZ \frac{\partial E_{3Z}}{\partial X}\delta_X = \delta_X \frac{\partial}{\partial X}\int_{-\delta_Z/2}^{\delta_Z/2} dZ \frac{\left(D_{3Z} + P_Z^{(2)}\right) - P_{S,Z}^{(2)}\delta(Z)}{\varepsilon_0 n(\omega_3)^2} \tag{2.152}$$

$$= -\frac{\delta_X}{\varepsilon_0 n'(\omega_3)^2}\frac{\partial P_{S,Z}^{(2)}}{\partial X}. \tag{2.153}$$

Here, $n'(\omega_3)$ is the refractive index at the interface, and $D_{3Z} + P_Z^{(2)}$ was neglected because it vanishes for a sufficiently small integration range along Z. Using these results,

$$\int (\nabla \times \mathbf{E}) \cdot d\mathbf{S} = (E_{3\mathrm{r}X} - E_{3\mathrm{t}X})\delta_X + \frac{\delta_X}{\varepsilon_0 n'(\omega_3)^2}\frac{\partial P_{S,Z}^{(2)}}{\partial X} \tag{2.154}$$

is obtained. As for the surface integration of $\partial\mathbf{B}/\partial t$,

$$\frac{\partial}{\partial t}\int \mathbf{B} \cdot d\mathbf{S} = 0 \tag{2.155}$$

for a sufficiently small integration area, because $\mathbf{B}$ does not have any singularities near the interface. Combining these results, the following boundary condition is finally obtained.

$$E_{3\mathrm{r}X} - E_{3\mathrm{t}X} = -\frac{1}{\varepsilon_0 n'(\omega_3)^2}\frac{\partial P_{S,Z}^{(2)}}{\partial X}. \tag{2.156}$$

Similarly, from the surface integration in the YZ-plane (right figure in Fig. 2.3(b)), the following boundary condition can be obtained.

$$E_{3\mathrm{r}Y} - E_{3\mathrm{t}Y} = -\frac{1}{\varepsilon_0 n'(\omega_3)^2}\frac{\partial P_{S,Z}^{(2)}}{\partial Y}. \tag{2.157}$$

These two boundary conditions can be rewritten in a more convenient form as

$$-E_{3\mathrm{rP}}\cos\theta_{3\mathrm{r}} - E_{3\mathrm{tP}}\cos\theta_{3\mathrm{t}} = -\frac{ik_{\mathrm{p}X}}{\varepsilon_0 n'(\omega_3)^2}P_{S,Z}^{(2)}, \tag{2.158}$$

$$E_{3\mathrm{rS}} - E_{3\mathrm{tS}} = 0. \tag{2.159}$$

- $\nabla \cdot \mathbf{B} = 0$

  Using Gauss' theorem, the volume integral of $\nabla \cdot \mathbf{B} = 0$ inside the cuboid shown in Fig. 2.3(c) can be evaluated.

$$0 = \int (\nabla \cdot \mathbf{B}) dV = \int \mathbf{B} \cdot d\mathbf{S} \tag{2.160}$$

$$= \iint dXdY(B_{3\mathrm{r}Z} - B_{3\mathrm{t}Z}) \tag{2.161}$$

$$= (B_{3\mathrm{r}Z} - B_{3\mathrm{t}Z})\delta_X\delta_Y. \tag{2.162}$$

In terms of the electric field, this can be rewritten as

$$\frac{n_a(\omega_3)}{c}E_{3\mathrm{r}\mathrm{S}}\sin\theta_{3\mathrm{r}} = \frac{n_b(\omega_3)}{c}E_{3\mathrm{t}\mathrm{S}}\sin\theta_{3\mathrm{t}}, \tag{2.163}$$

which is further simplified using Eq. (2.134) into

$$E_{3\mathrm{r}\mathrm{S}} = E_{3\mathrm{t}\mathrm{S}}. \tag{2.164}$$

- $\nabla \times \mathbf{H} = \frac{\partial(\mathbf{D}+\mathbf{P}^{(2)})}{\partial t}$

  Surface integrals within the rectangles shown in Fig. 2.3(d) are considered.

$$\int \boldsymbol{\nabla} \times \mathbf{H} \cdot d\mathbf{S} = \int \frac{\partial(\mathbf{D} + \mathbf{P}^{(2)})}{\partial t} \cdot d\mathbf{S}. \tag{2.165}$$

  First, the integration in the XZ-plane is evaluated. Using Stokes' theorem, the surface integration of $\boldsymbol{\nabla} \times \mathbf{H}$ can be executed.

$$\int (\nabla \times \mathbf{H}) \cdot d\mathbf{S} = \oint \mathbf{H} \cdot d\mathbf{r} \tag{2.166}$$

$$= \int dX(H_{3\mathrm{r}X} - H_{3\mathrm{t}X}) - \int dZ\{H_{3Z}(+\delta_X/2) - H_{3Z}(-\delta_X/2)\} \tag{2.167}$$

$$= (H_{3\mathrm{r}X} - H_{3\mathrm{t}X})\delta_X. \tag{2.168}$$

  Here, the contribution from H_{3Z} was neglected, because H_{3Z} does not have a singularity near the interface, and its contribution vanishes in the limit of $\delta_Z \to 0$. The surface integration of $\partial(\mathbf{D} + \mathbf{P}^{(2)})/\partial t$ is also evaluated.

$$\int \frac{\partial(\mathbf{D} + \mathbf{P}^{(2)})}{\partial t} \cdot d\mathbf{S} = \frac{\partial}{\partial t} \iint \left\{ D_{3Y} + P^{(2)}_{S,Y}\delta(Z) \right\} dZdX = 0 + \frac{\partial P^{(2)}_{S,Y}}{\partial t}\delta_X. \tag{2.169}$$

  Since $D_{3Y} = \varepsilon_0 n(\omega_3)^2 E_{3Y}$ does not have a singularity near the interface, its contribution vanishes in the limit of $\delta_Z \to 0$. Combining these results, the following boundary condition is obtained.

$$H_{3\mathrm{r}X} - H_{3\mathrm{t}X} = \frac{\partial P^{(2)}_{S,Y}}{\partial t}. \tag{2.170}$$

  Similarly, by considering the surface integral in the YZ-plane (right figure in Fig. 2.3(d)), another boundary condition can be derived.

$$H_{3\mathrm{r}Y} - H_{3\mathrm{t}Y} = -\frac{\partial P^{(2)}_{S,X}}{\partial t}. \tag{2.171}$$

  Expressing these equations in terms of the electric fields, the following boundary conditions can be finally obtained.

$$-c\varepsilon_0 n_a(\omega_3)E_{3\mathrm{r}\mathrm{S}}\cos\theta_{3\mathrm{r}} - c\varepsilon_0 n_b(\omega_3)E_{3\mathrm{t}\mathrm{S}}\cos\theta_{3\mathrm{t}} = -i\omega_3 P^{(2)}_{S,Y}, \tag{2.172}$$

$$-c\varepsilon_0 n_a(\omega_3)E_{3\mathrm{r}\mathrm{P}} + c\varepsilon_0 n_b(\omega_3)E_{3\mathrm{t}\mathrm{P}} = i\omega_3 P^{(2)}_{S,X}. \tag{2.173}$$

- Summary of the results

  From the boundary conditions discussed above, four independent equations can be obtained as shown below.

$$E_{3\mathrm{rS}} = E_{3\mathrm{tS}} \tag{2.174}$$

$$n_a(\omega_3)E_{3\mathrm{rS}}\cos\theta_{3\mathrm{r}} + n_b(\omega_3)E_{3\mathrm{tS}}\cos\theta_{3\mathrm{t}} = \frac{i\omega_3}{c\varepsilon_0}P^{(2)}_{S,Y} \tag{2.175}$$

$$-n_a(\omega_3)E_{3\mathrm{rP}} + n_b(\omega_3)E_{3\mathrm{tP}} = \frac{i\omega_3}{c\varepsilon_0}P^{(2)}_{S,X} \tag{2.176}$$

$$E_{3\mathrm{rP}}\cos\theta_{3\mathrm{r}} + E_{3\mathrm{tP}}\cos\theta_{3\mathrm{t}} = \frac{ik_{\mathrm{p}X}}{\varepsilon_0 n'(\omega_3)^2}P^{(2)}_{S,Z} \tag{2.177}$$

  These equations can be used to give theoretical expressions for the generated sum frequency electric fields.

2.4.4 Sum frequency electric field

The simultaneous equations derived from the boundary conditions can be used to express the sum frequency electric field in the reflection direction in terms of the surface nonlinear polarization.

$$E_{3\mathrm{rS}} = \frac{i\omega_3}{c\varepsilon_0}\frac{P^{(2)}_{S,Y}}{n_a(\omega_3)\cos\theta_{3\mathrm{r}} + n_b(\omega_3)\cos\theta_{3\mathrm{t}}}, \tag{2.178}$$

$$E_{3\mathrm{rP}} = \frac{i\omega_3}{c\varepsilon_0}\frac{-\cos\theta_{3\mathrm{t}}P^{(2)}_{S,X} + \frac{n_b(\omega_3)^2}{n'(\omega_3)^2}\sin\theta_{3\mathrm{t}}P^{(2)}_{S,Z}}{n_a(\omega_3)\cos\theta_{3\mathrm{t}} + n_b(\omega_3)\cos\theta_{3\mathrm{r}}}. \tag{2.179}$$

Using the interfacial Fresnel factors in Eqs. (2.121)-(2.123), they can be rewritten in a simpler and more organized form.

$$E_{3\mathrm{rS}} = \frac{i\omega_3}{2cn_a(\omega_3)\cos\theta_{3\mathrm{r}}}\frac{1}{\varepsilon_0}L^{\omega_3}_Y P^{(2)}_{S,Y}, \tag{2.180}$$

$$E_{3\mathrm{rP}} = \frac{i\omega_3}{2cn_a(\omega_3)\cos\theta_{3\mathrm{r}}}\frac{1}{\varepsilon_0}\left(-L^{\omega_3}_X\cos\theta_{3\mathrm{r}}P^{(2)}_{S,X} + L^{\omega_3}_Z\sin\theta_{3\mathrm{r}}P^{(2)}_{S,Z}\right). \tag{2.181}$$

Finally, by substituting the explicit expression of the surface nonlinear polarization given in Eqs. (2.126)-(2.130), the sum frequency electric field can be expressed as the function of the incident electric fields.

$$\begin{aligned} E_{3\mathrm{rS}} = \frac{i\omega_3}{2cn_a(\omega_3)\cos\theta_{3\mathrm{r}}}\Big(&L^{\omega_3}_Y L^{\omega_1}_Y L^{\omega_2}_Z \sin\theta_{2\mathrm{i}}\chi^{(2),\mathrm{dipole}}_{YYZ}E_{1\mathrm{iS}}E_{2\mathrm{iP}} \\ &+L^{\omega_3}_Y L^{\omega_1}_Z L^{\omega_2}_Y \sin\theta_{1\mathrm{i}}\chi^{(2),\mathrm{dipole}}_{YZY}E_{1\mathrm{iP}}E_{2\mathrm{iS}}\Big), \end{aligned} \tag{2.182}$$

$$\begin{aligned} E_{3\mathrm{rP}} = \frac{i\omega_3}{2cn_a(\omega_3)\cos\theta_{3\mathrm{r}}}\Big\{&L^{\omega_3}_Z L^{\omega_1}_Y L^{\omega_2}_Y \sin\theta_{3\mathrm{r}}\chi^{(2),\mathrm{dipole}}_{ZYY}E_{1\mathrm{iS}}E_{2\mathrm{iS}} \\ &+\Big(-L^{\omega_3}_X L^{\omega_1}_X L^{\omega_2}_Z \cos\theta_{3\mathrm{r}}\cos\theta_{1\mathrm{i}}\sin\theta_{2\mathrm{i}}\chi^{(2),\mathrm{dipole}}_{XXZ} \\ &- L^{\omega_3}_X L^{\omega_1}_Z L^{\omega_2}_X \cos\theta_{3\mathrm{r}}\sin\theta_{1\mathrm{i}}\cos\theta_{2\mathrm{i}}\chi^{(2),\mathrm{dipole}}_{XZX} \\ &+ L^{\omega_3}_Z L^{\omega_1}_X L^{\omega_2}_X \sin\theta_{3\mathrm{r}}\cos\theta_{1\mathrm{i}}\cos\theta_{2\mathrm{i}}\chi^{(2),\mathrm{dipole}}_{ZXX} \\ &+L^{\omega_3}_Z L^{\omega_1}_Z L^{\omega_2}_Z \sin\theta_{3\mathrm{r}}\sin\theta_{1\mathrm{i}}\sin\theta_{2\mathrm{i}}\chi^{(2),\mathrm{dipole}}_{ZZZ}\Big)E_{1\mathrm{iP}}E_{2\mathrm{iP}}\Big\}. \end{aligned} \tag{2.183}$$

These complicated equations can be greatly simplified by using the effective nonlinear susceptibilities.

$$E_{3\mathrm{rS}} = \frac{i\omega_3}{2cn_a(\omega_3)\cos\theta_{3\mathrm{r}}}\left(\chi^{(2)}_{\mathrm{eff,SSP}}E_{1\mathrm{iS}}E_{2\mathrm{iP}} + \chi^{(2)}_{\mathrm{eff,SPS}}E_{1\mathrm{iP}}E_{2\mathrm{iS}}\right), \tag{2.184}$$

$$E_{3\mathrm{rP}} = \frac{i\omega_3}{2cn_a(\omega_3)\cos\theta_{3\mathrm{r}}}\left(\chi^{(2)}_{\mathrm{eff,PSS}}E_{1\mathrm{iS}}E_{2\mathrm{iS}} + \chi^{(2)}_{\mathrm{eff,PPP}}E_{1\mathrm{iP}}E_{2\mathrm{iP}}\right), \tag{2.185}$$

with the effective nonlinear susceptibilities defined as

$$\chi^{(2)}_{\mathrm{eff,SSP}} = L_Y^{\omega_3}L_Y^{\omega_1}L_Z^{\omega_2}\sin\theta_{2\mathrm{i}}\chi^{(2),\mathrm{dipole}}_{YYZ}, \tag{2.186}$$

$$\chi^{(2)}_{\mathrm{eff,SPS}} = L_Y^{\omega_3}L_Z^{\omega_1}L_Y^{\omega_2}\sin\theta_{1\mathrm{i}}\chi^{(2),\mathrm{dipole}}_{YZY}, \tag{2.187}$$

$$\chi^{(2)}_{\mathrm{eff,PSS}} = L_Z^{\omega_3}L_Y^{\omega_1}L_Y^{\omega_2}\sin\theta_{3\mathrm{r}}\chi^{(2),\mathrm{dipole}}_{ZYY}, \tag{2.188}$$

$$\begin{aligned}\chi^{(2)}_{\mathrm{eff,PPP}} = &-L_X^{\omega_3}L_X^{\omega_1}L_Z^{\omega_2}\cos\theta_{3\mathrm{r}}\cos\theta_{1\mathrm{i}}\sin\theta_{2\mathrm{i}}\chi^{(2),\mathrm{dipole}}_{XXZ}\\ &- L_X^{\omega_3}L_Z^{\omega_1}L_X^{\omega_2}\cos\theta_{3\mathrm{r}}\sin\theta_{1\mathrm{i}}\cos\theta_{2\mathrm{i}}\chi^{(2),\mathrm{dipole}}_{XZX}\\ &+ L_Z^{\omega_3}L_X^{\omega_1}L_X^{\omega_2}\sin\theta_{3\mathrm{r}}\cos\theta_{1\mathrm{i}}\cos\theta_{2\mathrm{i}}\chi^{(2),\mathrm{dipole}}_{ZXX}\\ &+ L_Z^{\omega_3}L_Z^{\omega_1}L_Z^{\omega_2}\sin\theta_{3\mathrm{r}}\sin\theta_{1\mathrm{i}}\sin\theta_{2\mathrm{i}}\chi^{(2),\mathrm{dipole}}_{ZZZ}.\end{aligned} \tag{2.189}$$

These effective nonlinear susceptibilities (or their squared values) can be experimentally obtained from VSFG measurements.

2.5 VSFG due to the polarization in the bulk

When the bulk media does not have the inversion symmetry, the nonlinear polarization can be induced in the bulk, and VSFG arises from this nonlinear polarization in the bulk. This is practically important, because VSFG in quartz, which is often utilized as the reference, arises from this mechanism.

In the following part, it will be assumed that the upper medium does not have the nonlinearity and the nonlinear polarization is induced only in the lower medium, as shown in Fig. 2.4.

2.5.1 Wave propagation in the bulk media

Using two of the Maxwell equations,

$$\boldsymbol{\nabla}\times\mathbf{E} + \frac{\partial\mathbf{B}}{\partial t} = 0, \tag{2.190}$$

$$\boldsymbol{\nabla}\times\mathbf{H} = \frac{\partial\left(\mathbf{D}+\mathbf{P}^{(2)}\right)}{\partial t}, \tag{2.191}$$

the wave equation in the presence of the nonlinear polarization can be obtained.

$$\left(\boldsymbol{\nabla}^2 - \frac{n^2}{c^2}\frac{\partial^2}{\partial t^2}\right)\mathbf{E} - \boldsymbol{\nabla}(\boldsymbol{\nabla}\cdot\mathbf{E}) = \frac{1}{c^2\varepsilon_0}\frac{\partial\mathbf{P}^{(2)}}{\partial t}. \tag{2.192}$$

In the upper medium, $\mathbf{P}^{(2)} = 0$ and $\boldsymbol{\nabla}\cdot\mathbf{E} = 0$ according to Eq. (2.95). Therefore, this wave equation yields a simple plane wave solution.

$$\mathbf{E}_{3\mathrm{r}}(\mathbf{R},t) = \mathbf{E}_{3\mathrm{r}}(\mathbf{k}_{3\mathrm{r}},\omega_3)e^{i\mathbf{k}_{3\mathrm{r}}\cdot\mathbf{R}-i\omega_3 t}. \tag{2.193}$$

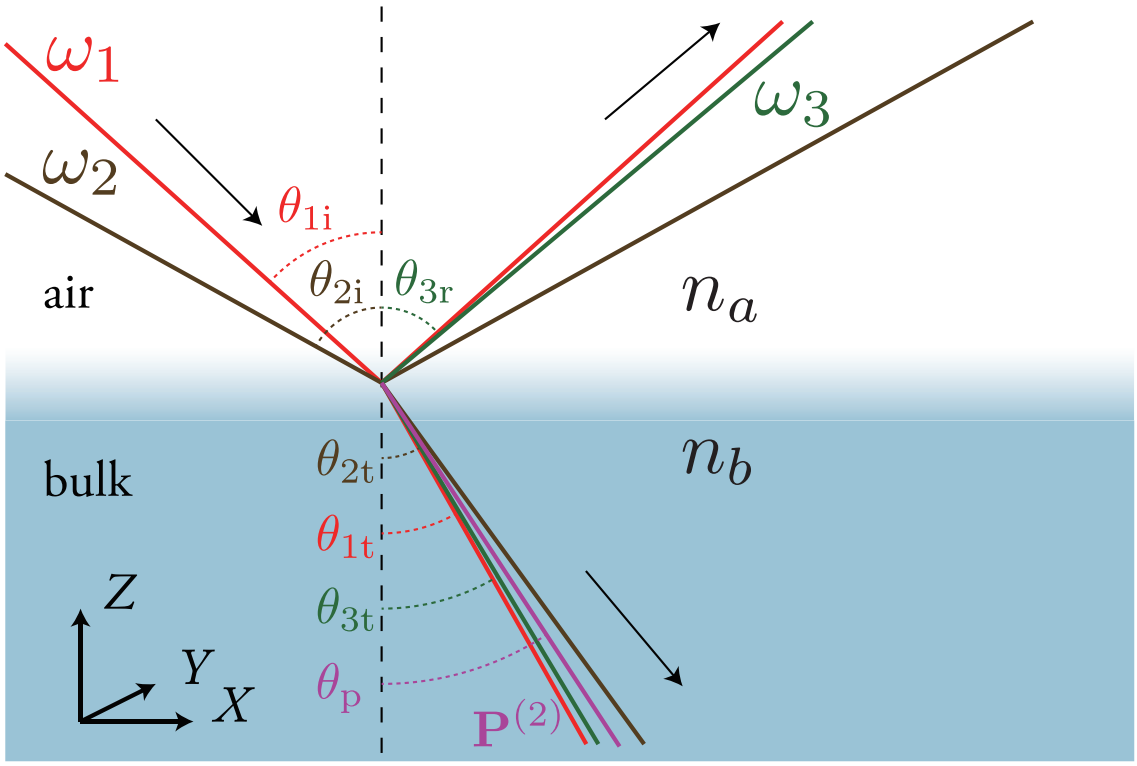

Figure 2.4: Optical configuration of VSFG. The nonlinear polarization is induced in the lower bulk medium.

On the other hand, in the lower medium, $\mathbf{P}^{(2)} \neq 0$. In such a case, the general solution, $\mathbf{E}_{\mathrm{T}}$, of the wave equation is given by the superposition of a homogeneous solution, $\mathbf{E}_{3\mathrm{t}}$, obtained in the absence of $\mathbf{P}^{(2)}$, and a particular solution, $\mathbf{E}_{\mathrm{p}}$, which arises from $\mathbf{P}^{(2)}$.

$$\mathbf{E}_{\mathrm{T}}(\mathbf{R},t) = \mathbf{E}_{3\mathrm{t}}(\mathbf{R},t) + \mathbf{E}_{\mathrm{p}}(\mathbf{R},t), \tag{2.194}$$

$$\mathbf{E}_{3\mathrm{t}}(\mathbf{R},t) = \mathbf{E}_{3\mathrm{t}}(\mathbf{k}_{3\mathrm{t}},\omega_3)e^{i\mathbf{k}_{3\mathrm{t}}\cdot\mathbf{R}-i\omega_3 t}, \tag{2.195}$$

$$\mathbf{E}_{\mathrm{p}}(\mathbf{R},t) = \mathbf{E}_{\mathrm{p}}(\mathbf{k}_{\mathrm{p}},\omega_3)e^{i\mathbf{k}_{\mathrm{p}}\cdot\mathbf{R}-i\omega_3 t}. \tag{2.196}$$

In this solution, $\mathbf{E}_{3\mathrm{t}}$ is a transverse wave, but $\mathbf{E}_{\mathrm{p}}$ is not necessarily a transverse wave because Eq. (2.95) no longer holds due to the presence of $\mathbf{P}^{(2)}$. Hence, in general, the longitudinal component of $\mathbf{E}_{\mathrm{p}}$ needs to be taken into consideration. In the treatment presented here, however, the longitudinal component is neglected for the sake of simplicity. Luckily, the final results given in Eqs. (2.252) and (2.253) are not altered by this simplification. In this treatment, $\boldsymbol{\nabla}\cdot\mathbf{E}_{\mathrm{p}} = 0$, and the particular solution, $\mathbf{E}_{\mathrm{p}}$, can be more explicitly related to the nonlinear polarization, $\mathbf{P}^{(2)}$, by substituting this expression into the wave equation.

$$\left(-|\mathbf{k}_{\mathrm{p}}|^2 + \frac{n_b(\omega_3)^2\omega_3^2}{c^2}\right)\mathbf{E}_{\mathrm{p}} = -\frac{\omega_3^2}{c^2\varepsilon_0}\mathbf{P}^{(2)}, \tag{2.197}$$

and hence

$$\mathbf{E}_{\mathrm{p}} = \frac{\mathbf{P}^{(2)}}{\varepsilon_0\left(\frac{c^2}{\omega_3^2}|\mathbf{k}_{\mathrm{p}}|^2 - n_b(\omega_3)^2\right)} = \frac{\mathbf{P}^{(2)}}{\varepsilon_0\left(n_{\mathrm{p}}^2 - n_b(\omega_3)^2\right)}. \tag{2.198}$$

Here, n_{p} was defined as

$$|\mathbf{k}_{\mathrm{p}}| \equiv \frac{n_{\mathrm{p}}\omega_3}{c}. \tag{2.199}$$

This equation shows that $\mathbf{E}_{\mathrm{p}}$ and $\mathbf{P}^{(2)}$ have the same coordinate and time dependence.

$$\mathbf{P}^{(2)}(\mathbf{R},t) = \mathbf{P}^{(2)}(\mathbf{k}_{\mathrm{p}},\omega_3)e^{i\mathbf{k}_{\mathrm{p}}\cdot\mathbf{R}-i\omega_3 t}. \tag{2.200}$$

The theoretical expression for $\mathbf{k}_{\mathrm{p}}$ can be obtained by evaluating $\mathbf{P}^{(2)}$ using the nonlinear susceptibility and the incident electric fields.

Other electromagnetic quantities, i.e. the incident and transmitted ω_1 and ω_2 light and the emitted sum frequency light in reflection and transmission directions, can be expressed in the same manner as before, and the same notation as in Eqs. (2.99)-(2.116) will be used.

2.5.2 Nonlinear polarization

The nonlinear polarization induced in the lower medium in Fig. 2.4 can be expressed using the nonlinear susceptibility, $\chi^{(2),\mathrm{dipole}}_{IJK}$, of this bulk medium and the electric fields of the incident light transmitted into the lower medium, $E_{1\mathrm{t}J}$ and $E_{2\mathrm{t}K}$.

$$P^{(2)}_I(\mathbf{R},t) = \varepsilon_0 \sum_{J,K} \chi^{(2),\mathrm{dipole}}_{IJK} E_{1\mathrm{t}J}(\mathbf{R},t) E_{2\mathrm{t}K}(\mathbf{R},t) \tag{2.201}$$

Since this equation is satisfied everywhere in the lower medium, the coordinate dependence of the left side and the right side of this equation must be identical. Hence,

$$\mathbf{k}_{1\mathrm{t}} + \mathbf{k}_{2\mathrm{t}} = \frac{n_b(\omega_1)\omega_1}{c}\begin{pmatrix}\sin\theta_{1\mathrm{t}}\\0\\-\cos\theta_{1\mathrm{t}}\end{pmatrix} + \frac{n_b(\omega_2)\omega_2}{c}\begin{pmatrix}\sin\theta_{2\mathrm{t}}\\0\\-\cos\theta_{2\mathrm{t}}\end{pmatrix} \tag{2.202}$$

$$= \mathbf{k}_{\mathrm{p}} \equiv \frac{n_{\mathrm{p}}\omega_3}{c}\begin{pmatrix}\sin\theta_{\mathrm{p}}\\0\\-\cos\theta_{\mathrm{p}}\end{pmatrix}. \tag{2.203}$$

where

$$n_{\mathrm{p}} = \sqrt{\frac{n_b(\omega_1)^2\omega_1^2 + n_b(\omega_2)^2\omega_2^2 + 2n_b(\omega_1)n_b(\omega_2)\omega_1\omega_2\cos(\theta_{1\mathrm{t}}-\theta_{2\mathrm{t}})}{(\omega_1+\omega_2)^2}}, \tag{2.204}$$

$$\theta_{\mathrm{p}} = \arctan\left[\frac{n_b(\omega_1)\omega_1\sin\theta_{1\mathrm{t}} + n_b(\omega_2)\omega_2\sin\theta_{2\mathrm{t}}}{n_b(\omega_1)\omega_1\cos\theta_{1\mathrm{t}} + n_b(\omega_2)\omega_2\cos\theta_{2\mathrm{t}}}\right]. \tag{2.205}$$

The incident electric fields transmitted into the lower medium can be conveniently expressed in terms of the incident electric field using the transmission Fresnel factors [39]. Transmission Fresnel factors can be obtained by replacing n' in the interfacial Fresnel factors (Eqs. (2.121)-(2.123)) by n_b.

$$F^{\omega}_X = \frac{2n_a(\omega)\cos\theta_{\mathrm{t}}}{n_a(\omega)\cos\theta_{\mathrm{t}} + n_b(\omega)\cos\theta_{\mathrm{i}}} = L^{\omega}_X, \tag{2.206}$$

$$F^{\omega}_Y = \frac{2n_a(\omega)\cos\theta_{\mathrm{i}}}{n_a(\omega)\cos\theta_{\mathrm{i}} + n_b(\omega)\cos\theta_{\mathrm{t}}} = L^{\omega}_Y, \tag{2.207}$$

$$F_Z^\omega = \frac{2n_b(\omega)\cos\theta_\mathrm{i}}{n_a(\omega)\cos\theta_\mathrm{t} + n_b(\omega)\cos\theta_\mathrm{i}} \left(\frac{n_a(\omega)}{n_b(\omega)}\right)^2 = \left(\frac{n'(\omega)}{n_b(\omega)}\right)^2 L_Z^\omega. \tag{2.208}$$

Using these transmission Fresnel factors, the induced nonlinear polarization can be expressed as

$$P_I^{(2)}(\mathbf{R},t) = \varepsilon_0 \sum_{J,K} F_J^{\omega_1} F_K^{\omega_2} \chi_{IJK}^{(2),\mathrm{dipole}} E_{1\mathrm{i}J}(\mathbf{R},t) E_{2\mathrm{i}K}(\mathbf{R},t). \tag{2.209}$$

In general, $\mathbf{P}^{(2)}$ given by this formula is not necessarily a transverse wave. However, it is now assumed to be a transverse wave for simplicity, and hence, the nonlinear polarization and the particular solution for the sum frequency light in the transmission direction can be expressed as shown below.

- Induced nonlinear polarization

$$\mathbf{k}_\mathrm{p} = \frac{n_\mathrm{p}\omega_3}{c} \begin{pmatrix} \sin\theta_\mathrm{p} \\ 0 \\ -\cos\theta_\mathrm{p} \end{pmatrix} \tag{2.210}$$

$$\mathbf{P}^{(2)} = \begin{pmatrix} P_\mathrm{P}^{(2)}\cos\theta_\mathrm{p} \\ P_\mathrm{S}^{(2)} \\ P_\mathrm{P}^{(2)}\sin\theta_\mathrm{p} \end{pmatrix} \tag{2.211}$$

- Particular solution for ω_3 in the transmission direction

$$\mathbf{k}_\mathrm{p} = \frac{n_\mathrm{p}\omega_3}{c} \begin{pmatrix} \sin\theta_\mathrm{p} \\ 0 \\ -\cos\theta_\mathrm{p} \end{pmatrix} \tag{2.212}$$

$$\mathbf{E}_\mathrm{p} = \begin{pmatrix} E_\mathrm{pP}\cos\theta_\mathrm{p} \\ E_\mathrm{pS} \\ E_\mathrm{pP}\sin\theta_\mathrm{p} \end{pmatrix} = \frac{\mathbf{D}_\mathrm{p}}{\varepsilon_0 n_b(\omega_3)^2} \tag{2.213}$$

$$\mathbf{B}_\mathrm{p} = \frac{n_p}{c} \begin{pmatrix} E_\mathrm{pS}\cos\theta_\mathrm{p} \\ -E_\mathrm{pP} \\ E_\mathrm{pS}\sin\theta_\mathrm{p} \end{pmatrix} = \frac{\mathbf{H}_\mathrm{p}}{c^2\varepsilon_0} \tag{2.214}$$

2.5.3 Boundary conditions

Boundary conditions can be derived from the Maxwell equations in almost the same manner as in the previous section.

First of all, since the boundary condition needs to be satisfied everywhere at the interface, the nonlinear polarization and all the ω_3 beams (the solution in the reflection direction, and the homogeneous and particular solutions in the transmission direction) must have the same coordinate dependence in X- and Y-directions. Thus, the X component of the wave vector need to be the same for all of them.

$$\frac{n_\mathrm{p}\omega_3}{c}\sin\theta_\mathrm{p} = \frac{n_a(\omega_3)\omega_3}{c}\sin\theta_{3\mathrm{r}} = \frac{n_b(\omega_3)\omega_3}{c}\sin\theta_{3\mathrm{t}}. \tag{2.215}$$

Next, the boundary conditions will be derived from the four Maxwell equations. This is mostly the same as the one discussed in the previous section, but it is much easier in this case, because no singularities exist at the interface.

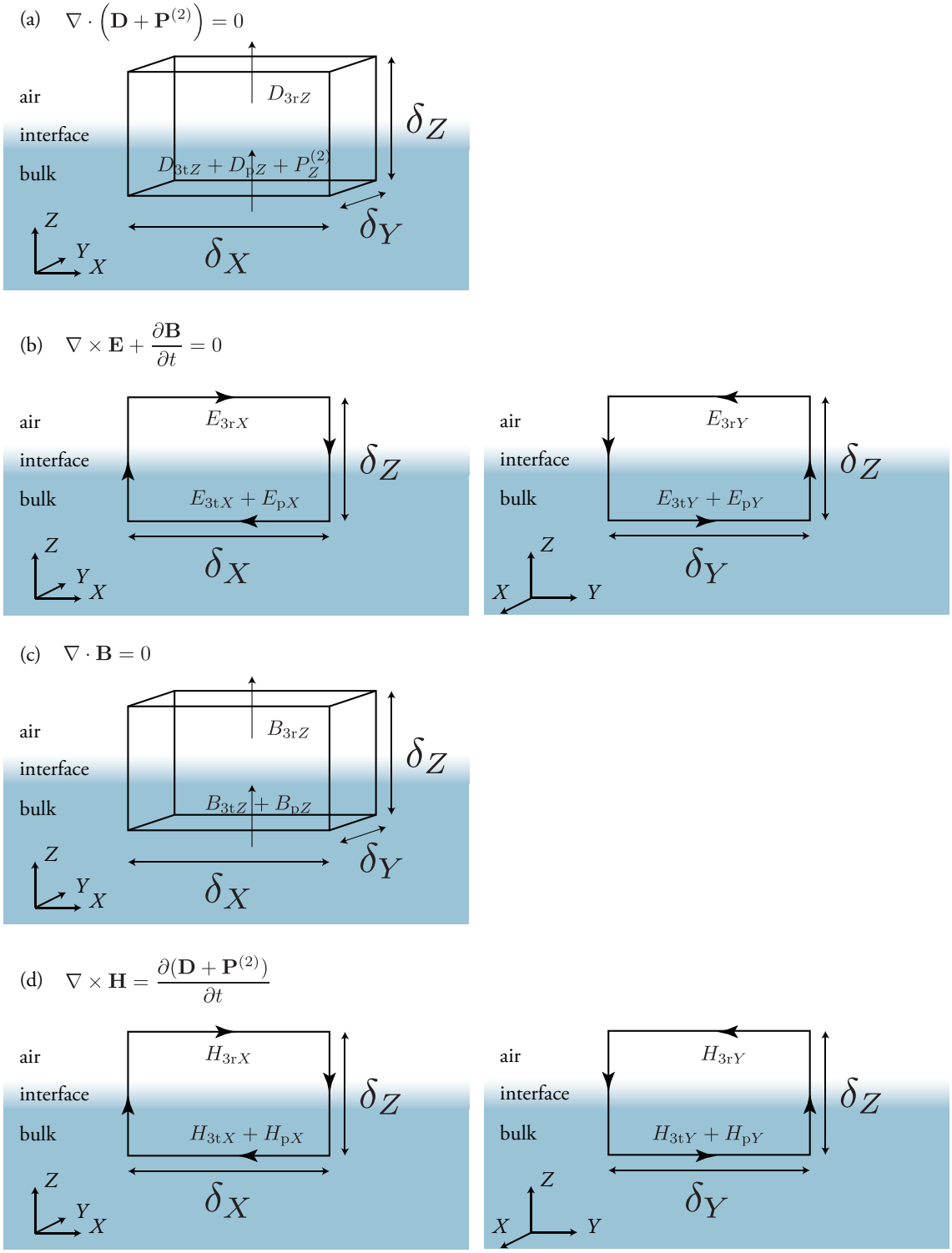

Figure 2.5: Figures showing the surface integration (a, c) and the contour integration (b, d) used for evaluating the integrated form of the Maxwell equations. Nonlinear polarization, $\mathbf{P}^{(2)}$, is induced in the lower bulk medium. δ_X, δ_Y, and δ_Z are all sufficiently smaller than the wavelength of the light.

- $\boldsymbol{\nabla} \cdot (\mathbf{D} + \mathbf{P}^{(2)}) = 0$

  Using the Gauss' theorem, the volume integral of this equation within the cuboid shown in Fig. 2.5(a) can be converted to the surface integral given as

$$\int \left(\mathbf{D} + \mathbf{P}^{(2)}\right) \cdot d\mathbf{S} = 0. \tag{2.216}$$

  Because no singularities exist at the interface, this equation simply means that the Z component of $\mathbf{D} + \mathbf{P}^{(2)}$ is continuous across the interface.

$$D_{3\mathrm{r}Z} = D_{3\mathrm{t}Z} + D_{\mathrm{p}Z} + P_Z^{(2)}, \tag{2.217}$$

  and hence,

$$\begin{aligned} &\varepsilon_0 n_a(\omega_3)^2 E_{3\mathrm{rP}} \sin\theta_{3\mathrm{r}} \\ &\qquad = \varepsilon_0 n_b(\omega_3)^2 E_{3\mathrm{tP}} \sin\theta_{3\mathrm{t}} + \varepsilon_0 n_b(\omega_3)^2 E_{\mathrm{pP}} \sin\theta_{\mathrm{p}} + P_{\mathrm{P}}^{(2)} \sin\theta_{\mathrm{p}}. \end{aligned} \tag{2.218}$$

  Using Eqs. (2.198) and (2.215), this is simplified to

$$n_a(\omega_3) E_{3\mathrm{rP}} = n_b(\omega_3) E_{3\mathrm{tP}} + \frac{n_{\mathrm{p}}}{\varepsilon_0 \left(n_{\mathrm{p}}^2 - n_b(\omega_3)^2\right)} P_{\mathrm{P}}^{(2)}. \tag{2.219}$$

- $\boldsymbol{\nabla} \times \mathbf{E} + \frac{\partial \mathbf{B}}{\partial t} = 0$

  The surface integral of this equation within the rectangles in Fig. 2.5(b) can be converted to a simple contour integral using Stokes' theorem as

$$\oint \mathbf{E} \cdot d\mathbf{r} = 0. \tag{2.220}$$

  This equation means that the X and Y components of $\mathbf{E}$ are continuous across the interface. In the present case, following two equations can be obtained from this boundary condition.

$$E_{3\mathrm{r}X} = E_{3\mathrm{t}X} + E_{\mathrm{p}X}, \tag{2.221}$$

$$E_{3\mathrm{r}Y} = E_{3\mathrm{t}Y} + E_{\mathrm{p}Y}, \tag{2.222}$$

  and hence, with the help of Eq. (2.198),

$$-E_{3\mathrm{rP}} \cos\theta_{3\mathrm{r}} = E_{3\mathrm{tP}} \cos\theta_{3\mathrm{t}} + \frac{\cos\theta_{\mathrm{p}}}{\varepsilon_0 \left(n_{\mathrm{p}}^2 - n_b(\omega_3)^2\right)} P_{\mathrm{P}}^{(2)}, \tag{2.223}$$

$$E_{3\mathrm{rS}} = E_{3\mathrm{tS}} + \frac{P_{\mathrm{S}}^{(2)}}{\varepsilon_0 \left(n_{\mathrm{p}}^2 - n_b(\omega_3)^2\right)}. \tag{2.224}$$

- $\boldsymbol{\nabla} \cdot \mathbf{B} = 0$

  The volume integral of this equation inside the cuboid shown in Fig. 2.5(c) combined with Gauss' theorem results in

$$\int \mathbf{B} \cdot d\mathbf{S} = 0. \tag{2.225}$$

This equation indicates that the Z component of $\mathbf{B}$ is continuous across the interface.

$$B_{3\mathrm{r}Z} = B_{3\mathrm{t}Z} + B_{\mathrm{p}Z}, \tag{2.226}$$

and hence,

$$\frac{n_a(\omega_3)}{c} E_{3\mathrm{rS}} \sin\theta_{3\mathrm{r}} = \frac{n_b(\omega_3)}{c} E_{3\mathrm{tS}} \sin\theta_{3\mathrm{t}} + \frac{n_p}{c} E_{\mathrm{pS}} \sin\theta_{\mathrm{p}}, \tag{2.227}$$

which can be rewritten using Eqs. (2.198) and (2.215) as

$$E_{3\mathrm{rS}} = E_{3\mathrm{tS}} + E_{\mathrm{pS}} = E_{3\mathrm{tS}} + \frac{P_{\mathrm{S}}^{(2)}}{\varepsilon_0 \left(n_{\mathrm{p}}^2 - n_b(\omega_3)^2\right)}. \tag{2.228}$$

- $\boldsymbol{\nabla} \times \mathbf{H} = \frac{\partial\left(\mathbf{D}+\mathbf{P}^{(2)}\right)}{\partial t}$

  The surface integrals within the rectangles in Fig. 2.5(d) can be converted to the contour integrals using Stokes' theorem.

$$\oint \mathbf{H} \cdot d\mathbf{r} = 0. \tag{2.229}$$

  This equation states that the X and Y components of $\mathbf{H}$ are continuous across the interface. Applied to the present case, following equations are obtained.

$$H_{3\mathrm{r}X} = H_{3\mathrm{t}X} + H_{\mathrm{p}X}, \tag{2.230}$$

$$H_{3\mathrm{r}Y} = H_{3\mathrm{t}Y} + H_{\mathrm{p}Y}, \tag{2.231}$$

  and hence,

$$-c\varepsilon_0 n_a(\omega_3) E_{3\mathrm{rS}} \cos\theta_{3\mathrm{r}} = c\varepsilon_0 n_b(\omega_3) E_{3\mathrm{tS}} \cos\theta_{3\mathrm{t}} + c\varepsilon_0 n_{\mathrm{p}} E_{\mathrm{pS}} \cos\theta_{\mathrm{p}}, \tag{2.232}$$

$$-c\varepsilon_0 n_a(\omega_3) E_{3\mathrm{rP}} = -c\varepsilon_0 n_b(\omega_3) E_{3\mathrm{tP}} - c\varepsilon_0 n_{\mathrm{p}} E_{\mathrm{pP}}. \tag{2.233}$$

  Using Eqs. (2.198) and (2.215), they become

$$-n_a(\omega_3) E_{3\mathrm{rS}} \cos\theta_{3\mathrm{r}} = n_b(\omega_3) E_{3\mathrm{tS}} \cos\theta_{3\mathrm{t}} + \frac{n_{\mathrm{p}} \cos\theta_{\mathrm{p}}}{\varepsilon_0 \left(n_{\mathrm{p}}^2 - n_b^2\right)} P_{\mathrm{S}}^{(2)}, \tag{2.234}$$

$$n_a(\omega_3) E_{3\mathrm{rP}} = n_b(\omega_3) E_{3\mathrm{tP}} + \frac{n_{\mathrm{p}}}{\varepsilon_0 \left(n_{\mathrm{p}}^2 - n_b(\omega_3)^2\right)} P_{\mathrm{P}}^{(2)}. \tag{2.235}$$

- Summary of the results

  In summary, the following four independent equations can be obtained from the consideration of the boundary conditions.

$$E_{3\mathrm{rS}} = E_{3\mathrm{tS}} + \frac{P_{\mathrm{S}}^{(2)}}{\varepsilon_0 \left(n_{\mathrm{p}}^2 - n_b(\omega_3)^2\right)} \tag{2.236}$$

$$-n_a(\omega_3) E_{3\mathrm{rS}} \cos\theta_{3\mathrm{r}} = n_b(\omega_3) E_{3\mathrm{tS}} \cos\theta_{3\mathrm{t}} + \frac{n_{\mathrm{p}} \cos\theta_{\mathrm{p}}}{\varepsilon_0 \left(n_{\mathrm{p}}^2 - n_b(\omega_3)^2\right)} P_{\mathrm{S}}^{(2)} \tag{2.237}$$

$$n_a(\omega_3) E_{3\mathrm{rP}} = n_b(\omega_3) E_{3\mathrm{tP}} + \frac{n_{\mathrm{p}}}{\varepsilon_0 \left(n_{\mathrm{p}}^2 - n_b^2(\omega_3)\right)} P_{\mathrm{P}}^{(2)} \tag{2.238}$$

$$-E_{3\mathrm{rP}} \cos\theta_{3\mathrm{r}} = E_{3\mathrm{tP}} \cos\theta_{3\mathrm{t}} + \frac{\cos\theta_{\mathrm{p}}}{\varepsilon_0 \left(n_{\mathrm{p}}^2 - n_b(\omega_3)^2\right)} P_{\mathrm{P}}^{(2)} \tag{2.239}$$

2.5.4 Sum frequency electric field

Using the simultaneous equations obtained at the last part of the previous section, the sum frequency electric field in the reflection direction can be evaluated.

$$E_{3\mathrm{rS}} = \frac{n_b(\omega_3)\cos\theta_{3\mathrm{t}} - n_\mathrm{p}\cos\theta_\mathrm{p}}{\varepsilon_0\left(n_\mathrm{p}^2 - n_b(\omega_3)^2\right)\left(n_a(\omega_3)\cos\theta_{3\mathrm{r}} + n_b(\omega_3)\cos\theta_{3\mathrm{t}}\right)}P_\mathrm{S}^{(2)}, \tag{2.240}$$

$$E_{3\mathrm{rP}} = \frac{n_\mathrm{p}\cos\theta_{3\mathrm{t}} - n_b(\omega_3)\cos\theta_\mathrm{p}}{\varepsilon_0\left(n_\mathrm{p}^2 - n_b(\omega_3)^2\right)\left(n_a(\omega_3)\cos\theta_{3\mathrm{t}} + n_b(\omega_3)\cos\theta_{3\mathrm{r}}\right)}P_\mathrm{P}^{(2)}. \tag{2.241}$$

These can be expressed in a more organized manner using the transmission Fresnel factors given in Eqs. (2.206)-(2.208).

$$E_{3\mathrm{rS}} = \frac{\omega_3}{2cn_a(\omega_3)\cos\theta_{3\mathrm{r}}}\frac{c\left(n_b(\omega_3)\cos\theta_{3\mathrm{t}} - n_\mathrm{p}\cos\theta_\mathrm{p}\right)}{\omega_3\left(n_\mathrm{p}^2 - n_b(\omega_3)^2\right)}\frac{F_Y^{\omega_3}P_Y^{(2)}}{\varepsilon_0} \tag{2.242}$$

$$= \frac{\omega_3}{2cn_a(\omega_3)\cos\theta_{3\mathrm{r}}}\frac{c\left(n_b(\omega_3)\cos\theta_{3\mathrm{t}} - \frac{n_b(\omega_3)\sin\theta_{3\mathrm{t}}}{\sin\theta_\mathrm{p}}\cos\theta_\mathrm{p}\right)}{\omega_3\left(n_\mathrm{p}^2 - n_b(\omega_3)^2\right)}\frac{F_Y^{\omega_3}P_Y^{(2)}}{\varepsilon_0} \tag{2.243}$$

$$= \frac{\omega_3}{2cn_a(\omega_3)\cos\theta_{3\mathrm{r}}}\frac{cn_b(\omega_3)\sin(\theta_\mathrm{p} - \theta_{3\mathrm{t}})}{\omega_3\left(n_\mathrm{p}^2 - n_b(\omega_3)^2\right)\sin\theta_\mathrm{p}}\frac{F_Y^{\omega_3}P_Y^{(2)}}{\varepsilon_0}, \tag{2.244}$$

$$E_{3\mathrm{rP}} = \frac{\frac{n_b(\omega_3)\sin\theta_{3\mathrm{t}}}{\sin\theta_\mathrm{p}}\cos\theta_{3\mathrm{t}} - n_b(\omega_3)\cos\theta_\mathrm{p}}{\varepsilon_0\left(n_\mathrm{p}^2 - n_b(\omega_3)^2\right)\left(n_a(\omega_3)\cos\theta_{3\mathrm{t}} + n_b(\omega_3)\cos\theta_{3\mathrm{r}}\right)}P_\mathrm{P}^{(2)} \tag{2.245}$$

$$= \frac{-n_b(\omega_3)\cos(\theta_\mathrm{p} + \theta_{3\mathrm{t}})\sin(\theta_\mathrm{p} - \theta_{3\mathrm{t}})}{\varepsilon_0\left(n_\mathrm{p}^2 - n_b(\omega_3)^2\right)\sin\theta_\mathrm{p}\left(n_a(\omega_3)\cos\theta_{3\mathrm{t}} + n_b(\omega_3)\cos\theta_{3\mathrm{r}}\right)}P_\mathrm{P}^{(2)} \tag{2.246}$$

$$= \frac{n_b(\omega_3)\sin(\theta_\mathrm{p} - \theta_{3\mathrm{t}})}{\varepsilon_0\left(n_\mathrm{p}^2 - n_b(\omega_3)^2\right)\sin\theta_\mathrm{p}}\frac{-\cos\theta_{3\mathrm{t}}\cos\theta_\mathrm{p}P_\mathrm{P}^{(2)} + \sin\theta_{3\mathrm{t}}\sin\theta_\mathrm{p}P_\mathrm{P}^{(2)}}{n_a(\omega_3)\cos\theta_{3\mathrm{t}} + n_b(\omega_3)\cos\theta_{3\mathrm{r}}} \tag{2.247}$$

$$= \frac{n_b(\omega_3)\sin(\theta_\mathrm{p} - \theta_{3\mathrm{t}})}{\varepsilon_0\left(n_\mathrm{p}^2 - n_b(\omega_3)^2\right)\sin\theta_\mathrm{p}}\frac{-\cos\theta_{3\mathrm{t}}P_{\mathrm{P},X}^{(2)} + \sin\theta_{3\mathrm{t}}P_{\mathrm{P},Z}^{(2)}}{n_a(\omega_3)\cos\theta_{3\mathrm{t}} + n_b(\omega_3)\cos\theta_{3\mathrm{r}}} \tag{2.248}$$

$$= \frac{n_b(\omega_3)\sin(\theta_\mathrm{p} - \theta_{3\mathrm{t}})}{\varepsilon_0\left(n_\mathrm{p}^2 - n_b(\omega_3)^2\right)\sin\theta_\mathrm{p}}\left(\frac{-F_X^{\omega_3}P_{\mathrm{P},X}^{(2)}}{2n_a(\omega_3)} + \frac{n_b(\omega_3)\sin\theta_{3\mathrm{t}}F_Z^{\omega_3}P_{\mathrm{P},Z}^{(2)}}{2n_a(\omega_3)^2\cos\theta_{3\mathrm{r}}}\right) \tag{2.249}$$

$$= \frac{\omega_3}{2cn_a(\omega_3)\cos\theta_{3\mathrm{r}}}\frac{cn_b(\omega_3)\sin(\theta_\mathrm{p} - \theta_{3\mathrm{t}})}{\omega_3\left(n_\mathrm{p}^2 - n_b(\omega_3)^2\right)\sin\theta_\mathrm{p}}\frac{-\cos\theta_{3\mathrm{r}}F_X^{\omega_3}P_{\mathrm{P},X}^{(2)} + \sin\theta_{3\mathrm{r}}F_Z^{\omega_3}P_{\mathrm{P},Z}^{(2)}}{\varepsilon_0}. \tag{2.250}$$

Because of Eq. (2.215), the relation shown below holds.

$$n_p^2 - n_b(\omega_3)^2 = \left(\frac{n_b(\omega_3)\sin\theta_{3\mathrm{t}}}{\sin\theta_\mathrm{p}}\right)^2 - n_b(\omega_3)^2 = -\frac{n_b(\omega_3)^2\sin(\theta_\mathrm{p} + \theta_{3\mathrm{t}})\sin(\theta_\mathrm{p} - \theta_{3\mathrm{t}})}{\sin^2\theta_\mathrm{p}}. \tag{2.251}$$

Finally, the sum frequency electric field can be expressed as

$$E_{3\mathrm{rS}} = -\frac{\omega_3}{2cn_a(\omega_3)\cos\theta_{3\mathrm{r}}}\frac{c\sin\theta_\mathrm{p}}{\omega_3 n_b(\omega_3)\sin(\theta_\mathrm{p} + \theta_{3\mathrm{t}})}\frac{F_Y^{\omega_3}P_Y^{(2)}}{\varepsilon_0}, \tag{2.252}$$

$$E_{3\mathrm{rP}} = -\frac{\omega_3}{2cn_a(\omega_3)\cos\theta_{3\mathrm{r}}}\frac{c\sin\theta_\mathrm{p}}{\omega_3 n_b(\omega_3)\sin(\theta_\mathrm{p} + \theta_{3\mathrm{t}})}\frac{-\cos\theta_{3\mathrm{r}}F_X^{\omega_3}P_{\mathrm{P},X}^{(2)} + \sin\theta_{3\mathrm{r}}F_Z^{\omega_3}P_{\mathrm{P},Z}^{(2)}}{\varepsilon_0}. \tag{2.253}$$

2.5.5 Example: Quartz

As the example, the sum frequency electric field generated at the air/z-cut quartz interface is evaluated. The air/z-cut quartz interface is often used as the reference to normalize the $\chi^{(2)}_{\mathrm{eff}}$ spectra obtained at sample interfaces, and the theoretical expression for the generated sum frequency electric field at that interface is necessary to determine the absolute intensity of the $\chi^{(2)}_{\mathrm{eff}}$ spectra at sample interfaces.

In the nonlinear susceptibility tensor of quartz, following four tensor elements are predominantly large and the others are negligibly small [40].

$$\chi^{(2)}_{xxx} = -\chi^{(2)}_{xyy} = -\chi^{(2)}_{yxy} = -\chi^{(2)}_{yyx} \equiv \chi^{(2)}_q = 8.0 \times 10^{-13}\ \mathrm{m\ V^{-1}}. \tag{2.254}$$

Here, x, y, and z represent the crystal coordinates. In the actual experiments, the quartz crystal is placed so that the crystal coordinates (x, y, and z) match the laboratory-fixed coordinates (X, Y, and Z).

$$x = X, \qquad y = Y, \qquad z = Z \tag{2.255}$$

Under this condition, the nonlinear polarization induced by this nonlinear susceptibility tensor is given using the incident electric fields and the transmission Fresnel factors (Eqs. (2.206)-(2.208)) as

$$P^{(2)}_X = \varepsilon_0 F^{\omega_1}_X F^{\omega_2}_X \chi^{(2)}_{xxx} E_{1\mathrm{i}X} E_{2\mathrm{i}X} + \varepsilon_0 F^{\omega_1}_Y F^{\omega_2}_Y \chi^{(2)}_{xyy} E_{1\mathrm{i}Y} E_{2\mathrm{i}Y}, \tag{2.256}$$

$$P^{(2)}_Y = \varepsilon_0 F^{\omega_1}_X F^{\omega_2}_Y \chi^{(2)}_{yxy} E_{1\mathrm{i}X} E_{2\mathrm{i}Y} + \varepsilon_0 F^{\omega_1}_Y F^{\omega_2}_X \chi^{(2)}_{yyx} E_{1\mathrm{i}Y} E_{2\mathrm{i}X}, \tag{2.257}$$

$$P^{(2)}_Z = 0. \tag{2.258}$$

Referring to Eqs. (2.100) and (2.106), these can be expressed in terms of S- and P-polarized electric fields and the incident angles.

$$P^{(2)}_X = \varepsilon_0 F^{\omega_1}_X F^{\omega_2}_X \cos\theta_{1\mathrm{i}} \cos\theta_{2\mathrm{i}} \chi^{(2)}_{xxx} E_{1\mathrm{iP}} E_{2\mathrm{iP}} + \varepsilon_0 F^{\omega_1}_Y F^{\omega_2}_Y \chi^{(2)}_{xyy} E_{1\mathrm{iS}} E_{2\mathrm{iS}}, \tag{2.259}$$

$$P^{(2)}_Y = \varepsilon_0 F^{\omega_1}_X F^{\omega_2}_Y \cos\theta_{1\mathrm{i}} \chi^{(2)}_{yxy} E_{1\mathrm{iP}} E_{2\mathrm{iS}} + \varepsilon_0 F^{\omega_1}_Y F^{\omega_2}_X \cos\theta_{2\mathrm{i}} \chi^{(2)}_{yyx} E_{1\mathrm{iS}} E_{2\mathrm{iP}}, \tag{2.260}$$

$$P^{(2)}_Z = 0. \tag{2.261}$$

Then, the sum frequency electric field can be evaluated according to Eqs. (2.252) and (2.253) as

$$\begin{aligned} E_{3\mathrm{rS}} = {} & \frac{\omega_3}{2cn_a(\omega_3)\cos\theta_{3\mathrm{r}}} \frac{c\sin\theta_{\mathrm{p}}}{\omega_3 n_b(\omega_3)\sin(\theta_{\mathrm{p}} + \theta_{3\mathrm{t}})} \\ & \times \left(F^{\omega_3}_Y F^{\omega_1}_X F^{\omega_2}_Y \cos\theta_{1\mathrm{i}} \chi^{(2)}_q E_{1\mathrm{iP}} E_{2\mathrm{iS}} + F^{\omega_3}_Y F^{\omega_1}_Y F^{\omega_2}_X \cos\theta_{2\mathrm{i}} \chi^{(2)}_q E_{1\mathrm{iS}} E_{2\mathrm{iP}} \right), \end{aligned} \tag{2.262}$$

$$\begin{aligned} E_{3\mathrm{rP}} = {} & \frac{\omega_3}{2cn_a(\omega_3)\cos\theta_{3\mathrm{r}}} \frac{c\sin\theta_{\mathrm{p}}}{\omega_3 n_b(\omega_3)\sin(\theta_{\mathrm{p}} + \theta_{3\mathrm{t}})} \\ & \times \Big(F^{\omega_3}_X F^{\omega_1}_X F^{\omega_2}_X \cos\theta_{3\mathrm{r}} \cos\theta_{1\mathrm{i}} \cos\theta_{2\mathrm{i}} \chi^{(2)}_q E_{1\mathrm{iP}} E_{2\mathrm{iP}} \\ & \qquad - F^{\omega_3}_X F^{\omega_1}_Y F^{\omega_2}_Y \cos\theta_{3\mathrm{r}} \chi^{(2)}_q E_{1\mathrm{iS}} E_{2\mathrm{iS}} \Big). \end{aligned} \tag{2.263}$$

In analogy to Eqs. (2.184) and (2.185) in the previous section, the effective nonlinear susceptibilities can be defined using the following equations.

$$E_{3\mathrm{rS}} = \frac{\omega_3}{2cn_a(\omega_3)\cos\theta_{3\mathrm{r}}}\left(\chi^{(2)}_{\mathrm{eff,SSP}}E_{1\mathrm{iS}}E_{2\mathrm{iP}} + \chi^{(2)}_{\mathrm{eff,SPS}}E_{1\mathrm{iP}}E_{2\mathrm{iS}}\right), \tag{2.264}$$

$$E_{3\mathrm{rP}} = \frac{\omega_3}{2cn_a(\omega_3)\cos\theta_{3\mathrm{r}}}\left(\chi^{(2)}_{\mathrm{eff,PSS}}E_{1\mathrm{iS}}E_{2\mathrm{iS}} + \chi^{(2)}_{\mathrm{eff,PPP}}E_{1\mathrm{iP}}E_{2\mathrm{iP}}\right). \tag{2.265}$$

It is to be noted that the complex unit "i" is missing in this definition, whereas it was present in Eqs. (2.184) and (2.185). Here, the effective nonlinear susceptibilities are given as

$$\chi^{(2)}_{\mathrm{eff,SSP}} = \frac{c\sin\theta_{\mathrm{p}}}{\omega_3 n_b(\omega_3)\sin(\theta_{\mathrm{p}}+\theta_{3\mathrm{t}})}F_Y^{\omega_3}F_Y^{\omega_1}F_X^{\omega_2}\cos\theta_{2\mathrm{i}}\chi^{(2)}_q, \tag{2.266}$$

$$\chi^{(2)}_{\mathrm{eff,SPS}} = \frac{c\sin\theta_{\mathrm{p}}}{\omega_3 n_b(\omega_3)\sin(\theta_{\mathrm{p}}+\theta_{3\mathrm{t}})}F_Y^{\omega_3}F_X^{\omega_1}F_Y^{\omega_2}\cos\theta_{1\mathrm{i}}\chi^{(2)}_q, \tag{2.267}$$

$$\chi^{(2)}_{\mathrm{eff,PSS}} = -\frac{c\sin\theta_{\mathrm{p}}}{\omega_3 n_b(\omega_3)\sin(\theta_{\mathrm{p}}+\theta_{3\mathrm{t}})}F_X^{\omega_3}F_Y^{\omega_1}F_Y^{\omega_2}\cos\theta_{3\mathrm{r}}\chi^{(2)}_q, \tag{2.268}$$

$$\chi^{(2)}_{\mathrm{eff,PPP}} = \frac{c\sin\theta_{\mathrm{p}}}{\omega_3 n_b(\omega_3)\sin(\theta_{\mathrm{p}}+\theta_{3\mathrm{t}})}F_X^{\omega_3}F_X^{\omega_1}F_X^{\omega_2}\cos\theta_{3\mathrm{r}}\cos\theta_{1\mathrm{i}}\cos\theta_{2\mathrm{i}}\chi^{(2)}_q. \tag{2.269}$$

These effective nonlinear susceptibilities can be evaluated, using the reported value for the nonlinear susceptibility, $\chi^{(2)}_q$, and the refractive index, n_b, and the experimentally obtained incident angles. Using these values, the experimental nonlinear susceptibilities at sample interfaces can be normalized and their intensities can be calibrated.

2.6 Conclusion

Theoretical treatment of vibrational sum frequency generation (VSFG) within the dipole approximation was reviewed. First, the theoretical expression for the induced nonlinear polarization due to the interaction among the molecular system and the two incident electric fields was derived from the microscopic viewpoint, and it was shown how the dipole approximation is used. Next, the properties of the induced polarization was examined based on the derived theoretical expression. When the bulk media are centrosymmetric, the nonlinear polarization is induced solely due to the interfacial molecules, and VSFG is interface-selective. However, if the bulk media lack the inversion symmetry, the nonlinear polarization is induced also in the bulk, and VSFG is no longer interface-selective. In contrast to these two cases, if the molecules have a centrosymmetric molecular structure or if they are randomly oriented at the interface, the nonlinear polarization is not induced even at the interface, and VSFG is forbidden at those interfaces within the dipole approximation. Finally, the theoretical expressions of the sum frequency electric field due to the nonlinear polarization localized at the interface or delocalized in the bulk are respectively derived. These formulae can be used to perform the normalization and the intensity calibration of the experimental $\chi^{(2)}_{\mathrm{eff}}$ spectra obtained at sample interfaces.

Part II

UV-excited time-resolved HD-VSFG spectroscopy

Chapter 3

Development of UV-excited time-resolved HD-VSFG spectroscopy

3.1 Introduction

Chemical reactions at interfaces have significant importance in various physical, chemical, and biological processes. Since many of these reactions are initiated by the electronic excitation by UV light, it is easy to imagine that the combination of UV pump light and HD-VSFG spectroscopy will give birth to a powerful and versatile time-resolved spectroscopic method for studying these interfacial reactions.

In spite of this expectation, UV-excited time-resolved HD-VSFG spectroscopy has never been reported at the air/liquid interfaces. Even the simpler and more primitive "homodyne"-detected version of UV-excited time-resolved VSFG spectroscopy is reported only by the Eisenthal group [41, 42]. They chose the air/coumarin 314 aqueous solution interface as the sample, and they observed the orientational motion of coumarin and the proximate water molecules after the photoexcitation of the coumarin molecules by the 423 nm pump light. In their experiment, no new chemical species are generated, and in this sense, I can safely say that the observation of chemical reactions at air/liquid interfaces, in which new chemical species are generated, has never been reported. Reports about the UV-pump experiments are much more scarce than the IR-pump counterparts [25, 27, 43, 44], probably because the photodegradation of the sample by the UV pump light imposes a great difficulty. In the UV-pump experiments, the accumulation of photoproducts easily occurs inside the excitation volume, and it is well known in the bulk time-resolved spectroscopy that the fresh sample solution needs to be continuously provided to replace the degraded sample using a flow cell, a rotating cell [45], or a liquid jet [46]. It is natural to think that such a sample replacement technique is essential also for the interface spectroscopy. However, the sample replacement at the interface is not straightforward, because it would easily cause a turbulence at the sample surface, making the VSFG measurements impossible. The situation is even more difficult for HD-VSFG spectroscopy, because the surface height stability of ~ 1 μm is necessary to enable the reliable determination of the complex phase of $\chi^{(2)}_{\mathrm{eff}}$, as will be shown in this chapter. This is the principal reason why the observation of chemical reactions at liquid surfaces was not possible so far. In this

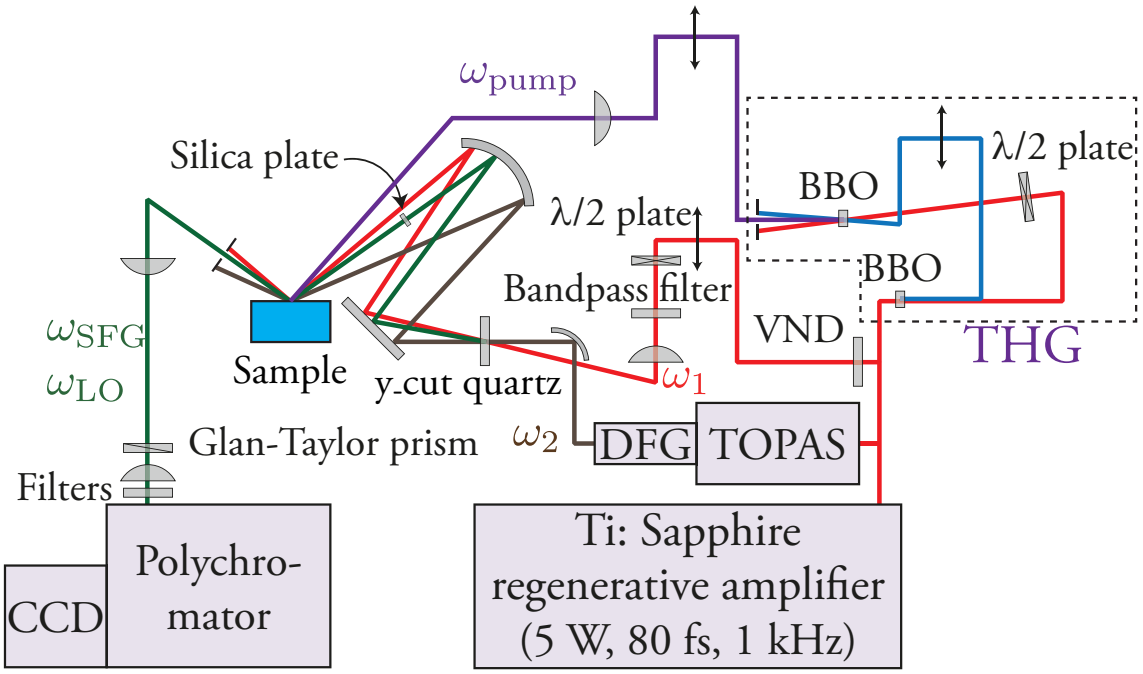

Figure 3.1: UV-excited time-resolved HD-VSFG spectrometer.

work, I overcame this great challenge by developing a new type of flow cell. Combined with the newly constructed UV-excited time-resolved HD-VSFG apparatus, it has now become possible to investigate the ultrafast dynamics of various chemical reactions at air/liquid interfaces. The details of this novel spectroscopic technique is described in this chapter.

Meanwhile, at the metal surface in vacuum, one group reported UV-excited time-resolved HD-VSFG spectroscopy with the pump wavelength of 400 nm [20, 47]. They observed the desorption of carbon monooxide (CO) adsorbed on the Pt(111) surface upon the electronic excitation of Pt. In their experiment, CO molecules desorb from the surface after the pump light irradiation, and fresh CO molecules are continuously provided to the surface by the spontaneous adsorption of CO molecules in the vacuum. In this way, they successfully avoided the problem of sample degradation by the UV pump light. However, this technique can be used only for the photodesorption experiments in the vacuum, and it is certainly unusable for observing the chemical reactions at air/liquid interfaces.

3.2 UV-excited time-resolved HD-VSFG spectrometer

3.2.1 Apparatus

The detailed description of the apparatus constructed in the present study (Fig. 3.1) is given in this section. A commercial Ti:Sapphire regenerative amplifier (Spectra Physics, Spitfire Ace) was used as the light source. The pulse energy was 5 mJ, the pulse duration was 80 fs, and the repetition rate was 1 kHz. 1 mJ of the output was attenuated by a variable neutral density (VND) filter, and spectrally narrowed by a bandpass filter (center wavelength: 795 nm, bandwidth: 20 cm^{-1}) to be used as the narrow band

visible light, ω_1. 2 mJ was introduced into a commercial optical parametric amplifier (Spectra Physics, TOPAS-C). The signal and idler outputs were introduced into a $AgGaS_2$ crystal to generate a tunable and broad band infrared beam (ω_2) by difference frequency generation. The remaining 2 mJ was used for generating the UV pump light (ω_{pump}). It was first converted to the second harmonic light in a β-barium borate (BBO) crystal (CASTECH, Type I). In order to maximize the conversion efficiency, the beam diameter of the fundamental light was adjusted before the introduction into the BBO crystal so that the photon density is slightly below the white light generation threshold of the optics. The residual fundamental light and the generated second harmonic light were separated by a dichroic mirror, and after optimizing the temporal overlap between the two beams using a delay stage, they were again overlapped with a dichroic mirror and were introduced into the second BBO crystal (CASTECH, Type I), where the sum frequency mixing of the two beams occured to give the third harmonic light at 267 nm. Because the fundamental and the second harmonic beams were introduced into the BBO crystal in a slightly noncollinear manner, the generated third harmonic beam could be spatially isolated from the incident beams using an iris. This UV light was used as the pump light, ω_{pump}.

The steady-state measurement of HD-VSFG was done in the following way. First, ω_1 and ω_2 beams were focused, and temporally and spatially overlapped in a thin crystal of y-cut quartz (thickness = 10 μm). ω_1 was focused by a plano-convex lens (f = 500 mm), and ω_2 was focused by an off-axis parabolic mirror (f = 100 mm). The incident angle was about 10° for ω_1 and 0° for ω_2. Inside the crystal, the sum frequency of ω_1 and ω_2 was generated, which was used as the local oscillator (ω_{LO}) for the heterodyne detection. The intensity of the local oscillator was adjusted by changing the angle of the quartz crystal around its y-axis. (The theoretically obtained angle dependence is given in the next section.) The generated local oscillator and the transmitted ω_1 and ω_2 beams were then refocused by a spherical concave mirror onto the sample surface. The incident angle and the polarization direction were 44° and S for ω_1, and 56° and P for ω_2. During the light propagation between the spherical mirror and the sample surface, ω_{LO} went through a silica plate of 3 mm thickness, corresponding to about 5 ps delay with respect to ω_1 and ω_2 beams. At the sample surface, VSFG took place and gave rise to the sum frequency light (ω_3). After leaving the sample surface, ω_3 and ω_{LO} propagated collinearly in the reflection direction. They were collimated by a plano-convex lens (f = 500 mm), analyzed by a Glan-Taylor prism, and introduced into a polychromator by a plano-convex lens (f = 50 mm). In this way, S-polarized sum frequency light was selectively detected. Inside the polychromator, ω_3 and ω_{LO} were frequency dispersed, and then detected by a CCD camera.

In the time-resolved measurements, the UV pump light (ω_{pump}) was focused onto the sample surface by a plano-convex lens (f = 350 mm). The incident angle was 25° and the polarization direction was P. The optical delay between ω_{pump} and ω_2 was adjusted by a computer-controlled delay stage. Sample solution was placed in a flow cell newly developed for interface experiments (details are described later),

and was continuously flowed during the measurements to avoid the accumulation of the photodegraded sample at the sample surface.

In order to determine the complex phase of $\chi^{(2)}_{\mathrm{eff}}$ with sufficiently high accuracy, the sample surface needs to be kept at the same height throughout the measurement with the precision of about 1 μm (The reason will be explained later in this section). Meanwhile, the surface height of liquid samples incessantly changes during the measurements by the sample evaporation or by the fluctuation of the flow rate of the sample solution, for instance. Hence, the height of the sample surface was continuously monitored during the measurements by a displacement sensor (Keyence, SI-F10), and the change of the sample surface height was promptly compensated by moving the sample cell in the vertical direction with an electronic translational stage.

3.2.2 Adjustment of the local oscillator intensity

As mentioned in the previous section, the local oscillator used for the heterodyne detection is generated by sum frequency mixing of ω_1 and ω_2 beams in a y-cut quartz crystal, and its intensity can be conveniently adjusted by simply rotating the crystal. Here, the theoretical background for this property is described.

With the laboratory-fixed coordinates defined as shown in Fig. 3.2, the S-polarized ω_1 light has the electric field only in the Y direction, and the P-polarized ω_2 light has the electric field only in the X direction because of the normal incidence. Then, in the SSP polarization combination, YYX is the only tensor element in the nonlinear susceptibility that needs to be evaluated. Using the YYX tensor element, the induced polarization is expressed as

$$P^{(2)}_Y = \varepsilon_0 \chi^{(2)}_{YYX} E_{1Y} E_{2X}, \tag{3.1}$$

where E_1 and E_2 are the electric fields of ω_1 and ω_2, respectively. In order to evaluate the nonlinear susceptibility in the laboratory-fixed coordinates, $\chi^{(2)}_{YYX}$, it needs to be related to the nonlinear susceptibility of quartz in the crystal coordinates. For a y-cut quartz crystal, y-axis of the crystal is normal to the crystal surface, and is identical to the Z-axis of the laboratory-fixed coordinates. The xz-plane in the crystal coordinates corresponds to the XY-plane in the laboratory-fixed coordinates, but the direction of the x- and z-axes and X- and Y-axes do not necessarily match. Defining the angle between x-axis and X-axis to be α as shown in Fig. 3.2(b), the Y-component of the nonlinear polarization in the laboratory-fixed coordinates is expressed in terms of the nonlinear polarization in the crystal coordinate as

$$P^{(2)}_Y = P^{(2)}_x \sin\alpha - P^{(2)}_z \cos\alpha. \tag{3.2}$$

In this expression, the induced polarization in the crystal coordinates is given in terms of the nonlinear

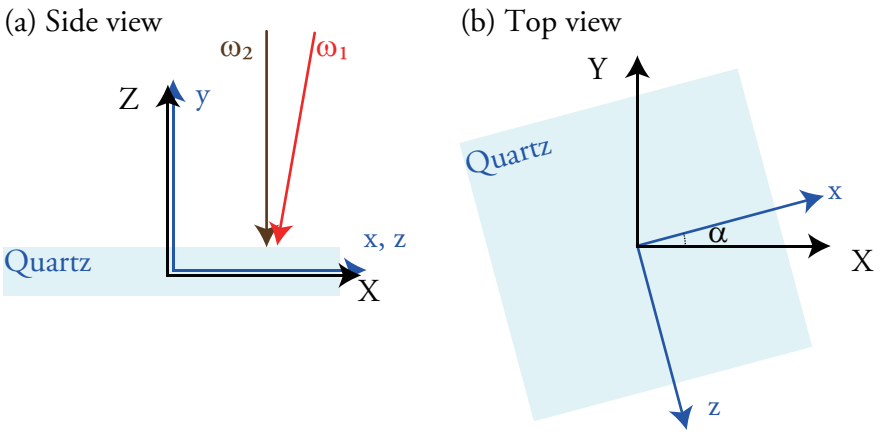

Figure 3.2: Laboratory-fixed coordinates (X, Y, and Z) and the crystal coordinates (x, y, and z).

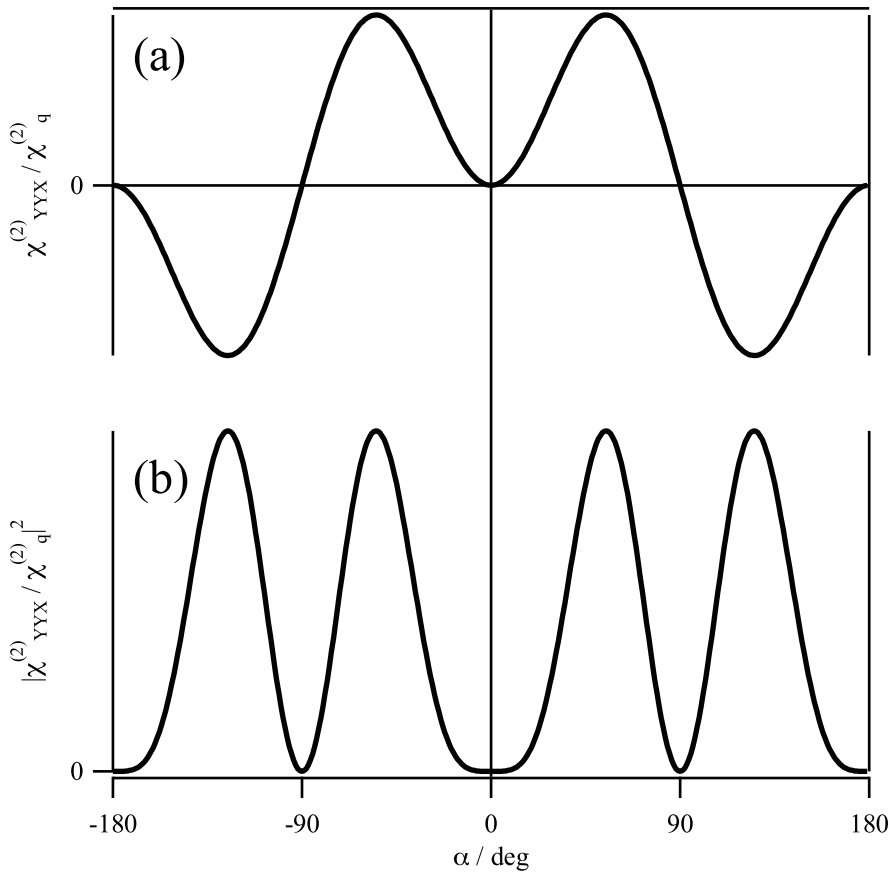

Figure 3.3: The theoretically calculated nonlinear susceptibility of y-cut quartz, $\chi^{(2)}_{YYX}$, plotted against the angle around the y-axis (α in Fig. 3.2(b)). (a) Amplitude ($\chi^{(2)}_{YYX}$). (b) Squared intensity ($|\chi^{(2)}_{YYX}|^2$).

susceptibility and the ω_1 and ω_2 electric fields as

$$P_i^{(2)} = \varepsilon_0 \sum_{i,j,k} \chi_{ijk}^{(2)} E_{1j} E_{2k}. \tag{3.3}$$

Here, the electric fields in the crystal coordinates are related to those in the laboratory-fixed coordinates as

$$E_x = E_X \cos\alpha + E_Y \sin\alpha, \tag{3.4}$$

$$E_y = E_Z, \tag{3.5}$$

$$E_z = E_X \sin\alpha - E_Y \cos\alpha, \tag{3.6}$$

and the nonlinear susceptibility of quartz is known to have the following properties [40].

$$\chi_{xxx}^{(2)} = -\chi_{xyy}^{(2)} = -\chi_{yxy}^{(2)} = -\chi_{yyx}^{(2)} \equiv \chi_q^{(2)}, \tag{3.7}$$

$$\text{Other tensor elements} \simeq 0. \tag{3.8}$$

Then, x- and z-components of the nonlinear polarization in the crystal coordinates can be given as

$$P_x^{(2)} = \varepsilon_0 \chi_{xxx}^{(2)} \sin\alpha \cos\alpha E_{1Y} E_{2X}, \tag{3.9}$$

$$P_z^{(2)} = 0. \tag{3.10}$$

Here, only the Y-component of E_1 and the X-component of E_2 were considered. Using this result, the Y-component of the induced polarization in the laboratory coordinates can be evaluated.

$$P_Y^{(2)} = \varepsilon_0 \chi_{xxx}^{(2)} \sin^2\alpha \cos\alpha E_{1Y} E_{2X}. \tag{3.11}$$

Hence, the YYX-component of the nonlinear susceptibility in the laboratory coordinates can be finally determined to be

$$\chi_{YYX}^{(2)} = \chi_q^{(2)} \sin^2\alpha \cos\alpha. \tag{3.12}$$

The electric field of the generated local oscillator is proportional to $\chi_{YYX}^{(2)}$, and this expression gives its angle dependence (Fig. 3.3). As can be seen from Fig. 3.3(b), $|\chi_{YYX}^{(2)}|^2$ takes minimum values at $\alpha = 0, \pm 90, \text{ and } 180°$. In the actual measurements, α is usually adjusted near 0° or 180° to generate the local oscillator which is weak enough for efficient heterodyne detection.

3.2.3 Sample height and the phase stability

In the heterodyne detection, the interference between the electric fields of ω_3 and ω_{LO} are detected and analyzed. For the successful detection, ω_3 and ω_{LO} electric fields needs to have a constant phase difference, $\Delta\Theta$, which can be achieved by keeping the sample surface at a constant height, Z. In this section, the relation between the uncertainty in Z and the uncertainty in $\Delta\Theta$ is quantitatively discussed.

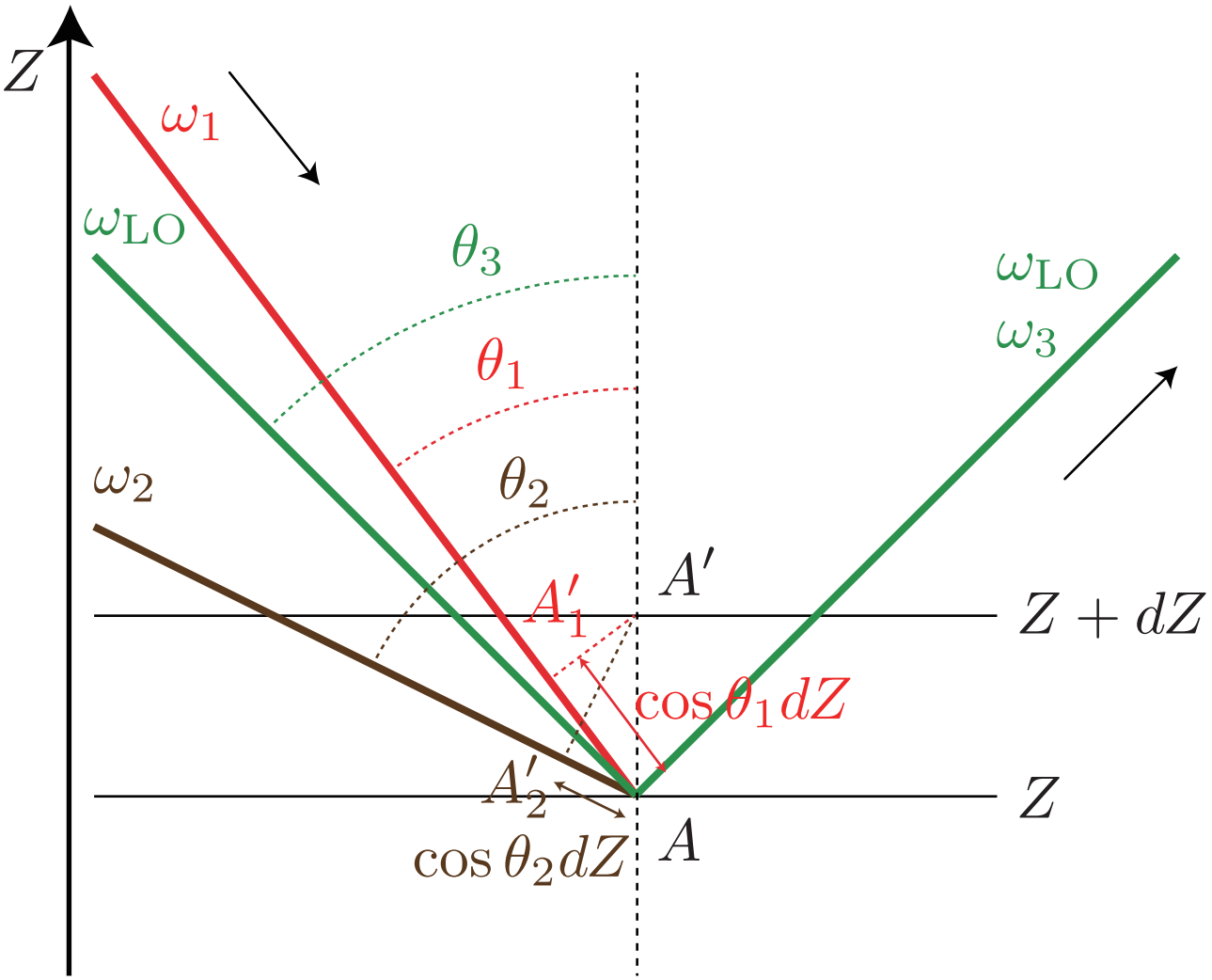

Figure 3.4: The phase change of the ω_1, ω_2, and ω_{LO} electric fields when the height of the interface changed from Z to $Z + dZ$ is evaluated. The phase of the ω_1 and ω_2 electric fields at the point A' is the same as that at A'_1 and A'_2, respectively.

At the point A in Fig. 3.4, let us assume that the phase of the ω_1, ω_2, and ω_{LO} electric fields are Θ_1, Θ_2, and Θ_{LO}, respectively. Then, the phase of the sum frequency electric field generated at A is $\Theta_3 = \Theta_1 + \Theta_2$. In this case, the phase difference between ω_{LO} and ω_3 is

$$\Delta\Theta \equiv \Theta_3 - \Theta_{\mathrm{LO}} = \Theta_1 + \Theta_2 - \Theta_{\mathrm{LO}}. \tag{3.13}$$

When the sample surface is displaced by the distance dZ, the phase difference needs to be evaluated at the point A'. For the ω_1 electric field, the phase at A' is the same as that at A'_1. This is because the ω_1 electric field is treated as a plane wave. Since the distance between A and A'_1 is $\cos\theta_1 dZ$, the phase at A' is

$$\Theta_1 - 2\pi\frac{\cos\theta_1 dZ}{\lambda_1}. \tag{3.14}$$

Similarly, the phase of ω_2 and ω_{LO} at A' are given respectively as

$$\Theta_2 - 2\pi\frac{\cos\theta_2 dZ}{\lambda_2}, \qquad \Theta_{\mathrm{LO}} - 2\pi\frac{\cos\theta_3 dZ}{\lambda_3}. \tag{3.15}$$

Hence, the phase difference at A' is

$$\Delta\Theta' = \left(\Theta_1 - 2\pi\frac{\cos\theta_1 dZ}{\lambda_1}\right) + \left(\Theta_2 - 2\pi\frac{\cos\theta_2 dZ}{\lambda_2}\right) - \left(\Theta_{\mathrm{LO}} - 2\pi\frac{\cos\theta_3 dZ}{\lambda_3}\right) \tag{3.16}$$

$$= \Delta\Theta - 2\pi\left(\frac{\cos\theta_1}{\lambda_1} + \frac{\cos\theta_2}{\lambda_2} - \frac{\cos\theta_3}{\lambda_3}\right)dZ. \tag{3.17}$$

By writing the change of the phase difference caused by the height change dZ as

$$d\Delta\Theta = \Delta\Theta' - \Delta\Theta, \tag{3.18}$$

the following relation can be obtained.

$$\frac{\partial\Delta\Theta}{\partial Z} = -2\pi\left(\frac{\cos\theta_1}{\lambda_1} + \frac{\cos\theta_2}{\lambda_2} - \frac{\cos\theta_3}{\lambda_3}\right). \tag{3.19}$$

In this expression, it is possible to rewrite θ_3 and λ_3 in terms of θ_1, θ_2, λ_1, and λ_2. According to Eq. (2.134),

$$n_a(\omega_3)\omega_3\sin\theta_3 = n_a(\omega_1)\omega_1\sin\theta_1 + n_a(\omega_2)\omega_2\sin\theta_2. \tag{3.20}$$

and because ω_3 is the sum frequency,

$$\omega_3 = \omega_1 + \omega_2. \tag{3.21}$$

Neglecting the dispersion of the air ($n_a(\omega_3) = n_a(\omega_1) = n_a(\omega_2)$) and rewriting in terms of the wavelength, these relations become

$$\frac{\sin\theta_3}{\lambda_3} = \frac{\sin\theta_1}{\lambda_1} + \frac{\sin\theta_2}{\lambda_2}, \tag{3.22}$$

$$\frac{1}{\lambda_3} = \frac{1}{\lambda_1} + \frac{1}{\lambda_2}. \tag{3.23}$$

Then, $\partial\Delta\Theta/\partial Z$ can be expressed in terms of θ_1, θ_2, λ_1, and λ_2 as

$$\frac{\partial\Delta\Theta}{\partial Z} = -2\pi\left\{\frac{\cos\theta_1}{\lambda_1} + \frac{\cos\theta_2}{\lambda_2} - \sqrt{\left(\frac{1}{\lambda_1} + \frac{1}{\lambda_2}\right)^2 - \left(\frac{\sin\theta_1}{\lambda_1} + \frac{\sin\theta_2}{\lambda_2}\right)^2}\right\}. \tag{3.24}$$

When $\lambda_1 = 795$ nm, $\lambda_2 = 3000$ nm, $\theta_1 = 44°$, and $\theta_2 = 56°$, this derivative can be evaluated as

$$\frac{\partial\Delta\Theta}{\partial Z} = 5\times10^{-2}\ \mathrm{rad}/\mu\mathrm{m} = 3°/\mu\mathrm{m}. \tag{3.25}$$

Because the complex phase of $\chi^{(2)}$ is directly related to the phase of the electric field, this estimation shows that the complex phase stability of 3° can be in principle achieved by suppressing the surface height change below 1 μm. In other words, the surface height stability of $\sim$ 1 μm is necessary to determine the complex phase of $\chi^{(2)}$ with reasonable accuracy.

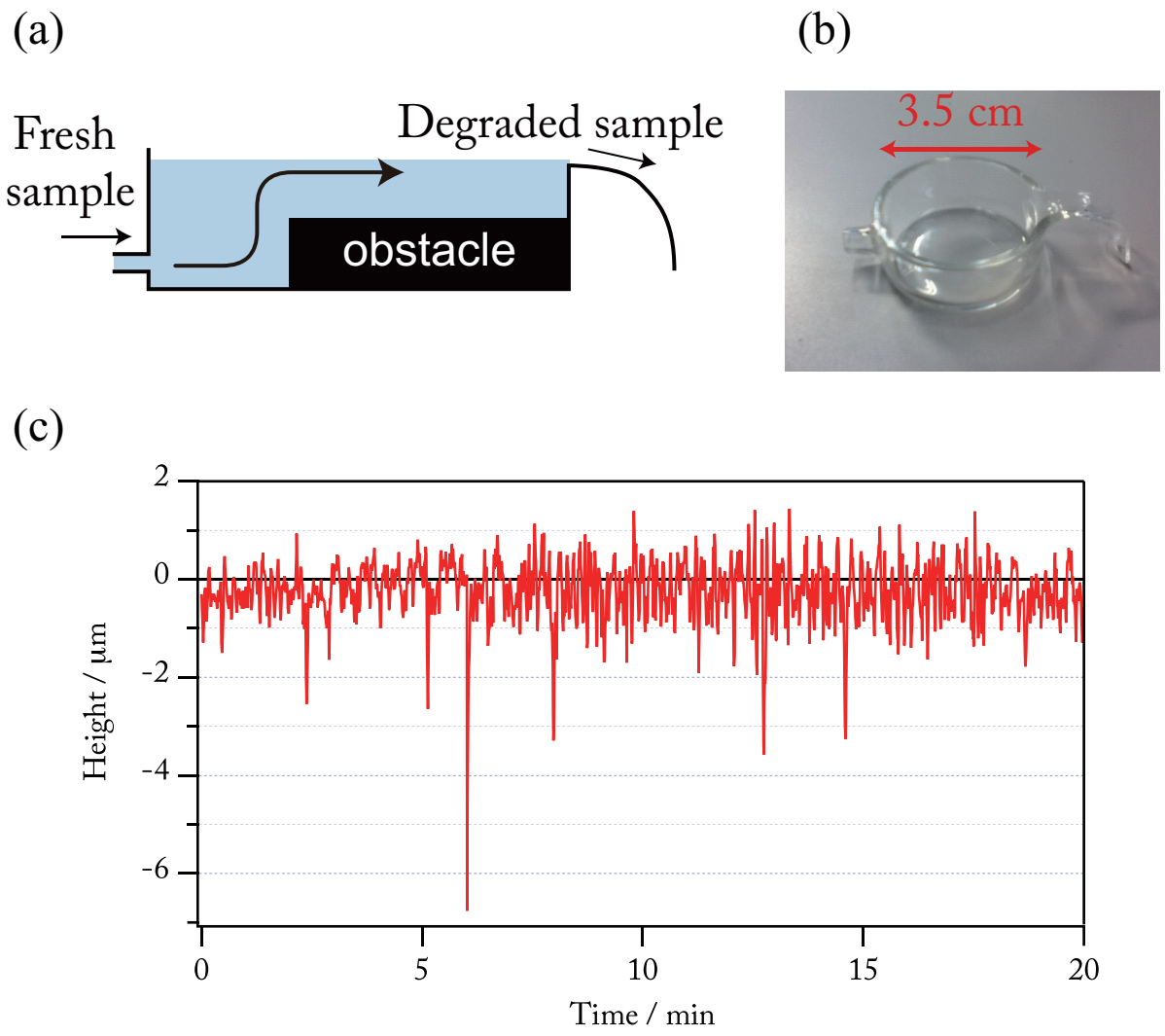

Figure 3.5: (a) The sketch and (b) the photograph of the developed flow cell. (c) Fluctuation of the liquid surface height while flowing the sample liquid (neat water) at 1 mL/sec.

3.2.4 Flow cell for interface experiments

In the UV-pump experiments, sample solution in the excitation volume needs to be continuously refreshed during the measurements. Meanwhile, as discussed in the previous section, the height of the sample surface must be kept constant with the accuracy of ~ 1 μm for the successful heterodyne detection. In order to simultaneously satisfy these two requirements, a new type of flow cell was developed. The sketch and the photograph of this flow cell is shown in Figs. 3.5(a) and (b).

This flow cell works in the following manner. First, a fresh sample solution is provided into the cell through the hole near the bottom by a magnetic gear pump (Micropump). With the addition of the fresh sample, the excess sample solution spontaneously flows out of the flow cell from the top, causing the sample solution at the surface to flow. By adding a guide for the liquid to flow smoothly out of the cell, the extremely stable flow of the solution near the sample surface was achieved. To make the surface flow even more efficient, a glass block was placed at the bottom of the flow cell as an obstacle to prevent the

sample flow in the deep bulk.

Fig. 3.5(c) shows the fluctuation of the sample surface height during the 20 minutes of monitoring. The sample was neat water, and the flow rate was about 1 mL/sec. Although sudden changes of the surface height were occasionally observed, the surface height was mostly kept within $\pm$ 1 μm. Hence, using this novel flow cell, it has become possible for the first time to conduct the HD-VSFG experiments while flowing the sample solution.

3.3 Principle and practice of the steady-state measurements

In the HD-VSFG experiments, the complex $\chi^{(2)}_{\rm eff}$ cannot be directly observed on the CCD camera, and some mathematical analysis is necessary before obtaining spectra as reported in the literature [18, 19]. The procedure and the theoretical background of that analysis are explained in this section. As an example, the actual experimental data of the air/neat water interface and the air/quartz interface (reference) are shown.

After VSFG at the sample surface, the sum frequency light and the local oscillator propagate collinearly, with the local oscillator temporally delayed for $T \simeq 5$ ps due to the silica plate placed in its optical path. This can be mathematically expressed as

$$E_3(t) + E_{\rm LO}(t-T) = \int d\omega E_3(\omega) e^{-i\omega t + i\Theta_3} + \int d\omega E_{\rm LO}(\omega) e^{-i\omega(t-T)+i\Theta_{\rm LO}} \tag{3.26}$$

$$= \int d\omega \left\{ E_3(\omega) e^{i\Theta_3} + E_{\rm LO}(\omega) e^{i\omega T + i\Theta_{\rm LO}} \right\} e^{-i\omega t}, \tag{3.27}$$

where E_3 and $E_{\rm LO}$ are the electric fields of the sum frequency light and the local oscillator, respectively. The phase factors, Θ_3 and $\Theta_{\rm LO}$, are the functions of the sample surface height, Z, as mentioned earlier in this chapter. Inside the polychromator, this is spectrally dispersed, and its intensity in the frequency domain is detected on the CCD camera. The actual experimental data are shown in Fig. 3.6. With the definition of $\Delta\Theta \equiv \Theta_3 - \Theta_{\rm LO}$, this intensity is given as

$$\left| E_3(\omega) e^{i\Theta_3} + E_{\rm LO}(\omega) e^{i\omega T + i\Theta_{\rm LO}} \right|^2$$

$$= |E_3(\omega)|^2 + |E_{\rm LO}(\omega)|^2 + 2{\rm Re}\left[E_3(\omega) E_{\rm LO}(\omega)^* e^{-i\omega T + i\Delta\Theta} \right]. \tag{3.28}$$

To isolate $E_3(\omega)$ from this expression, it is inverse Fourier transformed into the time domain.

$$\int d\omega \left[|E_3(\omega)|^2 + |E_{\rm LO}(\omega)|^2 \right] e^{-i\omega t}$$

$$+ \int d\omega \left[E_3(\omega) E_{\rm LO}(\omega)^* e^{-i\omega(T+t)+i\Delta\Theta} \right] + \int d\omega \left[E_3(\omega)^* E_{\rm LO}(\omega) e^{i\omega(T-t)-i\Delta\Theta} \right]. \tag{3.29}$$

The experimental data corresponding to this are shown in Fig. 3.7. In the figure, the contribution from these three terms appear separately near $t = 0, -T$, and T, respectively. Thus, the second term can be isolated in the time domain by using an appropriate filter function, $f(t+T)$.

$$f(t+T) \int d\omega \left[E_3(\omega) E_{\rm LO}(\omega)^* e^{-i\omega(T+t)+i\Delta\Theta} \right]. \tag{3.30}$$

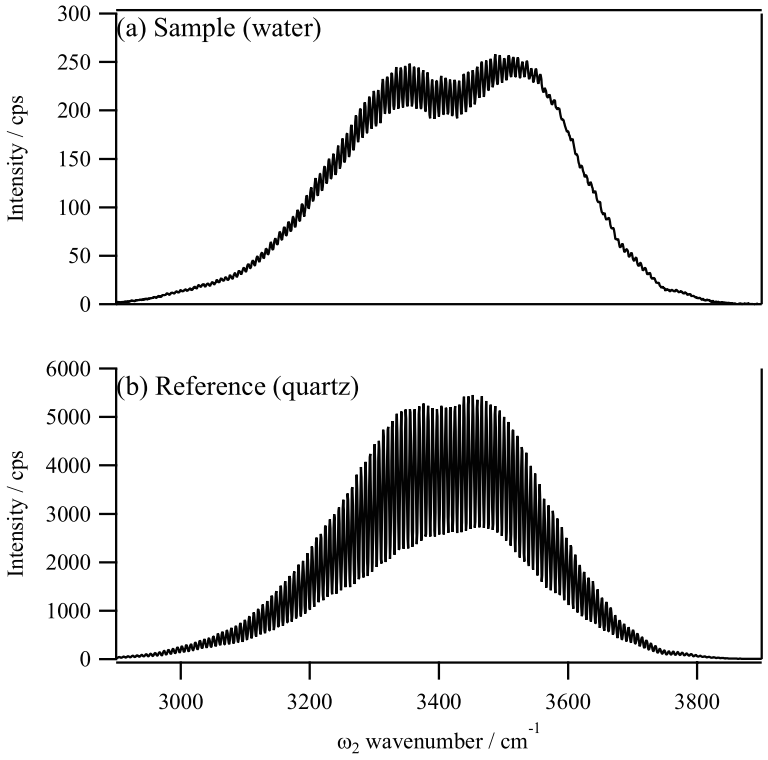

Figure 3.6: Raw spectra obtained at the (a) air/water and (b) air/quartz interfaces.

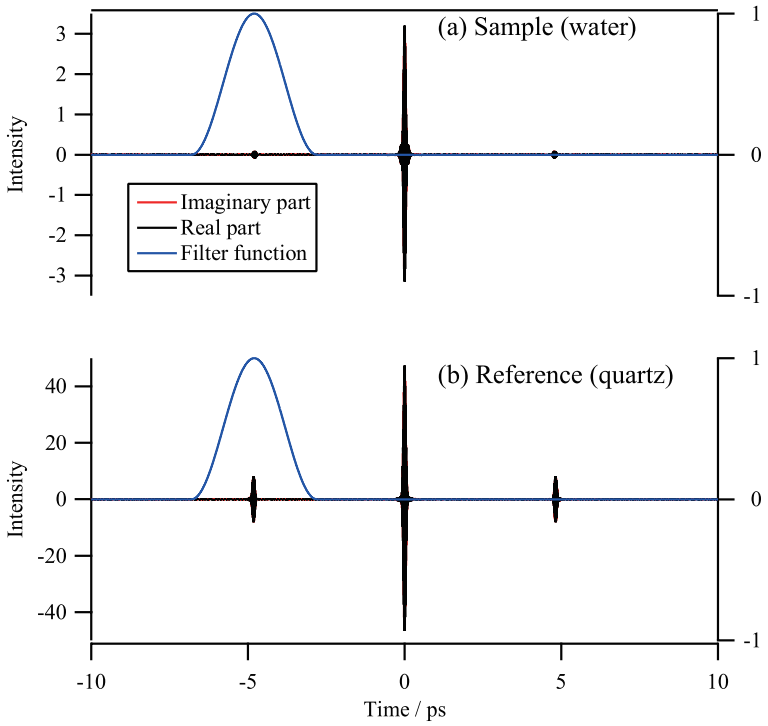

Figure 3.7: After inverse Fourier transformation into the time domain. The filter function used to extract the heterodyned term near -5 ps is also shown.

In the example shown in Fig. 3.7, Hanning function was chosen as the filter function [48].

The frequency domain spectrum of this term can be obtained by Fourier transformation.

$$\frac{1}{2\pi}\int dt e^{i\omega t} f(t+T)\int d\omega' \left[E_3(\omega')E_{\mathrm{LO}}(\omega')^* e^{-i\omega'(T+t)+i\Delta\Theta}\right] = \int d\omega' E_3(\omega')E_{\mathrm{LO}}(\omega')^* e^{-i\omega' T+i\Delta\Theta}\cdot\frac{1}{2\pi}\int dt f(t+T)e^{i(\omega-\omega')t}. \tag{3.31}$$

This is shown in Fig. 3.8. The meaning of this expression becomes clear by expanding the filter function into a Fourier series.

$$f(t+T) = \int d\omega'' f(\omega'')e^{-i\omega''(t+T)}. \tag{3.32}$$

Then,

$$\frac{1}{2\pi}\int dt f(t+T)e^{i(\omega-\omega')t} = \frac{1}{2\pi}\int d\omega'' f(\omega'')e^{-i\omega'' T}\int dt e^{i(\omega-\omega'-\omega'')t} \tag{3.33}$$

$$= \frac{1}{2\pi}\int d\omega'' f(\omega'')e^{-i\omega'' T}\cdot 2\pi\delta(\omega-\omega'-\omega'') \tag{3.34}$$

$$= f(\omega-\omega')e^{-i(\omega-\omega')T}, \tag{3.35}$$

and the extracted signal shown in Fig. 3.8 can be mathematically expressed as

$$e^{i\Delta\Theta}\int d\omega' E_3(\omega')E_{\mathrm{LO}}(\omega')^* f(\omega-\omega')e^{-i\omega T} = e^{i\Delta\Theta}\left[\{E_3(\omega)E_{\mathrm{LO}}(\omega)^*\}\otimes f(\omega)\right]e^{-i\omega T}. \tag{3.36}$$

Here, $\otimes$ is the convolution operator. When $f(\omega)$ can be regarded as a delta function, this can be simplified into

$$e^{i\Delta\Theta}E_3(\omega)E_{\mathrm{LO}}(\omega)^* e^{-i\omega T}. \tag{3.37}$$

In the following discussion, it will be assumed that this quantity is obtained by this analysis. Care must be taken in the choice of the filter function, $f(t)$, so as to make this approximation reasonably valid.

With the HD-VSFG measurements carried out for the sample and the reference (quartz), following two quantities can be extracted by the above mentioned analysis.

$$e^{i\Delta\Theta(Z_{\mathrm{sample}})}E_{3\mathrm{r}}^{\mathrm{sample}}E_{\mathrm{LO}}^{\mathrm{sample},*}e^{i\omega_3 T}, \tag{3.38}$$

$$e^{i\Delta\Theta(Z_{\mathrm{quartz}})}E_{3\mathrm{r}}^{\mathrm{quartz}}E_{\mathrm{LO}}^{\mathrm{quartz},*}e^{i\omega_3 T}. \tag{3.39}$$

Here, $E_{3\mathrm{r}}^{\mathrm{sample}}$ and $E_{3\mathrm{r}}^{\mathrm{quartz}}$ are the electric fields of the sum frequency light generated at the sample and quartz surfaces, respectively, in the reflection direction, $E_{\mathrm{LO}}^{\mathrm{sample}}$ and $E_{\mathrm{LO}}^{\mathrm{quartz}}$ are the electric fields of the local oscillator generated from the incident beams reflected at the sample and quartz surfaces, respectively, $T \simeq 5$ ps is the temporal delay introduced by the silica plate, and $*$ denotes taking the complex conjugate. For simplicity of discussion, the experimental nonlinear susceptibility, $\chi_{\mathrm{exp}}^{(2),\mathrm{sample}}$, is defined as shown below.

$$\chi_{\mathrm{exp}}^{(2),\mathrm{sample}} \equiv \frac{e^{i\Delta\Theta(Z_{\mathrm{sample}})}E_{3\mathrm{r}}^{\mathrm{sample}}E_{\mathrm{LO}}^{\mathrm{sample},*}e^{i\omega_3 T}}{ie^{i\Delta\Theta(Z_{\mathrm{quartz}})}E_{3\mathrm{r}}^{\mathrm{quartz}}E_{\mathrm{LO}}^{\mathrm{quartz},*}e^{i\omega_3 T}}. \tag{3.40}$$

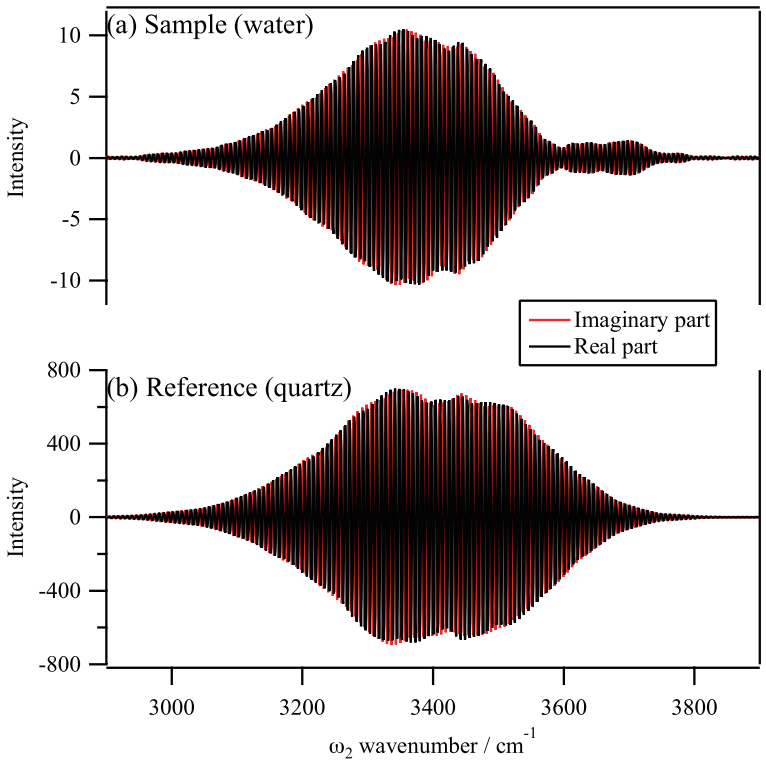

Figure 3.8: After Fourier transformation back into the frequency domain.

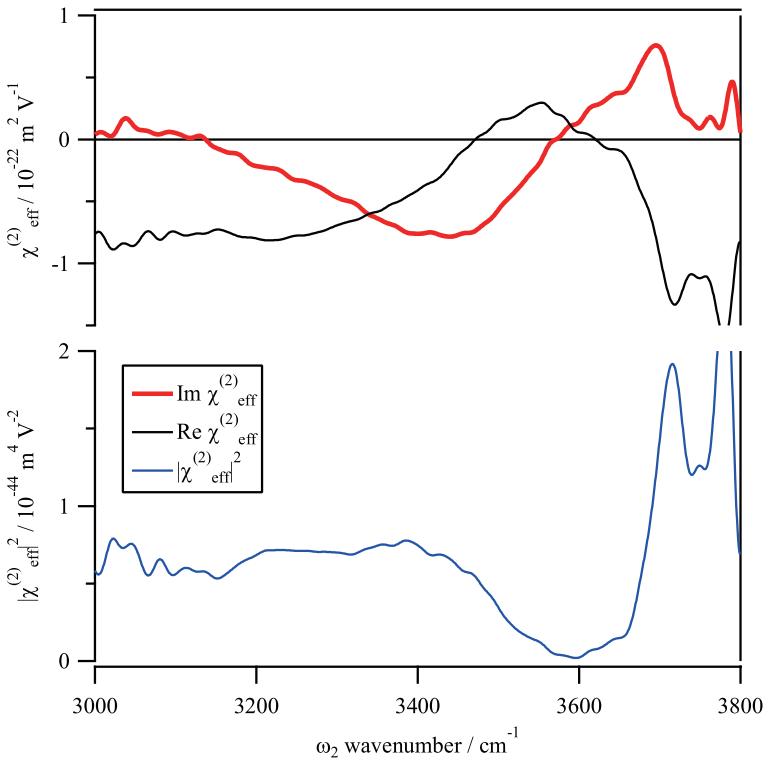

Figure 3.9: Complex $\chi^{(2)}_{\text{eff}}$ spectrum of the air/water interface.

In this equation, the sum frequency electric fields, $E_{3\mathrm{r}}^{\mathrm{sample}}$ and $E_{3\mathrm{r}}^{\mathrm{quartz}}$, can be expressed in terms of the effective nonlinear susceptibilities of the sample $\left(\chi_{\mathrm{eff}}^{(2),\mathrm{sample}}\right)$ and quartz $\left(\chi_{\mathrm{eff}}^{(2),\mathrm{quartz}}\right)$ as shown below.

$$E_{3\mathrm{r}}^{\mathrm{sample}} = \frac{i\omega_3}{2cn_a(\omega_3)\cos\theta_{3\mathrm{r}}}\chi_{\mathrm{eff}}^{(2),\mathrm{sample}}E_{1\mathrm{i}}E_{2\mathrm{i}}, \tag{3.41}$$

$$E_{3\mathrm{r}}^{\mathrm{quartz}} = \frac{\omega_3}{2cn_a(\omega_3)\cos\theta_{3\mathrm{r}}}\chi_{\mathrm{eff}}^{(2),\mathrm{quartz}}E_{1\mathrm{i}}E_{2\mathrm{i}}. \tag{3.42}$$

Here, the complex unit appears only in the first equation, because the induced nonlinear polarization is localized at the interface for the first equation, whereas it exists in the bulk for the second equation. Next, the local oscillator electric fields, $E_{\mathrm{LO}}^{\mathrm{sample}}$ and $E_{\mathrm{LO}}^{\mathrm{quartz}}$, are expressed using the reflectivities of the local oscillator at the sample and quartz surfaces. This is because the local oscillator is reflected at the sample or quartz surface before it becomes overlapped with the sum frequency light.

$$E_{\mathrm{LO}}^{\mathrm{sample}} = E_{\mathrm{LO}}^{0}r_{\mathrm{LO}}^{\mathrm{sample}}, \tag{3.43}$$

$$E_{\mathrm{LO}}^{\mathrm{quartz}} = E_{\mathrm{LO}}^{0}r_{\mathrm{LO}}^{\mathrm{quartz}}. \tag{3.44}$$

Here, $r_{\mathrm{LO}}^{\mathrm{sample}}$ and $r_{\mathrm{LO}}^{\mathrm{quartz}}$ are the complex reflectivities of the local oscillator at the sample and quartz surfaces, respectively, and E_{LO}^{0} is the electric field of the local oscillator which is expected to be observed when the reflectivity is unity. Using these properties, and assuming that the surface height is exactly the same for the sample and for the quartz ($Z_{\mathrm{sample}} = Z_{\mathrm{quartz}}$), the experimental nonlinear susceptibility can be expressed as

$$\chi_{\mathrm{exp}}^{(2),\mathrm{sample}} = \frac{\chi_{\mathrm{eff}}^{(2),\mathrm{sample}}}{\chi_{\mathrm{eff}}^{(2),\mathrm{quartz}}}\left(\frac{r_{\mathrm{LO}}^{\mathrm{sample}}}{r_{\mathrm{LO}}^{\mathrm{quartz}}}\right)^{*}, \tag{3.45}$$

and hence the effective nonlinear susceptibility of the sample is given by

$$\chi_{\mathrm{eff}}^{(2),\mathrm{sample}} = \left(\frac{r_{\mathrm{LO}}^{\mathrm{quartz}}}{r_{\mathrm{LO}}^{\mathrm{sample}}}\right)^{*}\chi_{\mathrm{eff}}^{(2),\mathrm{quartz}}\chi_{\mathrm{exp}}^{(2),\mathrm{sample}}. \tag{3.46}$$

In this formula, $\chi_{\mathrm{exp}}^{(2),\mathrm{sample}}$ is experimentally obtained using Eq. (3.40), and $\chi_{\mathrm{eff}}^{(2),\mathrm{quartz}}$ can be calculated following the equation derived at the end of the previous chapter. The complex reflectivities for S- and P-polarized light can be calculated from the following formulae using the complex refractive indices [49].

$$r_{\mathrm{S}} = \frac{n_a(\omega)\cos\theta_{\mathrm{i}} - n_b(\omega)\cos\theta_{\mathrm{t}}}{n_a(\omega)\cos\theta_{\mathrm{i}} + n_b(\omega)\cos\theta_{\mathrm{t}}}, \tag{3.47}$$

$$r_{\mathrm{P}} = \frac{n_b(\omega)\cos\theta_{\mathrm{i}} - n_a(\omega)\cos\theta_{\mathrm{t}}}{n_b(\omega)\cos\theta_{\mathrm{i}} + n_a(\omega)\cos\theta_{\mathrm{t}}}. \tag{3.48}$$

When the incident beams are far off-resonant with the reflecting medium, the refractive index can be regarded as a real constant. For the quartz, refractive index was taken to be 1.544 [50]. For the sample, an appropriate refractive index must be chosen for each sample.

3.4 Principle and practice of the time-resolved measurements

In the steady-state measurements, the air/quartz interface is used as the reference to obtain the complex $\chi^{(2)}_{\mathrm{eff}}$ spectra of the sample interface. In the time-resolved measurements, instead of quartz, the HD-VSFG signal from the sample surface with the pump delay at -20 ps is used. (The pump pulse arrives at the sample surface 20 ps after the HD-VSFG measurement.) Because of the negative delay of the pump light, this signal should be identical to the steady-state signal. Hereafter, the sum frequency and the local oscillator electric fields with the pump delay at t are denoted as $E^t_{3\mathrm{r}}$ and E^t_{LO}, respectively.

Following the same analysis procedure as for the steady-state measurements, the following quantities can be obtained for the sample (the air/sample solution interface with the pump delay at t) and for the reference (the air/sample solution interface with the pump delay at -20 ps).

$$e^{i\Delta\Theta(Z_{\mathrm{sample}})}E^t_{3\mathrm{r}}E^{t,*}_{\mathrm{LO}}e^{i\omega_3 T}, \tag{3.49}$$

$$e^{i\Delta\Theta(Z_{\mathrm{sample}})}E^{-20\ \mathrm{ps}}_{3\mathrm{r}}E^{-20\ \mathrm{ps},*}_{\mathrm{LO}}e^{i\omega_3 T}. \tag{3.50}$$

Here, the electric fields can be expressed in terms of nonlinear susceptibilities as

$$E^t_{3\mathrm{r}} = \frac{i\omega_3}{2cn_a(\omega_3)\cos\theta_{3\mathrm{r}}}\chi^{(2)}_{\mathrm{eff}}(t)E_{1\mathrm{i}}E_{2\mathrm{i}}, \tag{3.51}$$

$$E^{-20\ \mathrm{ps}}_{3\mathrm{r}} = \frac{i\omega_3}{2cn_a(\omega_3)\cos\theta_{3\mathrm{r}}}\chi^{(2)}_{\mathrm{eff}}(-20\ \mathrm{ps})E_{1\mathrm{i}}E_{2\mathrm{i}}. \tag{3.52}$$

In these expressions, $\chi^{(2)}_{\mathrm{eff}}(t)$ is the effective nonlinear susceptibility of the system at the delay t after the pump light irradiation. The experimental nonlinear susceptibility can be defined by taking the ratio between Eqs. (3.49) and (3.50).

$$\chi^{(2)}_{\mathrm{exp}}(t) \equiv \frac{e^{i\Delta\Theta(Z_{\mathrm{sample}})}E^t_{3\mathrm{r}}E^{t,*}_{\mathrm{LO}}e^{i\omega_3 T}}{e^{i\Delta\Theta(Z_{\mathrm{sample}})}E^{-20\ \mathrm{ps}}_{3\mathrm{r}}E^{-20\ \mathrm{ps},*}_{\mathrm{LO}}e^{i\omega_3 T}} = \frac{\chi^{(2)}_{\mathrm{eff}}(t)}{\chi^{(2)}_{\mathrm{eff}}(-20\ \mathrm{ps})}\left(\frac{r^t_{\mathrm{LO}}}{r^{-20\ \mathrm{ps}}_{\mathrm{LO}}}\right)^*. \tag{3.53}$$

Here, r^t_{LO} is the reflectivity of the local oscillator at the sample surface at the delay t after the pump light irradiation. When the transient species does not have a resonance at ω_3, the reflectivity does not change by the pump light irradiation, and the two reflectivities can be assumed to have the same value.

$$r^t_{\mathrm{LO}} = r^{-20\ \mathrm{ps}}_{\mathrm{LO}}. \tag{3.54}$$

Additionally, it is more covenient to express $\chi^{(2)}_{\mathrm{eff}}(t)$ and $\chi^{(2)}_{\mathrm{eff}}(-20\ \mathrm{ps})$ in terms of the steady-state susceptibility $\left(\chi^{(2)}_{\mathrm{eff,steady}}\right)$ and the transient susceptibility $\left(\Delta\chi^{(2)}_{\mathrm{eff}}(t)\right)$.

$$\chi^{(2)}_{\mathrm{eff}}(t) = \chi^{(2)}_{\mathrm{eff,steady}} + \Delta\chi^{(2)}_{\mathrm{eff}}(t), \tag{3.55}$$

$$\chi^{(2)}_{\mathrm{eff}}(-20\ \mathrm{ps}) = \chi^{(2)}_{\mathrm{eff,steady}}. \tag{3.56}$$

Using these equations, the experimental nonlinear susceptibility can be expressed as

$$\chi^{(2)}_{\mathrm{exp}}(t) = \frac{\chi^{(2)}_{\mathrm{eff,steady}} + \Delta\chi^{(2)}_{\mathrm{eff}}(t)}{\chi^{(2)}_{\mathrm{eff,steady}}}. \tag{3.57}$$

Then, $\Delta\chi^{(2)}_{\mathrm{eff}}(t)$ can be obtained by

$$\Delta\chi^{(2)}_{\mathrm{eff}}(t) = \left(\chi^{(2)}_{\mathrm{exp}}(t) - 1\right)\chi^{(2)}_{\mathrm{eff,steady}}. \tag{3.58}$$

In this expression, $\chi^{(2)}_{\mathrm{exp}}$ is obtained by the transient measurements, and $\chi^{(2)}_{\mathrm{eff,steady}}$ can be determined from a separate steady-state measurement. Hence, the transient spectra at the interface $\left(\Delta\chi^{(2)}_{\mathrm{eff}}(t)\right)$ can be obtained from these two measurements.

3.4.1 Necessity of heterodyne detection in transient measurements

When the conventional homodyne detection is used, only the absolute square of nonlinear susceptibilities can be obtained. This imposes a limitation to the steady-state measurements, because the information about the complex phase and the sign of $\chi^{(2)}_{\mathrm{eff}}$ is lost, which reflects the absolute orientation of molecules at the interface.

For the time-resolved measurement, homodyne detection becomes even more troublesome. With the pump delay at t, $|\chi^{(2)}_{\mathrm{eff}}(t)|^2$ is obtained, and with the pump delay at -20 ps, $|\chi^{(2)}_{\mathrm{eff}}(-20\ \mathrm{ps})|^2$ is obtained. The best thing that can be done to evaluate the transient response of the system from these data is to take the difference between the two.

$$|\chi^{(2)}_{\mathrm{eff}}(t)|^2 - |\chi^{(2)}_{\mathrm{eff}}(-20\ \mathrm{ps})|^2 = |\chi^{(2)}_{\mathrm{eff,steady}} + \Delta\chi^{(2)}_{\mathrm{eff}}(t)|^2 - |\chi^{(2)}_{\mathrm{eff,steady}}|^2 \tag{3.59}$$

$$= 2\mathrm{Re}\left[\chi^{(2),*}_{\mathrm{eff,steady}}\Delta\chi^{(2)}_{\mathrm{eff}}(t)\right] + |\Delta\chi^{(2)}_{\mathrm{eff}}(t)|^2 \tag{3.60}$$

As in the steady state measurement, $|\Delta\chi^{(2)}_{\mathrm{eff}}(t)|^2$ is obtained instead of $\Delta\chi^{(2)}_{\mathrm{eff}}(t)$, and the phase and sign of $\Delta\chi^{(2)}_{\mathrm{eff}}(t)$ is lost. What is worse, there is also a contribution from the unwanted cross term $\left(2\mathrm{Re}\left[\chi^{(2),*}_{\mathrm{eff,steady}}\Delta\chi^{(2)}_{\mathrm{eff}}(t)\right]\right)$. For these reasons, the use of heterodyne detection is essential in the time-resolved measurements.

3.4.2 Determining the time zero of the pump light and the instrumental response

Zinc oxide (ZnO) crystal was used to determine the time zero of the pump light and the instrumental response of the system. Because the band gap of ZnO is 3.0-3.2 eV (390-410 nm), it is reported that the electron-hole pairs can be generated by the irradiation of the UV light. These free carriers show an optical absorption in the mid-IR wavelength, and this has been studied by the transient absorption spectroscopy [51]. It is possible to observe the same transient response by UV-excited time-resolved HD-VSFG spectroscopy.

Through the time-resolved HD-VSFG measurements, $\Delta\chi^{(2)}_{\mathrm{eff}}(t)$ was observed at each pump delay t, and the integrated intensity given by

$$\left|\int d\omega_2 \Delta\chi^{(2)}_{\mathrm{eff}}(t)\right| \tag{3.61}$$

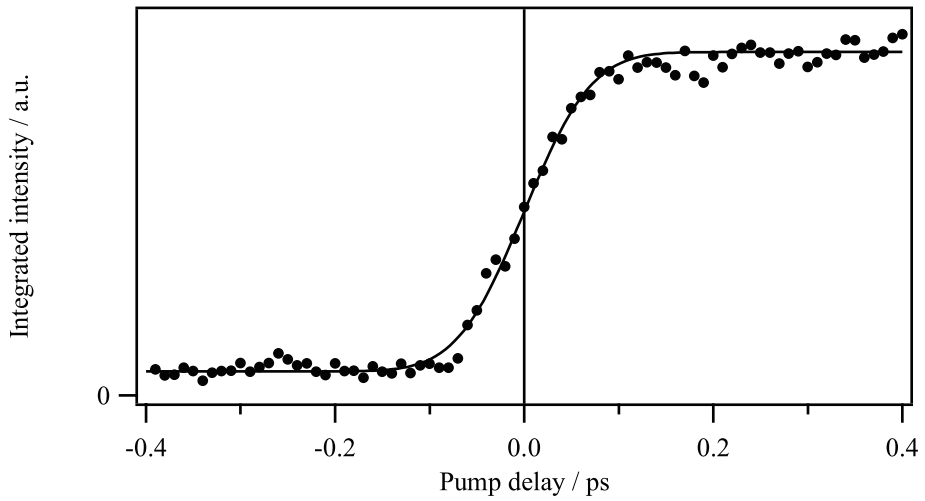

Figure 3.10: Transient response of zinc oxide crystal following the UV excitation. The integrated intensity $|\int d\omega_2 \Delta\chi^{(2)}_{\rm eff}(t)|$ was evaluated at each pump delay, and is given by the filled circles. The solid line shows the fit to a theoretical formula.

is plotted in Fig. 3.10. Assuming that the carriers are generated instantaneously after the photoexcitation, the intrinsic response of ZnO can be given by a step function, $f(t)$. The instrumental response can be approximated by a gaussian function, $g(t)$.

$$f(t) = \begin{cases} 0 & (t \le t_0) \\ A & (t > t_0) \end{cases}, \qquad g(t) = \frac{1}{\sqrt{\pi}\tau} e^{-\left(\frac{t}{\tau}\right)^2}. \tag{3.62}$$

In these formulae, A and τ are the parameters that are to be determined in the fitting. Then, the experimental data can be fitted by the convolution of these two functions and a constant offset, I_0.

$$I_0 + f(t) \otimes g(t) = I_0 + \int_{-\infty}^{\infty} dt' f(t-t') g(t') = I_0 + \frac{A}{\sqrt{\pi}} \int_{-\infty}^{t-t_0} \frac{dt'}{\tau} e^{-(t/\tau)^2} \tag{3.63}$$

$$= I_0 + \frac{A}{2}\left[1 + \frac{2}{\sqrt{\pi}} \int_0^{t-t_0} \frac{dt'}{\tau} e^{-(t/\tau)^2}\right] \tag{3.64}$$

$$\equiv I_0 + \frac{A}{2}\left[1 + \mathrm{erf}\left(\frac{t-t_0}{\tau}\right)\right]. \tag{3.65}$$

Here, $\otimes$ is the convolution operator, and erf is the error function. The time zero of the pump light is determined so that the t_0 obtained in the fitting becomes 0. The instrumental response can be evaluated from the full width at half maximum (FWHM) of the gaussian function, $g(t)$, which was equal to $2\sqrt{\ln 2}\,\tau = 130$ fs for the actual experimental data shown in Fig. 3.10.

3.5 Conclusion

UV-excited time-resolved HD-VSFG spectroscopy was developed to observed the ultrafast chemical reactions initiated by the UV pump light at air/liquid interfaces. Due to the femtosecond duration of the UV-pump light and the IR-probe light, the instrumental response as short as 130 fs was achieved. Additionally, a flow cell for interface experiments was developed to eliminate the photodegraded sample

from the sample surface. Owing to its unique design, efficient and extremely stable flow near the sample surface was achieved. The application of the developed method will be presented in the next chapter.

Chapter 4

Observation of hydrated electrons at the air/water interface

4.1 Introduction

Hydrated electron is a simple transient chemical species consisting only of one electron and several water molecules that solvate the electron. As the most fundamental anion species, the properties of hydrated electrons are well studied in the bulk water, especially by transient absorption spectroscopy [52–55]. The electronic spectrum of hydrated electrons obtained by transient absorption spectroscopy is characterized by a very broad band centering at 720 nm, which persists for several hundred nanoseconds [53]. In addition to the electronic spectrum, the vibrational spectrum is also acquired by transient Raman spectroscopy [56–61]. In the Raman spectrum, transient bands appear in the OH stretch region and in the OH bending region. These bands are due to the OH stretch and bending modes of water molecules that solvate the electron, whose intensity is enhanced by virtue of the electronic resonance to the optical absorption of the electron in the near-infrared.

Contrary to the wealth of understanding in the bulk water, the properties and even the existence/absence of hydrated electrons at the air/water interface are not well understood yet. Traditionally, it was considered that charged species never approach the air/water interface. Although it has recently become clear that some ions are actually surface active [62], it is still not very obvious whether the electrons prefer to reside at the air/water interface or not. To date, four studies have claimed that electrons exist at the air/water interface. A photoelectron study of hydrated electrons in liquid water jet found two electron binding motifs depending on how the electrons are generated, and the authors assigned one of them to partially hydrated electrons at the liquid water surface, while the other one was assigned to the fully hydrated electrons in bulk water [63]. (It is to be noted that the three other photoelectron studies of liquid water jet [64–66] found only the bulk hydrated electrons.) Meanwhile, on the same year, another experimental attempt to observe the hydrated electrons at the air/water interface was made using second harmonic generation (SHG) spectroscopy [67], and it was concluded that the electrons are fully hydrated at the air/water interface. From the theoretical perspective, two molecular dynamics (MD) simulations

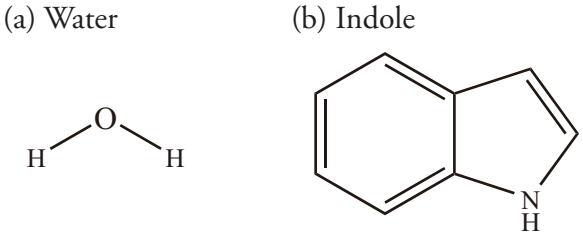

Figure 4.1: Molecular structure of (a) water and (b) indole.

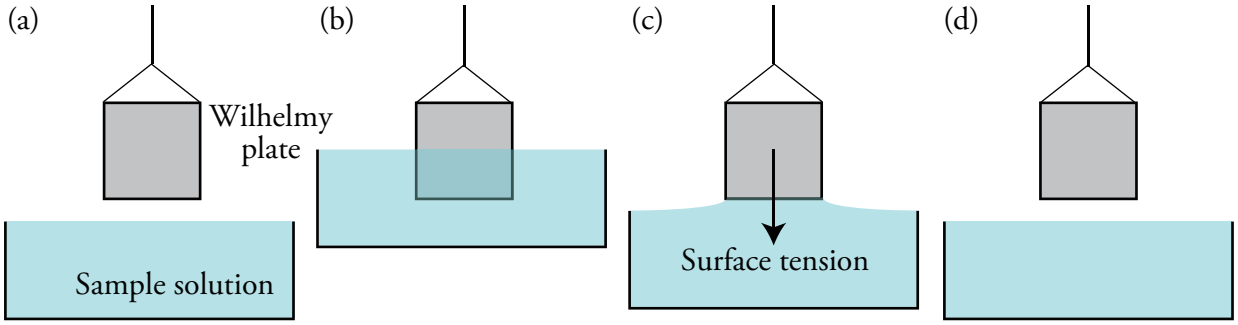

Figure 4.2: Surface tension measurement by the Wilhelmy plate method. (a) Move up the sample stage until the plate is dipped into the sample solution. (b) Gradually move down the sample stage. (c) Keep measuring the force while moving down the sample stage. (d) The plate loses contact with the sample solution. The measured force just before losing the contact corresponds to the surface tension.

are reported, and one of them claim that the electrons are partially hydrated at the air/water interface [68], while the other concludes that the electrons are fully hydrated [69]. In this way, the problem of the electron hydration at the air/water interface is a controversial topic, and it is attracting attention from both experimental and theoretical viewpoints.

In the present study, this problem is experimentally examined using the newly developed UV-excited time-resolved HD-VSFG spectroscopy described in the previous chapter. With the intrinsic interface selectivity of SFG and the detailed structural information based on vibrational spectroscopy, I aimed to give a detailed and conclusive answer to the existence and properties of the hydrated electrons at the air/water interface.

4.2 Experimental

4.2.1 Sample

High purity water (18.2 MΩ·cm resistivity) was obtained from a commercial water purification system (Millipore, Milli-Q Advantage A10). Indole (purity $>$ 99.0 %) was purchased from Tokyo Chemical Industry and was used without further purification.

4.2.2 Surface tension measurement

Surface tension of the indole aqueous solution at various bulk concentration was measured on a commercial tensiometer (KSV, Sigma 700) using the Wilhelmy plate method (Fig. 4.2). In this method, a Wilhelmy plate made of platinum is first dipped into the sample solution, and then the sample stage is gently moved away from the plate. Because of the surface tension, attractive force is observed to retract the plate back into the solution. The attractive force becomes larger as the sample is moved away, until the plate loses contact with the solution surface. The force imposed on the plate just before losing the contact is used for evaluating the surface tension. Surface pressure, Π, is finally obtained by subtracting the obtained surface tension, γ, from the surface tension of the neat solvent, γ^*.

$$\Pi = \gamma^* - \gamma. \tag{4.1}$$

Before each measurement, the Wilhelmy plate was burnt and thoroughly rinsed with high purity water to completely eliminate the contaminants.

The actual measurement was done in the following manner. First, high purity water was used as the sample, and the surface tension was measured (γ^*). Then, a small amount of 17 mM saturated indole aqueous solution was added to the high purity water, stirred, and the surface tension was again measured (γ). A small amount of saturated indole solution was repeatedly added to the sample solution, and after each addition, the sample solution was stirred and the surface tension was measured. In this way, surface tension of indole aqueous solution with various concentration was measured, which can be used to evaluate the surface excess of indole as will be discussed later. The room temperature during the measurement was 21 °C (294 K).

4.2.3 UV-vis absorption

Steady-state absorption spectrum was measured between 200 and 800 nm using a commercial UV-Visible/NIR spectrophotometer (Hitachi, U-3310). 0.23 mM indole aqueous solution was placed inside a quartz cell with the optical path length of 1 cm, and was used for the measurement. The obtained absorbance, A, was converted to molar absorption coefficient, ε, following the Beer-Lambert law [5],

$$\varepsilon = \frac{A}{c_M \ell}, \tag{4.2}$$

with the concentration $c_M = 0.23$ mM and the optical path length $\ell = 1$ cm.

4.2.4 Steady-state and time-resolved HD-VSFG measurement

Air/neat water and air/indole aqueous solution interfaces were used as the sample. At these two interfaces, electrons are transiently generated by the UV pump light through the two-photon ionization of water and the one-photon ionization of indole, respectively, as shown in the reaction scheme below.

$$\mathrm{H_2O} \xrightarrow{2h\nu, n\mathrm{H_2O}} \mathrm{OH} + \mathrm{H_3O^+} + e^-(\mathrm{H_2O})_n \tag{4.3}$$

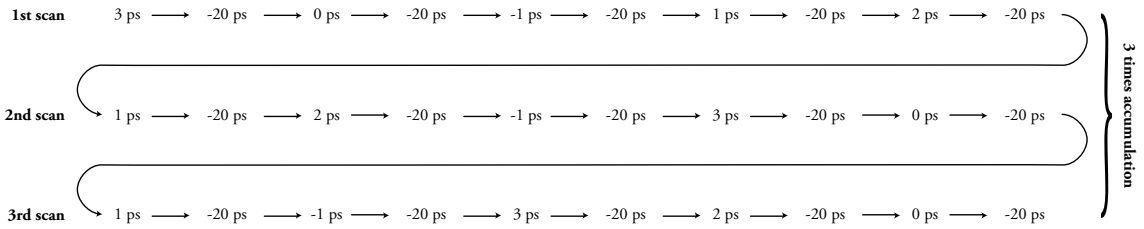

Figure 4.3: An example of the sequence of pump delays during a transient measurement. In each scan, pump delays were ordered randomly and followed by -20 ps. This random measurement was repeated many times to accumulate the data.

$$\text{indole} \xrightarrow{h\nu} \text{S}_1 \text{ indole} \xrightarrow{n\text{H}_2\text{O}} (\text{indole cation})^+ + e^-(\text{H}_2\text{O})_n \tag{4.4}$$

For the air/neat water interface, the high purity water was used as it is. For the air/indole solution interface, 17 mM indole solution was prepared by dissolving indole in the high purity water after about 5 hours of sonication.

The details of the experimental apparatus is given in the previous chapter. The intensity and the beam diameter of the pump light at the sample surface was optimized for each sample. Pump light intensity was 25 mW for the air/neat water interface, and 5 mW for the air/indole solution interface, except for the pump power dependence experiment. For the air/neat water interface, the pump light was focused more tightly than for the air/indole solution interface to make the two-photon absorption more efficient. In both cases, the beam diameter of the pump light was larger than that of ω_1 and ω_2 beams used for VSFG.

Since the sample surface is easily contaminated by a trace amount of surface active contaminants, a special care was taken to prevent the sample contamination. The flow cell was cleaned in concentrated sulfuric acid overnight, and rinsed with high purity water. The interior of the pump and the tubes that were used for providing sample solution into the flow cell was washed with acetone and thoroughly rinsed with high purity water.

For the transient spectra acquisition, the exposure time for one measurement was 30 sec and it was typically accumulated for about 30 times. In each measurement, 30 sec exposure at the pump delay t was immediately followed by another 30 sec exposure at the delay $t = -20$ ps. In each scan, the delays were measured in a random order as shown in Fig. 4.3 so as to minimize the artifacts arising from the order of the spectral acquisition.

4.3 Results and Discussion

4.3.1 Surface characterization

At the interface, the molecular concentration is sometimes greatly different from the bulk, especially when the molecules are surface active. Hence, the estimation of the molecular concentration at the interface (the number of molecules per unit surface area) is done in this section.

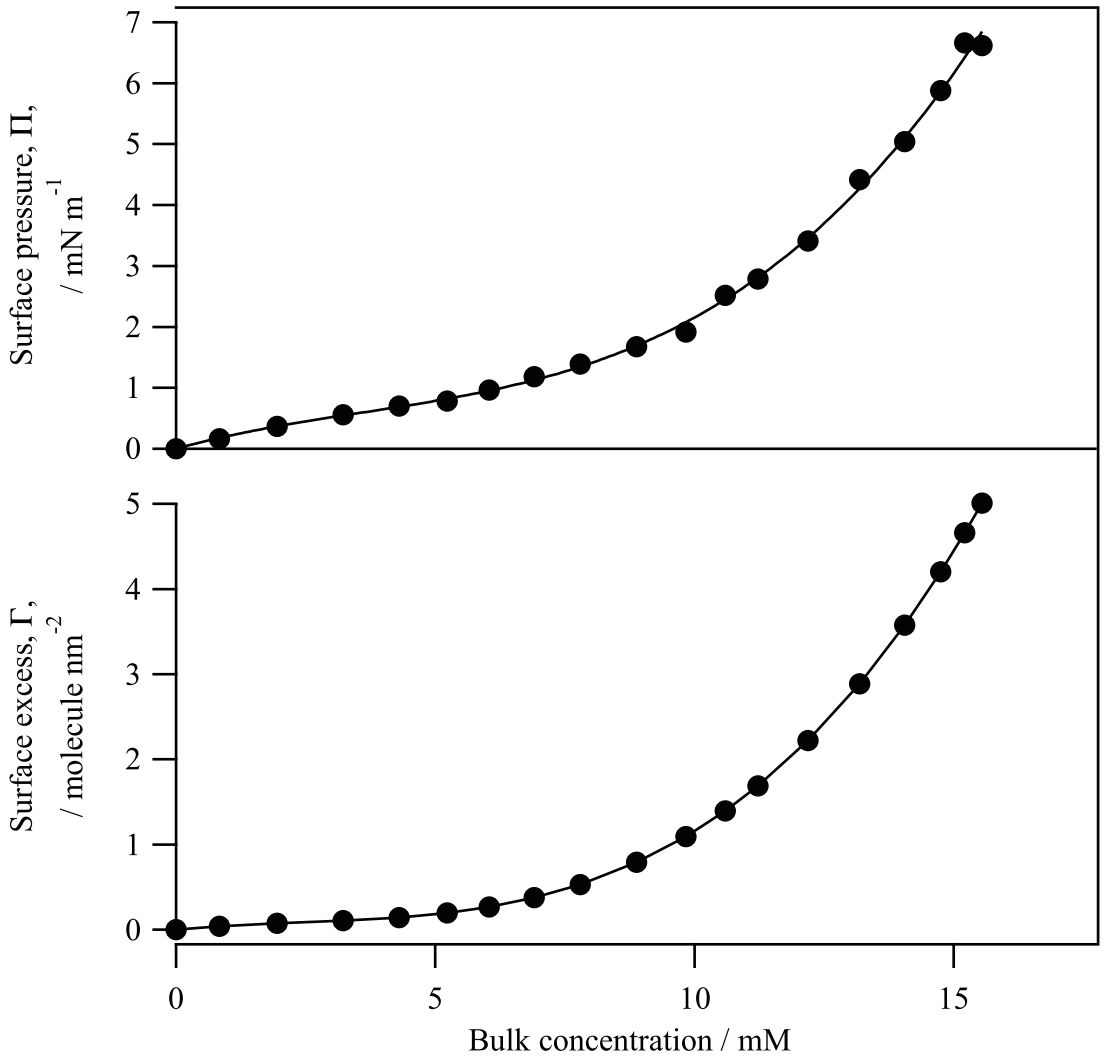

Figure 4.4: (a) Surface pressure, Π, and (b) surface excess, Γ, of the air/indole aqueous solution interface at various bulk concentration.

Air/neat water interface

Since water is not surface active, its concentration at the interface can be estimated from its bulk concentration. The density of bulk water is 1 g mL^{-1}, which corresponds to 33 molecules nm^{-3}. At the interface, the density is expected to be about the half of this bulk value, corresponding to 16 molecules nm^{-3}. Then, assuming that the thickness of the interface layer is 1 nm [70], the number of water molecules per unit surface area is estimated to be 16 molecules nm^{-2}.

Air/indole solution interface

Unlike water, indole is expected to be surface active, and the concentration of indole molecules at the interface cannot be deduced from the bulk concentration. The molecular concentration at the interface (the number of molecules per unit surface area) is called the surface excess, and it can be evaluated from the surface pressure of this interface.

Surface excess, Γ [molecules nm^{-2}], is related to the surface pressure, Π [mN m^{-1}], as [5]

$$\Gamma = \frac{c_M}{RT}\frac{\partial \Pi}{\partial c_M}. \tag{4.5}$$

Here, c_M [mM] is the bulk concentration, $R = 8.31$ J K^{-1} mol^{-1} is the gas constant, and T [K] is the temperature. This equation shows that the surface excess can be determined from the surface pressure at various bulk concentrations.

Fig. 4.4(a) shows the experimentally obtained surface pressure data at various bulk concentrations. In order to evaluate the surface excess, these surface pressure data were first fitted to a third-order polynomial of the bulk concentration, c_M [mM].

$$\Pi = \sum_{n=0}^{3} a_n c_M^n = 0.24 c_M - 0.030 c_M^2 + 0.0027 c_M^3 \quad [\mathrm{mN\,m^{-1}}]. \tag{4.6}$$

Using this analytical formula of the surface pressure, Π, the derivative $\partial\Pi/\partial c_M$ was evaluated, and the surface excess was expressed as the function of the bulk concentration.

$$\Gamma = \frac{1}{RT}\sum_{n=0}^{3} a_n n c_M^n = 0.058 c_M - 0.014 c_M^2 + 0.0020 c_M^3 \quad [\text{molecules nm}^{-2}]. \tag{4.7}$$

The result shows that the surface excess of indole is > 5 molecules nm^{-2} at $c > 15$ mM.

If the thickness of the interface is 1 nm, 5 molecules nm^{-2} corresponds to the concentration of 8 M. This is 5×10^2 times higher than the bulk concentration (15 mM), and it shows the high surface activity of indole.

4.3.2 Estimated number of generated electrons

The number of electrons generated at the interface can be estimated from the number of photons absorbed by the molecules in the interface layer and the quantum yield of ionization. Shown below is the estimation done for the electrons generated by the ionization of indole at the air/indole solution interface. This estimation was not done for the electrons generated by the two-photon ionization of water at the air/neat water interface, because the probability of two-photon absorption is strongly dependent on the temporal and spatial profile of the pump light, making the accurate estimation extremely difficult.

First, the absorbance, A, due to the indole molecules within the interface layer is determined following the Beer-Lambert law [5].

$$A = \varepsilon c_M \ell. \tag{4.8}$$

Here, ε is the molar absorption coefficient of indole, c_M is the molecular concentration of indole within the interface layer, and ℓ is the thickness of the interface layer. Molar absorption coefficient of indole can be estimated from the UV-vis absorption measurement in the bulk solution shown in Fig. 4.5. From this spectrum, the molar absorption coefficient at 267 nm is determined to be $\varepsilon = 4730$ L mol^{-1}

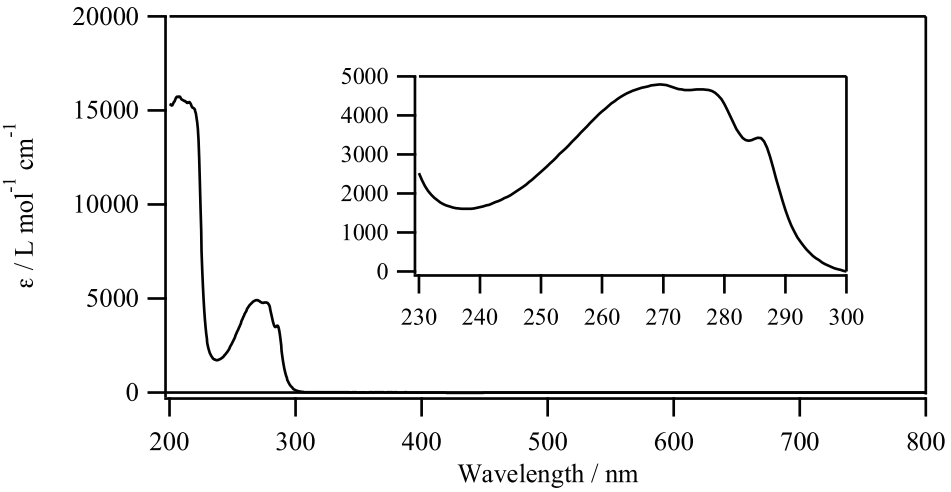

Figure 4.5: UV-vis absorption spectrum of indole dissolved in water.

$\mathrm{cm}^{-1} = 7.86 \times 10^{-4}$ molecules^{-1} nm^2. Strictly speaking, the molar absorption coefficient of indole at the air/water interface may be different from that in the bulk water because of the difference in the solvation environment. In this rough estimation, however, it should be acceptable to assume that the molar absorption coefficient is identical for the two cases. Meanwhile, the concentration, which is the number of molecules per unit volume, is obtained from the surface excess, $\Gamma \sim 5$ molecules nm^{-2}, corresponding to the number of molecules per unit surface area, and the thickness of the interface, ℓ.

$$c_M = \frac{\Gamma}{\ell}. \tag{4.9}$$

Using these formulae, the absorbance of the surface layer can be determined as

$$A = \varepsilon \frac{\Gamma}{\ell} \ell = \varepsilon \Gamma = 3.9 \times 10^{-3}. \tag{4.10}$$

Next, the number of irradiated and absorbed photons in the UV pump light is estimated. The number of irradiated photons is determined by the pulse energy and the beam diameter on the sample surface. For the transient measurement at the air/indole solution interface, the pulse energy of the pump light was $p = 5$ μJ pulse^{-1}. In terms of the number of photons, this corresponds to $\frac{p}{h\nu} = \frac{p\lambda}{hc}$ photons pulse^{-1}. Here, h is the Planck constant, c is the speed of light, and ν and λ are the frequency and the wavelength of the pump light, respectively. Assuming that the beam diameter was $d = 500$ μm, the number of irradiated photons per unit surface area, N_i, is

$$N_i = \frac{p\lambda}{hc} \frac{1}{\pi (d/2)^2} = 37 \text{ photons nm}^{-2} \text{ pulse}^{-1}. \tag{4.11}$$

Combining this value with the absorbance evaluated in the previous paragraph, the number of absorbed photons can be calculated. In terms of the number of incident photons, N_i, and the transmitted photons, N_f, the absorbance is defined as

$$A = -\log_{10} \frac{N_f}{N_i}. \tag{4.12}$$

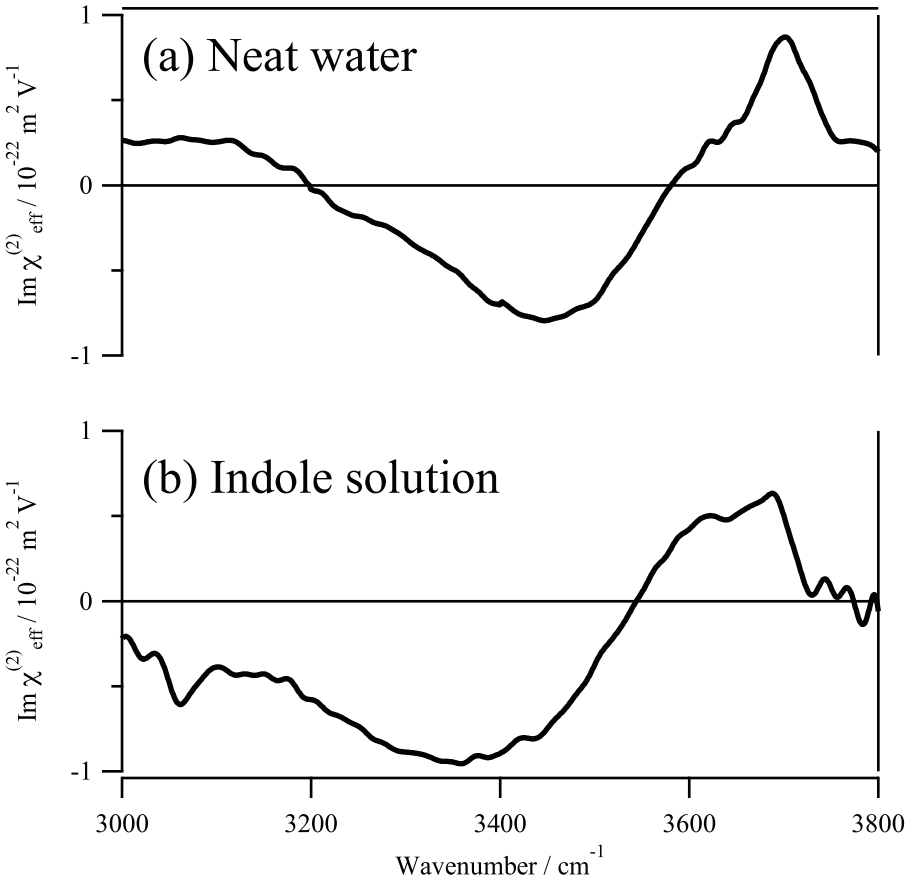

Figure 4.6: Steady-state Im $\chi^{(2)}_{\text{eff}}$ spectra of (a) the air/neat water and (b) the air/indole solution interfaces.

Hence, the number of the absorbed photons, ΔN, is

$$\Delta N = N_i - N_f = N_i \left\{ 1 - e^{-(\ln 10)A} \right\} \simeq (\ln 10) N_i A \tag{4.13}$$

$$= 0.33 \text{ photons nm}^{-2} \text{ pulse}^{-1}. \tag{4.14}$$

This is equal to the number of photo-excited indole molecules.

Finally, the number of generated electrons is obtained by multiplying the quantum yield of ionization to this value. The quantum yield of ionization for indole in the bulk aqueous solution is reported to be $\phi = 0.27$ [71]. Assuming that the quantum yield at the interface is the same as that in the bulk, the number of generated electron is estimated to be ~ 0.1 electron nm^{-2} pulse^{-1}.

4.3.3 Steady-state spectra

Air/neat water interface

The steady-state Im $\chi^{(2)}_{\text{eff}}$ spectrum of the air/neat water interface is shown in Fig. 4.6(a). The Im $\chi^{(2)}_{\text{eff}}$ spectrum of this interface is already reported by several groups [19, 72], and the present result is in agreement with those previous works. In this spectrum, three bands assigned to the OH stretch modes of different species are observed: the positive band at 3700 cm^{-1} is assigned to the free OH, the negative

band around 3400 cm^{-1} is assigned to the hydrogen bonded water, and the positive band at 3100 cm^{-1} is assigned to the pair of strongly hydrogen bonded water molecules [24, 73].

Air/indole solution interface

The steady-state Im $\chi^{(2)}_{\text{eff}}$ spectrum of the air/indole aqueous solution interface is shown in Fig. 4.6(b). With a broad negative band around 3400 cm^{-1} and a narrower positive band near 3700 cm^{-1}, the overall shape of the Im $\chi^{(2)}_{\text{eff}}$ spectrum of this interface was found to be similar to that of the air/neat water interface. However, several differences need to be noticed. First of all, the positive band near 3700 cm^{-1} is broader than that observed at the air/neat water interface. In fact, the positive band seems to be comprised of a narrow free OH band at 3700 cm^{-1} and a broader band near 3600 cm^{-1}. The appearance of a similar broad and positive band near 3600 cm^{-1} is reported at the air/water interface with a lipid monolayer, and the authors of this previous work assigned this broad band to the OH stretch mode of water molecules in the hydrophobic environment surrounded by the alkyl chains of the lipids [74]. Based on the similarity of the peak position and the spectral pattern, the positive broad band near 3600 cm^{-1} in Fig. 4.6(b) can be assigned to the OH stretch mode of water molecules interacting with the hydrophobic part of indole molecules. Secondly, the positive feature observed at the air/neat water interface below 3200 cm^{-1} is absent. This indicates that the hydrogen bonding network of water molecules at the interface is greatly perturbed. Thirdly, a sharp negative band was observed at 3064 cm^{-1}. This frequency corresponds to the aromatic CH stretch mode, and the band can be assigned to the CH stretch vibration of indole at the interface [75]. These three points all indicate that the sample surface is strongly affected by the presence of indole, which is consistent with the large surface excess of indole molecules estimated from the surface pressure measurement.

4.3.4 Transient spectra

Transient spectra at the air/neat water interface

The Im $\Delta\chi^{(2)}_{\text{eff}}$ spectra of the air/neat water interface are shown in Fig. 4.7(a). A positive transient band appeared almost instantaneously after the photo-excitation by the pump light, and it mostly decayed within 100 ps. The decay process was monotonous, and no appreciable spectral changes were observed. This behavior indicates that the entire set of transient spectra can be represented by only one transient component.

In order to determine the spectrum of this single transient component, all the transient spectra at various delays were added together and averaged. The averaged spectrum in Fig. 4.8(a) shows a positive transient band at 3270 cm^{-1}. The temporal change of this transient component was obtained by plotting the integrated intensity of the Im $\Delta\chi^{(2)}_{\text{eff}}$ spectra at each delay. As shown in Fig. 4.8(b), it shows a very quick rise within 500 fs and a slower decay on the 10 ps time scale.

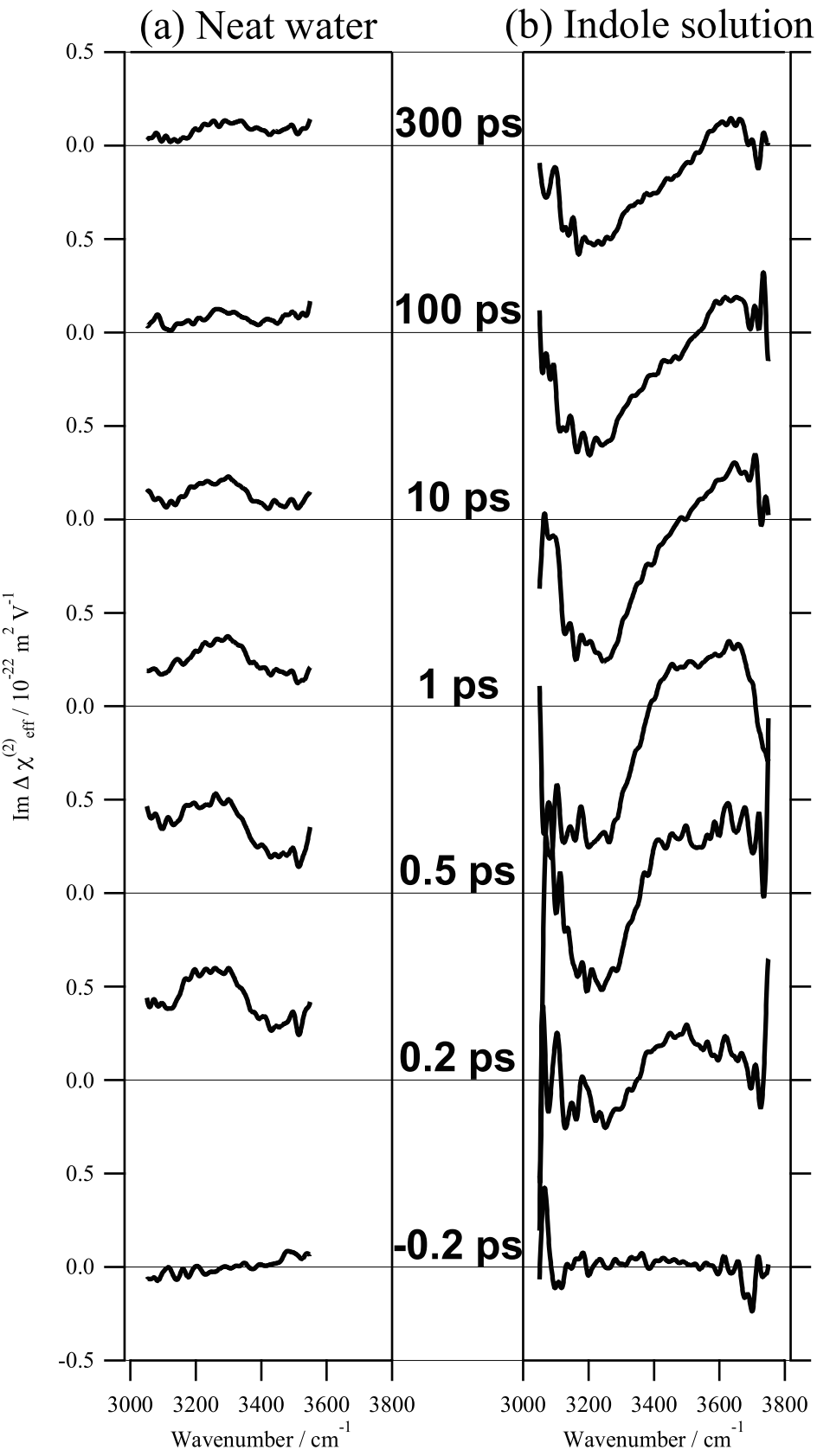

Figure 4.7: Time-resolved Im $\chi^{(2)}_{\mathrm{eff}}$ spectra (Im $\Delta\chi^{(2)}_{\mathrm{eff}}$) of (a) the air/neat water and (b) the air/indole solution interfaces.

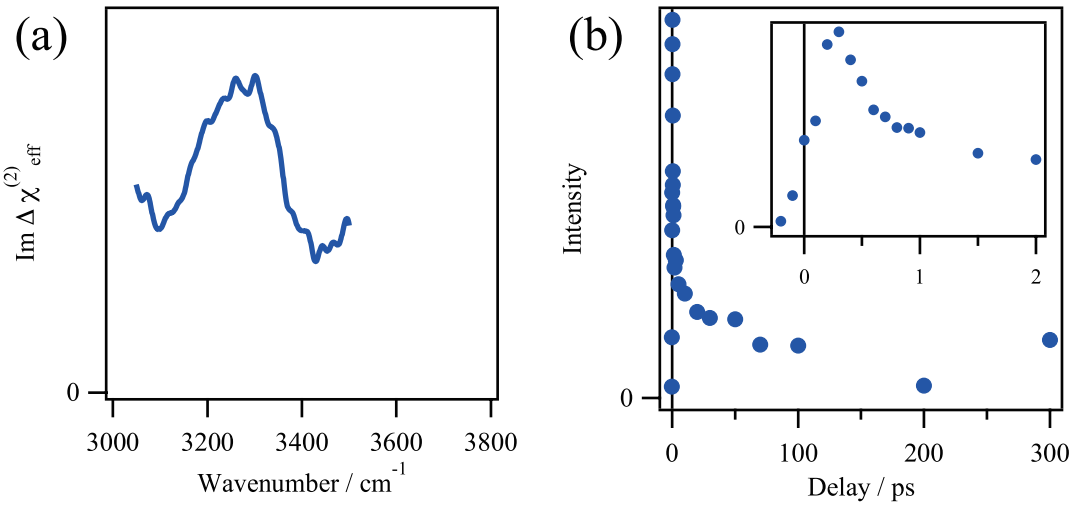

Figure 4.8: The transient component observed at the air/neat water interface. (a) Spectrum. (b) Temporal behavior. The inset shows the close-up view in the early delay.

Transient spectra at the air/indole solution interface

The Im $\Delta\chi^{(2)}_{\mathrm{eff}}$ spectra of the air/indole aqueous solution interface are shown in Fig. 4.7(b). Compared with the air/neat water interface, more complicated spectral changes were observed at this interface. The transient spectra show a negative band at 3230 cm^{-1} and a positive feature around 3500 cm^{-1}. While the overall positive and negative features persist for more than 300 ps, the positive feature shows a significant spectral change in the first 100 ps, i.e. the lower side of the positive band disappears and the band becomes much narrower in width. Meanwhile, for the delay later than 100 ps, the transient spectra no longer show any change. This result suggests that some dynamics takes place in the first 100 ps, and when the dynamics completes, only a long-lived transient species remains at the interface. The spectra at later delays (100 ps or later) can be interpreted as the spectrum of this long-lived transient species.

There are two possible causes for the spectral change in the early delay. First possibility is that it is due to the structural deformation of the transient species into its final more stable structure. In this case, the spectra would show a gradual change, e.g. the gradual peak shift of a band. As the second possibility, it may be caused by the depletion of a short-lived transient species. In this case, the band assigned to this species would simply decay without changing the spectral shape. In order to clarify the cause of the observed spectral change in the first 100 ps, the spectra at 100, 150, 200, 250, and 300 ps were averaged (Fig. 4.9(a)), and the averaged spectrum was subtracted from all the transient spectra later than 0.5 ps. The result is shown in Fig. 4.9(b). The subtracted spectra show that one positive band near 3400 cm^{-1} decays monotonously without any change of the spectral pattern. It can be concluded from this analysis that the observed spectral change results from the depletion of a transient species, and it is not due to the gradual structural change of a transient species.

The analysis described in the previous paragraph indicates that the transient spectra are comprised of

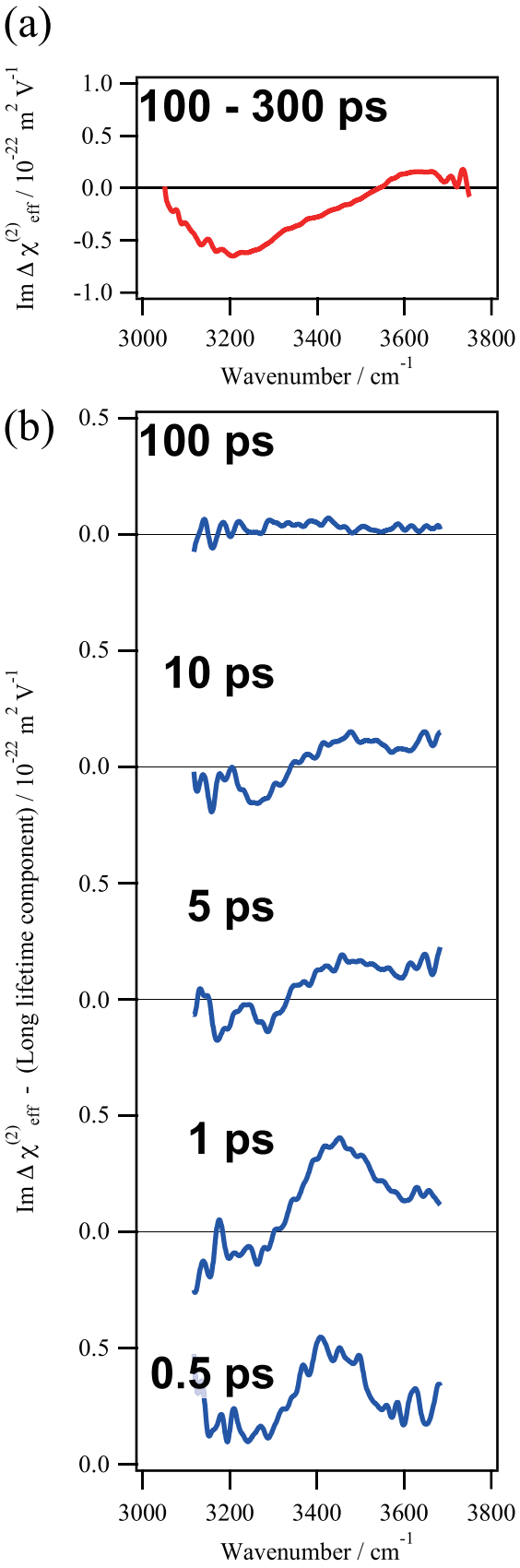

Figure 4.9: Analysis of the Im $\Delta\chi^{(2)}_{\mathrm{eff}}$ spectra at the air/indole solution interface. (a) The Im $\Delta\chi^{(2)}_{\mathrm{eff}}$ spectra in the later delay (100 - 300 ps) were averaged. This is interpreted as the spectrum of the long-lived species. (b) After subtracting the averaged Im $\Delta\chi^{(2)}_{\mathrm{eff}}$ shown in (a) from the Im $\Delta\chi^{(2)}_{\mathrm{eff}}$ spectra at each delay.

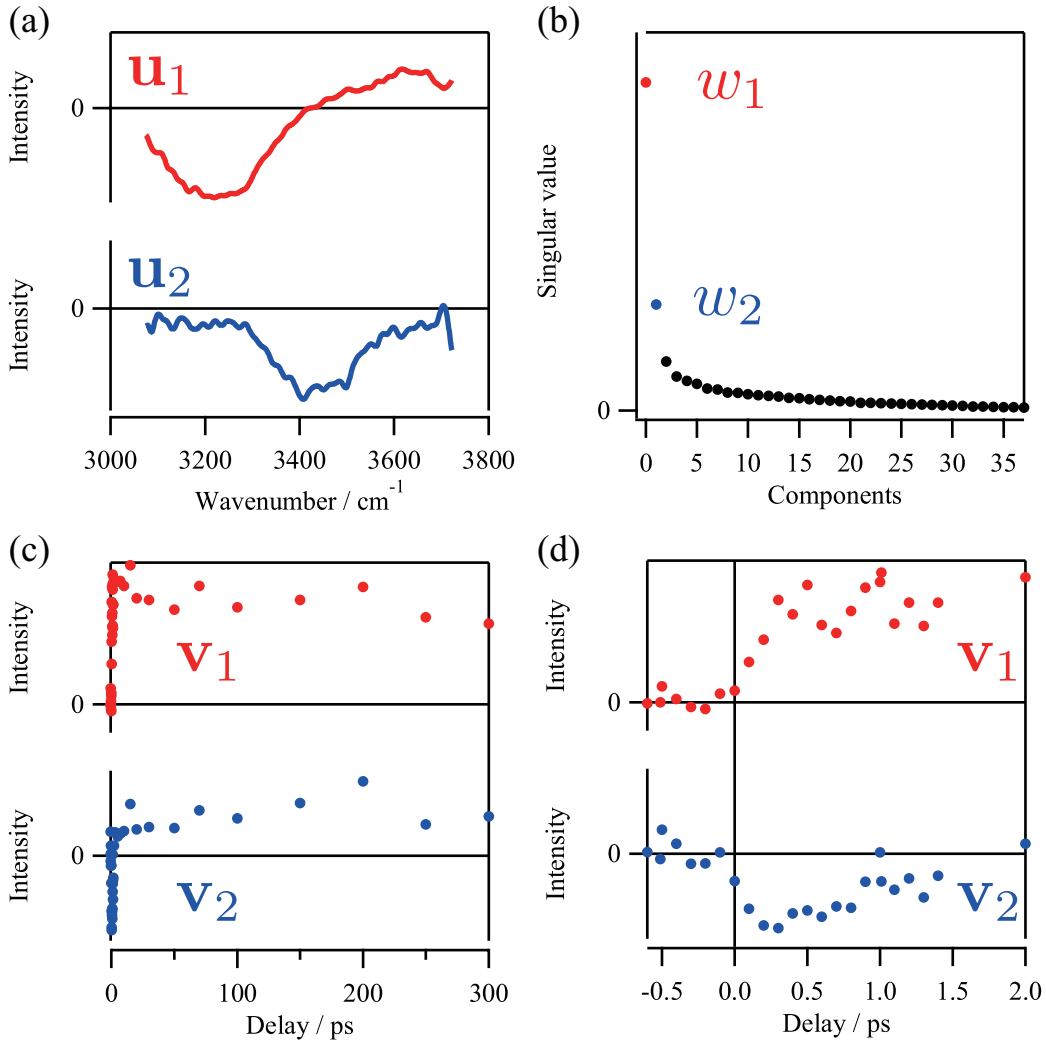

Figure 4.10: Decomposition of $\Delta\chi^{(2)}_{\mathrm{eff}}$ spectra obtained at the air/indole solution interface by the singular value decomposition (SVD) analysis. (a) Spectral components ($\mathbf{u}_1$ and $\mathbf{u}_2$). (b) Singular values ($w_1, w_2, \cdots$). (c) Temporal components ($\mathbf{v}_1$ and $\mathbf{v}_2$). (d) Close-up view of (c) in the early delay.

a long lifetime component and a short lifetime one, and that all the Im $\Delta\chi^{(2)}_{\mathrm{eff}}$ spectra can be expressed by the linear combination of these two transient components. In such a case, the singular value decomposition (SVD) analysis is a very powerful tool to analyze the transient spectra [48, 76]. To use the SVD analysis, all the $\Delta\chi^{(2)}_{\mathrm{eff}}$ spectra at various delays are first combined into one matrix denoted as M. SVD decomposes this matrix into the product of two orthogonal matrices (U and V) and a diagonal matrix (W).

$$M = UWV^{\dagger}. \tag{4.15}$$

Using the vector notation, this can be equivalently expressed as

$$\begin{pmatrix} \mathbf{m}_1 & \mathbf{m}_2 & \cdots \end{pmatrix} = \begin{pmatrix} \mathbf{u}_1 & \mathbf{u}_2 & \cdots \end{pmatrix} \begin{pmatrix} w_1 & 0 & \\ 0 & w_2 & \\ & & \ddots \end{pmatrix} \begin{pmatrix} \mathbf{v}_1^{\dagger} \\ \mathbf{v}_2^{\dagger} \\ \vdots \end{pmatrix} \tag{4.16}$$

$$= \sum_i w_i \mathbf{u}_i \mathbf{v}_i^\dagger. \tag{4.17}$$

Here, $\mathbf{m}_i$ is the experimentally obtained $\Delta\chi^{(2)}_{\text{eff}}$ spectra at each delay, $\mathbf{u}_i$ is the spectral component, $\mathbf{v}_i$ is the temporal component, and w_i is called the singular value. It is evident from the final expression that the decomposed component has a meaningful contribution to the original transient spectra $\left(\Delta\chi^{(2)}_{\text{eff}}\right)$ only when its singular value is large.

Applying this method to the present experimental data at the air/indole solution interface, the $\Delta\chi^{(2)}_{\text{eff}}$ spectra were decomposed as shown in Fig. 4.10. The singular values in Fig. 4.10(b) shows that the first two values (w_1 and w_2) are much larger than the rest of the singular values, indicating that the observed Im $\Delta\chi^{(2)}_{\text{eff}}$ spectra can be reproduced by taking the linear combination of only the first two components in this spectral decomposition. Hence, it is possible to make the following approximation.

$$\begin{pmatrix}\mathbf{m}_1 & \mathbf{m}_2 & \cdots\end{pmatrix} \simeq \begin{pmatrix}\mathbf{u}_1 & \mathbf{u}_2\end{pmatrix} \begin{pmatrix} w_1 & 0 \\ 0 & w_2 \end{pmatrix} \begin{pmatrix} \mathbf{v}_1^\dagger \\ \mathbf{v}_2^\dagger \end{pmatrix} \tag{4.18}$$

$$= \begin{pmatrix} w_1\mathbf{u}_1 & w_2\mathbf{u}_2 \end{pmatrix} \begin{pmatrix} \mathbf{v}_1^\dagger \\ \mathbf{v}_2^\dagger \end{pmatrix} \tag{4.19}$$

$$\equiv \begin{pmatrix}\tilde{\mathbf{u}}_1 & \tilde{\mathbf{u}}_2\end{pmatrix} \begin{pmatrix} \mathbf{v}_1^\dagger \\ \mathbf{v}_2^\dagger \end{pmatrix}. \tag{4.20}$$

Here, $\tilde{\mathbf{u}}_i \equiv w_i\mathbf{u}_i$ was defined to simplify the expression.

The spectral decomposition shown above is a purely mathematical result, and the obtained components do not have any physical significance by itself. For example, the time profile of the second component ($\mathbf{v}_2$ in Fig. 4.10(c) and (d)) shows that its contribution is initially negative but finally converges to a positive value, which is not physically reasonable. The physically meaningful transient spectra and time profile of the actual transient chemical species can be obtained by taking an appropriate linear combination of these two components. In the linear algebra, this can be expressed by using a transformation matrix,

$$C = \begin{pmatrix} c_{11} & c_{12} \\ c_{21} & c_{22} \end{pmatrix}, \tag{4.21}$$

as

$$\begin{pmatrix}\mathbf{m}_1 & \mathbf{m}_2 & \cdots\end{pmatrix} \simeq \begin{pmatrix}\tilde{\mathbf{u}}_1 & \tilde{\mathbf{u}}_2\end{pmatrix} \begin{pmatrix} c_{11} & c_{12} \\ c_{21} & c_{22} \end{pmatrix}^{-1} \begin{pmatrix} c_{11} & c_{12} \\ c_{21} & c_{22} \end{pmatrix} \begin{pmatrix} \mathbf{v}_1^\dagger \\ \mathbf{v}_2^\dagger \end{pmatrix} \tag{4.22}$$

$$\equiv \begin{pmatrix}\tilde{\mathbf{u}}'_1 & \tilde{\mathbf{u}}'_2\end{pmatrix} \begin{pmatrix} \mathbf{v}_1'^\dagger \\ \mathbf{v}_2'^\dagger \end{pmatrix}. \tag{4.23}$$

Here, the physically meaningful spectral components ($\tilde{\mathbf{u}}'_1$ and $\tilde{\mathbf{u}}'_2$) and temporal components ($\tilde{\mathbf{v}}'_1$ and $\tilde{\mathbf{v}}'_2$) are defined as

$$\begin{pmatrix}\tilde{\mathbf{u}}'_1 & \tilde{\mathbf{u}}'_2\end{pmatrix} \equiv \begin{pmatrix}\tilde{\mathbf{u}}_1 & \tilde{\mathbf{u}}_2\end{pmatrix} \begin{pmatrix} c_{11} & c_{12} \\ c_{21} & c_{22} \end{pmatrix}^{-1}, \tag{4.24}$$

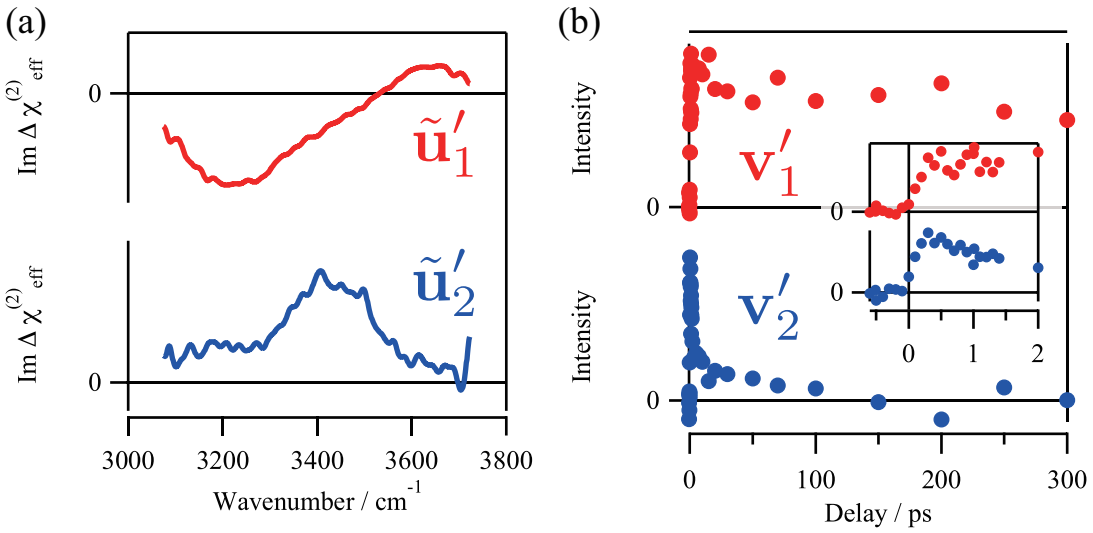

Figure 4.11: Physically meaningful transient components at the air/indole solution interface reconstructed after the SVD analysis. (a) Spectral components ($\tilde{\mathbf{u}}'_1$ and $\tilde{\mathbf{u}}'_2$). (b) Temporal components ($\mathbf{v}'_1$ and $\mathbf{v}'_2$).

$$\begin{pmatrix} \mathbf{v}'^{\dagger}_1 \\ \mathbf{v}'^{\dagger}_2 \end{pmatrix} \equiv \begin{pmatrix} c_{11} & c_{12} \\ c_{21} & c_{22} \end{pmatrix} \begin{pmatrix} \mathbf{v}^{\dagger}_1 \\ \mathbf{v}^{\dagger}_2 \end{pmatrix}. \tag{4.25}$$

In order to determine the transformation matrix, C, some assumptions are necessary. For the present case, it is possible to make an assumption about the time profile of the transient species. The qualitative discussion given earlier in this section suggested that there are a long-lived species (Fig. 4.9(a)) and a short-lived one (Fig. 4.9(b)). This can be made more quantitative based on the temporal components obtained in the SVD analysis (Figs. 4.10(c) and (d)): $\mathbf{v}_1$ is constant without any decay after 1 ps, and the decay observed in $\mathbf{v}_2$ is complete within 100 ps. Hence, it is possible to assume that the long lifetime component does not show any change after 1 ps and that the short lifetime component completely decays within 100 ps. Mathematically, this can be expressed as

$$\begin{pmatrix} \mathbf{v}'^{\dagger}_1 \\ \mathbf{v}'^{\dagger}_2 \end{pmatrix} \equiv \begin{pmatrix} c_{11}\mathbf{v}^{\dagger}_1 + c_{12}\mathbf{v}^{\dagger}_2 \\ c_{21}\mathbf{v}^{\dagger}_1 + c_{22}\mathbf{v}^{\dagger}_2 \end{pmatrix} \simeq \begin{pmatrix} \text{No change after 1 ps.} \\ \text{Completely zero after 100 ps.} \end{pmatrix}. \tag{4.26}$$

Under these assumptions, the coefficients for the linear combination can be determined in the least square manner.

$$C^{-1} = \begin{pmatrix} 1.07 & -0.09 \\ 1.23 & -1.63 \end{pmatrix}, \qquad C = \begin{pmatrix} 1.00 & -0.06 \\ 0.76 & -0.66 \end{pmatrix} \tag{4.27}$$

Using these coefficients, the physically meaningful spectral and temporal components of the actual transient species can be finally determined. The obtained result is shown in Fig. 4.11.

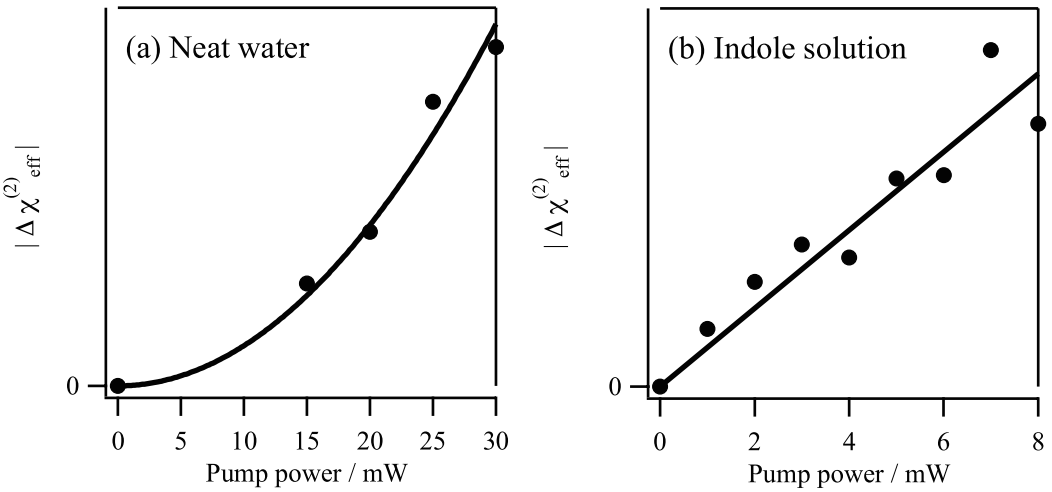

Figure 4.12: Pump power dependence of the transient signal intensity. (a) $|\Delta\chi^{(2)}_{\mathrm{eff}}|$ of the air/neat water interface at 1 ps delay. The solid line shows the fit to a quadratic function (I_{neat}). (b) $|\Delta\chi^{(2)}_{\mathrm{eff}}|$ of the air/indole solution interface at 10 ps delay. The solid line shows the fit to a linear function (I_{indole}).

4.3.5 Pump power dependence

Before discussing the assignment of the observed transient components, it is necessary to confirm that the transient species are really generated as expected following the reaction schemes shown below.

$$\mathrm{H_2O} \xrightarrow{2h\nu,\mathrm{H_2O}} \mathrm{OH} + \mathrm{H_3O^+} + e^-(\mathrm{H_2O})_n \tag{4.28}$$

$$\text{indole} \xrightarrow{h\nu} \mathrm{S_1}\ \text{indole} \xrightarrow{\mathrm{H_2O}} (\text{indole cation})^+ + e^-(\mathrm{H_2O})_n \tag{4.29}$$

This can be checked by evaluating the pump power dependence of the transient bands. Because the electrons are generated by the two-photon absorption of the pump light at the air/neat water interface, a quadratic pump power dependence is expected at this interface. Meanwhile, a linear power dependence is expected at the air/indole solution interface because the ionization takes place by the one-photon absorption.

Experimentally, $\Delta\chi^{(2)}_{\mathrm{eff}}$ spectra were measured with various pump power at the two interfaces, and the power dependence of $|\Delta\chi^{(2)}_{\mathrm{eff}}|$ was plotted as shown by the filled circles in Fig. 4.12. In these measurements, the delay of the pump light was fixed at 1 ps for the air/neat water interface and at 10 ps for the air/indole solution interface. It is to be noted that the pump light is more tightly focused at the air/neat water interface than at the air/indole solution interface to increase the probability of the two-photon absorption, which means that the photon density is higher at the former interface when the pump power is the same.

To analyze the pump power dependence, the power dependence at the air/neat water interface was fitted by a quadratic function (I_{neat}), and the power dependence at the air/indole solution interface was fitted by a linear function (I_{indole}).

$$I_{\mathrm{neat}}(p) = A_{\mathrm{neat}}p^2, \tag{4.30}$$

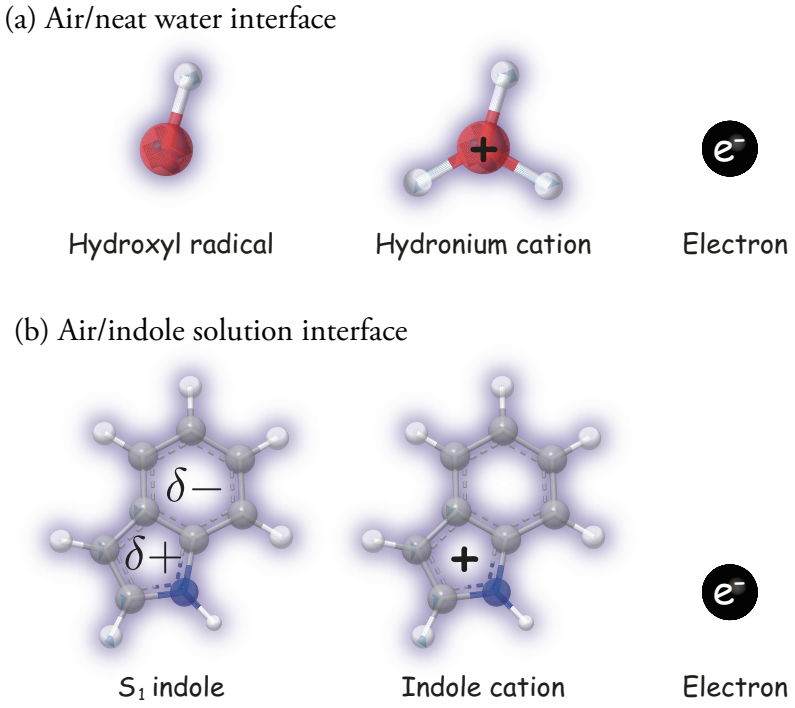

Figure 4.13: Transient species generated at (a) the air/neat water interface and (b) the air/indole solution interface.

$$I_{\mathrm{indole}}(p) = A_{\mathrm{indole}} p. \tag{4.31}$$

Here, p is the pump power, and A_{neat} and A_{indole} are the fitting parameters. The result of the fit is shown by the solid lines in Fig. 4.12. As can be seen from the figure, the experimental data points are well fitted by these functions, confirming that the observed transient species are generated by the two-photon absorption of the pump light at the air/neat water interface and by the one-photon absorption at the air/indole solution interface. These results strongly indicate that the transient species are generated by the reaction scheme shown at the begining of this section.

When the pump power became higher than the ones shown in Fig. 4.12, the observed $|\Delta\chi^{(2)}_{\mathrm{eff}}|$ deviated from the fitting curve, and the saturation effect was observed. For the acquisition of the transient spectra shown in Fig. 4.7, the pump power was 25 mW for the air/neat water interface and 5 mW for the air/indole solution interface, both of which are low enough to avoid the potential complication due to the saturation effect.

4.3.6 Assignment of the transient bands

As confirmed by the pump power dependence, the observed transient spectra are due to the two-photon ionization of water at the air/neat water interface and the one-photon ionization of indole at the air/indole solution interface. Hence, with the pump light irradiation, hydroxyl radical (OH), hydronium cation (H_3O^+), and electron (e^-) are generated at the air/neat water interface, and S_1 indole, indole cation, and electron (e^-) are generated at the air/indole solution interface. These transient species are figuratively

shown in Fig. 4.13.

Through the analysis of the Im $\Delta\chi^{(2)}_{\rm eff}$ spectra shown in Fig. 4.7, it was seen that one transient component exists at the air/neat water interface (Fig. 4.8) and two transient components exist at the air/indole solution interface (Fig. 4.11). Among these three, the transient component at the air/neat water interface (Fig. 4.8) and the short lifetime component at the air/indole solution interface ($\tilde{\mathbf{u}}'_2$ and $\mathbf{v}'_2$ in Fig. 4.11) show a remarkable similarity: Both spectra show positive and relatively narrow band, and the kinetics is almost identical. Because the electron is the only transient species that exists in common at the two interfaces, it is highly likely that both of these two components are related to the electron. In fact, as can be seen from Fig. 4.13, the other transients at the air/indole solution interface (S_1 indole and indole cation) are much bulkier than those at the air/neat water interface (OH and H_3O^+), and it is difficult to think that they show the same kinetics. Hence, it is possible to conclude that the electron is responsible for these two transient components. To be more precise, since the observed bands are in the OH stretch region (3270 $\rm cm^{-1}$ at the air/neat water interface and 3430 $\rm cm^{-1}$ at the air/indole solution interface), they must be assigned to the OH stretch mode of the water molecules interacting with an electron. The cause of the difference in the observed peak frequencies at the two interfaces will be discussed later.

Next, the assignment of the long lifetime component observed at the air/indole solution interface ($\tilde{\mathbf{u}}'_1$ and $\mathbf{v}'_1$ in Fig. 4.11) is discussed. Since the decay of the short lifetime component ($\mathbf{v}'_2$ in Fig. 4.11) is not accompanied by the rise of the long lifetime one ($\mathbf{v}'_1$ in Fig. 4.11), the short lifetime component is not the precursor of the long lifetime component, and these two should be considered to be completely independent from each other. Hence, because the short lifetime component is already ascribed to electron, the long lifetime component at the air/indole solution must be related to S_1 indole or to indole cation. The observation of a positive Im $\Delta\chi^{(2)}_{\rm eff}$ band at 3600 $\rm cm^{-1}$ in Fig. 4.11(a) ($\tilde{\mathbf{u}}'_1$) means that the Im $\chi^{(2)}_{\rm eff}$ band assigned to the OH stretch mode of water molecules in the hydrophobic environment (see Fig. 4.6(b)) is intensified. As shown in Eq. (2.69), $\chi^{(2)}$ is expressed by the following formula.

$$\chi^{(2)}_{IJK} = \frac{N}{\varepsilon_0}\sum_{i,j,k}\langle R_{Ii}R_{Jj}R_{Kk}\rangle_{\rm av}\beta_{ijk}. \tag{4.32}$$

This formula shows that there are three possible causes for the intensification of Im $\chi^{(2)}_{\rm eff}$ at 3600 $\rm cm^{-1}$. First possibility is that the number of water molecules in the hydrophobic region increased (N became large). This hypothesis, however, is not plausible, because the hydrophobic region should decrease when the polar transient species (S_1 indole, indole cation, and electron) are generated by the ionization. Second possibility is that the value of hyperpolarizability for the OH stretch mode increased (β becomes large). The quantum mechanical expression of β is given in Eq. (2.61) as

$$\beta_{ijk} = \sum_{s,v}\frac{\langle g|\hat{\mu}_i|s\rangle\langle s|\hat{\mu}_j|v\rangle\langle v|\hat{\mu}_k|g\rangle}{(\varepsilon_v-\varepsilon_g-\hbar\omega_2-i\gamma_{vg})(\varepsilon_s-\varepsilon_g-\hbar\omega_3-i\gamma_{sg})}. \tag{4.33}$$

As can be seen from this formula, β_{ijk} may become significantly large when the sum frequency light becomes resonant with an electronic state of the system, i.e. if $\varepsilon_s - \varepsilon_g \simeq \hbar\omega_3 \sim 650$ nm. Water itself does not have an energy level near $\hbar\omega_3$, and β_{ijk} for the OH stretch mode of water is usually not very large. Meanwhile, indole cation and S_1 indole both have an energy level near $\hbar\omega_3$ (In the bulk water, indole cation has an absoprtion near 580 nm, and S_1 indole has an absorption in the entire visible region [54].), and if the interaction between water and S_1 indole or indole cation is strong enough to cause the intermolecular mixing of the electronic states, β_{ijk} of the OH stretch mode may be enhanced by virtue of those electronic states. Such an intermolecular mixing of the electronic states involving vibronic coupling or Fano resonance is reported in the literature [9, 77]. By these mechanisms, however, it is difficult to account for the observed vibrational resonance of 3600 cm^{-1}. These mechanisms require that the detected OH group interact strongly enough with indole cation or S_1 indole to perturb the electronic state of those species, which is likely to shift the vibrational frequency of the OH stretch mode. Meanwhile, the observed peak frequency of the positive transient band is identical to that found in the steady-state spectrum, which is characteristic of the OH stretch mode of water molecules in the hydrophobic environment. Hence, this hypothesis is incompatible with the observed vibrational frequency. Third possibility is that Im $\chi^{(2)}_{\rm eff}$ became large because of the improved orientation of water molecules ($\langle R_{Ii}R_{Jj}R_{Kk}\rangle_{\rm av}$ became large). This can be caused by the positive charge of indole cation. Based on this hypothesis, the positive transient band can be interpreted as the OH stretch mode of water molecules existing above indole cation and more up oriented due to the positive charge. Negative transient band near 3200 cm^{-1} is due to the water molecules below the indole cation that are down oriented due to the positive charge of the cation. This hypothesis is supported by the similarity between the observed transient spectrum of the long lifetime component and the steady-state spectra of the air/water interfaces with a monolayer of cationic surfactant or lipid reported in the literature [78, 79]. According to these previous studies, the peak position of the negative band ($\sim 3200\ \mathrm{cm}^{-1}$) is much lower than that of the neutral air/water interface ($\sim 3400\ \mathrm{cm}^{-1}$, Fig. 4.6) because of the Fermi resonance with the overtone of the HOH bending mode [78]. In this way, the observed spectrum of the long lifetime component can be well accounted for by this hypothesis, and it can be concluded that the long lifetime component arises from this third possibility. The assigned species is shown in Fig. 4.14.

It was shown in the previous paragraph that the indole cation also has an contribution to the observed transient spectra at the air/indole solution interface. Then, the next question is whether or not the hydonium cation (H_3O^+) is observed at the air/neat water interface. The steady-state Im $\chi^{(2)}_{\rm eff}$ spectrum of H_3O^+ at the air/water interface is reported by Tian *et al.* [80]. They observed a broad negative band below 3500 cm^{-1}, which they decomposed into two contributions. According to their assignment, H_3O^+ itself gives rise to a broad negative band around 3100 cm^{-1}, while the water molecules that are down oriented because of the positive charge of H_3O^+ contribute to the negative band near 3300 cm^{-1}. The

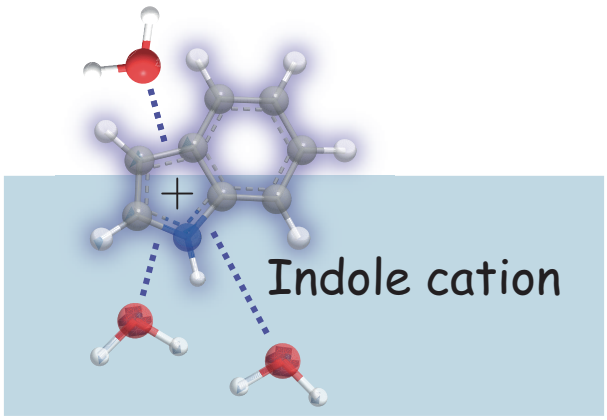

Figure 4.14: The long lifetime component observed at the air/indole solution interface is assigned to the OH stretch mode of water molecules oriented by the positive charge of indole cation. Water is "up" oriented above the indole cation, and "down" oriented below the cation.

transient spectra at the air/neat water interface obtained in the present study are clearly different from the Im $\chi^{(2)}_{\rm eff}$ spectrum of H_3O^+ reported by them. This comparison shows that H_3O^+ is not observed in the present study, probably because only a small number of H_3O^+ can be generated by the two-photon ionization of water.

In summary, the transient component at the air/neat water interface (Fig. 4.8) and the short lifetime component at the air/indole solution interface ($\tilde{\mathbf{u}}'_2$ and $\mathbf{v}'_2$ in Fig. 4.11) were assigned to the water molecules interacting with an electron ("hydrated electron"). These components decay quickly within 100 ps. Meanwhile, the long lifetime component at the air/indole solution interface ($\tilde{\mathbf{u}}'_1$ and $\mathbf{v}'_1$ in Fig. 4.11) was assigned to the water molecules interacting with an indole cation (Fig. 4.14), meaning that the indole cations remain at the air/water interface for more than 300 ps. The long lifetime of indole cation at the interface indicates that the quick decay of the former two components is not due to the recombination between the electron and the counter cation (H_3O^+ or indole cation). Instead, the decay reflects the disappearance of the electrons from the interfacial region due to their migration into the bulk.

4.3.7 Properties of hydrated electrons at the air/water interfaces

In the previous section, it was concluded that the "hydrated electrons" contribute to the observed transient spectra. More detailed picture about the interaction between the electron and the water molecules at the air/water interface can be elucidated by comparing the observed Im $\Delta\chi^{(2)}_{\rm eff}$ spectra with the vibrational spectra of water anion clusters in the gas phase and hydrated electrons in bulk water.

In the gas phase, the vibrational spectrum of water anion clusters are obtained by the vibrational predissociation spectroscopy [81]. In this experiment, the photodetached electrons following the IR light irradiation are detected.

$$(H_2O)_n^- \xrightarrow{h\nu} (H_2O)_n + e^- \tag{4.34}$$

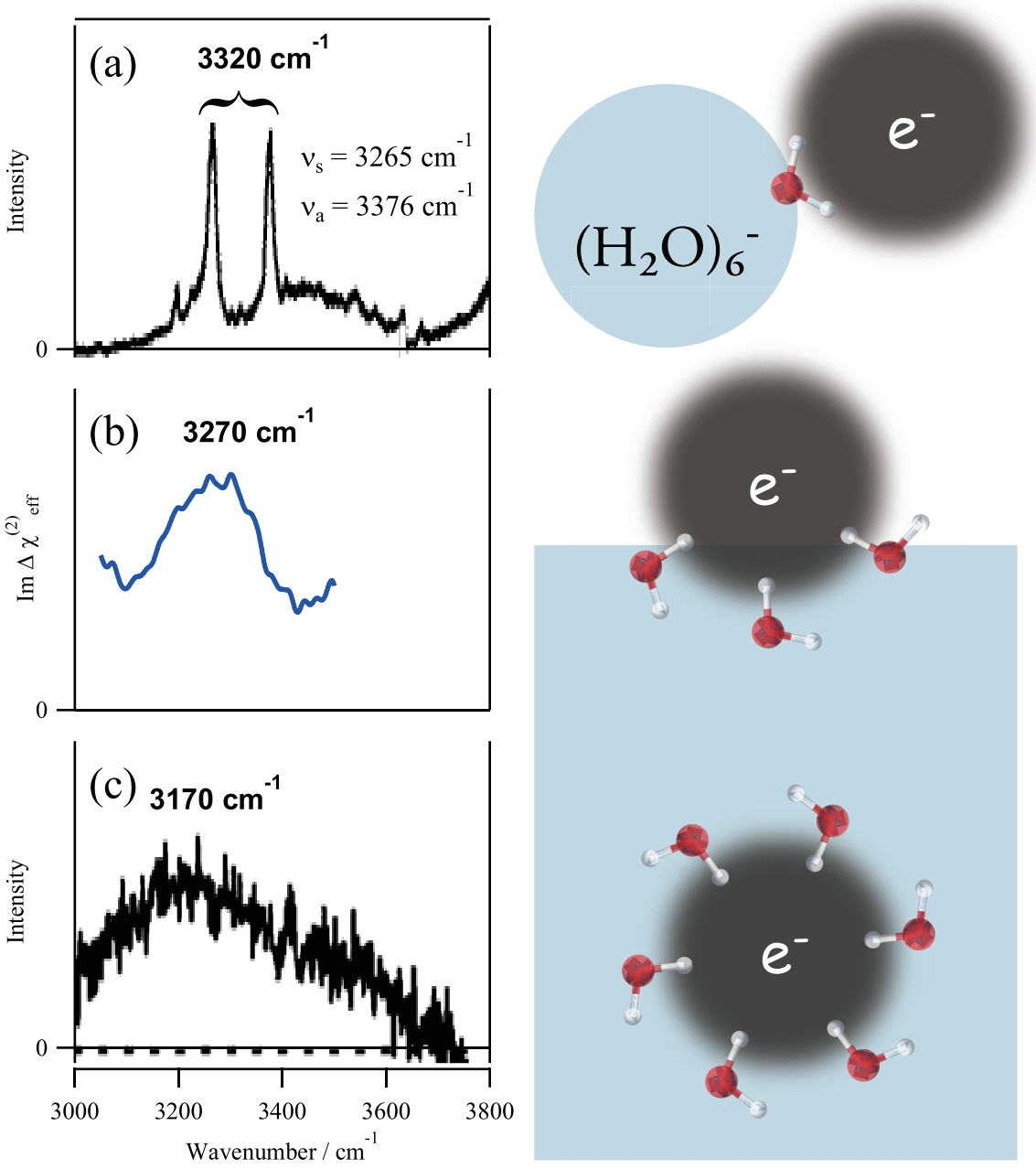

Figure 4.15: (a) Vibrational predissociation spectrum of $(H_2O)_6^-$ cluster [81]. (b) Im $\Delta\chi_{\text{eff}}^{(2)}$ spectrum of the hydrated electrons at the air/neat water interface obtained in this study. (c) Raman spectrum of the hydrated electrons in the bulk water [57]. [(a) was reprinted with permission from N. I. Hammer, J. R. Roscioli, J. C. Bopp, J. M. Headrick, and M. A. Johnson, *J. Chem. Phys.* **123**, 244311 (2005). Copyright 2005 AIP Publishing LLC. (c) was reprinted with permission from M. Mizuno and T. Tahara, *J. Phys. Chem. A* **107**, 2411 (2003). Copyright 2003 American Chemical Society.]

Because this electron detachment occurs efficiently only when the IR light is resonant with the vibrational frequencies of the anion clusters, IR spectrum can be obtained by scanning the wavelength of the IR light. Fig. 4.15(a) shows the IR spectrum of $(H_2O)_6^-$ clusters obtained by this method. According to their calculation, the excess electron is hydrated by the two OH groups of one water molecule residing at the surface of this cluster, and the observed sharp bands at 3265 and 3376 cm^{-1} are assigned to the symmetric and antisymmetric stretch modes, respectively, of that water molecule. Since the symmetric and antisymmetric stretch modes result from the mixing of the two OH stretch modes with the same vibrational frequency, the OH stretch frequency without this mixing can be estimated to be about 3320 cm^{-1}. This can be regarded as the vibrational frequency of the hydrated electron comprised of one electron and one water.

For the hydrated electrons in bulk water, vibrational spectra are measured by transient Raman spectroscopy, which takes advantage of the electronic resonance to the energy level near 720 nm [56–61]. In the OH stretch region, a very broad band centering at 3170 cm^{-1} is observed as shown in Fig. 4.15(c) [57]. It is known that an electron is solvated by six water molecules in bulk water [82], and the observed band is assigned to the OH stretch mode of these water molecules in the first solvation shell.

The Im $\Delta\chi_{\rm eff}^{(2)}$ spectra obtained at the air/neat water interface in the present study can be directly compared with these experimental data in the literature, because the molecular composition is almost identical and it is possible to think that electrons interact only with water molecules in all the three systems. Fig. 4.15(b) shows the spectrum of the transient component observed at the air/neat water interface. The peak frequency of this transient band is 3270 cm^{-1}, which is lower than the OH stretch frequency of the water anion cluster in the gas phase (3320 cm^{-1}, Fig. 4.15(a)) and higher than that of the hydrated electron in bulk water (3170 cm^{-1}, Fig. 4.15(c)). Also, the observed bandwidth is broader than that of the water anion clusters in the gas phase (Fig. 4.15(a)) and narrower than that of the hydrated electrons in bulk water (Fig. 4.15(c)). These comparisons of the peak position and the bandwidth indicate that the electrons at the air/water interface are more hydrated than in the gas phase cluster (Fig. 4.15(a)) and less hydrated than in bulk water (Fig. 4.15(c)), meaning that they are half hydrated. Assuming that the sign of the hyperpolarizability, β, for the OH stretch mode of water is not changed by the presence of an electron, the positive sign of the observed Im $\Delta\chi_{\rm eff}^{(2)}$ band can be interpreted as the indication that the water molecules involved in the electron hydration have the H-up orientation. Hence, it can be concluded that the electrons exist on top of the interface and they are partially hydrated by water molecules from below as schematically shown in Fig. 4.15(b). Considering the quick disappearance of this transient species from the interfacial region (Fig. 4.8(b)), this partially hydrated state is not as stable as the fully hydrated state in bulk water (Fig. 4.15(c)), and the electron migrates into the bulk within 100 ps to become fully hydrated.

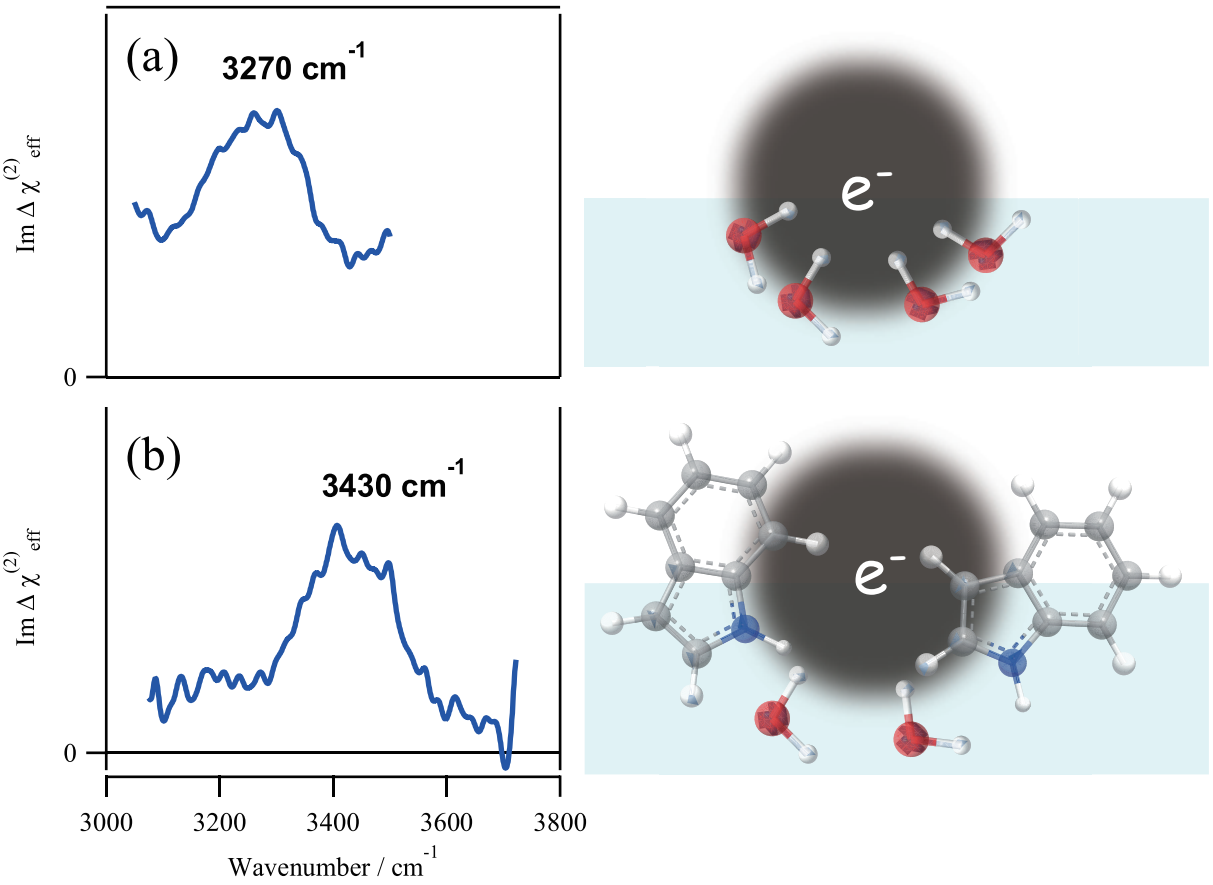

Figure 4.16: The spectra of (a) the transient component at the air/neat water interface (Fig. 4.8(a)) and (b) the short lifetime component at the air/indole solution interface ($\tilde{\mathbf{u}}_2'$ in Fig. 4.11(a)). Sketches of the assigned species are also shown.

With the detailed assignment in mind, it is now possible to discuss why the peak position of the transient component at the air/neat water interface (3270 cm^{-1}, Fig. 4.16(a)) and that of the short lifetime component at the air/indole solution interface (3430 cm^{-1}, Fig. 4.16(b)) are different, although they are both assigned to the same OH stretch mode of water molecules involved in the partial hydration of electrons. In the present assignment, the peak frequency reflects how strongly the OH group of the water molecules interacts with the electron. Higher peak frequency observed at the air/indole solution interface indicates that the interaction is weaker at this interface. Remembering that as many as $\sim$ 5 indole molecules exist every 1 nm^2 at the air/indole solution interface under the present experimental condition, it is not surprising that the interaction between the electron and the water molecules is disturbed and weakened by the indole molecules accumulated at the interface.

4.3.8 Comparison with the previous studies

As mentioned in the introduction, four studies on the hydrated electrons at the air/water interface are reported in the literature (two experimental and two theoretical studies), and they give contradictory conclusions. Similarities and differences between the present work and the previous works are discussed

here.

Siefermann *et al.* generated electrons in the liquid water jet in the vacuum by the two-photon ionization of water by the UV light at 267 nm, and recorded the photoelectron spectra using the extreme-UV light at 32 nm [63, 83]. In the observed photoelectron spectra, they found a band at the vertical binding energy of 1.6 eV, which is much smaller than that of the electrons in bulk water at 3.3 - 3.6 eV [63–66,83]. They assigned the 1.6 eV band to the electrons bound to the surface of the liquid water jet, based on its similarity to the vertical binding energy of the surface bound electrons in the water anion clusters [84]. In their experiment, they were able to selectively detect the interfacial species, because the high energy photoelectrons generated by the extreme-UV light are easily scattered by the molecules in the liquid jet, and the photoelectrons generated in the bulk liquid cannot come out into the vacuum to be detected. Although their assignment is in good agreement with the present study, the temporal behavior they observed is very different. The transient band they observed decayed only moderately within 100 ps, and its lifetime is much longer than the one observed in the present study. This discrepancy might be due to the difference in the temperature. While the time-resolved HD-VSFG experiments in the present study was done at 25 °C (298 K), the temperature of their liquid jet was 5 °C (278 K). Because the surface of the liquid jet is directly faced with the vacuum of 10^{-5} mbar, it is highly likely that the temperature at the surface is even lower due to the evaporation of water. Hence, it is possible that the dynamics they observed is slower due to the lower sample temperature in their experiments.

Sagar *et al.* measured second harmonic generation (SHG) of the incident light at 1400 nm at the air/sodium iodide aqueous solution interface following the one-photon ionization of iodide ion (I^-) by the UV pump light [67]. SHG is used for probing the electronic energy levels of the system, and it is interface selective for exactly the same reason as for VSFG. Based on the following three observations, the authors conclude that the electrons at the air/water interface are fully hydrated in the same manner as in bulk water. First, a transient signal was observed by probing at 700 nm, which is close to the absorption maximum of hydrated electrons in bulk water. Second, the decay of the signal could be well fitted by the formula which is often used to analyze the geminate recombination dynamics of hydrated electrons in bulk water [85]. Third, the intensity of the transient signal and its decay were not affected by adding a monolayer of 1-decanol at the air/water interface, from which they claim that the electrons are not directly facing the air. However, their data and discussion are not convincing enough to conclude that the electrons are fully hydrated. First, because their measurements are limited to one wavelength and they did not record any spectra, observing a transient signal at 700 nm does not mean that the absorption maximum of the transient band is near 700 nm. Second, the fitting formula they used is derived simply by solving the diffusion equation, and any decay processes whose rate is determined by diffusion will follow the same decay curve. Third, the monolayer of 1-decanol they added to the air/water interface does not seem to alter the environment at the interface very much, because the lack of change in the observed

transient signal indicates that the ionization of I^- and the generation of electrons at the interface occur in exactly the same manner even in the presence of 1-decanol. In such a case, it is possible that the properties of hydrated electrons are also not affected by the monolayer of 1-decanol even if the electrons are not fully hydrated. In fact, all of their observations are explainable based on the partially hydrated electron model proposed in this study.

From the theoretical point of view, two molecular dynamics simulations of electrons at the air/water interface are reported in the literature [68, 69]. Madarász *et al.* used the mixed quantum-classical molecular dynamics (QCMD) simulations to study the behavior of electrons at the air/water interface, in which water molecules are treated classically, the excess electron is treated quantum mechanically, and the interaction among the electron and the water molecules is described by a pseudopotential [68]. According to their simulation, an excess electron is initially stabilized at the surface of the liquid water, which they call the surface-bound state. The surface-bound state is characterized by the diffuse distribution of the electron which protrudes from the liquid phase into the air. The electron becomes more localized while it migrates into the bulk liquid phase on the 10 ps time scale. Actually, this view is almost identical to the conclusion of the present study.

Meanwhile, Uhlig *et al.* used the combined quantum mechanics/molecular mechanics (QM/MM) approach, where the excess electron and the nearby water molecules are treated quantum mechanically, and all the other water molecules are treated classically [69]. Based on their calculation, they conclude that the electrons are fully hydrated near the air/water interface. Although this conclusion seems to be completely the opposite of the conclusion given by Madarász *et al.* mentioned in the previous paragraph [68], the simulated electron distributions by the two groups are rather similar. In both simulations, a portion of the electron cloud protrudes from the liquid phase and exists in the air. As for the extent of this electron cloud protrusion, the two groups present different estimations. Madarász *et al.* claim that about 50 % of the electron cloud exists in the air [68], while Uhlig *et al.* think that it is only 10 % [69]. Hence, these two simulations differ only in the quantitative sense, and they give qualitatively the same conclusion. Both simulations show that the excess electron is partially hydrated, and they both agree that the electron escapes into the bulk liquid on a 10 ps time scale. These simulations are in full accord with the present study.

4.4 Conclusion

With the use of the newly developed UV-excited time-resolved HD-VSFG spectroscopy, transient spectra following the photoionization reactions at the air/neat water and air/indole solution interfaces were recorded. Through the combined analysis of the transient spectra at the two interfaces, transient components that can be assigned to hydrated electrons at the interface were found. The observed transient spectra and the temporal profiles indicate that the electrons initially exist at the air/water interfaces as the

partially hydrated species, and they migrate into the bulk water phase within 100 ps.

Part III

Electric quadrupolar theory for VSFG

Chapter 5

Quadrupolar theory for VSFG

5.1 Introduction

VSFG is now widely recognized as a powerful tool for studying interfaces, and the molecular orientation at interfaces has been discussed based on the observed spectra [86]. In these studies, the validity of the electric dipole approximation is implicitly assumed, which means that the gradient of the electric field is assumed to be negligible at the molecular scale of ~ 1 nm. Although this approximation is usually very accurate in the bulk optical processes, it may show a substantial breakdown at the interface region where the amplitude of the electric field changes abruptly due to the refractive index mismatch of the bonding media, resulting in a large electric field gradient within the interface layer as thin as ~ 1 nm [87–89]. Hence, the electric quadrupoles may have an important contribution to VSFG at interfaces. Since VSFG due to the quadrupole contribution originates from the discontinuity at the interface, it is irrelevant to the orientation of the interfacial molecules, and it must be clearly distinguished from VSFG due to the ordinary mechanism within the dipole approximation. It is possible to judge whether the observed VSFG spectrum is due to the ordinary dipolar mechanism or the quadrupolar one by examining if the appearance of the experimentally observed vibrational modes are consistent with the vibrational selection rules for each mechanism.

In this section, the theoretical treatment of VSFG involving an electric quadrupole contribution is presented, and the vibrational selection rule for this mechanism is derived.

5.2 Contribution beyond the dipole approximation

In the theoretical description of VSFG presented in Chapter 2, the electric dipole approximation was used to simplify the interaction Hamiltonian, $\mathcal{H}_{\rm int}$.

$$e^{i\mathbf{k}\cdot\hat{\mathbf{r}}} = e^{i\mathbf{k}\cdot\mathbf{R}}(1 + i\mathbf{k}\cdot\Delta\hat{\mathbf{r}} + \cdots) \simeq e^{i\mathbf{k}\cdot\mathbf{R}}. \tag{5.1}$$

Here,

$$\hat{\mathbf{r}} \equiv \mathbf{R} + \Delta\hat{\mathbf{r}}, \tag{5.2}$$

where $\hat{\mathbf{r}}$ is the coordinate operator in the laboratory-fixed coordinates and $\mathbf{R}$ represents the laboratory-fixed coordinate for the center of mass of a molecule. When the dipole approximation is not accurate enough, the second term in this expansion needs to be considered.

$$e^{i\mathbf{k}\cdot\hat{\mathbf{r}}} = e^{i\mathbf{k}\cdot\mathbf{R}}(1 + i\mathbf{k}\cdot\Delta\hat{\mathbf{r}} + \cdots) \simeq e^{i\mathbf{k}\cdot\mathbf{R}}(1 + i\mathbf{k}\cdot\Delta\hat{\mathbf{r}}). \tag{5.3}$$

This new term will give rise to the electric quadrupole contribution and the magnetic dipole contribution. These additional contributions will be discussed in this section.

5.2.1 Interaction Hamiltonian

With the contribution beyond the dipole approximation taken into account, the interaction Hamiltonian given in Eq. (2.27) becomes

$$\mathcal{H}_{\rm int} \simeq \sum_l \left[-\frac{z_l}{m_l}\mathbf{A}(\hat{\mathbf{r}}_l, t)\cdot\hat{\mathbf{p}}_l \right] \tag{5.4}$$

$$= \sum_l \int d\mathbf{k} \int d\omega \left[-\frac{z_l}{m_l}\left\{ \mathbf{A}(\mathbf{k},\omega) e^{i\mathbf{k}\cdot\hat{\mathbf{r}}_l - i\omega t} \right\}\cdot\hat{\mathbf{p}}_l \right] \tag{5.5}$$

$$\simeq \sum_l \int d\mathbf{k} \int d\omega \left[-\frac{z_l}{m_l}(1 + i\mathbf{k}\cdot\Delta\hat{\mathbf{r}}_l)\mathbf{A}(\mathbf{k},\omega)\cdot\hat{\mathbf{p}}_l e^{i\mathbf{k}\cdot\mathbf{R} - i\omega t} \right]. \tag{5.6}$$

The first term in the round bracket (1) is responsible for the electric dipole contribution already discussed in Chapter 2. The second term ($i\mathbf{k}\cdot\Delta\hat{\mathbf{r}}_l$) is further separated into symmetric and antisymmetric parts for later convenience [90].

$$\begin{aligned}\mathcal{H}_{\rm int} = \sum_l \int d\mathbf{k} \int d\omega \Bigg[-\frac{z_l}{m_l} \Big(&\mathbf{A}(\mathbf{k},\omega)\cdot\hat{\mathbf{p}}_l \\ &+ i\frac{\mathbf{k}\cdot\Delta\hat{\mathbf{r}}_l\mathbf{A}(\mathbf{k},\omega)\cdot\hat{\mathbf{p}}_l + \mathbf{k}\cdot\hat{\mathbf{p}}_l\mathbf{A}(\mathbf{k},\omega)\cdot\Delta\hat{\mathbf{r}}_l}{2} \\ &+ i\frac{\mathbf{k}\cdot\Delta\hat{\mathbf{r}}_l\mathbf{A}(\mathbf{k},\omega)\cdot\hat{\mathbf{p}}_l - \mathbf{k}\cdot\hat{\mathbf{p}}_l\mathbf{A}(\mathbf{k},\omega)\cdot\Delta\hat{\mathbf{r}}_l}{2} \Big) e^{i\mathbf{k}\cdot\mathbf{R} - i\omega t} \Bigg]\end{aligned} \tag{5.7}$$

$$\equiv \mathcal{H}_{\rm int}^{\rm dipole} + \mathcal{H}_{\rm int}^{\rm quad} + \mathcal{H}_{\rm int}^{\rm mag}. \tag{5.8}$$

Here,

$$\mathcal{H}_{\rm int}^{\rm dipole} \equiv \sum_l \int d\mathbf{k} \int d\omega \left[-\frac{z_l}{m_l}\mathbf{A}(\mathbf{k},\omega)\cdot\hat{\mathbf{p}}_l e^{i\mathbf{k}\cdot\mathbf{R} - i\omega t} \right], \tag{5.9}$$

$$\mathcal{H}_{\rm int}^{\rm quad} \equiv \sum_l \int d\mathbf{k} \int d\omega \left[-\frac{iz_l}{2m_l}\left(\mathbf{k}\cdot\Delta\hat{\mathbf{r}}_l\mathbf{A}(\mathbf{k},\omega)\cdot\hat{\mathbf{p}}_l + \mathbf{k}\cdot\hat{\mathbf{p}}_l\mathbf{A}(\mathbf{k},\omega)\cdot\Delta\hat{\mathbf{r}}_l \right) e^{i\mathbf{k}\cdot\mathbf{R} - i\omega t} \right], \tag{5.10}$$

$$\mathcal{H}_{\rm int}^{\rm mag} \equiv \sum_l \int d\mathbf{k} \int d\omega \left[-\frac{iz_l}{2m_l}\left(\mathbf{k}\cdot\Delta\hat{\mathbf{r}}_l\mathbf{A}(\mathbf{k},\omega)\cdot\hat{\mathbf{p}}_l - \mathbf{k}\cdot\hat{\mathbf{p}}_l\mathbf{A}(\mathbf{k},\omega)\cdot\Delta\hat{\mathbf{r}}_l \right) e^{i\mathbf{k}\cdot\mathbf{R} - i\omega t} \right]. \tag{5.11}$$

In the following part, it will be shown that $\mathcal{H}_{\rm int}^{\rm quad}$ represents the electric quadrupolar interaction and $\mathcal{H}_{\rm int}^{\rm quad}$ gives the magnetic dipolar interaction.

5.2.2 Electric quadrupole transition

First, the physical significance of $\mathcal{H}_{\rm int}^{\rm quad}$ is discussed. Remembering that

$$\hat{\mathbf{p}}_l = \frac{im_l}{\hbar}[\mathcal{H}_0, \Delta\hat{\mathbf{r}}_l], \tag{5.12}$$

$\mathcal{H}_{\rm int}^{\rm quad}$ can be reduced into

$$\mathcal{H}_{\rm int}^{\rm quad} = \sum_{I,J}\sum_l \int d\mathbf{k} \int d\omega \left[-\frac{iz_l}{2m_l} \left(k_J \Delta\hat{r}_{l,J} A_I(\mathbf{k},\omega)\hat{p}_{l,I} + k_J \hat{p}_{l,J} A_I(\mathbf{k},\omega)\Delta\hat{r}_{l,I} \right) e^{i\mathbf{k}\cdot\mathbf{R}-i\omega t} \right] \tag{5.13}$$

$$= \sum_{I,J}\sum_l \int d\mathbf{k} \int d\omega \left[-\frac{iz_l}{2m_l}\frac{im_l}{\hbar} k_J A_I(\mathbf{k},\omega) \right.$$

$$\left. \times \left(\Delta\hat{r}_{l,J}[\mathcal{H}_0, \Delta\hat{r}_{l,I}] + [\mathcal{H}_0, \Delta\hat{r}_{l,J}]\Delta\hat{r}_{l,I} \right) e^{i\mathbf{k}\cdot\mathbf{R}-i\omega t} \right] \tag{5.14}$$

$$= \sum_{I,J}\sum_l \int d\mathbf{k} \int d\omega \frac{z_l}{2\hbar} k_J A_I(\mathbf{k},\omega)[\mathcal{H}_0, \Delta\hat{r}_{l,J}\Delta\hat{r}_{l,I}] e^{i\mathbf{k}\cdot\mathbf{R}-i\omega t} \tag{5.15}$$

$$= \sum_{I,J} \int d\mathbf{k} \int d\omega \frac{1}{\hbar} k_J A_I(\mathbf{k},\omega)[\mathcal{H}_0, \hat{q}_{IJ}] e^{i\mathbf{k}\cdot\mathbf{R}-i\omega t}. \tag{5.16}$$

In the last line, the quadrupole moment operator was defined as

$$\hat{q}_{IJ} \equiv \sum_l \frac{z_l}{2}\Delta\hat{r}_{l,I}\Delta\hat{r}_{l,J} = \sum_l \frac{z_l}{2}\Delta\hat{r}_{l,J}\Delta\hat{r}_{l,I}. \tag{5.17}$$

The transition probability from $|i\rangle$ to $|f\rangle$ due to this interaction is given as

$$\langle f|\mathcal{H}_{\rm int}^{\rm quad}|i\rangle = \sum_{I,J} \int d\mathbf{k} \int d\omega \frac{1}{\hbar} k_J A_I(\mathbf{k},\omega)\langle f|[\mathcal{H}_0, \hat{q}_{IJ}(t)]|i\rangle e^{i\mathbf{k}\cdot\mathbf{R}-i\omega t} \tag{5.18}$$

$$= \sum_{I,J} \int d\mathbf{k} \int d\omega \frac{1}{\hbar} k_J A_I(\mathbf{k},\omega)\langle f|\hat{q}_{IJ}(t)|i\rangle(\varepsilon_f - \varepsilon_i) e^{i\mathbf{k}\cdot\mathbf{R}-i\omega t} \tag{5.19}$$

As discussed on page 14, this transition occurs only when $\varepsilon_f - \varepsilon_i \simeq \hbar\omega$ is satisfied.

$$\langle f|\mathcal{H}_{\rm int}^{\rm quad}|i\rangle \simeq \sum_{I,J} \int d\mathbf{k} \int d\omega\, \omega k_J A_I(\mathbf{k},\omega) e^{i\mathbf{k}\cdot\mathbf{R}-i\omega t}\langle f|\hat{q}_{IJ}(t)|i\rangle. \tag{5.20}$$

Because the electric field and the vector potential are related as

$$\mathbf{E}(\mathbf{R},t) = -\frac{\partial \mathbf{A}(\mathbf{R},t)}{\partial t}, \tag{5.21}$$

the electromagnetic part in this expression can be simplified as

$$\int d\mathbf{k} \int d\omega\, \omega k_J A_I(\mathbf{k},\omega) e^{i\mathbf{k}\cdot\mathbf{R}-i\omega t} = \frac{\partial^2}{\partial J \partial t} \int d\mathbf{k} \int d\omega A_I(\mathbf{k},\omega) e^{i\mathbf{k}\cdot\mathbf{R}-i\omega t} \equiv \frac{\partial^2 A_I(\mathbf{R},t)}{\partial J \partial t} \tag{5.22}$$

$$= -\frac{\partial E_I(\mathbf{R},t)}{\partial J}. \tag{5.23}$$

Hence, the transition probability is finally expressed as

$$\langle f|\mathcal{H}_{\rm int}^{\rm quad}|i\rangle \simeq -\sum_{I,J} \frac{\partial E_I(\mathbf{R},t)}{\partial J}\langle f|\hat{q}_{IJ}(t)|i\rangle. \tag{5.24}$$

This transition is called the electric quadrupole transition. The important point here is that the transition probability is proportional to the electric field gradient, $\partial E_I(\mathbf{R},t)/\partial J$, of the incident light. This is negligible in the bulk because of the small electric field gradient on the molecular scale, but it may become significant at the interface where a large electric field gradient exists due to the refractive index mismatch of the bonding media [91]. Detailed theoretical description of the electric field gradient at the interface will be given later.

5.2.3 Magnetic dipole transition

Next, the physical significance of $\mathcal{H}_{\rm int}^{\rm mag}$ is discussed.

$$\mathcal{H}_{\rm int}^{\rm mag} = \sum_l \int d\mathbf{k} \int d\omega \left[-\frac{iz_l}{2m_l} \left(\mathbf{k}\cdot\Delta\hat{\mathbf{r}}_l \mathbf{A}(\mathbf{k},\omega)\cdot\hat{\mathbf{p}}_l - \mathbf{k}\cdot\hat{\mathbf{p}}_l \mathbf{A}(\mathbf{k},\omega)\cdot\Delta\hat{\mathbf{r}}_l \right) e^{i\mathbf{k}\cdot\mathbf{R}-i\omega t} \right] \tag{5.25}$$

$$= \sum_l \int d\mathbf{k} \int d\omega \left[-\frac{iz_l}{2m_l} \left(\mathbf{k}\times\mathbf{A}(\mathbf{k},\omega) \right)\cdot\left(\Delta\hat{\mathbf{r}}_l \times \hat{\mathbf{p}}_l \right) e^{i\mathbf{k}\cdot\mathbf{R}-i\omega t} \right] \tag{5.26}$$

$$= -\left(\int d\mathbf{k} \int d\omega\, i\mathbf{k}\times\mathbf{A}(\mathbf{k},\omega) e^{i\mathbf{k}\cdot\mathbf{R}-i\omega t} \right) \cdot \left(\sum_l \frac{1}{2} \Delta\hat{\mathbf{r}}_l \times \frac{z_l\hat{\mathbf{p}}_l}{m_l} \right). \tag{5.27}$$

This can be further simplified by introducing the magnetic induction, $\mathbf{B}(\mathbf{R},t)$,

$$\mathbf{B}(\mathbf{R},t) = \boldsymbol{\nabla}\times\mathbf{A}(\mathbf{R},t) \equiv \boldsymbol{\nabla}\times\int d\omega \mathbf{A}(\omega) e^{i\mathbf{k}\cdot\mathbf{R}-i\omega t} = \int d\omega\, i\mathbf{k}\times\mathbf{A}(\omega) e^{i\mathbf{k}\cdot\mathbf{R}-i\omega t}, \tag{5.28}$$

and the magnetic dipole moment operator, $\hat{\mathbf{m}}$,

$$\hat{\mathbf{m}} \equiv \sum_l \frac{1}{2} \Delta\hat{\mathbf{r}}_l \times \frac{z_l\hat{\mathbf{p}}_l}{m_l}. \tag{5.29}$$

Using these two quantities, the interaction Hamiltonian can be expressed in a very compact form.

$$\mathcal{H}_{\rm int}^{\rm mag} = -\mathbf{B}(\mathbf{R},t)\cdot\hat{\mathbf{m}}. \tag{5.30}$$

The transition from $|i\rangle$ to $|f\rangle$ due to this interaction is expressed as

$$\langle f|\mathcal{H}_{\rm int}^{\rm mag}|i\rangle = -\mathbf{B}(\mathbf{R},t)\cdot\langle f|\hat{\mathbf{m}}(t)|i\rangle. \tag{5.31}$$

This is called the magnetic dipole transition. The magnetic dipole transition is usually negligible in the bulk, and it is expected to be negligible also at the interface. This is because this expression does not contain any factors that may make this contribution particularly large at the interface.

5.3 Induced dipole and induced quadrupole

As discussed in Chapter 2, the induced nonlinear polarization can be evaluated from the induced dipole of each molecule. The quadrupole contribution to the induced dipole can be taken into account by replacing one of the interaction Hamiltonians in Eq. (2.19) with $\mathcal{H}_{\rm int}^{\rm quad}$.

$$\boldsymbol{\mu}^{\rm quad1}(\mathbf{R},t) = \left(\frac{1}{i\hbar}\right)^2 \int_{-\infty}^{t} dt_1 \int_{-\infty}^{t_1} dt_2 \sum_{s,v} \langle g|\hat{\boldsymbol{\mu}}(t)|s\rangle\langle s|\mathcal{H}_{\rm int}^{\rm quad}(t_1)|v\rangle\langle v|\mathcal{H}_{\rm int}^{\rm dipole}(t_2)|g\rangle, \tag{5.32}$$

$$\boldsymbol{\mu}^{\mathrm{quad2}}(\mathbf{R},t)=\left(\frac{1}{i\hbar}\right)^2\int_{-\infty}^{t}dt_1\int_{-\infty}^{t_1}dt_2\sum_{s,v}\langle g|\hat{\boldsymbol{\mu}}(t)|s\rangle\langle s|\mathcal{H}_{\mathrm{int}}^{\mathrm{dipole}}(t_1)|v\rangle\langle v|\mathcal{H}_{\mathrm{int}}^{\mathrm{quad}}(t_2)|g\rangle. \tag{5.33}$$

Additionally, the induced quadrupole due to dipolar interactions must also be considered. This can be evaluated in the same manner as

$$\mathbf{q}(\mathbf{R},t)=\left(\frac{1}{i\hbar}\right)^2\int_{-\infty}^{t}dt_1\int_{-\infty}^{t_1}dt_2\sum_{s,v}\langle g|\hat{\mathbf{q}}(t)|s\rangle\langle s|\mathcal{H}_{\mathrm{int}}^{\mathrm{dipole}}(t_1)|v\rangle\langle v|\mathcal{H}_{\mathrm{int}}^{\mathrm{dipole}}(t_2)|g\rangle. \tag{5.34}$$

In the following part, these two quadrupole contribution schemes will be discussed. It will be assumed that ω_1 (visible light) and ω_2 (IR light) interact with the molecular system at t_1 and t_2, respectively, with $t_1 > t_2$.

5.3.1 Induced dipole with one quadrupole transition

A quadrupolar interaction with ω_1 at $t = t_1$

Using the explicit expressions for $\mathcal{H}_{\mathrm{int}}^{\mathrm{dipole}}$ and $\mathcal{H}_{\mathrm{int}}^{\mathrm{quad}}$, the induced dipole can be given as

$$\begin{aligned}\boldsymbol{\mu}^{\mathrm{quad1}}(\mathbf{R},t)=\left(\frac{1}{i\hbar}\right)^2\int_{-\infty}^{t}dt_1\int_{-\infty}^{t_1}dt_2\sum_{J,K,L}\sum_{s,v}\frac{\partial E_{1J}(\mathbf{R},t_1)}{\partial L}E_{2K}(\mathbf{R},t_2)\\ \times\langle g|\hat{\boldsymbol{\mu}}(t)|s\rangle\langle s|\hat{q}_{JL}(t_1)|v\rangle\langle v|\hat{\mu}_K(t_2)|g\rangle.\end{aligned} \tag{5.35}$$

These integrations can be evaluated in the same manner as in Chapter 2.

$$\begin{aligned}\boldsymbol{\mu}^{\mathrm{quad1}}(\mathbf{R},t)=\sum_{J,K,L}\sum_{s,v}\int d\omega_1\int d\omega_2\frac{\langle g|\hat{\boldsymbol{\mu}}|s\rangle\langle s|\hat{q}_{JL}|v\rangle\langle v|\hat{\mu}_K|g\rangle}{(\varepsilon_v-\varepsilon_g-\hbar\omega_2)\{\varepsilon_s-\varepsilon_g-\hbar(\omega_1+\omega_2)\}}\\ \times\frac{\partial E_{1J}(\mathbf{R},\omega_1)}{\partial L}E_{2K}(\mathbf{R},\omega_2)e^{-i(\omega_1+\omega_2)t}.\end{aligned} \tag{5.36}$$

The I component of $\boldsymbol{\mu}^{\mathrm{quad1}}$ can be expressed as

$$\mu_I^{\mathrm{quad1}}(\mathbf{R},t)=\sum_{J,K,L}\int d\omega_1\int d\omega_2\beta_{IJKL}^{\mathrm{quad1}}(\omega_1,\omega_2)\frac{\partial E_{1J}(\mathbf{R},\omega_1)}{\partial L}E_{2K}(\mathbf{R},\omega_2)e^{-i(\omega_1+\omega_2)t}. \tag{5.37}$$

with the hyperpolarizability tensor $\beta_{IJKL}^{\mathrm{quad1}}$ in the laboratory-fixed coordinates defined as

$$\beta_{IJKL}^{\mathrm{quad1}}(\omega_1,\omega_2)=\sum_{s,v}\frac{\langle g|\hat{\mu}_I|s\rangle\langle s|\hat{q}_{JL}|v\rangle\langle v|\hat{\mu}_K|g\rangle}{(\varepsilon_v-\varepsilon_g-\hbar\omega_2-i\gamma_{vg})\{\varepsilon_s-\varepsilon_g-\hbar(\omega_1+\omega_2)-i\gamma_{sg}\}}. \tag{5.38}$$

Here, the damping constants, γ_{vg} and γ_{sg}, were phenomenologically introduced to avoid the divergence of $\beta_{IJKL}^{\mathrm{quad1}}$ at the resonant frequencies. The summation of the induced dipole over all the molecules can be evaluated in the same manner as before.

$$\langle\mu_I^{\mathrm{quad1}}\rangle(\mathbf{R},t)=\sum_{n=1}^{N}\mu_I^{\mathrm{quad1}}(n) \tag{5.39}$$

$$=\sum_{J,K,L}\int d\omega_1\int d\omega_2\left(\sum_{n=1}^{N}\beta_{IJKL}^{\mathrm{quad1}}(n)\right)\frac{\partial E_{1J}(\mathbf{R},\omega_1)}{\partial L}E_{2K}(\mathbf{R},\omega_2)e^{-i(\omega_1+\omega_2)t} \tag{5.40}$$

$$= \varepsilon_0 \sum_{J,K,L} \int d\omega_1 \int d\omega_2 \chi^{(2),\mathrm{quad1}}_{IJKL}(\omega_1,\omega_2) \frac{\partial E_{1J}(\mathbf{R},\omega_1)}{\partial L} E_{2K}(\mathbf{R},\omega_2) e^{-i(\omega_1+\omega_2)t} \tag{5.41}$$

with the definition of the quadrupolar nonlinear susceptibility $\chi^{(2),\mathrm{quad1}}$ given using the rotation matrix, R, as

$$\chi^{(2),\mathrm{quad1}}_{IJKL} = \frac{1}{\varepsilon_0} \sum_{n=1}^{N} \beta^{\mathrm{quad1}}_{IJKL}(n) = \frac{1}{\varepsilon_0} \sum_{i,j,k,l} \left(\sum_{n=1}^{N} R_{Ii}(n) R_{Jj}(n) R_{Kk}(n) R_{Ll} \right) \beta^{\mathrm{quad1}}_{ijkl} \tag{5.42}$$

$$= \frac{N}{\varepsilon_0} \sum_{i,j,k} \langle R_{Ii} R_{Jj} R_{Kk} R_{Ll} \rangle_{\mathrm{av}} \beta^{\mathrm{quad1}}_{ijkl}. \tag{5.43}$$

A quadrupolar interaction with ω_2 at $t = t_2$

The induced dipole is given as

$$\boldsymbol{\mu}^{\mathrm{quad2}}(\mathbf{R},t) = \left(\frac{1}{i\hbar}\right)^2 \int_{-\infty}^{t} dt_1 \int_{-\infty}^{t_1} dt_2 \sum_{J,K,L} \sum_{s,v} E_{1J}(\mathbf{R},t_1) \frac{\partial E_{2K}(\mathbf{R},t_2)}{\partial L} \times \langle g|\hat{\boldsymbol{\mu}}(t)|s\rangle\langle s|\hat{\mu}_J(t_1)|v\rangle\langle v|\hat{q}_{KL}(t_2)|g\rangle. \tag{5.44}$$

This can be evaluated in exactly the same manner as above.

$$\mu^{\mathrm{quad2}}_I(\mathbf{R},t) = \sum_{J,K,L} \int d\omega_1 \int d\omega_2 \beta^{\mathrm{quad2}}_{IJKL} E_{1J}(\mathbf{R},\omega_1) \frac{\partial E_{2K}(\mathbf{R},\omega_2)}{\partial L} e^{-i(\omega_1+\omega_2)t}. \tag{5.45}$$

with

$$\beta^{\mathrm{quad2}}_{IJKL} = \sum_{s,v} \frac{\langle g|\hat{\mu}_I|s\rangle\langle s|\hat{\mu}_J|v\rangle\langle v|\hat{q}_{KL}|g\rangle}{(\varepsilon_v - \varepsilon_g - \hbar\omega_2 - i\gamma_{vg})\{\varepsilon_s - \varepsilon_g - \hbar(\omega_1+\omega_2) - i\gamma_{sg}\}}. \tag{5.46}$$

Summation over all the molecules gives

$$\langle \mu^{\mathrm{quad2}}_I \rangle(\mathbf{R},t) = \sum_{n=1}^{N} \mu^{\mathrm{quad2}}_I(n) \tag{5.47}$$

$$= \varepsilon_0 \sum_{J,K,L} \int d\omega_1 \int d\omega_2 \chi^{(2),\mathrm{quad2}}_{IJKL} E_{1J}(\mathbf{R},\omega_1) \frac{\partial E_{2K}(\mathbf{R},\omega_2)}{\partial L} e^{-i(\omega_1+\omega_2)t}. \tag{5.48}$$

where the quadrupolar nonlinear susceptibility $\chi^{(2),\mathrm{quad2}}$ was defined as

$$\chi^{(2),\mathrm{quad2}}_{IJKL} = \frac{N}{\varepsilon_0} \sum_{i,j,k} \langle R_{Ii} R_{Jj} R_{Kk} R_{Ll} \rangle_{\mathrm{av}} \beta^{\mathrm{quad2}}_{ijkl}. \tag{5.49}$$

5.3.2 Induced quadrupole with only dipole transitions

The induced quadrupole is given as

$$\mathbf{q}(\mathbf{R},t) = \left(\frac{1}{i\hbar}\right)^2 \int_{-\infty}^{t} dt_1 \int_{-\infty}^{t_1} dt_2 \sum_{J,K} \sum_{s,v} E_{1J}(\mathbf{R},t_1) E_{2K}(\mathbf{R},t_2) \times \langle g|\hat{\mathbf{q}}(t)|s\rangle\langle s|\hat{\mu}_J(t_1)|v\rangle\langle v|\hat{\mu}_K(t_2)|g\rangle. \tag{5.50}$$

Evaluating the integration, the following expression can be obtained.

$$\mathbf{q}(\mathbf{R},t) = \sum_{J,K}\sum_{s,v}\int d\omega_1 \int d\omega_2 \frac{\langle g|\hat{\mathbf{q}}|s\rangle\langle s|\hat{\mu}_J|v\rangle\langle v|\hat{\mu}_K|g\rangle}{(\varepsilon_v-\varepsilon_g-\hbar\omega_2)\{\varepsilon_s-\varepsilon_g-\hbar(\omega_1+\omega_2)\}} \times E_{1J}(\mathbf{R},\omega_1)E_{2K}(\mathbf{R},\omega_2)e^{-i(\omega_1+\omega_2)t}. \tag{5.51}$$

The IL component of $\mathbf{q}$ can be expressed as

$$q_{IL}(\mathbf{R},t) = \sum_{J,K}\int d\omega_1 \int d\omega_2 \beta^{\mathrm{quad3}}_{IJKL} E_{1J}(\mathbf{R},\omega_1)E_{2K}(\mathbf{R},\omega_2)e^{-i(\omega_1+\omega_2)t}, \tag{5.52}$$

with the hyperpolarizability tensor $\beta^{\mathrm{quad3}}_{IJKL}$ in the laboratory-fixed coordinates defined as

$$\beta^{\mathrm{quad3}}_{IJKL} = \sum_{s,v}\frac{\langle g|\hat{q}_{IL}|s\rangle\langle s|\hat{\mu}_J|v\rangle\langle v|\hat{\mu}_K|g\rangle}{(\varepsilon_v-\varepsilon_g-\hbar\omega_2-i\gamma_{vg})\{\varepsilon_s-\varepsilon_g-\hbar(\omega_1+\omega_2)-i\gamma_{sg}\}}. \tag{5.53}$$

To obtain the total induced quadrupole, this induced quadrupole for one molecule needs to be summed up for all the molecules.

$$\langle q_{IL}\rangle(\mathbf{R},t) = \sum_{n=1}^{N} q_{IL}(n) \tag{5.54}$$

$$= \sum_{J,K}\int d\omega_1 \int d\omega_2 \left(\sum_{n=1}^{N}\beta^{\mathrm{quad3}}_{IJKL}(n)\right) E_{1J}(\mathbf{R},\omega_1)E_{2K}(\mathbf{R},\omega_2)e^{-i(\omega_1+\omega_2)t} \tag{5.55}$$

$$= \varepsilon_0\sum_{J,K}\int d\omega_1 \int d\omega_2 \chi^{(2),\mathrm{quad3}}_{IJKL} E_{1J}(\mathbf{R},\omega_1)E_{2K}(\mathbf{R},\omega_1)e^{-i(\omega_1+\omega_2)t}. \tag{5.56}$$

Here, the quadrupolar nonlinear susceptibility $\chi^{(2),\mathrm{quad3}}$ was defined as

$$\chi^{(2),\mathrm{quad3}}_{IJKL} = \frac{1}{\varepsilon_0}\sum_{n=1}^{N}\beta^{\mathrm{quad3}}_{IJKL}(n) = \frac{1}{\varepsilon_0}\sum_{i,j,k,l}\left(\sum_{n=1}^{N}R_{Ii}(n)R_{Jj}(n)R_{Kk}(n)R_{Ll}\right)\beta^{\mathrm{quad3}}_{ijkl} \tag{5.57}$$

$$= \frac{N}{\varepsilon_0}\sum_{i,j,k}\langle R_{Ii}R_{Jj}R_{Kk}R_{Ll}\rangle_{\mathrm{av}}\beta^{\mathrm{quad3}}_{ijkl}. \tag{5.58}$$

5.3.3 Summary of the results

With both dipole and quadrupole contributions considered, the induced dipole and quadrupole can be expressed as

$$\langle\mu_I\rangle(\mathbf{R},t) = \langle\mu^{\mathrm{dipole}}_I\rangle + \langle\mu^{\mathrm{quad1}}_I\rangle + \langle\mu^{\mathrm{quad2}}_I\rangle \tag{5.59}$$

$$= \varepsilon_0\sum_{J,K}\int d\omega_1 \int d\omega_2 \chi^{(2),\mathrm{dipole}}_{IJK} E_{1J}(\mathbf{R},\omega_1)E_{2K}(\mathbf{R},\omega_2)e^{-i(\omega_1+\omega_2)t} + \varepsilon_0\sum_{J,K,L}\int d\omega_1 \int d\omega_2 \left(\chi^{(2),\mathrm{quad1}}_{IJKL}\frac{\partial E_{1J}(\mathbf{R},\omega_1)}{\partial L}E_{2K}(\mathbf{R},\omega_2) + \chi^{(2),\mathrm{quad2}}_{IJKL}E_{1J}(\mathbf{R},\omega_1)\frac{\partial E_{2K}(\mathbf{R},\omega_2)}{\partial L}\right)e^{-i(\omega_1+\omega_2)t}, \tag{5.60}$$

$$\langle q_{IL}\rangle(\mathbf{R},t) = \varepsilon_0 \sum_{J,K} \int d\omega_1 \int d\omega_2 \chi^{(2),\mathrm{quad3}}_{IJKL} E_{1J}(\mathbf{R},\omega_1) E_{2K}(\mathbf{R},\omega_2) e^{-i(\omega_1+\omega_2)t}. \tag{5.61}$$

When both ω_1 and ω_2 are approximated by monochromatic plane waves, the following simple expression can be obtained.

$$\begin{aligned}\langle \mu_I\rangle(\mathbf{R},t) = {} & \varepsilon_0 \sum_{J,K} \chi^{(2),\mathrm{dipole}}_{IJK} E_{1J}(\mathbf{R},t) E_{2K}(\mathbf{R},t) \\ & + \varepsilon_0 \sum_{J,K,L} \left(\chi^{(2),\mathrm{quad1}}_{IJKL} \frac{\partial E_{1J}(\mathbf{R},t)}{\partial L} E_{2K}(\mathbf{R},t) \right. \\ & \left. + \chi^{(2),\mathrm{quad2}}_{IJKL} E_{1J}(\mathbf{R},t) \frac{\partial E_{2K}(\mathbf{R},t)}{\partial L} \right), \end{aligned} \tag{5.62}$$

$$\langle q_{IL}\rangle(\mathbf{R},t) = \varepsilon_0 \sum_{J,K} \chi^{(2),\mathrm{quad3}}_{IJKL} E_{1J}(\mathbf{R},t) E_{2K}(\mathbf{R},t). \tag{5.63}$$

These expressions will be used in the following part.

5.4 Induced nonlinear polarization with a quadrupole contribution

The induced nonlinear polarization per volume up to the second order in the multipole expansion is given as

$$P^{(2)}_I(\mathbf{R},t) = \langle \mu_I\rangle(\mathbf{R},t) - \sum_L \frac{\partial \langle q_{IL}\rangle(\mathbf{R},t)}{\partial L}, \tag{5.64}$$

where $\langle \mu \rangle$ and $\langle q \rangle$ are the induced dipole and quadrupole per volume, respectively, discussed in the previous section, and I, J, K, and L represent the laboratory-fixed coordinates (I, J, K, L = X, Y, Z in Fig. 5.1). The contribution from the magnetic dipole has been neglected. Using the formulae derived in the previous section, the induced nonlinear polarization in Eq. (5.64) can be separated into the dipolar part and the quadrupolar part as

$$P^{(2)}_I = P^{(2),\mathrm{dipole}}_I + P^{(2),\mathrm{quad}}_I \tag{5.65}$$

with

$$P^{(2),\mathrm{dipole}}_I = \varepsilon_0 \sum_{J,K} \chi^{(2),\mathrm{dipole}}_{IJK} E_{1J} E_{2K}, \tag{5.66}$$

$$\begin{aligned} P^{(2),\mathrm{quad}}_I = {} & \varepsilon_0 \sum_{J,K,L} \left[\chi^{(2),\mathrm{quad1}}_{IJKL} \frac{\partial E_{1J}}{\partial L} E_{2K} + \chi^{(2),\mathrm{quad2}}_{IJKL} E_{1J} \frac{\partial E_{2K}}{\partial L} \right. \\ & \left. - \frac{\partial}{\partial L} \left(\chi^{(2),\mathrm{quad3}}_{IJKL} E_{1J} E_{2K} \right) \right]. \end{aligned} \tag{5.67}$$

Under the electric dipole approximation, only $P^{(2),\mathrm{dipole}}_I$ contributes to VSFG, and the VSFG spectra are usually interpreted based on this term. At the interface, however, an electric quadrupole contribution may become significant because $\partial E_{1J}/\partial L$ and $\partial E_{2K}/\partial L$ in Eq. (5.67) can become very large at the

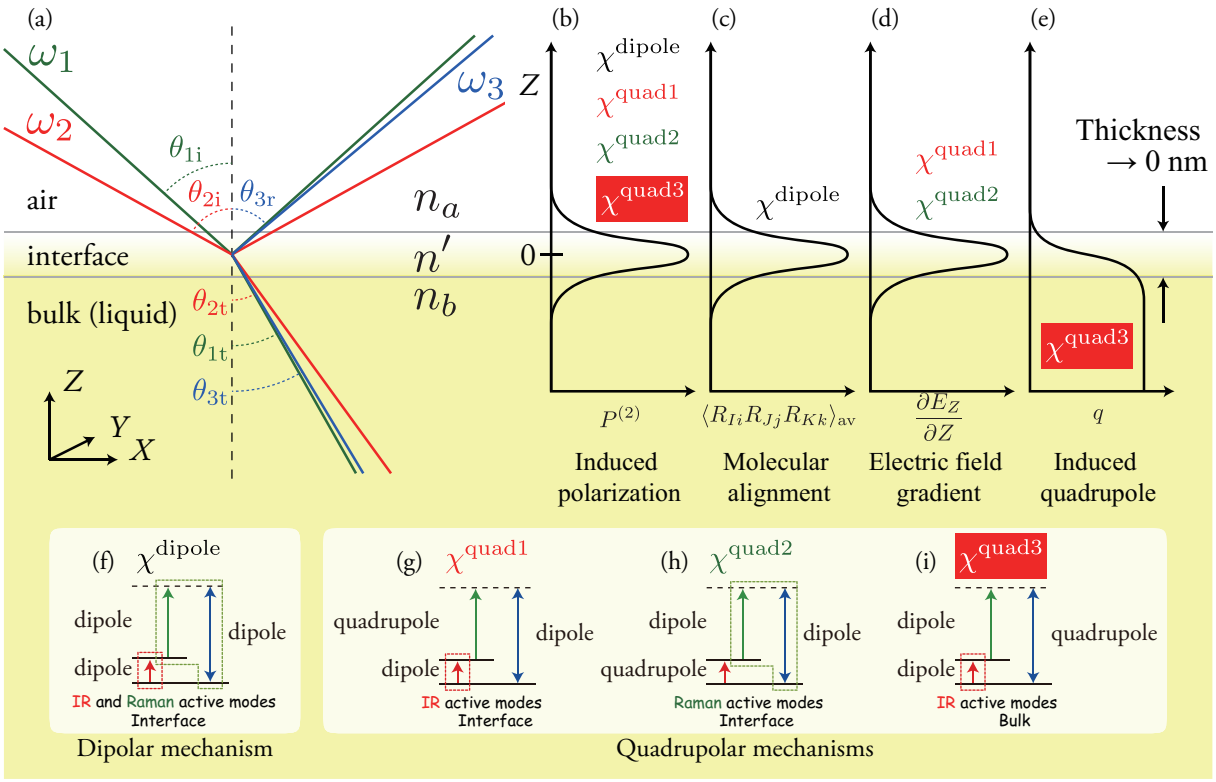

Figure 5.1: (a) Figurative sketch of an air/liquid interface. ω_1, ω_2, and ω_3 are the visible, infrared, and sum frequency light, respectively. θ_{1i}, θ_{1t}, θ_{2i}, and θ_{2t} are the incident and refraction angles for ω_1 and ω_2, respectively. θ_{3r} and θ_{3t} are the emission angles of ω_3 in the reflection and transmission directions. n_a, n_b, and n' are the refractive indices of the air, bulk liquid, and interface, respectively. (b) For all the mechanisms discussed in this chapter, the induced nonlinear polarization is localized at the interface. (c) The molecules may be oriented in a particular direction at the interface due to the anisotropic environment. This is the origin of the interface selectivity in the ordinary dipolar mechanism. (d) The ω_1 and ω_2 electric fields have a large gradient at the interface. The interface selectivity of the quad1 and quad2 mechanisms is due to this electric field gradient localized at the interface. (e) The induced quadrupole is negligible in the air, but has a large value in the bulk liquid. The quad3, which arises from this induced quadrupole, reflect bulk properties, although it contributes to the induced polarization localized at the interface as shown in (b). (f-i) The energy diagrams for VSFG by the dipolar and quadrupolar mechanisms. All the arrows in the dipolar diagram (f) represent dipole transitions, while one of them is replaced by a quadrupole transition in the quadrupolar mechanisms (g-i). The vibrational selection rule and the interface selectivity are indicated below each diagram.

interface. An interesting point here is that the abrupt change of the induced quadrupole at the interface can also give rise to a significant quadrupole contribution in the induced nonlinear polarization as can be seen from the second term in Eq. (5.64) and the final term in Eq. (5.67). This was independently noticed by Sipe *et al.* [92] and Guyot-Sionnest *et al.* [91]. In the present treatment, only the nonlinear polarization in the interface region is considered and the polarization induced in the bulk is neglected, even though the latter may in principle become significant owing to the large number of molecules that can add up to the bulk polarization. The neglect of the latter is justified by an experimental SFG study at vibrationally and electronically off-resonant wavelengths [89] and a theoretical VSFG study [93] which showed that the quadrupole contribution involving the polarization in the bulk is negligibly smaller than that involving the polarization at the interface for SFG observed in the reflection geometry.

In general, the evaluation of the derivatives in Eq. (5.67) is rather difficult, because it requires the full knowledge about the molecular distribution within the interface region. However, it can be greatly facilitated by assuming that the interface is infinitesimally thin. In this case, the electric field gradients can be evaluated only from the electric fields in the air and in the bulk liquid without any knowledge about the interface region. The incident electric fields in the air and in the bulk liquid can be related to each other by taking account of the boundary conditions at the interface in the same manner as in Section 2.5.3.

$$E_{\mathrm{i}X} + E_{\mathrm{r}X} = E_{\mathrm{t}X}, \tag{5.68}$$

$$E_{\mathrm{i}Y} + E_{\mathrm{r}Y} = E_{\mathrm{t}Y}, \tag{5.69}$$

$$D_{\mathrm{i}Z} + D_{\mathrm{r}Z} = D_{\mathrm{t}Z}. \tag{5.70}$$

Here, E is the electric field, D is the electric displacement, and i, r, and t in the subscript denote incident, reflected, and transmitted beams, respectively. Both ω_1 and ω_2 beams satisfy these boundary conditions independently from each other. As can be seen from these equations, the electric field gradient in X and Y directions are zero. For the Z direction, the boundary condition is given in terms of the electric displacement, which can be related to the electric field using the refractive index of the medium at the height Z, $n(\omega; Z)$ ($n(\omega; Z) = n_a(\omega)$ in the air and $n(\omega; Z) = n_b(\omega)$ in the bulk liquid), as

$$D_Z = \varepsilon_0 n(\omega; Z)^2 E_Z \tag{5.71}$$

$$= \varepsilon_0 n_a(\omega)^2 (E_{\mathrm{i}Z} + E_{\mathrm{r}Z}) = \varepsilon_0 n_b(\omega)^2 E_{\mathrm{t}Z}. \tag{5.72}$$

Because of the refractive index mismatch of the bonding media ($n_a(\omega) \neq n_b(\omega)$), the Z component of the electric field has a large gradient in the Z direction.

$$\frac{\partial E_J}{\partial L} = 0 \qquad (J \neq Z \text{ or } L \neq Z), \tag{5.73}$$

$$\frac{\partial E_Z}{\partial Z} = \frac{D_Z}{\varepsilon_0} \frac{\partial (1/n(\omega; Z)^2)}{\partial Z} = n_b(\omega)^2 E_{\mathrm{t}Z} \frac{\partial (1/n(\omega; Z)^2)}{\partial Z}. \tag{5.74}$$

Since an infinitesimally thin interface is now considered, the derivative can be replaced by Dirac's delta function.

$$\frac{\partial(1/n(\omega;Z)^2)}{\partial Z} = \left(\frac{1}{n_a(\omega)^2} - \frac{1}{n_b(\omega)^2}\right)\delta(Z), \tag{5.75}$$

and hence

$$\frac{\partial E_Z}{\partial Z} = \left(\frac{n_b(\omega)^2}{n_a(\omega)^2} - 1\right)E_{\mathrm{t}Z}\delta(Z), \tag{5.76}$$

where the coefficient of the delta function was chosen so that the integration across the interface results in the same value as the original formula.

$$\int_{-\infty}^{\infty} dZ \frac{\partial(1/n(\omega;Z)^2)}{\partial Z} = \frac{1}{n_a(\omega)^2} - \frac{1}{n_b(\omega)^2} = \int_{-\infty}^{\infty} dZ \left(\frac{1}{n_a(\omega)^2} - \frac{1}{n_b(\omega)^2}\right)\delta(Z). \tag{5.77}$$

The derivative of the induced quadrupole in Eq. (5.67) can be evaluated in the same manner by noticing that the derivative in the Z direction can be replaced by a delta function because of the discontinuity of the induced quadrupole at the interface.

$$\frac{\partial}{\partial L}\left(\chi^{(2),\mathrm{quad3}}_{IJKL}E_{1J}E_{2K}\right) = 0 \qquad (L \neq Z), \tag{5.78}$$

$$\begin{aligned}
&\frac{\partial}{\partial Z}\left(\chi^{(2),\mathrm{quad3}}_{IJKZ}E_{1J}E_{2K}\right) \\
&\quad= \left\{\chi^{(2),\mathrm{quad3}}_{IJKZ}(\mathrm{air})(E_{1\mathrm{i}J}+E_{1\mathrm{r}J})(E_{2\mathrm{i}K}+E_{2\mathrm{r}K}) - \chi^{(2),\mathrm{quad3}}_{IJKZ}(\mathrm{bulk})E_{1\mathrm{t}J}E_{2\mathrm{t}K}\right\}\delta(Z) &(5.79)\\
&\quad= -\chi^{(2),\mathrm{quad3}}_{IJKZ}(\mathrm{bulk})E_{1\mathrm{t}J}E_{2\mathrm{t}K}\delta(Z). &(5.80)
\end{aligned}$$

Here, the nonlinear susceptibilities above ($Z > 0$) and below ($Z > 0$) the interface were denoted as

$$\chi^{(2),\mathrm{quad3}}_{IJKZ} = \begin{cases}\chi^{(2),\mathrm{quad3}}_{IJKZ}(\mathrm{air}) & (Z > 0),\\ \chi^{(2),\mathrm{quad3}}_{IJKZ}(\mathrm{bulk}) & (Z < 0),\end{cases} \tag{5.81}$$

and $\chi^{(2),\mathrm{quad3}}_{IJKZ}(\mathrm{air})$ was taken to be zero because the nonlinearity of the air is usually negligibly smaller than that of the bulk liquid. In summary, the quadrupole contribution to the induced nonlinear polarization can be given as

$$\begin{aligned}
P^{(2),\mathrm{quad}}_I = {}& \varepsilon_0\chi^{(2),\mathrm{quad1}}_{IZIZ}\left(\frac{n_b(\omega_1)^2}{n_a(\omega_1)^2} - 1\right)E_{1\mathrm{t}Z}\delta(Z)E_{2I}\\
&+ \varepsilon_0\chi^{(2),\mathrm{quad2}}_{IIZZ}E_{1I}\left(\frac{n_b(\omega_2)^2}{n_a(\omega_2)^2} - 1\right)E_{2\mathrm{t}Z}\delta(Z)\\
&+ \varepsilon_0\sum_{J,K}\chi^{(2),\mathrm{quad3}}_{IJKZ}(\mathrm{bulk})E_{1\mathrm{t}J}E_{2\mathrm{t}K}\delta(Z).
\end{aligned} \tag{5.82}$$

Here, all the tensor elements except for $\chi^{(2),\mathrm{quad}}_{IIJJ}$, $\chi^{(2),\mathrm{quad}}_{IJIJ}$, $\chi^{(2),\mathrm{quad}}_{IJJI}$, and $\chi^{(2),\mathrm{quad}}_{IIII}$ were taken to be zero because they can be proven to vanish at the in-plane isotropic interfaces due to the polar vector nature of the polarization and the electric field in the same manner as in Section 2.3. The delta functions in this expression explicitly show that the nonlinear polarization is localized at the interface ($Z = 0$).

This interface selectivity is due to the discontinuity of the medium at the interface, and it has nothing to do with the breakdown of the inversion symmetry, which is the origin of VSFG in the ordinary dipolar mechanism.

The nonlinear polarization evaluated above is the polarization per unit volume. Meanwhile, it is more convenient to use the surface nonlinear polarization, which is the polarization per unit surface area, in the evaluation of the sum frequency electric field emitted from the induced polarization. When the interface layer is regarded to be infinitesimally thin as in the present case, the surface nonlinear polarization $P_S^{(2)}$ is defined in terms of the polarization per volume $P^{(2)}$ as [39]

$$P_{S,I}^{(2)} = \int_{-\infty}^{\infty} dZ P_I^{(2)}. \tag{5.83}$$

According to this definition, the surface nonlinear polarization arising from a quadrupole contribution can be evaluated as

$$\begin{aligned} P_{S,I}^{(2),\mathrm{quad}} = {} & \varepsilon_0 \left(\frac{n_b(\omega_1)^2}{n_a(\omega_1)^2} - 1 \right) \chi_{IZIZ}^{(2),\mathrm{quad1}}(\mathrm{interface}) E_{1\mathrm{t}Z} E'_{2I} \\ & + \varepsilon_0 \left(\frac{n_b(\omega_2)^2}{n_a(\omega_2)^2} - 1 \right) \chi_{IIZZ}^{(2),\mathrm{quad2}}(\mathrm{interface}) E'_{1I} E_{2\mathrm{t}Z} \\ & + \varepsilon_0 \sum_{J,K} \chi_{IJKZ}^{(2),\mathrm{quad3}}(\mathrm{bulk}) E_{1\mathrm{t}J} E_{2\mathrm{t}K}. \end{aligned} \tag{5.84}$$

Here, E'_{1I} and E'_{2I} are the electric field of ω_1 and ω_2 beams at the interface, respectively, and $\chi_{IZIZ}^{(2),\mathrm{quad1}}$(interface) and $\chi_{IIZZ}^{(2),\mathrm{quad2}}$(interface) are the nonlinear susceptibilities due to the interfacial molecules. They are ascribed to the interfacial properties at $Z = 0$ because of the delta functions in Eq. (5.82). An interesting point here is that $\chi_{IJKZ}^{(2),\mathrm{quad3}}$ in Eq. (5.84) reflects the bulk properties while $\chi_{IZIZ}^{(2),\mathrm{quad1}}$ and $\chi_{IIZZ}^{(2),\mathrm{quad2}}$ reflect interfacial properties, although they all contribute to the nonlinear polarization localized at the interface. In exactly the same manner as in Section 2.4.2, the electric field at the interface E'_I can be conveniently expressed in terms of the incident electric field $E_{\mathrm{i}I}$ as

$$E'_I = L_I^{\omega} E_{\mathrm{i}I}, \tag{5.85}$$

where L_I^{ω} is the interfacial Fresnel factor defined as [39]

$$L_X^{\omega} = \frac{2n_a(\omega)\cos\theta_{\mathrm{t}}}{n_a(\omega)\cos\theta_{\mathrm{t}} + n_b(\omega)\cos\theta_{\mathrm{i}}}, \tag{5.86}$$

$$L_Y^{\omega} = \frac{2n_a(\omega)\cos\theta_{\mathrm{i}}}{n_a(\omega)\cos\theta_{\mathrm{i}} + n_b(\omega)\cos\theta_{\mathrm{t}}}, \tag{5.87}$$

$$L_Z^{\omega} = \frac{2n_b(\omega)\cos\theta_{\mathrm{i}}}{n_a(\omega)\cos\theta_{\mathrm{t}} + n_b(\omega)\cos\theta_{\mathrm{i}}} \left(\frac{n_a(\omega)}{n'(\omega)} \right)^2, \tag{5.88}$$

with $n'(\omega)$ being the refractive index of the interface. The electric field of the transmitted light $E_{\mathrm{t}I}$ can be expressed in a similar manner using the transmission Fresnel factors F_I^{ω} as in Section 2.5.2, which can be obtained by replacing $n'(\omega)$ in the interface Fresnel factors with $n_b(\omega)$ [49]:

$$E_{\mathrm{t}I} = F_I^{\omega} E_{\mathrm{i}I}, \tag{5.89}$$

with

$$F_X^\omega = \frac{2n_a(\omega)\cos\theta_\mathrm{t}}{n_a(\omega)\cos\theta_\mathrm{t} + n_b(\omega)\cos\theta_\mathrm{i}} = L_X^\omega, \tag{5.90}$$

$$F_Y^\omega = \frac{2n_a(\omega)\cos\theta_\mathrm{i}}{n_a(\omega)\cos\theta_\mathrm{i} + n_b(\omega)\cos\theta_\mathrm{t}} = L_Y^\omega, \tag{5.91}$$

$$F_Z^\omega = \frac{2n_b(\omega)\cos\theta_\mathrm{i}}{n_a(\omega)\cos\theta_\mathrm{t} + n_b(\omega)\cos\theta_\mathrm{i}} \left(\frac{n_a(\omega)}{n_b(\omega)}\right)^2 = \left(\frac{n'(\omega)}{n_b(\omega)}\right)^2 L_Z^\omega. \tag{5.92}$$

Finally, the surface nonlinear polarization in Eq. (5.84) can be expressed in a simplified form using the incident electric fields, instead of the interfacial and transmitted electric fields, as

$$\begin{aligned} P_{S,I}^{(2),\mathrm{quad}} = {} & \varepsilon_0 L_Z^{\omega_1} L_I^{\omega_2} \frac{n'(\omega_1)^2}{n_b(\omega_1)^2} \left(\frac{n_b(\omega_1)^2}{n_a(\omega_1)^2} - 1\right) \chi_{IZIZ}^{\mathrm{quad1}}(\mathrm{interface}) E_{1\mathrm{i}Z} E_{2\mathrm{i}I} \\ & + \varepsilon_0 L_I^{\omega_1} L_Z^{\omega_2} \frac{n'(\omega_2)^2}{n_b(\omega_2)^2} \left(\frac{n_b(\omega_2)^2}{n_a(\omega_2)^2} - 1\right) \chi_{IIZZ}^{\mathrm{quad2}}(\mathrm{interface}) E_{1\mathrm{i}I} E_{2\mathrm{i}Z} \\ & + \varepsilon_0 \sum_{J,K} F_J^{\omega_1} F_K^{\omega_2} \chi_{IJKZ}^{\mathrm{quad3}}(\mathrm{bulk}) E_{1\mathrm{i}J} E_{2\mathrm{i}K}. \end{aligned} \tag{5.93}$$

This equation shows that three terms contribute to the surface nonlinear polarization. These three ways of contributions will be referred to as the quad1, quad2, and quad3 mechanisms in this thesis.

In this derivation, the simple formula in Eq. (5.83) was used to define the surface nonlinear polarization. On the other hand, Shen claims that the following definition should be used to evaluate the surface nonlinear polarization when the nonlocality of the electric field, i.e. the position dependence of the electric field, is concerned [87]:

$$P_{S,I}^{(2)} = \int_\mathrm{int} dZ f_I(Z) P_I^{(2)}, \tag{5.94}$$

where

$$f_I(Z) = \begin{cases} 1 & (I \neq Z), \\ \frac{n'(\omega_3)^2}{n(\omega_3;Z)^2} & (I = Z), \end{cases} \tag{5.95}$$

and the integration is done only inside the interface. Here, $\omega_3 (= \omega_1 + \omega_2)$ denotes the sum frequency. The function $f_I(Z)$ was introduced because the emitted sum frequency electric field in the Z direction depends on the refractive index $n(\omega_3; Z)$ at the position where the sum frequency was generated. This effect was neglected in my simple definition, and I assumed that the refractive index is equal to $n'(\omega_3)$ everywhere inside the interface. In the limit of an infinitesimally thin interface, however, the definition in Eq. (5.94) gives exactly the same result as my definition in Eq. (5.83). This is because the nonlinear polarization has a delta function distribution along the Z axis in the infinitesimally thin interface approximation as shown in Eq. (5.82), and only $f_I(Z = 0) = 1$ $(I = X, Y, Z)$ contributes to the integration in Eq. (5.94), with the interfacial refractive index defined as

$$n'(\omega_3) \equiv n(\omega_3; Z = 0). \tag{5.96}$$

This result shows that the Z dependence of the sum frequency electric field, which arises from the Z dependence of $n(\omega_3; Z)$, does not have any effect on the surface nonlinear polarization in the infinitesimally thin interface approximation.

In summary, the surface nonlinear polarization due to a quadrupole contribution can be expressed in terms of the quad1, quad2, and quad3 mechanisms as in Eq. (5.93), wherein the quad1 and quad2 mechanisms reflect the interfacial properties, while the quad3 mechanism reflects the bulk properties. Hereafter, (interface) and (bulk) will be omitted from the nonlinear susceptibilities for simplicity.

5.5 Polarization dependence of the effective nonlinear susceptibility

In VSFG spectroscopy, the polarization direction of the electric field is usually discussed in terms of S and P, instead of the Cartesian coordinates X, Y, and Z shown in Fig. 5.1(a). The electric field of the S-polarized light, E_{S}, is perpendicular to the plane of incidence, and the electric field of the P-polarized light, E_{P}, oscillates within the plane of incidence. For the incident electric fields (ω_1 and ω_2), E_{S} and E_{P} can be related to E_X, E_Y, and E_Z as

$$E_{\mathrm{S}} = E_Y, \tag{5.97}$$

$$E_{\mathrm{P}} = E_X \cos\theta_{\mathrm{i}} + E_Z \sin\theta_{\mathrm{i}}, \tag{5.98}$$

or alternatively,

$$E_X = E_{\mathrm{P}} \cos\theta_{\mathrm{i}}, \tag{5.99}$$

$$E_Y = E_{\mathrm{S}}, \tag{5.100}$$

$$E_Z = E_{\mathrm{P}} \sin\theta_{\mathrm{i}}. \tag{5.101}$$

These relations can be used to rewrite the polarization direction of the incident electric fields in Eq. (5.93) in terms of S and P. Remembering that the tensor elements of $\chi^{(2),\mathrm{quad3}}$ take nonzero values only for $\chi^{(2),\mathrm{quad3}}_{IIJJ}$, $\chi^{(2),\mathrm{quad3}}_{IJIJ}$, $\chi^{(2),\mathrm{quad3}}_{IJJI}$, and $\chi^{(2),\mathrm{quad3}}_{IIII}$, the surface nonlinear polarization for X, Y, and Z directions can be obtained as shown below.

$$\begin{aligned} P^{(2),\mathrm{quad}}_{S,X} = {} & \varepsilon_0 L^{\omega_1}_Z L^{\omega_2}_X \sin\theta_{1\mathrm{i}} \cos\theta_{2\mathrm{i}} \frac{n'(\omega_1)^2}{n_b(\omega_1)^2} \left\{ \left(\frac{n_b(\omega_1)^2}{n_a(\omega_1)^2} - 1 \right) \chi^{(2),\mathrm{quad1}}_{XZXZ} + \chi^{(2),\mathrm{quad3}}_{XZXZ} \right\} E_{1\mathrm{iP}} E_{2\mathrm{iP}} \\ & + \varepsilon_0 L^{\omega_1}_X L^{\omega_2}_Z \cos\theta_{1\mathrm{i}} \sin\theta_{2\mathrm{i}} \frac{n'(\omega_2)^2}{n_b(\omega_2)^2} \left\{ \left(\frac{n_b(\omega_2)^2}{n_a(\omega_2)^2} - 1 \right) \chi^{(2),\mathrm{quad2}}_{XXZZ} + \chi^{(2),\mathrm{quad3}}_{XXZZ} \right\} E_{1\mathrm{iP}} E_{2\mathrm{iP}}, \end{aligned} \tag{5.102}$$

$$\begin{aligned} P^{(2),\mathrm{quad}}_{S,Y} = {} & \varepsilon_0 L^{\omega_1}_Z L^{\omega_2}_Y \sin\theta_{1\mathrm{i}} \frac{n'(\omega_1)^2}{n_b(\omega_1)^2} \left\{ \left(\frac{n_b(\omega_1)^2}{n_a(\omega_1)^2} - 1 \right) \chi^{(2),\mathrm{quad1}}_{YZYZ} + \chi^{(2),\mathrm{quad3}}_{YZYZ} \right\} E_{1\mathrm{iP}} E_{2\mathrm{iS}} \\ & + \varepsilon_0 L^{\omega_1}_Y L^{\omega_2}_Z \sin\theta_{2\mathrm{i}} \frac{n'(\omega_2)^2}{n_b(\omega_2)^2} \left\{ \left(\frac{n_b(\omega_2)^2}{n_a(\omega_2)^2} - 1 \right) \chi^{(2),\mathrm{quad2}}_{YYZZ} + \chi^{(2),\mathrm{quad3}}_{YYZZ} \right\} E_{1\mathrm{iS}} E_{2\mathrm{iP}}, \end{aligned} \tag{5.103}$$

$$P^{(2),\mathrm{quad}}_{S,Z} = \varepsilon_0 \Big[L^{\omega_1}_X L^{\omega_2}_X \cos\theta_{1\mathrm{i}} \cos\theta_{2\mathrm{i}} \chi^{(2),\mathrm{quad3}}_{ZXXZ} + L^{\omega_1}_Z L^{\omega_2}_Z \sin\theta_{1\mathrm{i}} \sin\theta_{2\mathrm{i}}$$

$$
\begin{aligned}
&\times \left\{ \frac{n'(\omega_1)^2}{n_b(\omega_1)^2} \left(\frac{n_b(\omega_1)^2}{n_a(\omega_1)^2} - 1 \right) \chi^{(2),\mathrm{quad1}}_{ZZZZ} + \frac{n'(\omega_2)^2}{n_b(\omega_2)^2} \left(\frac{n_b(\omega_2)^2}{n_a(\omega_2)^2} - 1 \right) \chi^{(2),\mathrm{quad2}}_{ZZZZ} \right. \\
&\left. + \frac{n'(\omega_1)^2 n'(\omega_2)^2}{n_b(\omega_1)^2 n_b(\omega_2)^2} \chi^{(2),\mathrm{quad3}}_{ZZZZ} \right\] E_{1\mathrm{iP}} E_{2\mathrm{iP}} \\
&+ \varepsilon_0 L^{\omega_1}_Y L^{\omega_2}_Y \chi^{(2),\mathrm{quad3}}_{ZYYZ} E_{1\mathrm{iS}} E_{2\mathrm{iS}}. \qquad (5.104)
\end{aligned}
$$

From these induced polarizations, the sum frequency light is emitted. The emitted sum frequency (ω_3) electric field in S- and P-polarization directions can be respectively expressed in the same manner as the dipolar case in Section 2.4.4 using the surface nonlinear polarization as

$$
E_{3\mathrm{rS}} = \frac{i\omega_3}{2cn_a(\omega_3)\cos\theta_{3\mathrm{r}}} \frac{1}{\varepsilon_0} L^{\omega_3}_Y P^{(2),\mathrm{quad}}_{S,Y}, \qquad (5.105)
$$

$$
E_{3\mathrm{rP}} = \frac{i\omega_3}{2cn_a(\omega_3)\cos\theta_{3\mathrm{r}}} \frac{1}{\varepsilon_0} \left(-\cos\theta_{3\mathrm{r}} L^{\omega_3}_X P^{(2),\mathrm{quad}}_{S,X} + \sin\theta_{3\mathrm{r}} L^{\omega_3}_Z P^{(2),\mathrm{quad}}_{S,Z} \right). \qquad (5.106)
$$

By substituting $P^{(2),\mathrm{quad}}_{S,I}$ in Eqs. (5.102)-(5.104) into these expressions, the sum frequency electric field can be expressed by the nonlinear susceptibilities and the incident electric fields. It can be seen from the derived result that VSFG due to a quadrupole contribution occurs only for SSP, SPS, PSS, and PPP polarization combinations (the first, second, and third letters correspond to the polarization direction of ω_3, ω_1, and ω_2, respectively), which is exactly the same as ordinary VSFG within the dipole approximation. The four nonzero effective nonlinear susceptibilities, $\chi^{(2)}_{\mathrm{eff,SSP}}$, $\chi^{(2)}_{\mathrm{eff,SPS}}$, $\chi^{(2)}_{\mathrm{eff,PSS}}$, and $\chi^{(2)}_{\mathrm{eff,PPP}}$, can then be defined using the following equations [89].

$$
E_{3\mathrm{rS}} = \frac{i\omega_3}{2cn_a(\omega_3)\cos\theta_{3\mathrm{r}}} \left(\chi^{(2)}_{\mathrm{eff,SSP}} E_{1\mathrm{iS}} E_{2\mathrm{iP}} + \chi^{(2)}_{\mathrm{eff,SPS}} E_{1\mathrm{iP}} E_{2\mathrm{iS}} \right), \qquad (5.107)
$$

$$
E_{3\mathrm{rP}} = \frac{i\omega_3}{2cn_a(\omega_3)\cos\theta_{3\mathrm{r}}} \left(\chi^{(2)}_{\mathrm{eff,PSS}} E_{1\mathrm{iS}} E_{2\mathrm{iS}} + \chi^{(2)}_{\mathrm{eff,PPP}} E_{1\mathrm{iP}} E_{2\mathrm{iP}} \right). \qquad (5.108)
$$

Comparing these equations, the effective nonlinear susceptibilities for all the four polarization combinations can be obtained.

$$
\chi^{(2)}_{\mathrm{eff,SSP}} = L^{\omega_3}_Y L^{\omega_1}_Y L^{\omega_2}_Z \sin\theta_{2\mathrm{i}} \frac{n'(\omega_2)^2}{n_b(\omega_2)^2} \left\{ \left(\frac{n_b(\omega_2)^2}{n_a(\omega_2)^2} - 1 \right) \chi^{(2),\mathrm{quad2}}_{YYZZ} + \chi^{(2),\mathrm{quad3}}_{YYZZ} \right\}, \qquad (5.109)
$$

$$
\chi^{(2)}_{\mathrm{eff,SPS}} = L^{\omega_3}_Y L^{\omega_1}_Z L^{\omega_2}_Y \sin\theta_{1\mathrm{i}} \frac{n'(\omega_1)^2}{n_b(\omega_1)^2} \left\{ \left(\frac{n_b(\omega_1)^2}{n_a(\omega_1)^2} - 1 \right) \chi^{(2),\mathrm{quad1}}_{YZYZ} + \chi^{(2),\mathrm{quad3}}_{YZYZ} \right\}, \qquad (5.110)
$$

$$
\chi^{(2)}_{\mathrm{eff,PSS}} = L^{\omega_3}_Z L^{\omega_1}_Y L^{\omega_2}_Y \sin\theta_{3\mathrm{r}} \chi^{(2),\mathrm{quad3}}_{ZYYZ}, \qquad (5.111)
$$

$$
\begin{aligned}
\chi^{(2)}_{\mathrm{eff,PPP}} = &- L^{\omega_3}_X L^{\omega_1}_Z L^{\omega_2}_X \cos\theta_{3\mathrm{r}} \sin\theta_{1\mathrm{i}} \cos\theta_{2\mathrm{i}} \frac{n'(\omega_1)^2}{n_b(\omega_1)^2} \left\{ \left(\frac{n_b(\omega_1)^2}{n_a(\omega_1)^2} - 1 \right) \chi^{(2),\mathrm{quad1}}_{XZXZ} + \chi^{(2),\mathrm{quad3}}_{XZXZ} \right\} \\
&- L^{\omega_3}_X L^{\omega_1}_X L^{\omega_2}_Z \cos\theta_{3\mathrm{r}} \cos\theta_{1\mathrm{i}} \sin\theta_{2\mathrm{i}} \frac{n'(\omega_2)^2}{n_b(\omega_2)^2} \left\{ \left(\frac{n_b(\omega_2)^2}{n_a(\omega_2)^2} - 1 \right) \chi^{(2),\mathrm{quad2}}_{XXZZ} + \chi^{(2),\mathrm{quad3}}_{XXZZ} \right\} \\
&+ L^{\omega_3}_Z L^{\omega_1}_X L^{\omega_2}_X \sin\theta_{3\mathrm{r}} \cos\theta_{1\mathrm{i}} \cos\theta_{2\mathrm{i}} \chi^{(2),\mathrm{quad3}}_{ZXXZ} \\
&+ L^{\omega_3}_Z L^{\omega_1}_Z L^{\omega_2}_Z \sin\theta_{3\mathrm{r}} \sin\theta_{1\mathrm{i}} \sin\theta_{2\mathrm{i}} \left\{ \frac{n'(\omega_1)^2}{n_b(\omega_1)^2} \left(\frac{n_b(\omega_1)^2}{n_a(\omega_1)^2} - 1 \right) \chi^{(2),\mathrm{quad1}}_{ZZZZ} \right. \\
&\left. + \frac{n'(\omega_2)^2}{n_b(\omega_2)^2} \left(\frac{n_b(\omega_2)^2}{n_a(\omega_2)^2} - 1 \right) \chi^{(2),\mathrm{quad2}}_{ZZZZ} + \frac{n'(\omega_1)^2 n'(\omega_2)^2}{n_b(\omega_1)^2 n_b(\omega_2)^2} \chi^{(2),\mathrm{quad3}}_{ZZZZ} \right\}. \qquad (5.112)
\end{aligned}
$$

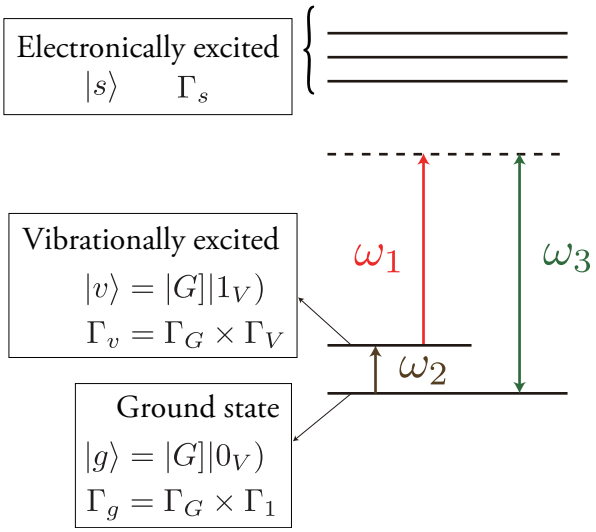

Figure 5.2: The energy levels involved in the optical process of VSFG. $|\cdot\rangle$ is the vibronic ket, $|\cdot]$ is the electronic ket, and $|n_V)$ is the vibrational ket with a vibrational quantum number of n for a normal mode V. The corresponding representations for each state are also shown.

These complex effective nonlinear susceptibilities are directly measurable by the experiments using HD-VSFG spectroscopy, and the theoretical predictions as to what kind of spectra will be observed can be made based on these theoretical expressions. For example, it can be predicted that only the bulk molecules should be detectable in the PSS polarization combination while both bulk and interface molecules may contribute to the spectra in other polarization combinations. This is because, as have already been shown in the previous section, $\chi^{(2),\mathrm{quad1}}$ and $\chi^{(2),\mathrm{quad2}}$ give interfacial contributions whereas $\chi^{(2),\mathrm{quad3}}$ gives a bulk contribution. In fact, a much more detailed selection rule can be derived by analyzing the microscopic expressions for $\chi^{(2),\mathrm{quad1}}$, $\chi^{(2),\mathrm{quad2}}$, and $\chi^{(2),\mathrm{quad3}}$ using the group theory.

5.6 Microscopic expressions for the quadrupolar nonlinear susceptibilities

It was shown earlier in this chapter that the microscopic expressions for $\chi^{(2),\mathrm{quad1}}$, $\chi^{(2),\mathrm{quad2}}$, and $\chi^{(2),\mathrm{quad3}}$ can be given as

$$\chi^{(2),\mathrm{quad1}}_{IJKL} = \frac{N}{\varepsilon_0} \sum_{i,j,k,l} \langle R_{Ii} R_{Jj} R_{Kk} R_{Ll} \rangle_{\mathrm{av}} \beta^{\mathrm{quad1}}_{ijkl}, \tag{5.113}$$

$$\chi^{(2),\mathrm{quad2}}_{IJKL} = \frac{N}{\varepsilon_0} \sum_{i,j,k,l} \langle R_{Ii} R_{Jj} R_{Kk} R_{Ll} \rangle_{\mathrm{av}} \beta^{\mathrm{quad2}}_{ijkl}, \tag{5.114}$$

$$\chi^{(2),\mathrm{quad3}}_{IJKL} = \frac{N}{\varepsilon_0} \sum_{i,j,k,l} \langle R_{Ii} R_{Jj} R_{Kk} R_{Ll} \rangle_{\mathrm{av}} \beta^{\mathrm{quad3}}_{ijkl}, \tag{5.115}$$

where I, J, K, and L are the laboratory-fixed coordinates, i, j, k, and l are the molecular-fixed coordinates, N is the number of molecules per unit volume, R_{Ii} is a rotation matrix, $\langle R_{Ii} R_{Jj} R_{Kk} R_{Ll} \rangle_{\mathrm{av}}$ is the product of four rotation matrices averaged over all the molecules, and $\beta^{\mathrm{quad1}}_{ijkl}$, $\beta^{\mathrm{quad2}}_{ijkl}$, and $\beta^{\mathrm{quad3}}_{ijkl}$

are the molecular hyperpolarizability tensors with a quadrupole contribution. An important thing to note here is that $\langle R_{Ii}R_{Jj}R_{Kk}R_{Ll}\rangle_{\rm av}$ is nonzero even when the molecules have a random orientation and the inversion symmetry exists in the system. In this case, the sign of $\chi^{(2),\rm quad}$ is determined by the sign of the hyperpolarizability $\beta^{\rm quad}$, and it is irrelevant to the molecular orientation. It is instructive to compare these quadrupolar nonlinear susceptibilities with the ordinary dipolar susceptibility:

$$\chi^{(2),\rm dipole}_{IJK} = \frac{N}{\varepsilon_0}\sum_{i,j,k}\langle R_{Ii}R_{Jj}R_{Kk}\rangle_{\rm av}\beta^{\rm dipole}_{ijk}. \tag{5.116}$$

In the dipolar susceptibility, the rotation matrices appear only three times, and the average $\langle R_{Ii}R_{Jj}R_{Kk}\rangle_{\rm av}$ becomes zero when molecules are randomly oriented [18, 19, 37], which is the origin of the interface selectivity in ordinary dipolar VSFG. The sign of $\chi^{(2),\rm dipole}$ reflects the absolute orientation of molecules at the interface which is given by $\langle R_{Ii}R_{Jj}R_{Kk}\rangle_{\rm av}$ [18, 19]. This comparison indicates that the quadrupolar mechanism should give a predominant contribution to VSFG when the molecules are randomly oriented at the interface.

Further differences between the quadrupolar and dipolar mechanisms can be found in the selection rule by examining the quadrupolar molecular hyperpolarizabilities in Eq. (5.113)-(5.115) that are explicitly given as

$$\beta^{\rm quad1}_{ijkl} = \sum_{s,v}\frac{\langle g|\hat{\mu}_i|s\rangle\langle s|\hat{q}_{jl}|v\rangle\langle v|\hat{\mu}_k|s\rangle}{(\varepsilon_v-\varepsilon_g-\hbar\omega_2-i\gamma_{vg})(\varepsilon_s-\varepsilon_g-\hbar\omega_3-i\gamma_{sg})}, \tag{5.117}$$

$$\beta^{\rm quad2}_{ijkl} = \sum_{s,v}\frac{\langle g|\hat{\mu}_i|s\rangle\langle s|\hat{\mu}_j|v\rangle\langle v|\hat{q}_{kl}|s\rangle}{(\varepsilon_v-\varepsilon_g-\hbar\omega_2-i\gamma_{vg})(\varepsilon_s-\varepsilon_g-\hbar\omega_3-i\gamma_{sg})}, \tag{5.118}$$

$$\beta^{\rm quad3}_{ijkl} = \sum_{s,v}\frac{\langle g|\hat{q}_{il}|s\rangle\langle s|\hat{\mu}_j|v\rangle\langle v|\hat{\mu}_k|s\rangle}{(\varepsilon_v-\varepsilon_g-\hbar\omega_2-i\gamma_{vg})(\varepsilon_s-\varepsilon_g-\hbar\omega_3-i\gamma_{sg})}, \tag{5.119}$$

where $|g\rangle$, $|v\rangle$, and $|s\rangle$ are the vibronic kets of the ground state, a vibrationally excited state, and an electronically excited state, respectively, as shown in Fig. 5.2, $\hat{\mu}$ and $\hat{q}$ are the transition dipole and quadrupole moment operators, respectively, ε_m is the eigneenergy of the eigenvector $|m\rangle$, and γ_{nm} is the damping constant. Meanwhile, the ordinary dipolar hyperpolarizability in Eq. (5.116) can be expressed as

$$\beta^{\rm dipole}_{ijk} = \sum_{s,v}\frac{\langle g|\hat{\mu}_i|s\rangle\langle s|\hat{\mu}_j|v\rangle\langle v|\hat{\mu}_k|s\rangle}{(\varepsilon_v-\varepsilon_g-\hbar\omega_2-i\gamma_{vg})(\varepsilon_v-\varepsilon_g-\hbar\omega_3-i\gamma_{sg})}. \tag{5.120}$$

The transition is considered to be allowed if the hyperpolarizability tensor has at least one nonzero tensor element. Thus, the selection rules can be derived by considering the group theoretical condition for the hyperpolarizabilities to have a nonzero tensor element.

In the group theory, a representation is assigned to each of the bra and ket vectors and the dipole and quadrupole moment operators. For the dipole and quadrupole moment operators, the representations can be determined by expressing the operators using the charge and the intramolecular coordinate operators

as

$$\hat{\mu}_i = \sum_n z_n \Delta\hat{r}_{n,i}, \tag{5.121}$$

$$\hat{q}_{ij} = \sum_n \frac{z_n}{2} \Delta\hat{r}_{n,i} \Delta\hat{r}_{n,j}. \tag{5.122}$$

Here, z_n is the charge of the nth particle (a nucleus or an electron which constitutes the molecule), and $\Delta\hat{r}_{n,i}$ is a coordinate operator in the i direction for the nth particle. Because the coordinate operator $\Delta\hat{r}_{n,i}$ belongs to the irreducible representation Γ_i, the representations for the dipole and quadrupole moment operators are

$$\hat{\mu}_i \in \Gamma_i, \tag{5.123}$$

$$\hat{q}_{ij} \in \Gamma_i \times \Gamma_j, \tag{5.124}$$

where $\times$ denotes taking the direct product between the two representations. Bra and ket vectors are eigenvectors of the Hamiltonian, and they belong to an irreducible representation Γ_s.

$$\langle s| \in \Gamma_s, \tag{5.125}$$

$$|s\rangle \in \Gamma_s. \tag{5.126}$$

Then, the group theoretical requirement for $\langle a|\hat{\mu}_i|b\rangle \neq 0$, for example, is

$$\Gamma_a \times \Gamma_i \times \Gamma_b \supset \Gamma_1. \tag{5.127}$$

Here, Γ_1 is the totally symmetric representation. The dipole transition from $|b\rangle$ to $|a\rangle$ is said to be allowed when this condition is satisfied for at least one element i, which can be mathematically expressed as

$$\Gamma_a \times \sum_i \Gamma_i \times \Gamma_b \supset \Gamma_1. \tag{5.128}$$

Using these equations, the selection rules for the dipolar mechanism and for the quadrupolar mechanisms (quad1, quad2, and quad3) can be derived as shown below.

5.6.1 The dipolar mechanism

From Eq. (5.120), the following relations need to be satisfied for some sets of suffixes, i, j, and k, to have nonzero $\chi^{(2),\mathrm{dipole}}_{IJK}$.

$$\langle g|\hat{\mu}_i|s\rangle \neq 0, \tag{5.129}$$

$$\langle s|\hat{\mu}_j|v\rangle \neq 0, \tag{5.130}$$

$$\langle v|\hat{\mu}_k|g\rangle \neq 0. \tag{5.131}$$

Group theoretically, these conditions can be expressed as

$$\Gamma_g \times \sum_i \Gamma_i \times \Gamma_s \supset \Gamma_1, \tag{5.132}$$

$$\Gamma_s \times \sum_j \Gamma_j \times \Gamma_v \supset \Gamma_1, \tag{5.133}$$

$$\Gamma_v \times \sum_k \Gamma_k \times \Gamma_g \supset \Gamma_1. \tag{5.134}$$

From the first equation, we obtain

$$\Gamma_s \subset \Gamma_g \times \sum_i \Gamma_i. \tag{5.135}$$

Then, combined with the second equation,

$$\Gamma_v \subset \Gamma_s \times \sum_j \Gamma_j \subset \Gamma_g \times \sum_{i,j} (\Gamma_i \times \Gamma_j) \tag{5.136}$$

is obtained. Meanwhile, from the third equation, the following equation can be derived.

$$\Gamma_v \subset \Gamma_g \times \sum_k \Gamma_k. \tag{5.137}$$

Thus, Eqs. (5.136) and (5.137) specify the requirements for VSFG to occur under the dipolar mechanism with the vibronic state $|v\rangle$ as the intermediate state.

The vibrational selection rule can then be derived from here by expressing the vibronic kets, $|g\rangle$ and $|v\rangle$, as the product of an electronic ket and a vibrational ket under the Born-Oppenheimer approximation.

$$|g\rangle = |G]|0_V), \tag{5.138}$$

$$|v\rangle = |G]|1_V), \tag{5.139}$$

Here, $|G]$ is the electronic ket for the electronic ground state, and $|n_V)$ is the vibrational ket with the vibrational quantum number n for the normal mode V. The vibrational quantum number in the initial state $|g\rangle$ was taken to be zero and the possibility of the hot band was neglected, because I focus on the CH stretch modes in the experimental part in the next chapter, and the excited-state population of the CH stretch modes is negligible at the room temperature. Group theoretically, the definitions in Eqs. (5.138) and (5.139) reduce to

$$\Gamma_g = \Gamma_G \times \Gamma_1, \tag{5.140}$$

$$\Gamma_v = \Gamma_G \times \Gamma_V, \tag{5.141}$$

where Γ_G is the irreducible representation for $|G]$, and Γ_V is the irreducible representation for the normal mode V. It is to be noted that $|0_V)$ belongs to the totally symmetric representation, because the vibrational modes are not excited at all.

By using these equations, the vibrational selection rules corresponding to Eqs. (5.136) and (5.137) can be obtained as

$$\Gamma_V \subset \Gamma_G \times \Gamma_G \times \sum_{i,j} (\Gamma_i \times \Gamma_j), \tag{5.142}$$

$$\Gamma_V \subset \Gamma_G \times \Gamma_G \times \sum_k \Gamma_k. \tag{5.143}$$

These selection rules are identical to those of Raman scattering [94] and IR absorption, respectively. In fact, if the electronic ground state is nondegenerate,

$$\Gamma_G \times \Gamma_G = \Gamma_1, \tag{5.144}$$

and the selection rules are simplified to

$$\Gamma_V \subset \sum_{i,j} (\Gamma_i \times \Gamma_j), \tag{5.145}$$

$$\Gamma_V \subset \sum_k \Gamma_k. \tag{5.146}$$

These are usually known as the selection rules of Raman scattering and IR absorption, whereas Eqs. (5.142) and (5.143) provide more general selection rules that are valid even if the electronic ground state is degenerate.

Since these two conditions need to be satisfied simultaneously, only the vibrational modes that are Raman active and IR active at the same time are allowed in the dipolar mechanism. Additionally, it was already discussed that VSFG due to the dipolar mechanism takes place only at the interfacial region where the inversion symmetry is broken. Hence, the IR active and Raman active modes of interfacial molecules are allowed in the dipolar mechanism.

5.6.2 The quad1 mechanism

From Eq. (5.117), the following inequalities must be simultaneously satisfied for some sets of suffixes, i, j, k, and l, to have nonzero $\chi^{(2),\mathrm{quad1}}_{IJKL}$.

$$\langle g|\hat{\mu}_i|s\rangle \neq 0, \tag{5.147}$$

$$\langle s|\hat{q}_{jl}|v\rangle \neq 0, \tag{5.148}$$

$$\langle v|\hat{\mu}_k|g\rangle \neq 0. \tag{5.149}$$

Group theoretically, these conditions are expressed as

$$\Gamma_g \times \sum_i \Gamma_i \times \Gamma_s \supset \Gamma_1, \tag{5.150}$$

$$\Gamma_s \times \sum_{j,l} (\Gamma_j \times \Gamma_j) \times \Gamma_v \supset \Gamma_1, \tag{5.151}$$

$$\Gamma_v \times \sum_k \Gamma_k \times \Gamma_g \supset \Gamma_1. \tag{5.152}$$

The first equation can be rewritten as

$$\Gamma_s \subset \Gamma_g \times \sum_i \Gamma_i. \tag{5.153}$$

When combined with the second equation,

$$\Gamma_g \times \Gamma_v \times \sum_{i,j,l} (\Gamma_i \times \Gamma_j \times \Gamma_l) \supset \Gamma_1 \tag{5.154}$$

is obtained. By noticing that

$$\sum_{i,j,l} (\Gamma_i \times \Gamma_j \times \Gamma_l) = \sum_i \Gamma_i \times \sum_{j,l} (\Gamma_j \times \Gamma_l) \supset \sum_i \Gamma_i \times \Gamma_1 = \sum_i \Gamma_i, \tag{5.155}$$

the sufficient condition for fulfilling Eqs. (5.150) and (5.151) is found to be

$$\Gamma_g \times \Gamma_v \times \sum_i \Gamma_i \supset \Gamma_1. \tag{5.156}$$

This is identical to Eq. (5.152), and hence this is the requirement for VSFG to occur by the quad1 mechanism. Since this equation is the same as Eq. (5.137), the vibrational selection rule is given by

$$\Gamma_V \subset \Gamma_G \times \Gamma_G \times \sum_k \Gamma_k, \tag{5.157}$$

and the intermediate state $|v\rangle$ in this mechanism needs to involve IR active modes.

In addition to the selection rule derived here, it was already shown that the quad1 mechanism reflects the interfacial properties. Both selection rules combined, it can be finally concluded that the IR active modes of the interfacial molecules are allowed to be detected in the quad1 mechanism.

5.6.3 The quad2 mechanism

From Eq. (5.118), following inequalities must be satisfied for some sets of suffixes, i, j, k, and l, to have nonzero $\chi^{(2),\mathrm{quad2}}_{IJKL}$.

$$\langle g|\hat{\mu}_i|s\rangle \neq 0, \tag{5.158}$$

$$\langle s|\hat{\mu}_j|v\rangle \neq 0, \tag{5.159}$$

$$\langle v|\hat{q}_{kl}|g\rangle \neq 0. \tag{5.160}$$

Group theoretically, these conditions can be expressed as

$$\Gamma_g \times \sum_i \Gamma_i \times \Gamma_s \supset \Gamma_1, \tag{5.161}$$

$$\Gamma_s \times \sum_j \Gamma_j \times \Gamma_v \supset \Gamma_1, \tag{5.162}$$

$$\Gamma_v \times \sum_{k,l} (\Gamma_k \times \Gamma_l) \times \Gamma_g \supset \Gamma_1. \tag{5.163}$$

The first equation is equivalent to

$$\Gamma_s \subset \Gamma_g \times \sum_i \Gamma_i. \tag{5.164}$$

Then, from the second equation,

$$\Gamma_g \times \sum_{i,j} (\Gamma_i \times \Gamma_j) \times \Gamma_v \supset \Gamma_1. \tag{5.165}$$

This is the same as the third equation. Therefore, this is the vibronic selection rule for VSFG due to the quad2 mechanism. Since this equation is identical to Eq. (5.136), the vibrational selection rule is given by

$$\Gamma_V \subset \Gamma_G \times \Gamma_G \times \sum_{i,j} (\Gamma_i \times \Gamma_j), \tag{5.166}$$

which is satisfied by the Raman active modes. Since the interfacial molecules contribute to the nonlinear susceptibility $\chi^{(2),\mathrm{quad2}}$, the Raman active modes of the interfacial molecules are allowed in the quad2 mechanism.

5.6.4 The quad3 mechanism

From Eq. (5.119), following inequalities must be satisfied for some set of suffixes, i, j, k, and l, to have nonzero $\chi^{(2),\mathrm{quad3}}_{IJKL}$.

$$\langle g|\hat{q}_{il}|s\rangle \neq 0, \tag{5.167}$$

$$\langle s|\hat{\mu}_j|v\rangle \neq 0, \tag{5.168}$$

$$\langle v|\hat{\mu}_k|g\rangle \neq 0. \tag{5.169}$$

Group theoretically, these conditions can be expressed as

$$\Gamma_g \times \sum_{i,l} (\Gamma_i \times \Gamma_l) \times \Gamma_s \supset \Gamma_1, \tag{5.170}$$

$$\Gamma_s \times \sum_{j} \Gamma_j \times \Gamma_v \supset \Gamma_1, \tag{5.171}$$

$$\Gamma_v \times \sum_{k} \Gamma_k \times \Gamma_g \supset \Gamma_1. \tag{5.172}$$

If the first equation is rewritten as

$$\Gamma_s \subset \Gamma_g \times \sum_{i,l} (\Gamma_i \times \Gamma_l) \tag{5.173}$$

and combined with the second equation,

$$\Gamma_g \times \sum_{i,j,l} (\Gamma_i \times \Gamma_j \times \Gamma_l) \times \Gamma_v \supset \Gamma_1 \tag{5.174}$$

is obtained. This equation and the third equation are identical to the vibronic selection rule for the quad1 mechanism. Hence, the vibrational selection rule for the quad3 mechanism can also be given by

$$\Gamma_V \subset \Gamma_G \times \Gamma_G \times \sum_{i} \Gamma_i, \tag{5.175}$$

and the IR active modes are allowed. However, unlike in the quad1 mechanism, bulk molecules contribute to the nonlinear susceptibility $\chi^{(2),\mathrm{quad3}}$ as was already shown. Hence, the IR active modes of bulk molecules are allowed to be observed via the quad3 mechanism.

5.7 Polarization dependent selection rule for quadrupole-induced VSFG

Since the VSFG experiments are done using the SSP, SPS, PSS, and PPP polarization combinations, it is practically more useful to determine the vibrational selection rule for the effective nonlinear susceptibilities, $\chi^{(2)}_{\mathrm{eff,SSP}}$, $\chi^{(2)}_{\mathrm{eff,SPS}}$, $\chi^{(2)}_{\mathrm{eff,PSS}}$, and $\chi^{(2)}_{\mathrm{eff,PPP}}$, rather than the bare nonlinear susceptibilities, $\chi^{(2),\mathrm{quad1}}$, $\chi^{(2),\mathrm{quad2}}$, and $\chi^{(2),\mathrm{quad3}}$. This can be done by combining the expressions for the effective nonlinear susceptibilities in Eqs. (5.109)-(5.112) and the selection rule for the bare nonlinear susceptibilities determined in the previous section.

For the SSP polarization combination, $\chi^{(2),\mathrm{quad2}}_{YYZZ}$ and $\chi^{(2),\mathrm{quad3}}_{YYZZ}$ appear in $\chi^{(2)}_{\mathrm{eff,SSP}}$ as can be seen from Eq. (5.109), and thus, the Raman active modes of the interfacial molecules and the IR active modes of the bulk molecules are allowed to be observed. For the SPS polarization combination, $\chi^{(2),\mathrm{quad1}}_{YZYZ}$ and $\chi^{(2),\mathrm{quad3}}_{YZYZ}$ appear in $\chi^{(2)}_{\mathrm{eff,SPS}}$, and the IR active modes of both the interfacial and the bulk molecules are allowed. For the PSS polarization combination, only $\chi^{(2),\mathrm{quad3}}_{ZYYZ}$ contributes to $\chi^{(2)}_{\mathrm{eff,PSS}}$, and only the IR active modes of bulk molecules are allowed to be observed. This polarization combination can be effectively used to examine the mechanism of observed VSFG, because interfacial molecules give no contribution to VSFG when it is due to the quadrupolar mechanism. If bulk vibrational modes are experimentally observed in the PSS polarization combination, VSFG is due to the quadrupolar mechanism, and if interfacial vibrational modes are observed, it is due to the ordinary dipolar mechanism. This property will be used to analyze the experimental data later. For the PPP polarization combination, $\chi^{(2),\mathrm{quad1}}_{XZXZ}$, $\chi^{(2),\mathrm{quad1}}_{ZZZZ}$, $\chi^{(2),\mathrm{quad2}}_{XXZZ}$, $\chi^{(2),\mathrm{quad2}}_{ZZZZ}$, $\chi^{(2),\mathrm{quad3}}_{XZXZ}$, $\chi^{(2),\mathrm{quad3}}_{XXZZ}$, and $\chi^{(2),\mathrm{quad3}}_{ZZZZ}$ contribute to $\chi^{(2)}_{\mathrm{eff,PPP}}$, and the IR and Raman active modes of the interfacial molecules and the IR active modes of the bulk molecules may appear in the spectra. Because various tensor elements contribute to the effective susceptibility, the interpretation of the spectra is in general complicated, but still, no tensor elements allow the Raman active and IR inactive modes of bulk molecules to be observed. For all the other polarization combinations, $\chi^{(2)}_{\mathrm{eff}} = 0$ and VSFG will not occur within the present mechanism. The selection rule of VSFG due to a quadrupole contribution is summarized in Table 5.1.

One thing to be noted here is that this selection rule gives no information about the absolute intensity of the vibrational bands observed in the VSFG spectra. The group theoretical consideration in the previous section can predict that some vibrational bands are completely absent in the spectra due to a symmetry reason, but it does not tell anything about the intensity of the band when its appearance is allowed. This means that even if a vibrational mode is allowed in this selection rule, it may not appear as a band in the experimental spectra if its intensity is below the noise level. In other words, this selection

Table 5.1: Vibrational selection rule for VSFG by the quadrupolar mechanism. Vibrational mode selectivity and interface selectivity are shown. ◯ means "active" and × means "inactive". The left column indicates the polarization combination in the VSFG measurements.

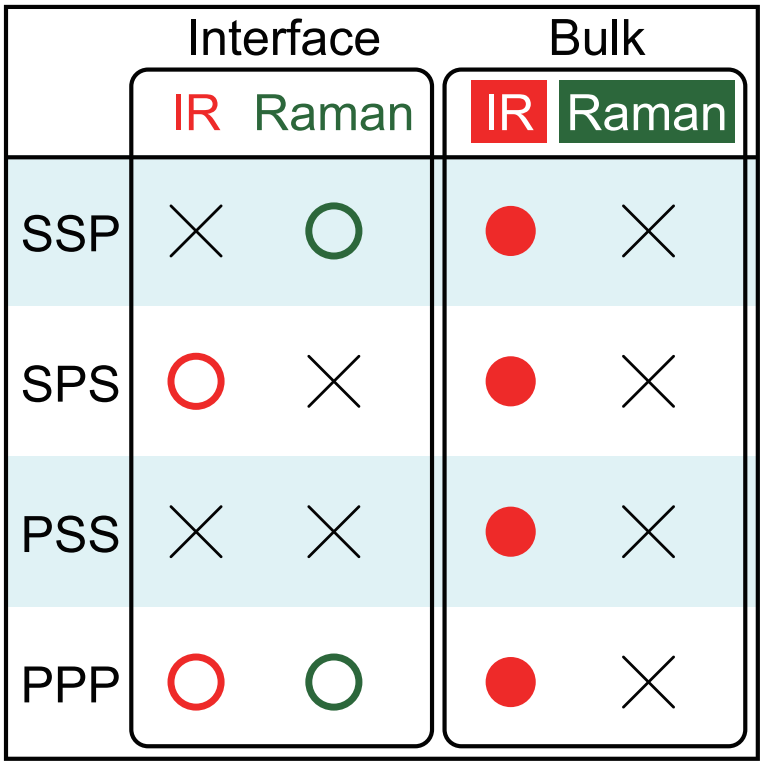

rule can only predict which vibrational modes are never observed.

5.8 Conclusion

Theoretical description of VSFG involving one electric quadrupolar interaction was presented. It was shown that the electric quadrupole can contribute to the VSFG process in three different schemes, denoted as quad1, quad2, and quad3. Because of the quadrupole contribution, VSFG due to these mechanisms is no longer sensitive to the molecular orientation, and it shows a more complicated interface selectivity. In the quad1 and quad2 mechanisms, interfacial molecules contribute to VSFG, while bulk properties are observed when VSFG is due to the quad3 mechanism, although the nonlinear polarization is localized at the interface for all the three mechanisms. Based on these three mechanisms, the vibrational selection rule of VSFG with a quadrupole contribution was derived for all the four polarization combinations (SSP, SPS, PSS, and PPP). This selection rule is summarized in Table 5.1.

Chapter 6

Quadrupole contribution in experimental VSFG

6.1 Introduction

In 2003, Hommel and Allen reported the experimental VSFG spectrum of the air/benzene interface [32]. This was a surprising result, because benzene is a centrosymmetric molecule, and within the dipole approximation, VSFG is forbidden for the system comprised of such centrosymmetric molecules. To explain their experimental observation, they speculated that the molecular structure of benzene is distorted and the inversion symmetry is lost at the interface because of the anisotropic environment, thus allowing VSFG to occur within the dipole approximation. More rigorous theoretical investigation into the mechanism of VSFG at the air/benzene interface was given by Kawaguchi *et al.*, in which they explained based on their molecular dynamics (MD) simulation data that at least some part of the observed VSFG signal is due to the symmetry breaking of benzene molecules at the interface [93].

However, it is also possible that the inversion symmetry of benzene molecules is preserved at the interface, and VSFG at the air/benzene interface is caused by the electric quadrupoles. The electric quadrupole is the second order term in the multipole expansion, with the electric dipole being the first order term. Since the first order term (electric dipoles) is zero for centrosymmetric molecules, it is natural to consider the contribution from the second order term (electric quadrupoles) when molecules have an inversion center. Using the quadrupolar selection rule derived in the previous chapter, it is possible to judge whether the qudrupolar mechanism applies or not.

In the above mentioned case, VSFG is dipole forbidden because the molecules themselves have an inversion symmetry. Meanwhile, even if the molecules themselves are not centrosymmetric, VSFG is still forbidden within the dipole approximation if the molecules are randomly oriented at the interface, because the inversion symmetry is macroscopically preserved in this case. This may happen for molecules with an extremely low polarity, such as n-alkanes. Actually, the molecular orientation at the air/n-alkane interfaces well above the freezing point is still under controversy. From the theoretical perspective, one MD simulation study suggests that the n-alkane molecules are oriented perpendicular to the

interface [95], while another MD simulation study concludes that the molecules have a random orientation at the interface [96]. Experimentally, a grazing incidence X-ray diffraction study shows the absence of an ordered crystalline structure at the interface [97], whereas some groups claim that the molecules are aligned and thus the inversion symmetry is broken at the air/n-alkane interfaces based on the observation of VSFG at such interfaces [98, 99]. Among these conflicting results, the discussion based on VSFG is not thorough enough, because even if the interfacial molecules have a random orientation and the inversion symmetry is preserved, VSFG may still take place through the quadrupolar mechanism discussed in the previous chapter. Therefore, in this study, I intended to point out the importance of carefully analyzing the mechanism of VSFG in order to correctly elucidate the interface structure from the experimental VSFG spectra.

In the following part, the experimental HD-VSFG spectra of the air/benzene, air/cyclohexane, and air/decane interfaces are presented and discussed. Owing to the heterodyne detection, the peak frequency of the vibrational bands can be determined very accurately, which is essential for the reliable band assignments. Based on the quadrupolar selection rule derived in the previous section, the observed bands in the Im $\chi^{(2)}_{\mathrm{eff}}$ spectra at the air/benzene and air/cyclohexane interfaces are ascribed to the quadrupolar mechanism. These results show for the first time that the quadrupolar mechanism can actually contribute to VSFG processes. As for the air/decane interface, the observed spectra are not compatible with the selection rule of the quadrupolar mechanism. This result indicates that VSFG at the air/decane interface is largely due to the ordinary dipolar mechanism, and that decane molecules have a polar alignment at the interface.

6.2 Experiment

6.2.1 Sample

Spectroscopy-grade benzene and cyclohexane were supplied from nacalai tesque, and anhydrous decane was purchased from Sigma-Aldrich. All the samples were used as received without further purification.

Commercial organic liquids are sometimes contaminated by a trace amount of water. To confirm that the obtained experimental spectra are not affected by the water contamination, anhydrous benzene (Sigma-Aldrich) which was further dried using Molecular Sieves 4A 1/16 (Wako), and dehydrated benzene (Kanto Chemical, water $< 0.001\%$) were also measured in the PPP polarization combination. The spectra obtained from these thoroughly dehydrated benzene samples were identical to that of the benzene provided by nacalai tesque, showing that the present experimental data are not affected at all by the potential contamination from water.

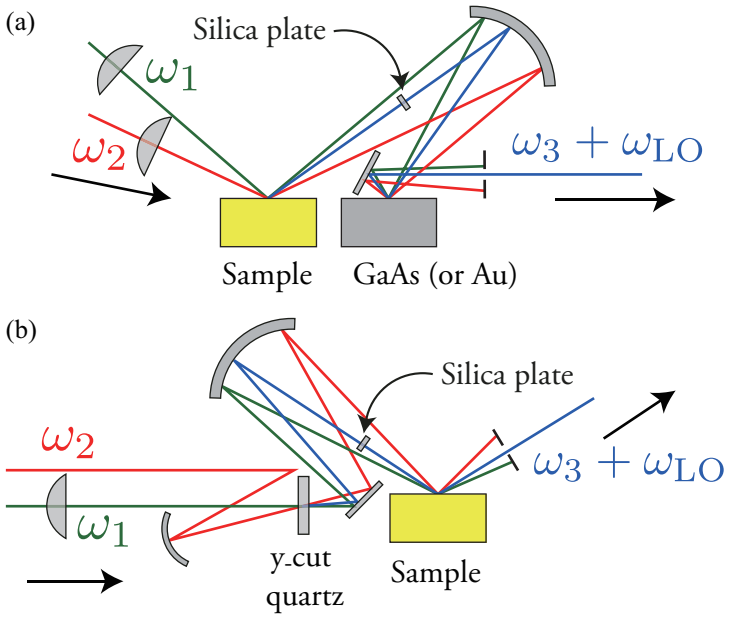

Figure 6.1: Experimental configuration for setup 1 (a) and for setup 2 (b). Local oscillator (ω_{LO}) is generated by GaAs (or Au) in (a) and by y-cut quartz in (b).

6.2.2 IR and Raman measurement

The IR and Raman spectra of neat bulk liquid benzene, cyclohexane, and decane were measured by a commercial FTIR spectrometer (Shimadzu, IRPrestige-21) and a commercial Raman spectrometer (Horiba Jobin Yvon, LabRAM; excited by the 514.5 nm line of an Ar^+ laser), respectively. The molar absorption coefficient of benzene at each frequency was obtained by multiplying the IR spectrum of benzene with a constant factor so that the integrated molar absorption coefficient of the CH stretch bands matches the value reported in the literature [100]. To determine the molar absorption coefficient of cyclohexane and decane, separate experiments were conducted to measure the IR spectra of cyclohexane/benzene and decane/benzene mixtures, in which the molar absorption coefficients of cyclohexane and decane were determined using the vibrational bands of benzene as the internal standard. The absorbance in the IR spectra of neat cyclohexane and decane were converted to the molar absorption coefficient following the values obtained from these binary mixture experiments.

6.2.3 HD-VSFG measurement

The VSFG measurements were performed on two multiplex HD-VSFG setups previously developed in our laboratory, which I shall refer to as setup 1 [19] and setup 2. As shown in Fig. 6.1 and described below, the difference between the two setups is the method of the local oscillator (ω_{LO}) generation which is used for the heterodyne detection. In the setup 1 (Fig. 6.1(a)), ω_{LO} is generated after VSFG at the sample surface using the reflected incident beams, whereas in the setup 2 (Fig. 6.1(b)), the ω_{LO} generation is done prior to VSFG at the sample surface. I empirically found that the first setup yields

spectra with a better signal-to-noise ratio (S/N), but the measurement is easily affected by the absorption of the infrared beam (ω_2) by the sample vapor. The second setup is efficient at eliminating the effect of the ω_2 absorption owing to the reduced optical path near the sample, but the S/N is often not as good as the former one. In this study, the air/benzene and air/decane interfaces were measured by the setup 1. For the air/cyclohexane interface, the setup 2 was used to avoid being affected by the severe absorption of the ω_2 light by the cyclohexane vapor.

Since the accurate determination of the peak frequency is critical in this study, I took a special care for the wavenumber calibration of the $\chi^{(2)}_{\rm eff}$ spectra, which was done in the following way. First, a thin film of liquid benzene, cyclohexane, or decane was placed in the optical path of the ω_2 light. The $|\chi^{(2)}_{\rm eff}|^2$ spectrum of a z-cut quartz crystal was then measured using this ω_2 light, resulting in the appearance of a characteristic dip structure in the observed spectrum which is due to the absorption of the ω_2 light by the liquid film. Since the position of the dip is identical to the vibrational frequency of each liquid observed in the IR spectrum, the wavenumber axis of the $\chi^{(2)}_{\rm eff}$ spectra can be calibrated with high accuracy through the comparison with the IR spectra. Frequency of each vibrational resonance can then be precisely determined from the $\mathrm{Im}\ \chi^{(2)}_{\rm eff}$ spectra, which are free from the spectral distortion caused by the interference between the nonresonant and resonant contributions and that between the resonant contributions.

Setup 1

The details of this setup are described in the literature [19, 101]. Briefly, a part of the output from a Ti:Sapphire regenerative amplifier (Spectra Physics, Spitfire Pro XP; average power: $\sim$ 3.3 W, repetition rate: 1 kHz, pulse width: $\sim$ 100 fs, center wavelength: 795 nm) was spectrally narrowed by the combination of a bandpass filter (center wavelength: 795 nm, bandwidth: 1 nm = 16 cm^{-1}) and a Fabry-Pérot interferometer, and was used as the narrowband visible light (ω_1, center wavelength: 795 nm, bandwidth: 0.4 nm = 6 cm^{-1}) for VSFG. The other part of the amplifier output was used as the input of a commercial optical parametric amplifier and a difference frequency generator (Spectra Physics, TOPAS-C & DFG1) to generate the broadband IR light (ω_2, 2600-3400 cm^{-1}). The visible and IR beams were spatially and temporally overlapped on the sample surface with the incident angles of 48° and 61°, respectively, to generate the sum frequency light (ω_3). During the sample measurement, the sample surface height was continuously monitored by a displacement sensor (Keyence, SI-F10), and the position of the sample surface was kept constant with the accuracy of about 1 μm. For the SSP, SPS, and PPP polarization combinations, the two incident beams reflected from the sample surface were refocused onto the GaAs(110) surface by a spherical concave mirror to generate a local oscillator ($\omega_{\rm LO}$) for the heterodyne detection. For the PSS polarization combination, Au was used instead of GaAs to attenuate the intensity of the $\omega_{\rm LO}$ and to make it comparable to that of the ω_3 light. The ω_3 light was delayed with respect to the

ω_{LO} by letting it pass through a 2 mm thick silica plate located in between the sample and the concave mirror. Finally, the ω_3 and ω_{LO} pulses were introduced into a polychromator and detected by a CCD camera. Inside the polychromator, the ω_3 and ω_{LO} pulses were dispersed and temporally stretched, and hence they interfered with each other to generate an interference fringe pattern in the frequency domain. The frequency domain spectrum was inversely Fourier transformed, and the heterodyned signal was extracted using a suitable filter function in the time domain. Then, the extracted heterodyned component was Fourier transformed back to the frequency domain. Similarly, the frequency-domain heterodyne-detected spectrum of a z-cut quartz crystal was recorded as a reference to calibrate the intensity and phase of the complex $\chi^{(2)}_{\mathrm{eff}}$ spectrum of the sample. Using the reported second-order nonlinear susceptibility of quartz, the imaginary (Im) and real (Re) spectra of the sample can be determined with the unit of $\mathrm{m}^2\ \mathrm{V}^{-1}$ [40, 89]. The details of this calibration procedure is given below.

As explained in Chapter 3, the experimental nonlinear susceptibility shown below can be obtained from the experimental data.

$$\chi^{(2),\mathrm{sample}}_{\mathrm{exp}} \equiv \frac{e^{i\Delta\Theta(Z_{\mathrm{sample}})} E^{\mathrm{sample}}_{3\mathrm{r}} E^{\mathrm{sample},*}_{\mathrm{LO}} e^{i\omega_3 T}}{i e^{i\Delta\Theta(Z_{\mathrm{quartz}})} E^{\mathrm{quartz}}_{3\mathrm{r}} E^{\mathrm{quartz},*}_{\mathrm{LO}} e^{i\omega_3 T}}, \tag{6.1}$$

with the ω_3 electric fields, $E^{\mathrm{sample}}_{3\mathrm{r}}$ and $E^{\mathrm{quartz}}_{3\mathrm{r}}$, given in terms of the effective nonlinear susceptibilities of the sample $\left(\chi^{(2),\mathrm{sample}}_{\mathrm{eff}}\right)$ and quartz $\left(\chi^{(2),\mathrm{quartz}}_{\mathrm{eff}}\right)$ as

$$E^{\mathrm{sample}}_{3\mathrm{r}} = \frac{i\omega_3}{2cn_a(\omega_3)\cos\theta_{3\mathrm{r}}} \chi^{(2),\mathrm{sample}}_{\mathrm{eff}} E_{1\mathrm{i}} E_{2\mathrm{i}}, \tag{6.2}$$

$$E^{\mathrm{quartz}}_{3\mathrm{r}} = \frac{\omega_3}{2cn_a(\omega_3)\cos\theta_{3\mathrm{r}}} \chi^{(2),\mathrm{quartz}}_{\mathrm{eff}} E_{1\mathrm{i}} E_{2\mathrm{i}}. \tag{6.3}$$

It is assumed that the surface height is adjusted to be the same for the sample (Z_{sample}) and for the quartz (Z_{quartz}).

$$\Delta\Theta(Z_{\mathrm{sample}}) = \Delta\Theta(Z_{\mathrm{quartz}}). \tag{6.4}$$

Unlike in Chapter 3, for this experimental configuration, the ω_{LO} electric fields, $E^{\mathrm{sample}}_{\mathrm{LO}}$ and $E^{\mathrm{quartz}}_{\mathrm{LO}}$, are expressed using the reflectivity of the incident beams at the sample or quartz surface, because ω_{LO} is generated using the incident beams reflected at the sample or quartz surface as shown in Fig. 6.1(a).

$$E^{\mathrm{sample}}_{\mathrm{LO}} = E^{0}_{\mathrm{LO}} r_1^{\mathrm{sample}} r_2^{\mathrm{sample}}, \tag{6.5}$$

$$E^{\mathrm{quartz}}_{\mathrm{LO}} = E^{0}_{\mathrm{LO}} r_1^{\mathrm{quartz}} r_2^{\mathrm{quartz}}. \tag{6.6}$$

Here, r_i^{sample} and r_i^{quartz} $(i = 1, 2)$ are the complex reflectivities of ω_i at the sample and quartz surfaces, respectively, and E^{0}_{LO} is the electric field of ω_{LO} which is expected to be observed when the reflectivity is unity for both ω_1 and ω_2. Using these properties, the experimental nonlinear susceptibility can be expressed as

$$\chi^{(2),\mathrm{sample}}_{\mathrm{exp}} = \frac{\chi^{(2),\mathrm{sample}}_{\mathrm{eff}}}{\chi^{(2),\mathrm{quartz}}_{\mathrm{eff}}} \left(\frac{r_1^{\mathrm{sample}} r_2^{\mathrm{sample}}}{r_1^{\mathrm{quartz}} r_1^{\mathrm{quartz}}} \right)^{*}, \tag{6.7}$$

and hence the effective nonlinear susceptibility of the sample is given by

$$\chi_{\mathrm{eff}}^{(2),\mathrm{sample}} = \left(\frac{r_1^{\mathrm{quartz}} r_1^{\mathrm{quartz}}}{r_1^{\mathrm{sample}} r_2^{\mathrm{sample}}} \right)^* \chi_{\mathrm{eff}}^{(2),\mathrm{quartz}} \chi_{\mathrm{exp}}^{(2),\mathrm{sample}}. \tag{6.8}$$

In this formula, $\chi_{\mathrm{exp}}^{(2),\mathrm{sample}}$ is experimentally obtained using Eq. (6.1), and $\chi_{\mathrm{eff}}^{(2),\mathrm{quartz}}$ can be calculated as shown in Section 2.5.5. The complex reflectivities for S- and P-polarized light can be calculated from the following formulae using the complex refractive indices [49].

$$r_{\mathrm{S}} = \frac{n_a(\omega)\cos\theta_{\mathrm{i}} - n_b(\omega)\cos\theta_{\mathrm{t}}}{n_a(\omega)\cos\theta_{\mathrm{i}} + n_b(\omega)\cos\theta_{\mathrm{t}}}, \tag{6.9}$$

$$r_{\mathrm{P}} = \frac{n_b(\omega)\cos\theta_{\mathrm{i}} - n_a(\omega)\cos\theta_{\mathrm{t}}}{n_b(\omega)\cos\theta_{\mathrm{i}} + n_a(\omega)\cos\theta_{\mathrm{t}}}. \tag{6.10}$$

When the incident beams are far off-resonant with the reflecting medium, the refractive index can be regarded as a real constant. For the quartz, refractive index was taken to be 1.544 at both ω_1 and ω_2 wavelengths [50]. For the sample, the refractive index can be regarded as a real constant at the ω_1 wavelength, and it was taken to be 1.511 for benzene and 1.409 for decane [50]. However, at the ω_2 wavelength, the refractive index must be treated as a complex quantity because of the vibrational resonance. Using the molar absorption coefficient $\varepsilon(\omega_2)$ of each liquid obtained from the IR measurements, the imaginary part of the complex refractive index can be determined as

$$\mathrm{Im}\; n(\omega_2) = \frac{\ln 10}{4\pi} \frac{c_M}{\tilde{\nu}_2} \varepsilon(\omega_2), \tag{6.11}$$

where c_M is the molar concentration of the neat liquids (mole per unit volume) and $\tilde{\nu}_2$ is the wavenumber of ω_2. Combining this imaginary refractive index and the reported real refractive index in the off-resonant region, the complex refractive index can be deduced using the Kramers-Kronig relation (Integration range: $\tilde{\nu}_2$ = 500-3500 cm^{-1}). The complex reflectivity is then obtained from this complex refractive index. Correction of the $\chi_{\mathrm{eff}}^{(2),\mathrm{sample}}$ spectra by the complex reflectivity is important, because spectral distortion is caused by the wavenumber dependence of the reflectivity as discussed in the literature [24]. All the $\mathrm{Im}\;\chi_{\mathrm{eff}}^{(2)}$ spectra of benzene and decane were corrected for the reflectivity before presenting.

Setup 2

The light source for this setup was a Ti:Sapphire regenerative amplifier (Coherent, Legend Elite DUO; average power: $\sim$ 8 W, repetition rate: 1 kHz, pulse width: $\sim$ 75 fs, center wavelength: 800 nm). A portion of the laser output was spectrally narrowed by the combination of a bandpass filter and a Fabry-Pérot interferometer, and was used as the ω_1 beam in VSFG (center wavelength: 795 nm, bandwidth: 0.4 nm = 6 cm^{-1}). Another portion was converted to mid-IR light using a commercial optical parametric amplifier and a difference frequency generator unit (Coherent, TOPAS-C & DFG1), and was used as the ω_2 beam (2700-3100 cm^{-1}). In this setup, ω_1 and ω_2 were first focused into a thin crystal of y-cut quartz (thickness = 10 μm) where the local oscillator (ω_{LO}) is generated. ω_{LO} and the transmitted ω_1 and ω_2

were refocused onto the sample surface using a concave spherical mirror. The incident angles for ω_1 and ω_2 beams were 60° and 48°, respectively. Before reaching the sample surface, ω_{LO} was temporally delayed for about 5 ps when it went through a silica plate of 3 mm thickness. Because of this temporal delay, ω_{LO} and the sum frequency light (ω_3) from the sample surface showed an interference pattern on the CCD camera after they were dispersed in a polychromator, which can be analyzed to yield a complex $\chi^{(2)}_{\mathrm{eff}}$ spectrum in the same manner as for the setup 1. In this configuration, propagation length of the incident beams near the sample was shortened, and the spectra were less affected by the absorption of the infrared light (ω_2) by the sample vapor.

In exactly the same manner as for the apparatus presented in Chapter 3, ω_{LO} is reflected at the sample surface in this scheme, instead of the incident beams as in the setup 1. Thus, the detected ω_{LO} intensity is proportional to the reflectivity of ω_{LO} at the sample or quartz surface.

$$E_{\mathrm{LO}}^{\mathrm{sample}} = E_{\mathrm{LO}}^{0} r_{\mathrm{LO}}^{\mathrm{sample}}, \tag{6.12}$$

$$E_{\mathrm{LO}}^{\mathrm{quartz}} = E_{\mathrm{LO}}^{0} r_{\mathrm{LO}}^{\mathrm{quartz}}. \tag{6.13}$$

In this case, the effective nonlinear susceptibility of the sample is given by

$$\chi_{\mathrm{eff}}^{(2),\mathrm{sample}} = \left(\frac{r_{\mathrm{LO}}^{\mathrm{quartz}}}{r_{\mathrm{LO}}^{\mathrm{sample}}} \right)^{*} \chi_{\mathrm{eff}}^{(2),\mathrm{quartz}} \chi_{\mathrm{exp}}^{(2),\mathrm{sample}}. \tag{6.14}$$

Here, $r_{\mathrm{LO}}^{\mathrm{sample}}$ and $r_{\mathrm{LO}}^{\mathrm{quartz}}$ are the reflectivity of ω_{LO} at the sample and quartz surface, respectively, and $\chi_{\mathrm{exp}}^{(2),\mathrm{sample}}$ is the experimental nonlinear susceptibility defined in Eq. (6.1). Since both electronic and vibrational resonances are absent at the ω_{LO} wavelength, the refractive index and the reflectivity are both purely real. Hence, this setup is free from the spectral distortion caused by the complex nature of reflectivity. Refractive indices of quartz and cyclohexane were taken to be 1.544 and 1.423, respectively [50], and the reflectivities were calculated following Eqs. (6.9) and (6.10).

6.3 Results and Discussion

For each sample, HD-VSFG measurements were conducted for all the four polarization combinations that gives rise to VSFG at the in-plane isotropic interfaces (SSP, SPS, PSS, and PPP), and the obtained $\mathrm{Im}\ \chi^{(2)}_{\mathrm{eff}}$ spectra are compared with IR and Raman spectra of the same sample in the bulk liquid phase. The assignment of each band is determined based on their vibrational frequencies, and the mechanism of VSFG is discussed using these band assignments.

6.3.1 Benzene

It is widely believed that benzene has an almost perfect $D_{6\mathrm{h}}$ structure in the liquid- and gas-phase, and because of its high symmetry, it is a convenient molecule for discussing the selection rules. Figs. 6.2(e) and (f) show the IR and Raman spectra of bulk liquid-phase benzene. As can be readily seen, the rule

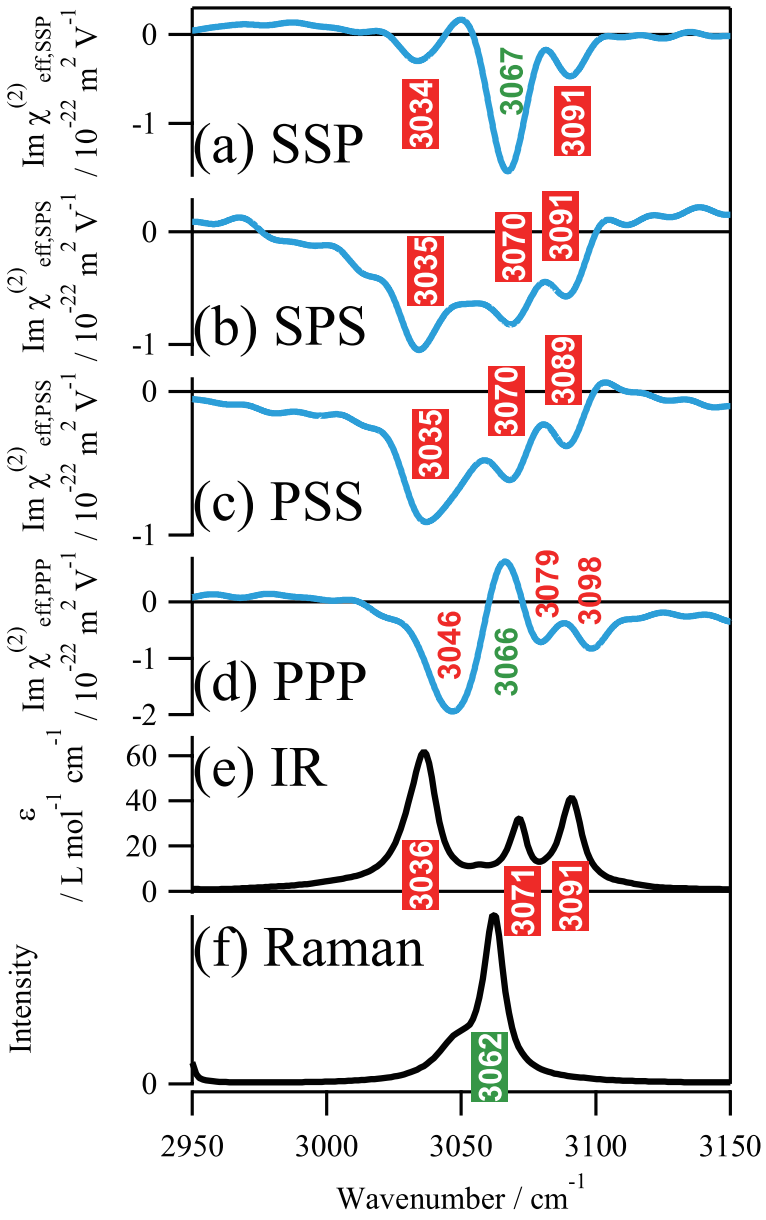

Figure 6.2: (a-d) HD-VSFG spectra of the air/benzene interface with SSP, SPS, PSS, and PPP polarization combinations, respectively. (e, f) IR and Raman spectra, respectively, of the bulk liquid-phase benzene.

Table 6.1: The CH stretch frequencies [cm^{-1}] of the interfacial benzene molecules observed in the HD-VSFG measurements with SSP and PPP polarization combinations. The corresponding frequencies in the gas- [102, 103] and liquid-phases are also shown.

	E_{1u} (IR)	A_{1g} (Raman)	E_{1u} (IR)	E_{1u} (IR)
Gas [102, 103]	3048	3074	3079	3101
HD-VSFG		3067 (SSP)		
	3046 (PPP)	3066 (PPP)	3079 (PPP)	3098 (PPP)
Liquid	3036	3062	3071	3091

Table 6.2: Summary of the experimentally observed vibrational modes at the air/benzene interface for each polarization combination.

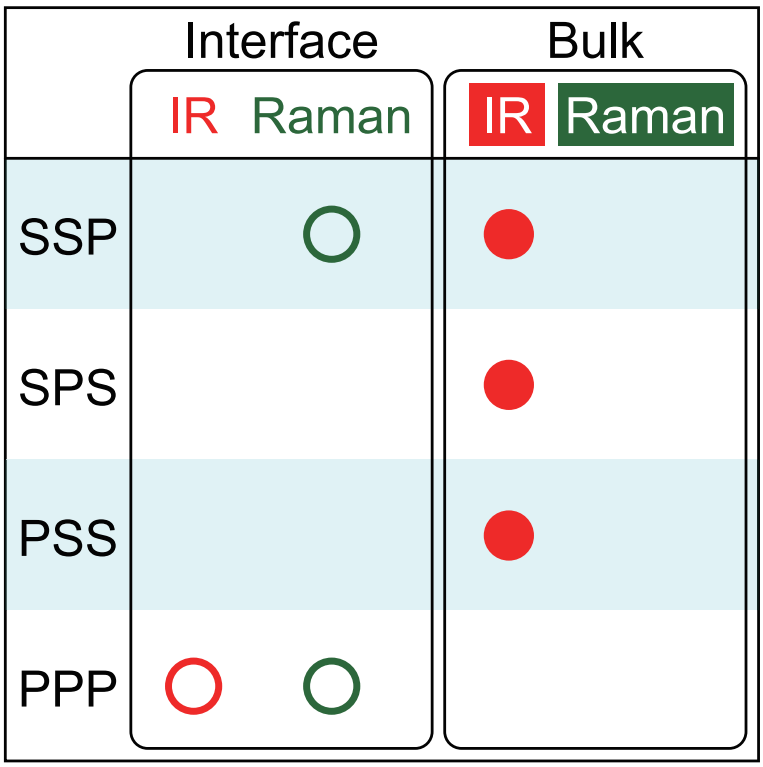

of mutual exclusion perfectly holds between these two spectra, providing an experimental proof for the highly symmetric structure of benzene molecules in the liquid phase. Benzene has six CH stretch modes, and under the D_{6h} symmetry, they are given by the symmetry species $A_{1g} + E_{2g} + B_{1u} + E_{1u}$ [104]. Since the electronic ground state of benzene is not degenerate, the vibrational selection rules for IR absorption and Raman scattering are given respectively as $\Gamma_V \subset \sum_i \Gamma_i = A_{2u} + E_{1u}$ and $\Gamma_V \subset \sum_{i,j} (\Gamma_i \times \Gamma_j) = 2A_{1g} + E_{1g} + E_{2g}$ (The antisymmetrized part of the direct product, i.e. A_{2g}, was dropped from the linear combination [105].). Experimentally, the E_{1u} mode is observed in the IR spectrum at 3036, 3071, and 3091 cm^{-1}, and the A_{1g} and E_{2g} modes are observed in the Raman spectrum at 3062 and 3048 cm^{-1}, respectively. The E_{1u} bands are observed as a triad due to the Fermi resonance with two combination modes of E_{1u} symmetry [102]. The E_{2g} mode at 3048 cm^{-1} appears as a shoulder, and it will be neglected in the following analysis because the signal-to-noise ratio of the Im $\chi^{(2)}_{\text{eff}}$ spectra are not good enough to discuss the band shape.

With these bulk spectra in mind, the Im $\chi^{(2)}_{\text{eff}}$ spectra of the air/benzene interface obtained with the SSP, SPS, PSS, and PPP polarization combinations shown in Fig. 6.2(a), (b), (c), and (d), respectively, can be discussed. One striking finding is that the peak frequency of some of the bands matches well with the bulk IR frequencies. Namely, the two bands in the SSP spectrum at 3034 and 3091 cm^{-1}, and all the bands in the SPS and the PSS spectra coincide with the peak frequencies in the bulk IR spectrum. Since vibrational frequencies are very sensitive to the structure of molecules and the local environment around them, the good frequency match indicates that what is observed is essentially the bulk benzene molecules. In fact, the vibrational frequency of benzene in the gas-phase and in the liquid-phase differs by as much as 10 cm^{-1} (Table 6.1) even though the D_{6h} symmetry is practically preserved in both cases, which confirms that the environmental effect on the vibrational frequency is indeed significant. Hence, the only possible assignment for these bands is the IR active modes of bulk liquid-phase benzene molecules. Another point to be noticed is that all the other bands have peak frequencies that do not match with any vibrational frequencies in the bulk liquid-phase nor gas-phase benzene. Since the vibrational frequencies are not observed in the bulk, those bands should be assigned to the vibrational modes of the interfacial molecules.

The assignment of these bands becomes evident by considering the symmetry of benzene molecules at the interface, i.e. whether the D_{6h} symmetry is preserved or not. Previous studies about VSFG at the air/benzene interface proposed that benzene molecules have a distorted structure at the interface due to the anisotropic environment [32, 93]. The anisotropy at the interface can be understood in the following way. At the interface, a benzene molecule is attracted to the liquid phase by the van der Waals force from other benzene molecules. Since this attractive force acts only towards the liquid phase, it may cause the elongation of the bonds selectively in that direction, resulting in the symmetry breaking of the molecular structure. Since this force originates from the presence of solvation in the liquid side and its absence in

the gas side, its strength F can be estimated from the gradient of enthalpy, H, across the interface.

$$F = \frac{\partial H}{\partial Z}. \tag{6.15}$$

Using the enthalpy of vaporization for benzene ($\Delta_{\mathrm{vap}}H = 33.83\ \mathrm{kJ\,mol^{-1}}$ at 25 °C [50]), and the thickness of the interface ($\Delta Z = 1\ \mathrm{nm}$ [93]), the force can be quantitatively evaluated as

$$F = \frac{\Delta_{\mathrm{vap}}H}{\Delta Z} = 6 \times 10^{-11}\ \mathrm{N}. \tag{6.16}$$

As a demonstration, the elongation of the CH bonds due to this force is evaluated. Using the typical force constant value for CH stretch modes, $k = 5 \times 10^2\ \mathrm{N\,m^{-1}}$, the elongation of a CH bond can be estimated as 1×10^{-4} nm. This is negligible at the room temperature, because the fluctuation of the CH bond length due to the thermal energy, $k_B T = 4 \times 10^{-21}$ J, is as large as 4×10^{-3} nm. In fact, it can be easily shown that the bond elongation is smaller than the thermal fluctuation whenever $k > 0.5\ \mathrm{N\,m^{-1}}$, which applies to all the vibrational modes of benzene. This simple calculation suggests that the distortion of the molecular structure caused by the anisotropic environment at the interface is negligible, and it is reasonable to consider that the benzene molecules have $D_{6\mathrm{h}}$ symmetry not only in the bulk but also at the interface.

Considering this conservation of the molecular symmetry, the vibrational frequency is expected to change gradually across the interface, without any abrupt change of the spectral pattern. That is to say, the vibrational frequency of the interfacial molecules will be in between those of the gas- and liquid-phase molecules. The assignment for the bands having the frequency different from the bulk can be readily made based on this consideration, because all of them show a frequency that is higher than the liquid-phase molecules and lower than the gas-phase molecules. The result of the assignment is shown in Table 6.1. The interesting point to be noted from this assignment is that the Fermi triad is observed also for the interfacial benzene molecules in the PPP spectrum at 3046, 3079, and 3098 $\mathrm{cm^{-1}}$. The Fermi resonance cannot be observed if the symmetry breaking takes place. For instance, it is reported that a weak interaction between a metal cation and the π electrons of benzene can readily eliminate the Fermi splitting [106]. Thus, the appearance of the Fermi triad confirms the correctness of my estimation in the last paragraph that the interfacial benzene preserves the $D_{6\mathrm{h}}$ symmetry. The observed vibrational modes at the air/benzene interface for each polarization combination are summarized in Table 6.2.

With the $D_{6\mathrm{h}}$ symmetry, benzene has a center of inversion, and VSFG is forbidden under the dipole approximation. In other words, it is impossible to explain the experimental observation within the dipole approximation, and a higher order interaction needs to be taken into account. Thus, it is natural to consider a contribution from the electric quadrupoles to VSFG. In order to test this hypothesis, each of the experimentally observed bands were examined to see if it is allowed in the selection rule for VSFG by the quadrupolar mechanism. In the SSP polarization combination, the IR active E_{1u} modes of bulk

molecules and the Raman active A_{1g} mode of interfacial molecules are observed, all of which are allowed in the selection rule shown in Table 5.1. Similarly, the observation of IR active E_{1u} modes of bulk molecules in the SPS and PSS polarization combinations, and the appearance of the IR active E_{1u} modes and the Raman active A_{1g} mode of the interfacial molecules in the PPP polarization combination are also allowed in the selection rule. Thus, the experimental data are fully consistent with the quadrupolar mechanism. The PSS polarization combination provides the strongest test for the validity of this correspondence, because the quadrupolar selection rule predicts the observation of only the bulk IR active modes, whereas only the interfacial frequencies are detectable in the ordinary dipolar mechanism. Experimentally, the frequency of the observed bands in the PSS polarization combination matched well with the bulk IR frequencies, which strongly indicates that VSFG at the air/benzene interface is due to the quadrupolar mechanism.

6.3.2 Cyclohexane

Although cyclohexane has a less rigid structure as compared with benzene, it can still be regarded as a centrosymmetric molecule in the condensed phase for the following reasons. It is known that cyclohexane has two kinds of conformers, i.e. chair and twist-boat [109]. Chair is the most stable conformer. It belongs to the $D_{3\mathrm{d}}$ point group and it has a center of inversion. Twist-boat is the second most stable conformation. It belongs to the D_2 point group and it does not have the inversion symmetry. Since the two conformers can freely convert to each other, these two species are in equilibrium at the room temperature. However, due to the energy difference as large as 20-25 kJ mol^{-1}, more than 99.9 % of the cyclohexane molecules take the chair conformation, and the experimental data at the room temperature exclusively show the feature of the chair conformers [109]. In fact, the observation of the twist-boat conformers is only possible with special techniques such as matrix isolation [109, 110]. In other words, it is a good approximation to think that all the cyclohexane molecules exist as the chair conformer in the liquid phase, and regard cyclohexane as a centrosymmetric molecule, just as in the same manner as benzene.

Under this assumption, the vibrational modes of cyclohexane can be discussed group theoretically under $D_{3\mathrm{d}}$ symmetry. Cyclohexane has 12 CH stretch modes, and under the $D_{3\mathrm{d}}$ symmetry, the irreducible representations of those modes are given by $2A_{1g} + 2A_{2u} + 2E_g + 2E_u$ [111]. Among these modes, the A_{2u} and E_u modes are IR active, and the A_{1g} and E_g modes are Raman active. The experimental IR and Raman spectra of bulk liquid cyclohexane are shown in Fig. 6.3(e) and (f). Although the assignment of these CH stretch bands has been attempted for a long time, various different and conflicting assignments are proposed [107, 111–114], and it is hard to say that the vibrational assignment of these bands has been conclusively determined. Since the correctness of the assignment does not have a critical importance in this study, I will proceed by simply adopting the assignment by Takahashi and

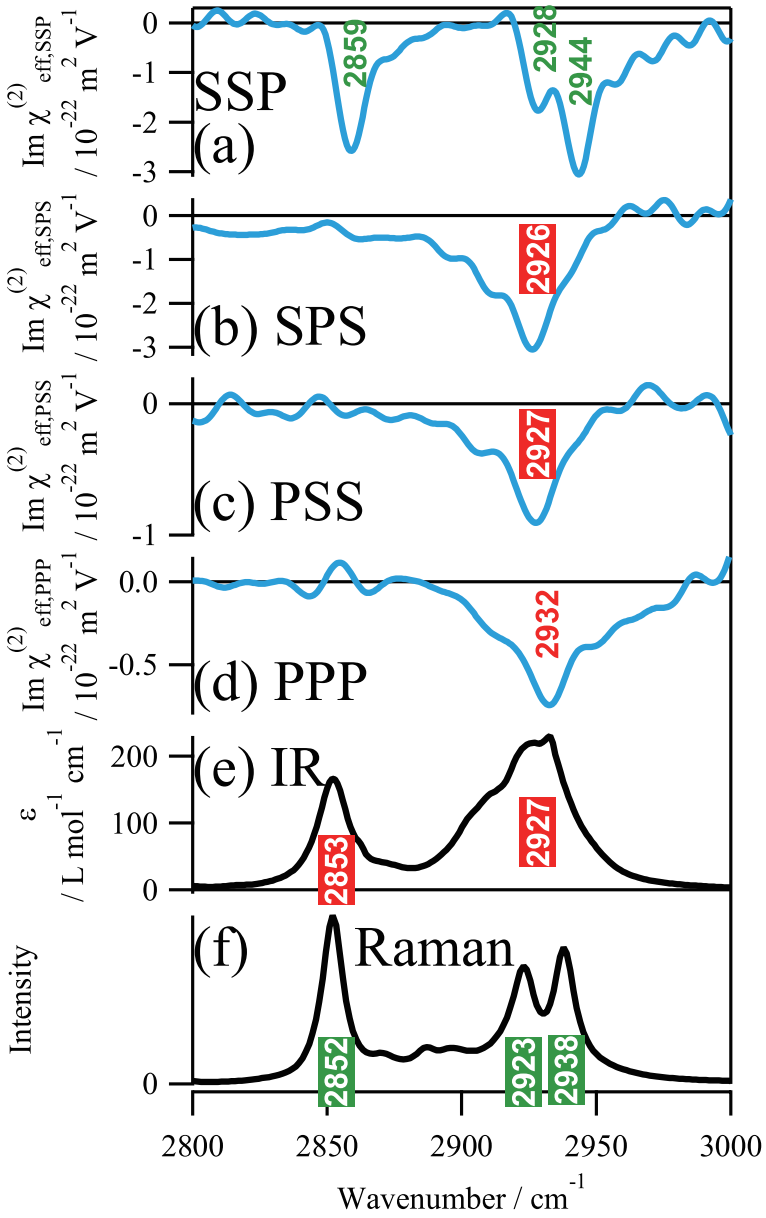

Figure 6.3: (a-d) HD-VSFG spectra of the air/cyclohexane interface with SSP, SPS, PSS, and PPP polarization combinations, respectively. (e, f) IR and Raman spectra, respectively, of the bulk liquid-phase cyclohexane.

Table 6.3: The CH stretch frequencies [cm^{-1}] of the interfacial cyclohexane molecules observed in the HD-VSFG measurements with SSP and PPP polarization combinations. The corresponding frequencies in the gas- [107, 108] and liquid-phases are also shown.

	E_u (IR)	A_{1g} (Raman)	E_g (Raman)	A_{2u}-E_u (IR)	A_{1g} (Raman)
Gas [107, 108]	2863	2864	2935	2934	2950
HD-VSFG		2859 (SSP)	2928 (SSP)		2944 (SSP)
				2932 (PPP)	
Liquid	2853	2852	2923	2927	2938

Table 6.4: Summary of the experimentally observed vibrational modes at the air/cyclohexane interface for each polarization combination.

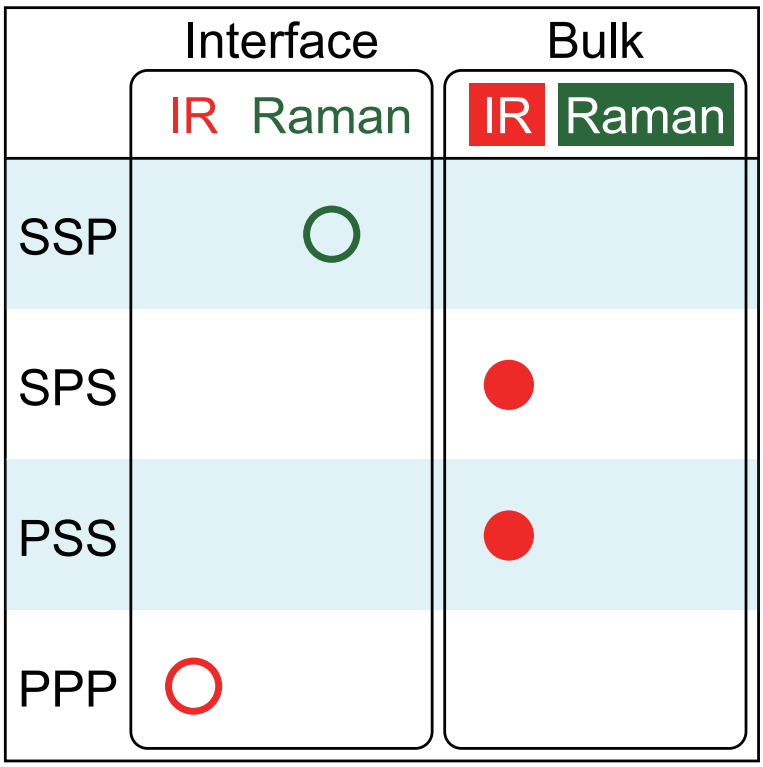

Shimanouchi [113]. According to their assignment, in the IR spectrum (Fig. 6.3(e)), the band at 2853 cm^{-1} is assigned to an E_u mode, and the 2927 cm^{-1} band is assigned to A_{2u} and E_u modes, with the two modes having a coincidental frequency. The shoulder at 2903 cm^{-1} is due to an A_{2u} mode, but this will be neglected in the following analysis. In the Raman spectrum (Fig. 6.3(f)), the 2852 and 2938 cm^{-1} bands are assigned to A_{1g} modes, and the 2923 cm^{-1} band is due to an E_g mode. One of the small features near 2900 cm^{-1} is probably assignable to the other E_g mode, but it will be neglected due to its low intensity.

The $\mathrm{Im}\ \chi^{(2)}_{\mathrm{eff}}$ spectra of the air/cyclohexane interface recorded with the SSP, SPS, PSS, and PPP polarization combinations are given in Fig. 6.3(a), (b), (c), and (d). Just as in the case of benzene, the 2926 cm^{-1} band in the SPS spectrum and the 2927 cm^{-1} band in the PSS spectrum show good frequency match with the 2927 cm^{-1} band in the bulk IR spectrum of liquid cyclohexane, and they can be assigned to the IR active A_{2u}-E_u modes of bulk cyclohexane. The observation of the bulk frequency unambiguously shows that there is a contribution from the electric quadrupoles. Appearance of the bulk IR active modes in SPS and PSS polarization is also consistent with the selection rule of quadrupole-induced VSFG in Table 5.1.

Other bands exhibit a vibrational frequency higher than in the liquid-phase and lower than in the gas-phase as shown in Table 6.3. Using the enthalpy of vaporization for cyclohexane ($\Delta_{\mathrm{vap}}H = 33.01\ \mathrm{kJ\ mol^{-1}}$ at 25 °C [50]), and following the same discussion as for benzene, it can be easily seen that the distortion of the molecular structure at the air/cyclohexane interface is negligible, and the cyclohexane molecules preserve a centrosymmetric structure. Then, it is straightforward to assign these bands to the corresponding vibrational modes of the interfacial molecules because the vibrational frequencies are expected to show a gradual shift from the liquid-phase to the gas-phase. In the SSP spectrum, the bands at 2859 and 2944 cm^{-1} are ascribed to the A_{1g} modes, and the 2928 cm^{-1} band to the E_g mode of cyclohexane molecules at the interface. Likewise, the 2932 cm^{-1} band in the PPP spectrum is assigned to the A_{2u}-E_u modes of the interfacial cyclohexane molecules. The summary of the observed vibrational modes for each polarization combination is given in Table 6.4. The observation of the Raman active modes of interfacial molecules in the SSP polarization combination, and the IR active modes of the interfacial molecules in the PPP polarization combination is again consistent with the selection rule of VSFG involving the quadrupoles. In addition, the absence of the bands due to the interfacial molecules in the PSS polarization combination further supports this argument. Hence, it is possible to conclude that VSFG at the air/cyclohexane interface arises from the quadrupolar mechanism.

This result shows that VSFG due to quadrupoles is not limited to benzene, and it is a general mechanism of VSFG. It is necessary to take a special care in interpreting the spectra when the quadrupole contribution may be significant. Since quadrupole-induced VSFG is insensitive to the molecular orientation, the appearance of VSFG signal does not necessarily mean that molecules have a polar alignment

at the interface. Through the quadrupolar mechanism, interface-selective VSFG spectra can be obtained even if molecules are randomly oriented at the interface. In fact, in the case of the air/benzene interface, MD simulation suggests that benzene molecules are randomly oriented at the interface [93]. Another important point is that bulk properties may appear in the spectra arising from this mechanism, and this bulk contribution can never be separated from the interface contribution, even if VSFG is measured in both reflection and transmission geometries. This is because the nonlinear polarization in this quadrupolar mechanism is localized within the thin interface layer, even though the bulk properties appear, and the observed VSFG signal intensity is not dependent on the coherent length.

6.3.3 Decane

Decane is another typical nonpolar organic liquid consisting only of carbon and hydrogen atoms. Contrary to the former two molecules, decane does not have a center of inversion in the liquid phase because the alkyl chain is flexible and the molecules are not necessarily in the all-*trans* conformation. However, because it is nonpolar, it may have a random orientation at the interface region and VSFG might be forbidden within the dipole approximation, as suggested by an MD simulation [96] and an X-ray diffraction experiment [97]. Hence, the observed VSFG spectra need to be interpreted with great care as I have discussed in the previous paragraph.

The bulk IR and Raman spectra of liquid-phase decane are shown in Figs. 6.4(e) and (f). Decane has as many as 22 CH stretch modes and it is not practical to assign a normal mode to each of the bands. Instead, qualitative band assignment based on the functional groups is given. In the IR spectrum, the bands at 2856 and 2874 cm^{-1} are assigned to the symmetric stretch modes of CH_2 and CH_3 groups, respectively, and the 2925 and 2959 cm^{-1} bands are ascribed to the antisymmetric stretch modes of the CH_2 and CH_3 groups, respectively. For the Raman spectrum, the 2850 and 2861 cm^{-1} bands are due to the CH_2 symmetric stretch mode with Fermi resonance, 2874 and 2938 cm^{-1} bands arise from the symmetric CH_3 stretch mode with Fermi resonance, and the 2961 cm^{-1} band is ascribed to the CH_3 antisymmetric stretch mode. The broad feature near 2900 cm^{-1} is caused by the CH_2 symmetric stretch modes with Fermi resonance [115].

Figs. 6.4(a), (b), (c), and (d) show the Im $\chi^{(2)}_{\rm eff}$ spectra of the air/decane interface recorded with the SSP, SPS, PSS, and PPP polarization combinations, respectively. The band assignment is given in the literature as follows [99, 116]. In the SSP spectrum, the 2861 and 2881 cm^{-1} bands are due to the symmetric stretch of CH_2 and CH_3 groups, respectively. The 2926 and 2946 cm^{-1} bands are the result of Fermi resonance of the CH_2 and CH_3 symmetric stretch modes, respectively. In the SPS, PSS, and PPP spectra, the two bands at $\sim$ 2921 and $\sim$ 2968 cm^{-1} are due to the CH_2 and CH_3 antisymmetric stretch modes, respectively. Although the interpretation and comparison of the spectra are not so simple as in the cases of benzene and cyclohexane, it is clear that the peak frequencies of the bands in the PSS

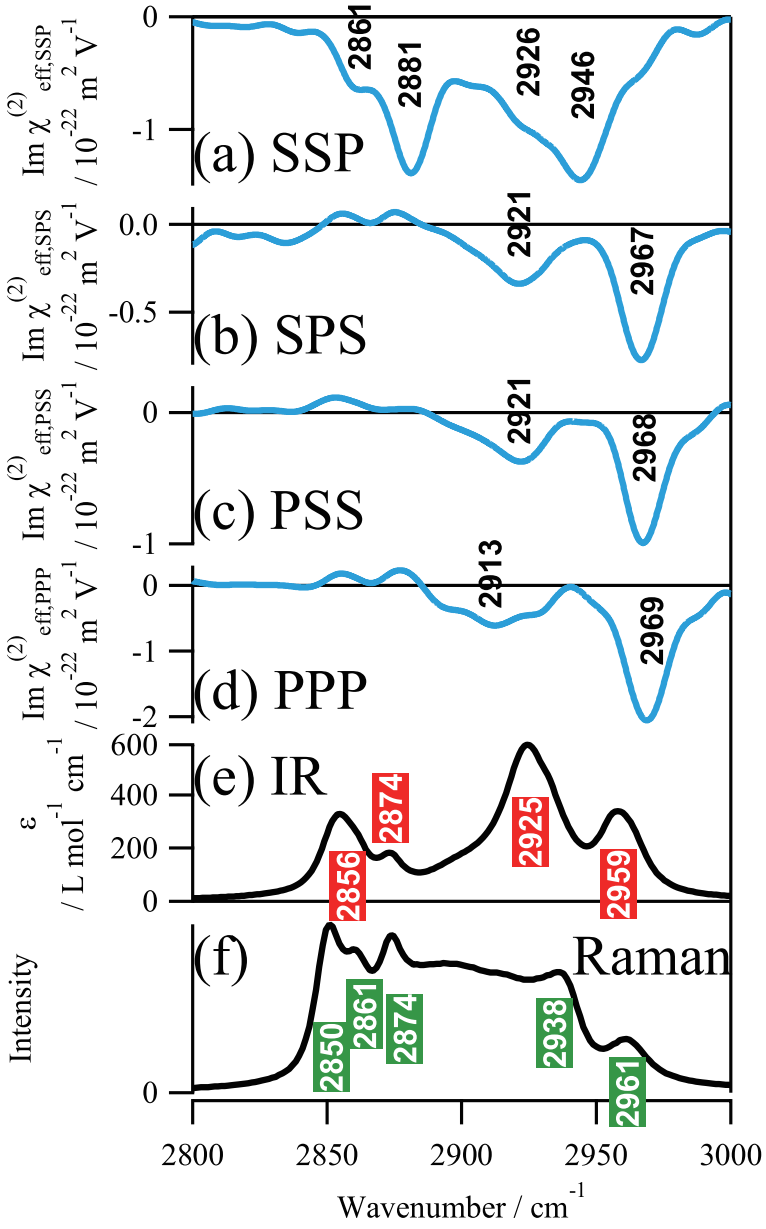

Figure 6.4: (a-d) HD-VSFG spectra of the air/decane interface with SSP, SPS, PSS, and PPP polarization combinations, respectively. (e, f) IR and Raman spectra, respectively, of the bulk liquid-phase decane.

spectrum at 2921 and 2968 cm^{-1} are deviated from those found in the IR spectrum of bulk liquid-phase decane at 2925 and 2959 cm^{-1}, which indicates that these bands are due to the interfacial molecules. One might argue that decane in the bulk liquid phase may have some IR active normal modes with the frequencies of 2921 and 2968 cm^{-1}, and although they are weak and not observed in the IR spectrum, they give a prominent contribution to the PSS spectrum through the quad3 mechanism. This hypothesis, however, is not plausible because the intensity of the bands due to the quad3 mechanism depends on the IR transition probability as can be seen in Eq. (5.119), and the bands which give negligible contributions to the IR spectrum are not likely to become the predominant bands in the PSS spectrum. Hence, the possibility of the bulk contribution can be safely rejected, and these two bands can be ascribed to the vibrational modes of the interfacial molecules. The observation of the interfacial frequencies in the PSS polarization combination provides a proof that the ordinary dipolar mechanism contributes to VSFG at the air/decane interface, because the quadrupolar selection rule does not allow the interfacial frequencies to appear in the PSS spectrum. Another thing to be noted here is that no Im $\chi^{(2)}_{\rm eff}$ bands in any polarization combination, aside from the 2926 cm^{-1} band in the SSP spectrum, show coincidental frequency with the four prominent bulk IR bands at 2856, 2874, 2925, and 2959 cm^{-1}, whereas such a coincidence was observed for multiple bands in the air/benzene and air/cyclohexane interfaces. This again supports the present conclusion that the dipolar mechanism largely contributes to VSFG at the air/decane interface.

The appearance of the dipolar-origin VSFG bands is a clear indication of the broken inversion symmetry at the interface, because VSFG is forbidden in a centrosymmetric system within the dipole approximation. Hence, the present experimental result and analysis unambiguously proves for the first time that there is a macroscopic alignment of decane molecules at the air/decane interface well above the freezing temperature of decane. Although the same conclusion has already been given by several groups for the air/n-alkane interfaces using VSFG spectroscopy [98, 99], their proof was insufficient because they did not rule out the possibility that all the observed bands are due to the quadrupolar mechanism, in which case the n-alkane molecules may actually be randomly oriented at the interface. The Shen group tried to eliminate the possibility of the quadrupole contribution by showing that all the bands observed in the $|\chi^{(2)}_{\rm eff}|^2$ spectrum with the SSP polarization combination are due to the interfacial molecules [98], but this is still not thorough enough because the SSP spectrum may be predominantly due to the interfacial molecules even if VSFG is due to the quadrupolar mechanism as can be seen from the case of the air/cyclohexane interface. Thus, the present study shows the critical importance of analyzing the mechanism of VSFG carefully before discussing the surface structure based on the VSFG spectra, which can be done by examining whether or not the selection rule for the quadrupolar mechanism derived in the previous chapter applies to the experimental spectra obtained for each polarization combination.

6.4 Conclusion

Using the quadrupolar selection rule derived in the previous chapter, the mechanism of VSFG at the air/benzene, air/cyclohexane, and air/decane interfaces was analyzed. For the air/benzene and air/cyclohexane interfaces, VSFG was shown to be due to the quadrupolar mechanism. These results show for the first time that the quadrupolar mechanism can actually contribute to VSFG, and they suggest that this mechanism may have a considerable contribution to VSFG also at various other interfaces. Since the quadrupolar mechanism is irrelevant to the breakdown of the inversion symmetry, the observation of VSFG at these two interfaces does not mean that benzene and cyclohexane molecules have a polar orientation at the interface. On the other hand, for the air/decane interface, the ordinary dipolar mechanism was found to contribute to VSFG. This result indicates that the decane molecules have a polar alignment at the interface, in spite of its extremely low polarity.

Part IV

Conclusion

Chapter 7

Summary and prospects

7.1 Summary of the thesis

In this thesis, experimental and theoretical developments for heterodyne-detected vibrational sum frequency generation (HD-VSFG) spectroscopy at air/liquid interfaces were reported to make it available for wider applications in which HD-VSFG spectroscopy has never been used in the past.

First, HD-VSFG has previously provided only the static structural information of interfaces, and it has never been utilized to extract the transient structure and orientation of short-lived reaction intermediates at interfaces arising from the electronic excitation of molecules. The transient measurement of those short-lived species was realized by the development of UV-excited time-resolved HD-VSFG spectroscopy as described in Part II. In this method, chemical reactions are initiated by the femtosecond UV pump light, and the generated short-lived intermediate species are probed by HD-VSFG using the picosecond visible light and the femtosecond IR light. Owing to the femtosecond pulse duration of the UV-pump and IR-probe beams, the delay between pump and probe can be determined with the femtosecond resolution, resulting in the instrumental response as short as 130 fs. In the experiments involving the UV pump light, the accumulation of photoproducts due to the UV light is often problematic. In order to prevent this photoproduct accumulation at the sample surface, a novel flow cell was developed, which is capable of flowing the sample solution efficiently near the sample surface while keeping the surface height fluctuation below ~ 1 μm.

This novel technique was applied to the observation of hydrated electrons at the air/water interfaces. Electrons were prepared by the two-photon ionization of water at the air/water interface and by the one-photon ionization of indole at the air/indole aqueous solution interface. In the transient spectra in the OH stretch region, one transient spectral component was observed in common at the two interfaces, and this component was assigned to the OH stretch mode of the water molecules interacting with electrons. The analysis of the obtained transient spectra and their time evolution revealed that the electrons are partially hydrated at the air/water interfaces and they escape into bulk water within 100 ps. This behavior is greatly

different from the hydrated electrons in bulk water, where the electrons are fully hydrated and survive for several hundred nanoseconds [53]. I believe that the present finding has a significant contribution to put an end to the controversy about how the electrons exist at the air/water interface.

Second, HD-VSFG has never been used to study interfaces when they are comprised of molecules having the inversion symmetry or when the molecules at the interfaces are randomly oriented. This is because the ordinary theory within the dipole approximation predicts that VSFG is forbidden at those interfaces, and it was impossible to interpret the experimentally observed spectra. It was shown in Part III that the observation of VSFG at those interfaces can be explained by considering the higher order electric quadrupole contribution. Based on the extended theory of VSFG with the quadrupole contribution, it is possible to discuss the physical implications of the observed spectra. This was explicitly shown by deriving the vibrational selection rule for the quadrupolar mechanism with the use of the group theory. The practical significance of this mechanism is that VSFG due to the electric quadrupole does not reflect molecular orientation and some bulk properties also appear in the observed signal, which is in sharp contrast to VSFG due to the ordinary dipolar mechanism. Hence, it is critically important to discern the mechanism before interpreting the spectra.

With this in mind, the mechanism of VSFG at the air/benzene, air/cyclohexane, and air/decane interfaces was investigated by HD-VSFG spectroscopy. All of these interfaces are comprised of nonpolar molecules, and in particular, benzene and cyclohexane are centrosymmetric. For the air/benzene and air/cyclohexane interfaces, the observed vibrational modes were fully consistent with the selection rule of the quadrupolar mechanism, and VSFG was shown to be caused by the quadrupole contribution. This study shows for the first time that VSFG at air/liquid interfaces can actually take place due to the quadrupole contribution. Meanwhile, for the air/decane interface, the observed modes were inconsistent with the quadrupolar selection rule, and VSFG was found to be due to the ordinary dipolar mechanism. This means that the orientation of decane is not random at the interface, and that there is a preferential direction for decane molecules to be oriented, which is surprising considering the low polarity of the decane molecules.

7.2 Prospects

The UV-excited time-resolved HD-VSFG spectroscopy reported in Part II enables the observation of chemical reactions at air/liquid interfaces for the first time. Since many of the interfacial reactions are unique to the interface and are clearly distinct from the reactions in the bulk, they cannot be understood from the extrapolation of the bulk properties. For instance, the two-dimensional proton diffusion on biological membranes is reported to be much faster than the three-dimensional diffusion in the solution phase [117]. Another example is that the rate of some reactions such as Diels-Alder and Wittig reactions

is greatly enhanced at the interface [118]. Hence, it is crucial to study those reactions *in situ* at the interface using a time-resolved and interface-selective method, i.e. the UV-excited time-resolved HD-VSFG spectroscopy developed in this study. Using this method, it is possible to investigate how the reactant molecules interact with each other, undergo structural changes, and result in the product molecules, and whethere or not each of these steps is different from those in the bulk reactions based on the structural information provided by the vibrational spectroscopy. Thus, the present method should be capable of providing valuable new insights into the molecular-level origin of those reaction anomalies at the interface. In other words, it can help us have a better understanding about what makes the interface different from the bulk.

The quadrupole contribution to the VSFG process discussed in Part III is probably shocking for many of the VSFG spectroscopists who have implicitly assumed that the electric dipole approximation is always accurate, because the present result suggests that their interpretation of VSFG spectra based on the ordinary dipolar theory might be sometimes incorrect. For example, it was previously speculated that benzene molecules are distorted at the air/benzene interface based merely on the observation of VSFG at this interface [32]. This is because VSFG is forbidden for centrosymmetric molecules according to the theory within the dipole approximation. However, the detailed analysis of VSFG at the air/benzene interface presented in this thesis revealed that the benzene molecules at the interface are free from distortion and that VSFG is caused by the quadrupolar mechanism. In this sense, the present quadrupolar theory complements the ordinary dipolar theory of VSFG, and it enabled for the first time to correctly interpret the VSFG spectra. Then, the next question would be how significant the quadrupole contribution is in general, as compared with the dipole contribution. Since the selection rule presented in this thesis was derived merely by using the group theory, it does not provide any information about the intensity of the observed vibrational bands. The quantitative estimation of the band intensities can be accomplished using the theoretical formulae presented in this thesis (Eqs. (5.109)-(5.112) and (5.113)-(5.115)). In these formulae, the quadrupolar hyperpolarizability, $\beta_{ijkl}^{\mathrm{quad}}$, can be evaluated from *ab inito* quantum chemical calculations, and the averaged molecular orientation, $\langle R_{Ii}R_{Jj}R_{Kk}R_{Ll}\rangle_{\mathrm{av}}$, and the number of molecules at the interface, N, can be obtained from the molecular dynamics (MD) simulations. The systematic application of these quantitative estimations to various interfaces might provide a general rule as to when the quadrupole contribution becomes predominant and when it is neglegible. Such a general rule will be practically important for extracting the interfacial properties from the observed VSFG spectra.

IR absorption was discovered in the 19th century, and Raman scattering was discovered in 1932 [119]. These two methods have now grown into well-established standard techniques for obtaining vibrational spectra of bulk sample, that are used not only by physical chemists but also by organic chemists

and many other people. Meanwhile, the first interface spectrum by VSFG was obtained only in 1987 [10], and the multiplex acquisition of Im $\chi^{(2)}_{\mathrm{eff}}$ spectra by HD-VSFG became possible as late as in 2009 [19]. As is obvious from this comparison, HD-VSFG spectroscopy has a much shorter history than IR and Raman spectroscopy, and it is still in the course of development. I believe that the works presented in this thesis have made some contribution to bring this technique up to a more mature state.

Bibliography

[1] C. T. Williams and D. A. Beattie, *Surf. Sci.* **500**, 545 (2002).

[2] K. Tanabe and W. F. Holderich, *Appl. Catal. A* **181**, 399 (1999).

[3] D. E. Clapham, *Cell* **97**, 547 (1999).

[4] M. A. Tolbert, *Science* **264**, 527 (1994).

[5] P. Atkins and J. d. Paula, *Atkins' Physical Chemistry*, 7 ed. (Oxford University Press, New York, 2002).

[6] A. Hartstein, J. R. Kirtley, and J. C. Tsang, *Phys. Rev. Lett.* **45**, 201 (1980).

[7] M. Fleischmann, P. J. Hendra, and A. J. McQuillan, *Chem. Phys. Lett.* **26**, 163 (1974).

[8] M. G. Albrecht and J. A. Creighton, *J. Am. Chem. Soc.* **99**, 5215 (1977).

[9] K. Matsuzaki, R. Shimada, and H. Hamaguchi, *Langmuir* **29**, 2471 (2013).

[10] X. D. Zhu, H. Suhr, and Y. R. Shen, *Phys. Rev. B* **35**, 3047 (1987).

[11] Y. M. Chang, L. Xu, and H. W. K. Tom, *Phys. Rev. Lett.* **78**, 4649 (1997).

[12] S. Yamaguchi and T. Tahara, *J. Phys. Chem. B* **109**, 24211 (2005).

[13] Y. R. Shen, *Annu. Rev. Phys. Chem.* **64**, 129 (2013).

[14] R. Superfine, J. Y. Huang, and Y. R. Shen, *Opt. Lett.* **15**, 1276 (1990).

[15] V. Ostroverkhov, G. A. Waychunas, and Y. R. Shen, *Phys. Rev. Lett.* **94**, 046102 (2005).

[16] N. Ji, V. Ostroverkhov, C.-Y. Chen, and Y.-R. Shen, *J. Am. Chem. Soc.* **129**, 10056 (2007).

[17] I. V. Stiopkin, H. D. Jayathilake, A. N. Bordenyuk, and A. V. Benderskii, *J. Am. Chem. Soc.* **130**, 2271 (2008).

[18] S. Yamaguchi and T. Tahara, *J. Chem. Phys.* **129**, 101102 (2008).

[19] S. Nihonyanagi, S. Yamaguchi, and T. Tahara, *J. Chem. Phys.* **130**, 204704 (2009).

[20] K. Watanabe, K. Inoue, I. F. Nakai, and Y. Matsumoto, *Phys. Rev. B* **81**, 241408 (2010).

[21] X. Chen, W. Hua, Z. Huang, and H. C. Allen, *J. Am. Chem. Soc.* **132**, 11336 (2010).

[22] R. E. Pool, J. Versluis, E. H. G. Backus, and M. Bonn, *J. Phys. Chem. B* **115**, 15362 (2011).

[23] Q. Du, E. Freysz, and Y. R. Shen, *Science* **264**, 826 (1994).

[24] S. Nihonyanagi, T. Ishiyama, T.-k. Lee, S. Yamaguchi, M. Bonn, A. Morita, and T. Tahara, *J. Am. Chem. Soc.* **133**, 16875 (2011).

[25] S. Nihonyanagi, P. C. Singh, S. Yamaguchi, and T. Tahara, *Bull. Chem. Soc. Jpn.* **85**, 758 (2012).

[26] W. Xiong, J. E. Laaser, R. D. Mehlenbacher, and M. T. Zanni, *Proc. Natl. Acad. Sci. U. S. A.* **108**, 20902 (2011).

[27] P. C. Singh, S. Nihonyanagi, S. Yamaguchi, and T. Tahara, *J. Chem. Phys.* **137**, 094706 (2012).

[28] H. Graener, G. Seifert, and A. Laubereau, *Phys. Rev. Lett.* **66**, 2092 (1991).

[29] M. C. Asplund, M. T. Zanni, and R. M. Hochstrasser, *Proc. Natl. Acad. Sci. U. S. A.* **97**, 8219 (2000).

[30] T. P. Dougherty and E. J. Heilweil, *Opt. Lett.* **19**, 129 (1994).

[31] H. Hamaguchi and T. L. Gustafson, *Annu. Rev. Phys. Chem.* **45**, 593 (1994).

[32] E. L. Hommel and H. C. Allen, *Analyst* **128**, 750 (2003).

[33] N. Bloembergen, R. K. Chang, S. S. Jha, and C. H. Lee, *Phys. Rev.* **174**, 813 (1968).

[34] Y. R. Shen, *J. Phys. Chem. C* **116**, 15505 (2012).

[35] P. A. M. Dirac, *The Principles of Quantum Mechanics*, 4 ed. (Oxford University Press, London, 1958).

[36] Y. R. Shen, *The Principles of Nonlinear Optics* (Wiley, New York, 1984).

[37] S. S. Andrews, *J. Chem. Educ.* **81**, 877 (2004).

[38] L. Velarde, X. Y. Zhang, Z. Lu, A. G. Joly, Z. Wang, and H. F. Wang, *J. Chem. Phys.* **135**, 241102 (2011).

[39] T. F. Heinz, *Modern Problems in Condensed Matter Sciences* (Elsevier, Amsterdam, 1991), pp. 353–416, Chapter 5 - Second-Order Nonlinear Optical Effects at Surfaces and Interfaces.

[40] X. Wei, S. Hong, A. Lvovsky, H. Held, and Y. Shen, *J. Phys. Chem. B* **104**, 3349 (2000).

[41] Y. Rao, D. Song, N. J. Turro, and K. B. Eisenthal, *J. Phys. Chem. B* **112**, 13572 (2008).

[42] Y. Rao, N. J. Turro, and K. B. Eisenthal, *J. Phys. Chem. C* **114**, 17703 (2010).

[43] J. A. McGuire and Y. R. Shen, *Science* **313**, 1945 (2006).

[44] S. Nihonyanagi, J. A. Mondal, S. Yamaguchi, and T. Tahara, *Annu. Rev. Phys. Chem.* **64**, 579 (2013).

[45] W. Kiefer and H. J. Bernstein, *Appl. Spectrosc.* **25**, 500 (1971).

[46] K. Iwata and H. Hamaguchi, *Chem. Phys. Lett.* **196**, 462 (1992).

[47] K. Inoue, K. Watanabe, and Y. Matsumoto, *J. Chem. Phys.* **137**, 024704 (2012).

[48] W. H. Press, B. P. Flannery, S. A. Teukolsky, and W. T. Vetterling, *Numerical Recipes in C: The Art of Scientific Computing* (Cambridge University Press, New York, 1988).

[49] J. D. Jackson, *Classical Electrodynamics*, 3 ed. (Wiley, New York, 1998).

[50] *CRC Handbook of Chemistry and Physics*, 81 ed. (CRC Press, Boca Raton, 2000).

[51] R. Katoh, A. Furube, K. Hara, S. Murata, H. Sugihara, H. Arakawa, and M. Tachiya, *J. Phys. Chem. B* **106**, 12957 (2002).

[52] E. J. Hart and J. W. Boag, *J. Am. Chem. Soc.* **84**, 4090 (1962).

[53] D. N. Nikogosyan, A. A. Oraevsky, and V. I. Rupasov, *Chem. Phys.* **77**, 131 (1983).

[54] J. Peon, G. C. Hess, J.-M. L. Pecourt, T. Yuzawa, and B. Kohler, *J. Phys. Chem. A* **103**, 2460 (1999).

[55] P. Kambhampati, D. H. Son, T. W. Kee, and P. F. Barbara, *J. Phys. Chem. A* **106**, 2374 (2002).

[56] M. Mizuno and T. Tahara, *J. Phys. Chem. A* **105**, 8823 (2001).

[57] M. Mizuno and T. Tahara, *J. Phys. Chem. A* **107**, 2411 (2003).

[58] M. Mizuno, S. Yamaguchi, and T. Tahara, *J. Phys. Chem. A* **109**, 5257 (2005).

[59] M. J. Tauber and R. A. Mathies, *J. Phys. Chem. A* **105**, 10952 (2001).

[60] M. J. Tauber and R. A. Mathies, *Chem. Phys. Lett.* **354**, 518 (2002).

[61] M. J. Tauber and R. A. Mathies, *J. Am. Chem. Soc.* **125**, 1394 (2003).

[62] P. B. Petersen and R. J. Saykally, *Annu. Rev. Phys. Chem.* **57**, 333 (2006).

[63] K. R. Siefermann, Y. Liu, E. Lugovoy, O. Link, M. Faubel, U. Buck, B. Winter, and B. Abel, *Nat. Chem.* **2**, 274 (2010).

[64] Y. Tang, H. Shen, K. Sekiguchi, N. Kurahashi, T. Mizuno, Y. Suzuki, and T. Suzuki, *Phys. Chem. Chem. Phys.* **12**, 3653 (2010).

[65] A. T. Shreve, T. A. Yen, and D. M. Neumark, *Chem. Phys. Lett.* **493**, 216 (2010).

[66] A. Lubcke, F. Buchner, N. Heine, I. V. Hertel, and T. Schultz, *Phys. Chem. Chem. Phys.* **12**, 14629 (2010).

[67] D. M. Sagar, C. D. Bain, and J. R. R. Verlet, *J. Am. Chem. Soc.* **132**, 6917 (2010).

[68] A. Madarasz, P. J. Rossky, and L. Turi, *J. Chem. Phys.* **126**, 234707 (2007).

[69] F. Uhlig, O. Marsalek, and P. Jungwirth, *J. Phys. Chem. Lett.* **4**, 338 (2013).

[70] K. Shiratori and A. Morita, *J. Chem. Phys.* **134**, 234705 (2011).

[71] F. Saito, S. Tobita, and H. Shizuka, *J. Photochem. Photobiol. A* **106**, 119 (1997).

[72] N. Ji, V. Ostroverkhov, C. Tian, and Y. Shen, *Phys. Rev. Lett.* **100**, 096102 (2008).

[73] T. Ishiyama, H. Takahashi, and A. Morita, *Phys. Rev. B* **86**, 035408 (2012).

[74] J. A. Mondal, S. Nihonyanagi, S. Yamaguchi, and T. Tahara, *J. Am. Chem. Soc.* **134**, 7842 (2012).

[75] M. Majoube and G. Vergoten, *J. Raman Spectrosc.* **23**, 431 (1992).

[76] S. Yamaguchi and H. Hamaguchi, *J. Chem. Phys.* **109**, 1397 (1998).

[77] R. Shimada and H. Hamaguchi, *J. Chem. Phys.* **134**, 034516 (2011).

[78] S. Nihonyanagi, S. Yamaguchi, and T. Tahara, *J. Am. Chem. Soc.* **132**, 6867 (2010).

[79] J. A. Mondal, S. Nihonyanagi, S. Yamaguchi, and T. Tahara, *J. Am. Chem. Soc.* **132**, 10656 (2010).

[80] C. Tian, N. Ji, G. A. Waychunas, and Y. R. Shen, *J. Am. Chem. Soc.* **130**, 13033 (2008).

[81] N. I. Hammer, J. R. Roscioli, J. C. Bopp, J. M. Headrick, and M. A. Johnson, *J. Chem. Phys.* **123**, 244311 (2005).

[82] L. Kevan, *Acc. Chem. Res.* **14**, 138 (1981).

[83] K. R. Siefermann and B. Abel, *Angew. Chem. Int. Ed.* **50**, 5264 (2011).

[84] J. R. R. Verlet, A. E. Bragg, A. Kammrath, O. Cheshnovsky, and D. M. Neumark, *Science* **307**, 93 (2005).

[85] M. U. Sander, K. Luther, and J. Troe, *J. Phys. Chem.* **97**, 11489 (1993).

[86] X. Zhuang, P. B. Miranda, D. Kim, and Y. R. Shen, *Phys. Rev. B* **59**, 12632 (1999).

[87] Y. R. Shen, *Frontiers in Laser Spectroscopy, Proceedings of the International School of Physics "Enrico Fermi"* (North-Holland, Amsterdam, 1994), pp. 139–165.

[88] K. Shiratori and A. Morita, *Bull. Chem. Soc. Jpn.* **85**, 1061 (2012).

[89] S. Yamaguchi, K. Shiratori, A. Morita, and T. Tahara, *J. Chem. Phys.* **134**, 184705 (2011).

[90] J. J. Sakurai, *Advanced Quantum Mechanics* (Addison-Wesley, 1967).

[91] P. Guyot-Sionnest and Y. R. Shen, *Phys. Rev. B* **35**, 4420 (1987).

[92] J. E. Sipe, V. Mizrahi, and G. I. Stegeman, *Phys. Rev. B* **35**, 9091 (1987).

[93] T. Kawaguchi, K. Shiratori, Y. Henmi, T. Ishiyama, and A. Morita, *J. Phys. Chem. C* **116**, 13169 (2012).

[94] H. Hamaguchi, *J. Chem. Phys.* **69**, 569 (1978).

[95] J. G. Harris, *J. Phys. Chem.* **96**, 5077 (1992).

[96] M. Kawamata and T. Yamamoto, *J. Phys. Soc. Jpn.* **66**, 2350 (1997).

[97] B. M. Ocko, X. Z. Wu, E. B. Sirota, S. K. Sinha, O. Gang, and M. Deutsch, *Phys. Rev. E* **55**, 3164 (1997).

[98] G. A. Sefler, Q. Du, P. B. Miranda, and Y. R. Shen, *Chem. Phys. Lett.* **235**, 347 (1995).

[99] O. Esenturk and R. A. Walker, *J. Chem. Phys.* **125**, 174701 (2006).

[100] J. E. Bertie and C. D. Keefe, *J. Chem. Phys.* **101**, 4610 (1994).

[101] K. Matsuzaki, S. Nihonyanagi, S. Yamaguchi, T. Nagata, and T. Tahara, *J. Phys. Chem. Lett.* **4**, 1654 (2013).

[102] R. H. Page, Y. R. Shen, and Y. T. Lee, *J. Chem. Phys.* **88**, 5362 (1988).

[103] S. N. Thakur, L. Goodman, and A. G. Ozkabak, *J. Chem. Phys.* **84**, 6642 (1986).

[104] E. R. Wilson, J. C. Decius, and P. C. Cross, *Molecular Vibrations, The Theory of Infrared and Raman Vibrational Spectra* (Dover, New York, 1955).

[105] P. Atkins and R. Friedman, *Molecular Quantum Mechanics* (Oxford, New York, 2005).

[106] T. D. Jaeger, E. D. Pillai, and M. A. Duncan, *J. Phys. Chem. A* **108**, 6605 (2004).

[107] K. B. Wiberg, V. A. Walters, and W. P. Dailey, *J. Am. Chem. Soc.* **107**, 4860 (1985).

[108] K. B. Wiberg and A. Shrake, *Spectrochim. Acta, Part A* **27**, 1139 (1971).

[109] M. Squillacote, R. S. Sheridan, O. L. Chapman, and F. A. L. Anet, *J. Am. Chem. Soc.* **97**, 3244 (1975).

[110] J. L. Offenbach, L. Fredin, and H. L. Strauss, *J. Am. Chem. Soc.* **103**, 1001 (1981).

[111] E. Matrai, M. Gal, and G. Keresztury, *Spectrochim. Acta, Part A* **46**, 29 (1990).

[112] F. A. Miller and H. R. Golob, *Spectrochim. Acta* **20**, 1517 (1964).

[113] H. Takahashi, T. Shimanouchi, K. Fukushima, and T. Miyazawa, *J. Mol. Spectrosc.* **13**, 43 (1964).

[114] C. D. Keefe and J. E. Pickup, *Spectrochim. Acta, Part A* **72**, 947 (2009).

[115] R. G. Snyder, S. L. Hsu, and S. Krimm, *Spectrochim. Acta, Part A* **34**, 395 (1978).

[116] M. R. Watry, T. L. Tarbuck, and G. L. Richmond, *J. Phys. Chem. B* **107**, 512 (2002).

[117] A. Y. Mulkidjanian, J. Heberle, and D. A. Cherepanov, *Biochim. Biophys. Acta* **1757**, 913 (2006).

[118] S. Tiwari and A. Kumar, *J. Phys. Chem. A* **113**, 13685 (2009).

[119] C. V. Raman and K. S. Krishnan, *Nature* **121**, 501 (1928).

Acknowledgements

First of all, I would like to express my sincerest gratitude to Professor Takashi Nagata and Professor Tahei Tahara at RIKEN for giving me a chance to conduct my research at their laboratories. Under their supervision, I was always able to concentrate on the research topic I was interested in without any inconvenience, and I very much enjoyed doing the research during these three years. Additionally, being involved in two laboratories helped me to have a broader view about science.

Among the friendly and very competent colleagues at the two laboratories, I am especially grateful to Dr. Shoichi Yamaguchi and Dr. Satoshi Nihonyanagi. It was my greatest excitement to work with and learn from these two researchers who have actually developed heterodyne-detected sum frequency generation. Without their patient support, I would not have been able to accomplish any of the works presented in this thesis.

Last but not least, I would like to thank my family for their emotional as well as financial support.